Targeting Sirt1 and Its Pathway for Therapeutic Intervention of Cancer: Drug Design and Biological Evaluation

THESIS

Submitted in partial fulfillment

of the requirements for the degree of

DOCTOR OF PHILOSOPHY

by

VENKAT KOUSHIK PULLA

ID No 2011PHXF024H

Under the Supervision of

Prof. P. YOGEESWARI

BITS Pilani tg

Pilani | Dubai | Goa | Hyderabad

BIRLA INSTITUTE OF TECHNOLOGY AND SCIENCE, PILANI

2015

BIRLA INSTITUTE OF TECHNOLOGY AND SCIENCE, PILANI

CERTIFICATE

This is to certify that the thesis entitled "**Targeting Sirt1 and its pathway for therapeutic intervention of cancer: Drug design and Biological evaluation**" and submitted by **VENKAT KOUSHIK PULLA** ID No. **2011PHXF024H** for award of Ph.D. of the Institute embodies original work done by him under my supervision.

Signature of the Supervisor:

Name in capital letters: **P.YOGEESWARI**

Designation: **Professor**

Date:

ACKNOWLEDGEMENT

First and foremost I would like to thank God Almighty who has given me this opportunity.

I would like to give heart full thanks to my supervisor, Prof.P.Yogeeswari, Professor and Associate Dean (Sponsored Research and Consultancy Division), Department of Pharmacy, BITS-Pilani Hyderabad Campus for her continuous guidance, suggestions and support. She was always an inspiration to me. I am thankful for her enthusiasm, patience and love for research. She always encourage new thoughts and give constant support throughout the project.. The experiences gained under her guidance are memorable and will be cherished throughout my life.

I deeply acknowledge and heartfelt thanks to Prof.D.Sriram, Professor, Department of Pharmacy, BITS-Pilani Hyderabad Campus for his valuable suggestions, guidance offered to me during this period.

I am thankful to acknowledge my DAC member Dr. Vamsi Krishna Venuganti, for his support and encouragement during this period.

I am grateful to Prof.Bijendra N. Jain, Vice-Chancellor, BITS-Pilani Campus and Prof.V.S.Rao, Director, BITS-Pilani Hyderabad Campus for allowing me to carry out my doctoral research work in the institute.

I am thankful to Prof.M.M.S.Anand, Registrar and Prof.S.K.Verma, Dean, Acamedic Research (Ph.D. Programme), BITS-Pilani for their support to do my research work.

I would like to Prof.M.B.Srinivas, Dean, Administration and Prof.Vidya Rajesh, Associate Dean, Academic Research (Ph.D Programme), BITS-Pilani Hyderabad Campus for their continuous support and encouragement during my research work. I would like to express my gratitude to Prof..Srikanth Charde, Associate Professor & Head, Department of Pharmacy, BITS-Pilani Hyderabad Campus for providing me with all necessary laboratory facilities and for having helped me at various stages of my research work.

I sincerely acknowledge the help rendered by Prof.Punna Rao, Prof.Sajeli Begum, and other Faculty members, Department of Pharmacy, BITS-Pilani Hyderabad Campus.

I am grateful to express my sincere thanks to all my friends Dr. Monika, Dr. Mallika, Dr. Aditya, Jean, Patrisha, Rahul, Praveen, Srikanth, Rukkaiyya, Mahibalan, Madhu Babu, Shailender, Brindha, Manoj, Reshma.A, Shalini, Ganesh.S, Saketh, Gangadhar, Poorna, Ganesh.P, Santhosh, Brahmam, Renuka, Priyanka.S, Radhika, Vijay, Suman, Bobesh, Anup, Sridevi, Preeti, Hasitha, Omkar, Peter, Bomba, Reshma.L, Priyanka.P, late Thimmappa and late Srividya for the time they had spent for me and helped me to complete my work.

I am very much thankful to the post graduate students Nancy malik, Shruthi for their help in setting up the experiments.

I express my thanks to our laboratory attenders and demonstrators Mr. Rajesh, Mr.Venkat, Mr.Seenu, Ms.Saritha and Ms.Rekha for all their support.

I deeply acknowledge Department of Biotechnology (DBT) New Delhi, India for financial funding in the initial stage and later Council of Scientific and Industrial Research (CSIR), for financial assistance in the form of CSIR SRF award [09/1026(0014)/2014.EMR-I].

At the end, but from my heart, I thank and deeply appreciate my family P. Upender Reddy (Father), P. Nageshwari (Mother) and P. Pravalika (Sister) for their faith in me and for continuous support. It was under their influence I gained so much drive and an ability to tackle challenges head on. No words can express how grateful I am for their love and support. Finally, I would like to thank my wife (J. Renuka) for her constant support at various phase of my life, because of her; every day is new and blissful.

Venkat Koushik Pulla

ABSTRACT

Cancer is a complicated disease so is its treatment. For the past many decades, research has been progressing, yet tip of the iceberg are only known about its etiology. The understanding about the characteristics and the hallmarks of cancer have been increasing day by day. Similarly, research on various proteins and their role in cancer complication has been the primary focus of research. Discovering small molecule modulators of these proteins (enzymes) might fill the large gap in cancer therapeutics. Further, it also might help in understanding the mechanistic role in various pathways. Human SIRT1, a homologous protein of yeast sir2 enzyme, deacetylates histone and non histone proteins. It modulates the epigenetic regulation of various genes involved in cancer, which include various transcription factors and DNA repair enzymes. Further, it was known to be overexpressed in many cancer conditions and partial suppression of SIRT1 activity had reduced cancer symptoms. SIRT1 function is modulated by NAD^+ levels in the cell, which acts as a co-substrate for SIRT1 activity. NAMPT is a rate limiting enzyme involved in the synthesis of NAD^+ and interestingly, it was also found overexpressed in many cancer conditions. Hence the prime objective of our study was to design small molecule inhibitors against SIRT1 and NAMPT to treat cancer conditions. Thus, we employed both structure and ligand based drug designing strategies to discover small molecule inhibitors against both the proteins (SIRT1 and NAMPT).

In the present study, a diverse and novel set of molecules as SIRT1 and NAMPT inhibitors were initially identified and were further experimentally evaluated employing in-vitro enzymatic

assays. Potent molecules where further studied their anticancer activates in various cancer cell lines and molecules showing best activity were further evaluated their activity in benign prostate hyperplasia animal model.

Among all the identified SIRT1 inhibitors, **Lead17** was found to be most potent with IC_{50} of 4.34 μM and GIC_{50} of 360 nM on LnCAP cells (Prostate). After further analyses employing cell cycle analyses and apoptosis assay, it was confirmed that **Lead17** inhibit the prostate cancer (LnCAP) cell growth *via* inducing apoptosis. Interestingly, **Lead17** has also significantly reduced prostate weight to body weight ratio compared to the testosterone treated animal in benign prostate hyperplasia animal model. Histopathology of prostate tissue has further confirmed that there was a reduction in prostate hyperplasia in the animals treated with **Lead17** comparable with finasteride treated animals.

Similarly, NAMPT inhibitors such as **Lead5**, **Lead13**, **Lead RR2** and **Lead ND2** were identified with IC_{50}'s of 13.77 μM, 5.62 μM, 2.73 μM and 3.11 μM respectively. Upon, further analyses of potent leads, it proved to induce cell death *via* apoptosis. The role of SIRT1 and NAMPT inhibitors in reducing the reactive oxygen species were determined and showed there is a significant reduction in mRNA levels of inflammatory cytokines (IL-6 and TNF-α). Further testing of inhibitors in reducing the acute inflammation of paw (induced by carrageenan), proved that SIRT1 and NAMPT inhibitors were found to reduce inflammatory conditions comparable to indomethacin (NSAID).

Thus, in this study for the first time identified novel structural inhibitors of SIRT1 and NAMPT, employing two different drug design strategies and developed a prototypical lead for next generation therapeutics in treating both cancer and inflammatory disease conditions.

Table of contents

List of tables

List of Figures

Abbreviations

3D-QSAR	Three dimensional -quantitative structural activity relationship
ADP	Adenosine diphosphate
AIDS	Acquired immune deficiency syndrome
APC	Adenomatous polyposis coli
AR	Androgen receptor
ARTs	ADP-ribose transferases
ATCC	American Type Cell Collection
ATP	Adenosine triphosphate
BCL6	B cell lymphoma 6
BEDROC	Boltzmann-enhanced discrimination of receiver operating characteristic
BITS-Pilani	Birla Institute of Technology and Science, Pilani
BRCA	Breast cancer antigen
BSA	Bovine serum albumin
CC50	Cytotoxic concentration 50
CpG	Cytosine-phosphate-Guanine
CYP2C9	Cytochrome P450 2C9
DCFDAE	2',7' dichlorofluorescin diacetate
DMSO	Dimethyl sulfoxide
DNA	Deoxyribose nucleic acid
DNMTs	DNA methyl transferase
DSF	Differential scanning fluorimetry
DTT	Dithiothreitol
EF	Enrichment factor
eNOS	Endothelial nitric oxide synthase
e-pharmacophore	Energy based pharmacophore
ERK	Extracellular signal-regulated kinase
Foxo	Forkhead box, class O
GAPDH	Glyceraldehyde-3-Phosphate Dehydrogenase
GH	Goodness of hits
GOLD	Genetic Optimization for Ligand Docking
H3K9me3	H3 tri methyl K9
HCLO4	Perchloric acid
HCT116	Human colon carcinoma cell line 116
HDACs	Histone deacetylases

HIC1	Hypermethylated in cancer 1
HTS	High-Throughput Screening
HTVS	High throughput virtual screening
IC50	Half maximal inhibitory concentration
IEAC	Institute animal ethical committee
IL	Interleukin
IPTG	Isopropyl β-D-1-thiogalactopyranoside
K2CO3	Pottasium carbonate
KOH	Pottasium hydroxide
L	Liter
LB	Luria-Bertani
LnCAP	Lymph Node Carcinoma of the Prostate
LOO	Leave one out
LPS	Lipopolysaccharide
MAPK	Mitogen-activated protein kinases
MDAMB-231	M.D. Anderson - metastatic breast-231 cell line
mg	Milligram
MgCl2	Magnesium chloride
MiRs	Micro ribose nucleic acids
MLH1	MutL homolog 1
mRNA	Messenger RNA
MTT	(4,5-dimethylthiazol-2-yl)-2,5-diphenyltetrazolium bromide
NAD	Nicotinamide adenine dinucleotide
NAM	Nicotinamide
NAMPT	Nicotinamide phosphoribosyl transferase
NF-kB	nuclear factor kappa B
nM	Nanomolar
NMN	Nicotinamide mono nucleotide
NMNAT	Nicotinamide mononucleotide adenylyltransferase
p53	Phosphoprotein 53
p73	Phosphoprotein 73
PARPs	Poly (ADP-ribose) polymerase
PBEF	pre-B-cell colony-enhancing factor
PBS	Phosphate buffered saline
PCR	Polymerase Chain Reaction
PDB	Protein Data Bank
pIC50	Negative logarithm of IC50
PLS	Partial leave square
pRb	Retinoblastoma protein
PRESS	Predictive residual sum of squares
PRPP	5-Phosphoribosyl pyrophosphate

Qrtpcr	Quantitative reverse transcriptase Polymerase chain reaction
RMSD	Root mean square deviation
RMSE	Root mean square error
ROS	Reactive oxygen species
RPM	Rotation per minute
RPMI	Roswell Park Memorial Institute medium
RT	Room temperature
SAR	Structure activity relationship
SCF	Stem cell factor
SD	Standard deviation
SDS-PAGE	Sodium dodecyl sulpahte-polyacrylamide gel electrophoresis
SFRP1	Secreted frizzled related protein
Sir2	Silent information regulator 2
SiRNA	Small interfering RNA
SIRT	Silent information regulator
SMAD	Mothers against decapentaplegic homolog
SP	Standard precision
SUV39H1	Suppressor Of Variegation 3-9 Homolog 1
TM	Melting temperature
TNF-α	Tumour necrosis factor alpha
TRAIL	TNF- related apoptosis inducing ligand
TRAIL	TNF-related apoptosis-inducing ligand
U87 cell line	Human astrocytoma cell line
VEFGR	Vascular endothelial growth factor
XP	Extra precision
µg	Microgram
µM	Micromolar

Chapter 1: Introduction

1.1. Cancer

Cancer is very common term used in day to day life. However the etiology and types of cancers is a huge subject and equally complicated. It is known that more than one fifth of all deaths in industrialized countries are due to the cancer, which depicts the importance of studying cancer (Schulz W A., 2005). Principally the health conditions in less-industrialized countries differ significantly with the high industrialized part of the world, because of the continuing, recurring or newly emerging infectious diseases, which include malaria, tuberculosis and AIDS. However, cancer is equally important in these countries, characterizing different patterns of incidence and often with higher mortalities. The most prominent cancers manifested in less industrialized countries include stomach, liver, bladder, oesophagus and cervix (Danaei, V. H., *et al.,* 2005). Conversely, out of four major cancers (lung, large intestine, breast and prostate cancers) reported in industrialized countries, lung cancer has shown high impact in developing countries(Schulz W. A., 2005).

After three decades of continuous cancer research, complex data of knowledge has been generated, revealing cancer to be a dynamic disease (Hanahan D and Weinberg R. A., 2000). There has been many mutations discovered, resulting in recessive loss of tumor suppressor gene function. Many scientists would argue that search for the origin and treatment of this disease would carry on for another few decades, adding more complex layers of scientific knowledge (Hanahan D and Weinberg R. A., 2000). Based on literature, logically Hanahan and Weinberg foresee few hallmarks of cancer, which was widely accepted. They were self-sufficiency in growth signals, insensitivity to antigrowth signals, tissue invasion and metastasis, limitless replicative potential, sustained angiogenesis and evading apoptosis (Hanahan D and Weinberg R. A., 2011).

1.2. Causes of cancer

The genetic makeup of human population hardly changed within a century and differed moderately between populations with different geographic background. The change in pattern of incidence over time and geographic background, could be inferred for the effect of environment as a major contribution to cancer (Danaei, V. H., *et al.,* 2005). Besides, we should not forget the role of endogenous processes in the body, which also contribute to cancer on their own or by interacting with exogenous agents. To define exact mechanism of cancer in human is very complicated being multifactorial. Each factor may act on different mechanism at different stages of cancer (Schulz W. A., 2005). Each factor could be categorized into initiator, promoter or co-carcinogen while studying cancer in animal models. Because, carcinogens were applied in individual steps and the result could be studied more precisely. However, these distinctions were hard to make in real human cancers. For instance, tobacco smoke causing cancer is a general fact, which we know and believe that tobacco smoke is a carcinogen. Besides it contains variety of carcinogens, some of them act like initiators and some as promoters and some as both. Considering nicotine as an example, we could say that it is not a direct carcinogen; however, it is an alkaloid which acts on the central nervous system influencing cell signaling and interactions. Hence nicotine was be classified as co-carcinogen (Schulz W. A., 2005). From the above discussions, it is often complex to elucidate exactly by which mechanism a potential carcinogen acts, even though it has been identified to be associated with specific cancer through epidemiological data (Hussain S.P., and Harris C.C., 2000). Necessary steps must be taken before the relationship between a carcinogen and cancer could be fully developed. However, clear elucidation of mechanism using molecular biology techniques could be a good beginning to prevent cancer. Carcinogens are generally divided into two categories; one being exogenous carcinogens, which include chemical, physical, and biological agents and the other one being endogenous processes, which include DNA replication, DNA repair, and chronic inflammation (Hussain S. P., and Harris C. C., 2000). How effective exogenous carcinogens elicit cancer in a specific person depends strongly on an individual's exposure, and general health. Besides, there are some cases where cancer could be caused due to endogenous processes.

In general metabolism generate various carcinogenic compounds like nitrosoamines, aromatic amines, quinines, estrogens and some reactive oxygen species (Bolt., 1996; Yager., 2000). The concentration of these compounds could depend on one's physical activity and diet. Nevertheless, body maintain several detoxification procedures to eliminate these potential carcinogens, but they could never be absolute sure. In the same way the other endogenous processes include DNA replication. Damage to DNA occurs at a minimum rate during cell proliferation. Due to errors in DNA replication or errors in DNA repair mechanism, damaged cells are removed by apoptosis and other mechanisms. All these protective mechanisms could not be perfect always. It was known recently that, as the age of an individual increases the protective mechanisms might become less efficient. This results in increased risk of cancer incidence (Hussain S. P., and Harris C. C., 2000). While the above process takes place in any time in humans, it could be a high risk when the tissues are proliferating after incurring the damage. Besides, fetal development is also an important stage, where the chance of genetic and epigenetic errors could be high. This might cause cancer in children either in young age or it could also favor cancer development in later stage in life (Esteller M., 2008).

1.3. Epigenetics

Conrad Waddington used the word 'epigenetics' first time in the early 1940s (Waddington C. H., 2012), which was used in current context to explain heritable changes in gene expression through mitotic and meiotic cell division, without altering the DNA sequence (Berger, K., 2009). Epigenetic regulation includes DNA methylation and histone modifications.

DNA methylation usually takes place at the 5' position of the cytosine ring within CpG dinucleotides, which results in silencing of genes. There are three DNA methyltransferases (DNMTs), which includes DNMT1 (maintains existing methylation pattern following DNA replication) and DNMT3A and DNMT3B (targeting previously unmethylated CpGs) (Bird A., 2002). CpG sites are present either in CpG islands, located at CpG rich DNA regions located mostly in human gene promoters or in the large repetitive sequences (Bird A., 2002)(Wang Y., and Leung F. C., 2004). CpG present in the large repetitive sequences like in

centromers are methylated majorly to prevent chromosome instability. However, some naturally occurring CpG island methylation occurs during X chromosome inactivation (during development). It is interesting to know that there are some chances of DNA methylation even at the non-cpG island promoters, for which further investigation is necessary for a clearer elucidation of DNA methylation.

All the epigenetic modifications has some relationship with chromatin, which are highly ordered structures consisting of DNA, histones and non histone proteins (Johnstone W. R., 2002). Chromatin is categorized into two distinct conformation states, one as heterochromatin and other as euchromatin. Heterochromatin is densely compact and inert to transcription. Conversely, euchromatin is less condensed and transcriptionally active (Jenuwein T., and Allis C. D., 2001). Histones are small basic proteins containing a globular domain and a flexible charged NH2 terminus known as histone tail. In general, regulation of gene expression occurs through posttranslational modifications of the histone tails (Wang, A., *et al*. 2007). The modifications seen at the histone tails include, acetylation sumoylation, proline isomerization and ADP- ribosylation (Wang, A., *et al*. 2007). Interestingly many studies revealed various combinations of the above modifications, like a histone code to more open or closed state of chromatin structure, which finally could result in the activation or repression of gene expression (Jenuwein, T., and Allis, C. D., 2001).

1.3.1. Epigenetic deregulation in cancer development

After understanding the importance of epigenetics, it is important to understand its role in cancer. The epigenetic mechanisms controlling transcription of genes involved in cell differentiation, proliferation and survival are often targets for deregulation in malignant development. Further to this, epigenetic mechanisms could also affect non coding microRNAs (MiRs), which could regulate the expression of various cellular proteins by affecting the mRNA stability. It is becoming more clear about the role of epigenetic deregulation that occur much before transforming event like mutations in tumor suppressors and in proto-oncogenes (Das, P. M., and Singal, R., 2004). The deregulation of epigenetic enzymes has been known to have important role in malignancies and disruption caused by

mutations, deletions or sometimes over expression could be very supportive in stating the critical role of epigenetic effectors in malignancies (Miremadi, A., Oestergaard, M. Z., *et al*. 2007). Surprisingly all the genes and miRs could epigenetically deregulate to promote the hallmarks of the cancer including self sufficiency in growth signals, insensitivity to growth inhibitory signals, evasion of apoptosis, increase in proliferation, sustained angiogenesis and capability of metastasis and invasion (Esteller 2008; Reid, Gallais *et al*., 2009; Hanahan and Weinberg 2011). It has been known that histone modifications undoubtedly play critical roles in epigenetic deregulation, acetylation and deacetylation of histones that have been clinically associated with various epigenetic disruptions in cancer cells (Seligson, H., *et al*., 2005).

1.3.2. Histone deacetylation and cancer

The main role of histone deacetylases (HDACs) is to oppose the activity of histone acetyl transferees (HATs) and regulate transcription by removing the acetyl groups from lysine residues of histone tails and targeted deacetylation of non histone substrates (Bolden, P., *et al.,* 2006). HDACs are categorized into four classes: class I consists of HDAC 1, 2, 3 and 8, which are believed to be localized in nucleus. Class II consists of HDAC 4, 5, 6, 7, 9 and 10 (found in both nucleus and cytoplasm). Class III consists of sirtuins (SIRT1-7); and finally class IV consist of HDAC 11, which has both the characteristic features of class I and II HDACS (Glozak, M., and Seto, E., 2007). It is interesting to know that class I, II and IV HDACs have similar sequence and structure and all require zinc ion for catalytic activity. Besides class III including sirtuins, do not have any similarities with other class of HDACs and require nicotinamide adenine dinucleotide (NAD+) for catalytic activity (Bolden, Peart et al., 2006). As Class I HDACs are present inside the nucleus, they regulate the histone acetylation and thus the chromatin structure (Bolden, P., *et al.,* 2006). However, it was clear that not all class I HDACs function in same way. For instance, knock down of HDAC1 and 2 but not HDAC3 suppressed the proliferation of colon carcinoma cells (Weichert, R., *et al.* 2008) and lymphocytic leukemia cells to TRAIL induced apoptosis (Inoue, M., *et al.* 2006). In contrast, there was a study which inferred that the knock down of HDAC3 was more effective in inhibiting the growth of colon carcinoma than the knockdown of HDAC1 or 2

(Wilson, B., *et al.,* 2006). In addition to this it was also suggested that the knock down of HDAC3 and HDAC2 induced DNA damage and resulted in concomitant apoptosis (Bhaskara, C., *et al.* 2008). Class II and IV HDACs are mainly found in cytoplasm and it was obvious that they mainly deacetylase non histone proteins (Bolden, P., *et al.,* 2006). Within the class II HDACs, there were functional differences between the proteins of this family. For example, knock down of HDAC4 resulted in inhibiton of cell proliferation resulting in induction of apoptosis (Wilson, B., *et al.*, 2008), whereas knock down of HDAC7 in endothelial cells did not affect cell survival but surprisingly inhibited cell migration and capacity to form capillaries (The hallmark of the cancer) (Mottet, B., *et al.,* 2007). In addition, other class II HDACs also showed role in angiogenesis, which knock down of HDAC6 and HDAC10 resulted in depletion of VEGFR1 and VEGFR2 (Park, K., *et al.,* 2008).

To summarize briefly, class I HDACs were mostly involved in cell proliferation and apoptosis whereas class II HDACs were more specifically involved in regulation of cell migration and angiogenesis. While much of the focus about HDACs and cancer was centered only on class I, II and IV HDACs, it was been shown that class III HDACs (sirtuins) also played an important role in regulating tumor onset and progression. Sirtuins deacetylate protein substrates including histones, and could mediate ADP ribosylation (Michan, S., and Sinclair, D., 2007)). Initially, these enzymes (Sirtuins) were studied for their role in regulating caloric restriction and lifespan of lower organisms (Michan, S., and Sinclair, D., 2007). Besides, sirtuins regulate cellular senescence, DNA repair, chromosomal stability, cell cycle progression and transcriptional activity of p53, p73, pRb, NF-kB and Foxo family of proteins. Supporting this, it was shown that SIRT1, SIRT2, SIRT3 and SIRT7 were found overexpressed in a variety of tumors (Michan, S., and Sinclair. D., 2007). Further to this, SIRT1 role in regulating tumor development, growth and survival was reported in recent studies and that pharmacological inhibition of SIRT1 activity or knock down of SIRT1 using siRNA resulted in reactivation of tumor suppressor genes like, SFRP1, SFRP2 and MLH1 and reduction in clonogenic cell growth (Pruitt, Z., *et al.,* 2006). Surprisingly the promoter regions of these reactivated genes remained highly methylated indicating that, histone deacetylation through SIRT1 is dominant mechanism in gene silencing. However, in contrast to the above reports, few studies also inferred that the re-expression of class III HDACs in

glioma derived cell lines reduced their clonogenic capacity. This could be infered that in certain situations sirtuins could also act as tumor suppressors (Michan, S., and Sinclair, D., 2007) (Saunders, L., and Verdin, E., 2007). Currently there is ambiguity in sirtuins activity over oncogenesis. However, the data infer that the HDACs altered function might play a critical role in tumor onset and progression and also highlight the therapeutic importance of HDACs.

1.4. Relation between cancer and inflammation

The concept of relation between cancer and inflammation is not new, as it was first proposed by Virchow, who hypothesized that the origin of cancer was at sites of chronic inflammation (Coussens, L. M., and Werb, Z., 2002). It is now clear that cell proliferation is not only the reason for cancer; instead it requires microenvironment rich in inflammatory cells, growth factors, activated stroma and DNA-damage promoting agents (Balkwill, F., and Mantovani, A., 2001). It is also clear that during wound healing, cell proliferation gets enhanced while the tissue needs to be regenerated. However, proliferation and inflammation subside soon after the removal of assaulting agents. Conversely, cells which proliferate, sustaining DNA damage continue to proliferate, in a sense that tumors act as wounds that fail to heal (Dvorak, H. F., 1986).

1.4.1 Inflammation and neoplastic progression

Peyton Rous was the first person to recognize that cancers develop from sub-threshold neoplastic states caused by viral or chemical carcionogens that induce somatic changes (Rous, P., and Kidd, J. G., 1941). This state is now known as initiation phase, involving DNA alterations that are irreversible and could persist in normal tissues until the occurrence of a second type of stimulation called promotion. Promotion occurs due to various chemical irritants, like phobol esters, factors released at the site of wound, hormones and inflammation (Coussens, L. M., and Werb, Z., 2002). Interestingly, many promoters which induce cell

proliferation would recruit inflammatory cells, in turn secretes ROS leading to DNA damage. Functionally, it also reduces DNA repairing capacity, thus resulting in DNA replication and proliferation of cells that get lost during normal growth control, resulting in cancer (Coussens, L. M., and Werb, Z., 2002).

1.4.2. Cancer associated with chronic inflammation

There are growing evidences suggesting many malignancies that arise from areas of infection and inflammation (Coussens, L. M., and Werb, Z., 2002). As chronic infections induce persistant inflammation, white blood cells such as leukocytes and phagocytic cells induce DNA damage in proliferating cells through generation of ROS and RNS, that are produced normally by these cells to fight infection (Maeda, H., and Akaike, T., 1998). These highly active species react to form mutagenic agent like peroxynitrite. Repeated tissue damage thus results in permanent genomic alterations in proliferating epithelium. In addition to this, at the site of inflammation various chemokines get released, which further help in metastasis and angiogenesis (Muller, H., *et al.,* 2001; Coussens, L. M., and Werb, Z., 2002). From the above information it is clear that anti-inflammatory therapy could also be effective towards early neoplastic progression and malignant conversion. In malignancy state, there are excess of inflammatory cells in the tumor microenvironment. That means tumor might need inflammation to help foster angiogenesis and metastasis. The challenge for the future would be to normalize the inflammatory network to regain a normal host response overall. Thus, there is urgency in the selection of targets to treat cancer, which are equally important in inflammation. Further chapters explain more information about the targets chosen and their role in cancer.

Chapter 2: Literature review

2.1 SIRT1

SIRT1 is a member of silent information regulator 2 (Sir2) protein family and one of the seven sirutins in human. SIRT1, a 747 aminoacid protein with molecular weight of 83 kDa influence a myriad of biological processes, including oncogenesis, inflammation, aging and metabolism. Interestingly in yeast, increased activity of Sir2 protein resulted in chromatin silencing, suppression of recombination and life span extension (Kaeberlein, M., *et al.,* 1999)(Imai, A., *et al.,* 2000). SIRT1 influence cellular process through transcriptional and mitochondria mediated mechanisms.

To understand the molecular aspects of SIRT1, the structural details need to be known. Common to all sirtuins is a deacetylase domain, which is approximately 250 aminoacids and is located between 250 and 500 residues. It is important to know that the N- and C- terminal domains can be phosphorylated, that increases SIRT1 deacetylase activity (Sasaki, M., *et al.,* 2008). Structural aspects could be further known by analyzing the crystal structures of closely related proteins. Crystal structure of *Archaeoglobus fulgidis* Sir2 revealed that the catalytic domain of HDAC class III had a rossmann fold along with zinc binding segment. NAD^+ bind in a cleft formed at the junction of rossmann fold and zinc binding domain (Min, L., *et al.,* 2001). Besides, additional structural features determined the binding of natural substrates (peptides) (Avalos, C., *et al.,* 2002). So far, few SIRT1 homologous crystal structures were revealed, which include human SIRT2 (1J8F, 1YC5) (Avalos, C., *et al.,* 2002), SIRT3 (3GLS, 4FZ3, 4JSR, 4JT8, 4JT9, 4C78, 4C7B) (Jin, W., *et al.,* 2009), SIRT5 (**2**FZQ) (Schuetz, M., *et al.,* 2007) and SIRT6 (**3**K35) (Pan, F *et al.*, 2011). Among all the deacetylase domains of human SIRT1 was most similar to that of SIRT2, which was 45% identical and 69% homologous. Contrastingly, SIRTs 6 and 7 had the least similarities with SIRT1, approximately 22% identical and only 40% homologous. As the therapeutic importance of SIRT1 was significant, recently efforts were made in crystallizing SIRT1 protein and they were successful in revealing SIRT1 in various conformations. Among them,

the crystal structure 4KXQ was obtained in (closed confirmation) complex with adenosine-5-diphosphoribose (APR), beta-mercaptoethanol, glycerol and zinc ion. The other crystal structure with PDB ID 4IG9 (open conformation) was crystallized with zinc ion alone. However in the year 2013, Xun and colleagues proposed a crystal structure of human SIRT1 catalytic domain **(**4I51**)** for the first time with a resolution of 2.5 A^0 bound with NAD^+ and an indole molecule (EX527 analogue) (Zhao, A., *et al.,* 2013) .

2.1.1 Binding of NAD^+ and inhibitor to the catalytic domain

SIRT1 crystal structure revealed that the inhibitor was deeply buried and NAD^+ was bound lengthwise across the mouth of binding site. The adenine moiety of NAD^+ was clamped between the R466 side chain and single turn α-2 helix following the β-1 strand, which formed two hydrogen bonds with SIRT1. One hydrogen bond was formed between 6- amine and D483 residue and the other was between position 1 nitrogen and nitrogen of C482 residue (Zhao, A., *et al.,* 2013). The nucleotide ribose hydroxyl distal to the adenine formed a hydrogen bond with Nδ2 of N465. R274 formed a salt bridge with the first NAD^+ phosphate and hydrogen bonds with the second phosphate through its side chain guanidinium group. Additional hydrogen bonds were found between the first phosphate and the F273 backbone nitrogen and Oγ of S442 and between the second phosphate and Oγ of S441 and the A262 backbone nitrogen. A bridging water molecule (W38) was found in the active site between NAD^+ and the inhibitor. This water was triply coordinated by the second phosphate of NAD^+, N346 Oδ1, and the indole nitrogen of the inhibitor. The NAD+ nicotinamide was tightly packed through van der Waals interaction between a trio of phenylalanine side chain contributed by residues F273, F297, and F414 (Zhao, A., et al., 2013).

However, the inhibitor (EX527 analogue) was found to interact with SIRT1 primarily through hydrophobic interactions unlike NAD^+. It was found deep within the active site just behind the ribose and nicotinamide of NAD^+ The crystal structure signified that only S-enantiomer was present in the pocket. It also represented that there was a hydrophobic cage surrounding the inhibitor. The hydrophobic cage was made with the following residues I347,

I270, I279, F273, F297, I347, I411 and F413. The binding of inhibitor also included hydrogen bonds along with hydrophobic interactions (Zhao, A., *et al.,* 2013). Especially, hydrogen bonds were formed between the amide substituent of the seven member ring of the inhibitor and D348 residue of the side chain. In addition to that, van der Waals interactions were also seen between the chlorophenyl group of the inhibitor with NAD^+ nicotinamide ring.

Using the crystal structure of SIRT1/NAD^+/crystal ligand complex and Sir2 cyrstal structure bound to the H4 peptide and carbaNAD (1SZC) it was clear on the mechanism of inhibition by inhibitor (Cosgrove, B., *et al.,* 2006). Interestingly, the amide group of (Cosgrove, B., et al., 2006) the seven membered ring was bound in the same way as the amide of NAD^+ nicotinamide. Usually, NAD^+ wrapped back around the α-2 helix to form hydrogen bonds with D118 residue and O117 backbone nitrogen. Besides, the F273 side chain rotated inward to form π stacking interaction with the indole moiety of inhibitor, which formed an additional steric block to the binding of $NAD^{+.}$ This binding forced NAD^+ into an extended conformation positioned diagonally across the binding groove. In the Sir2/H4/carbaNAD crystal structure, the acetylated substrate lysine side chain insinuated deeply into the catalytic pocket. Coupled to NAD^+ bound in the active conformation as observed in the 1SZC crystal structure, this placed the acetyl group of the substrate lysine proximal to the flank of the kinked NAD^+, exposing the nicotinamide ribose for nucleophilic attack by the acetyl-lysine substrate. However, the extended conformation of NAD^+ blocked access to the channel infiltrated by the acetylated lysine substrate. In addition, crystal ligand (35) extended far enough from the amide binding site such that the 5-chrorophenyl would also sterically inhibit catalytic placement of the acetylated lysine. Therefore, the mechanism of inhibition by crystal ligand (35) was 2-fold: first, the binding of 35 mimiced binding of NAD^+ amide and forced the cofactor into an alternate extended inactive conformation, and second, the forced extended conformation of the cofactor sterically blocked the substrate binding by occluding the channel occupied by the acetylated lysine (Zhao, A., *et al.,* 2013).

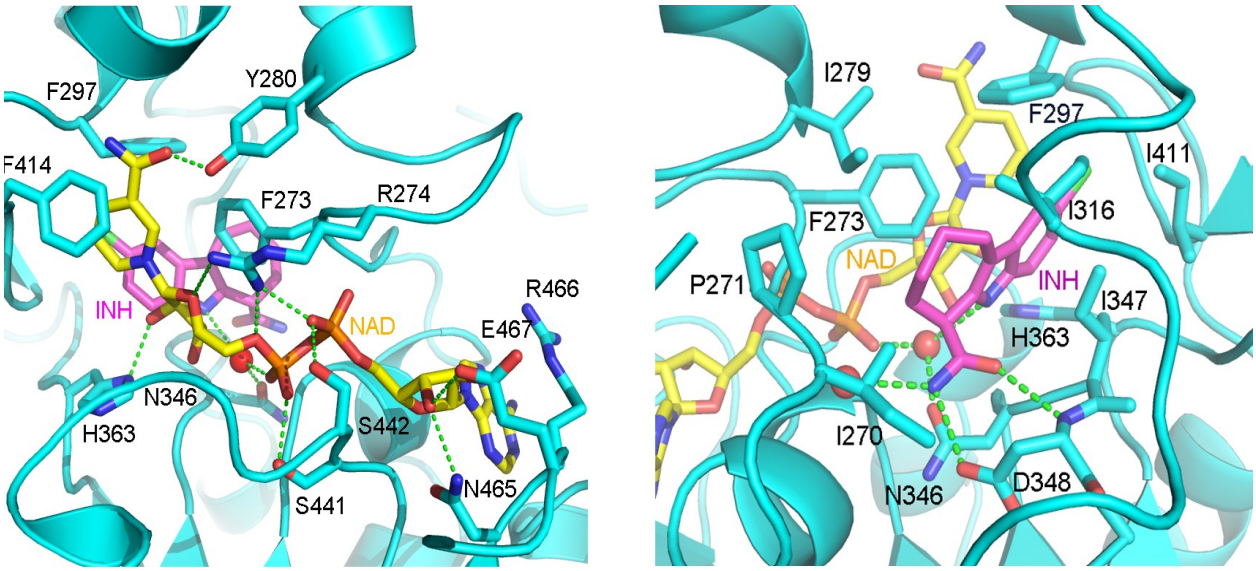

Figure 1: Binding pattern of NAD^+ and EX527

Illustrating binding pattern of NAD^+ and 35 (EX527) in the SIRT1/NAD^+/35 crystal structure (Zhao, A., *et al*., 2013). SIRT1 protein is represented by ribbons and interacting side chains represented as sticks (Cyan), NAD^+ (yellow) and 35 (Magneta). Hydrogen bonds are shown in green lines.

2.1.2. Histones as a substrates for SIRT1

As discussed in the introduction chapter, SIRT1 deacetylate various histone and non histone proteins. It was usually recruited to chromatin and interacts with various transcription factors and co-regulators. In the nucleus, SIRT1 deacetylate histone proteins on specific aminoacid residues, which include H1 lysine 26, H3 lysine 9 and H4 lysine 16 (Vaquero, S., *et al.,* 2004; Liu, L., *et al.,* 2009). Further histone also regulate the histone-modifying enzymes as it inhibit the function of histone acetyl-transferase p300, thereby indirectly promoting histone hypoacetylation (Liu, L., *et al*., 2009).

2.1.3 Regulation of gene expression by deacetylating non histone proteins

SIRT1 regulates gene expression by modification of non histone proteins. There are three groups of non histone proteins modified by SIRT1. The first group include transcription factors, like P53, P73, androgen receptor (AR), Forkhead box subgroup O (FOXO) proteins, E2F1, hypermethylated in cancer 1 (H1C1), B cell lymphoma 6 (BCL6) and nuclear factor kappa B (NF-κB) (Heltweg, G., *et al.,* 2006; Wang, C., *et al.,* 2006; Liu, L., *et al.,* 2009). Second group include signaling factors: SMAD7 and endothelial nitric oxide synthase (eNOS) (Liu, L., *et al.,* 2009) and the third group include DNA repair proteins: Ku-70 and MRE11-RAD50-NBS1 (MRN). SIRT1 deacetylation also regulates histone methylation. SIRT1 increases the methyltransferase function of histone methyl trasferase SUV39H1, by recruiting and deacetylating the catalytic domain of SUV39H1, which result in increased levels of H3K9me3 at SIRT1 target sites. It was interesting to know that SIRT1 localize at the promoter regions of tumor suppressor genes, which had been aberrantly silenced by hypermethylation. However, upon inhibition of SIRT1 activity reactivation of these genes, presumably through the reversal of hypermethylation was reported (Pruitt, Z., *et al.,* 2006). One major tumor suppressor gene inhibited by SIRT1 was CDH1, which was repressed during epithelial tumor genesis, progression and also in metastasis. It was also reported that SIRT1 inhibited the function of mismatch repair gene *MLH1* through epigenetic alterations (Pruitt, Z., *et al.,* 2006). So far from the above discussions, it was clear that SIRT1 was involved in myriad of functions through epigenetic alterations. Interestingly, it was also known to play an important role in tumor promoter as SIRT1 protein was over expressed in many cancer tissues, cancer cell line and murine tumors. This led to the presumption of SIRT1 to be a tumor promoter (Chen, W., *et al.,* 2005; Ford, A., *et al.,* 2008). It has been established that SIRT1 was overexpressed in mouse and human prostate cancers, human primary colon cancers, acute myeloid leukemia, cutaneous human squamous cell and basal cell carcinoma (Lim, C. S., 2006; Huffman, G., *et al.,* 2007; Stünkel, P., *et al.,* 2007). Supporting to the role of SIRT1 in cancer progression, Ford *et al.,* showed that SIRT1 silencing induced growth arrest and apoptosis in epithelial cancer cell line of human (Ford, J., *et al.,* 2005). It was also reported that inhibition of SIRT1 activity by cambinol during genotoxic stress led to hyperacetylation of key stress response proteins and promoted cell

cycle arrest (Heltweg, G., *et al.,* 2006). Further scientists have reported that reduced SIRT1 expression by small interfering RNA duplex decreased the chemoresistacnce of CP-r (cisplatin resistant) cells to cisplatin treatment by 20-fold (Liang, F., *et al.,* 2008). From this it could be significantly inferred that gain of SIRT1 function by overexpression could inhibit apoptosis of cancer cells and decrease the sensitivity of cells to anti-cancer drugs. Similar to that, loss of SIRT1 function resulted in contrasting effects on apoptosis and chemosensitivity. Interestingly, it was also reported that SIRT1 could deacetylate p53 and FOXO, thereby inhibiting P53 and FOXO dependent transcription or apoptosis (Brunet, S., *et al.,* 2004; Kim, C., *et al.,* 2008). In addition to the above studies in cell lines, in-vivo studies were also performed. However, SIRT1 role in tumorogensis was hard to assess as knock out of SIRT1 gene was lethal to most of the embryos (McBurney, Y., *et al.,* 2003). SIRT1 knockout mouse embryonic fibroblasts showed chromosomal instability due to impaired DNA repair and histone modification (Wang, S., *et al.,* 2008; Yuan, P., *et al.,* 2009). Nevertheless, all the above information suggested that SIRT1 act as potential tumor promoters

.

In contrast to the above findings, some investigators have presented data to suggest SIRT1 as tumor suppressor. Down regulation of SIRT1 earlier showed that it could act as tumor promoter, however overexpession of SIRT1 did not show any tumorogenesis (Banks, K., *et al.,* 2008; Pfluger, H., *et al.,* 2008; Zhang, W., *et al.,* 2008). Few investigators also proposed that knock down of SIRT1 might induce activation of endogenous p53 (Ford, J., *et al.,* 2005). Interestingly, Firestein *et al.,* showed that overexpression of SIRT1 in adenomatous polyposis coli (APC) mutated transgenic mice reduced colon cancer by inactivation of β-catenin through SIRT1 deacetylation (Firestein, B., *et al.,* 2008). Few investigators found that SIRT1 expression was lower in BRCA1 (breast cancer 1) associated breast cancer than non-BRCA1 associated breast cancer (Wang, Z., *et al.,* 2008). They further illustrated that resveratrol, a SIRT1 activity enhancer, promotes apoptosis of these cell lines. NFκB was found responsible for the upregulation of gene products required for cell survival. It was shown that SIRT1 inhibited) the function of NFκB by deacetylating its subunits (RelA/p65) and subsequently promoting TNF-α- induced apoptosis (Yeung, H., *et al.,* 2004). Thus this evidence also suggested that SIRT1 could also act as potential tumor suppressor.

The controversial roles of SIRT1 in tumorogenesis suggested that SIRT1 might play a dual role depending on the temporal and special distribution of different SIRT1 up and downstream factors in different tissue contexts. It was obvious that SIRT1 was only one of the representative molecules in a very complicated network showing association with cell proliferation, apoptosis, senescence and angiogenesis. Nevertheless, we could infer that it was the balance between tumor promoters and tumor suppressors which played a pivotal role in tumorogenesis. Therefore, further studies are required to focus on addressing the role of SIRT1 in specific tumorogenesis.

2.1.4. Medicinal chemistry of SIRT1 inhibitors

After knowing the therapeutic importance of SIRT1 inhibitors, many groups had focused on developing novel small molecule SIRT1 inhibitors. Most of them were moderately selective over SIRT2 and SIRT3, with single-digit micromolar IC_{50} values against SIRT1 (Blum, C. A., *et al.,* 2010). However, there were few exceptions, which included indole-based inhibitors (EX-527, IC_{50} = 0.098 μM) and suramin (IC_{50} = 0.3 μM). The compound EX527 was shown to be orally bioavailable in mice with half-life of 194 min. Instead, suramin with anionic moiety, had limited utility as small molecule inhibitor. In order to evaluate potential of SIRT1 inhibition in drug discovery program, inhibitors with more potent and selective leads are required. Recent efforts in search of novel SIRT1 inhibitors have not yet resulted in more potent and selective SIRT1 inhibitor than the benchmark compounds (EX527). However optimization efforts are in progress for known SIRT1 inhibitor scaffolds (Blum, C. A., *et al.,* 2010).

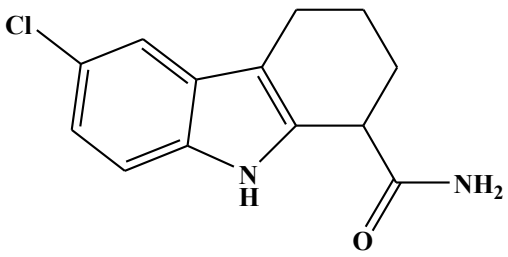

EX527

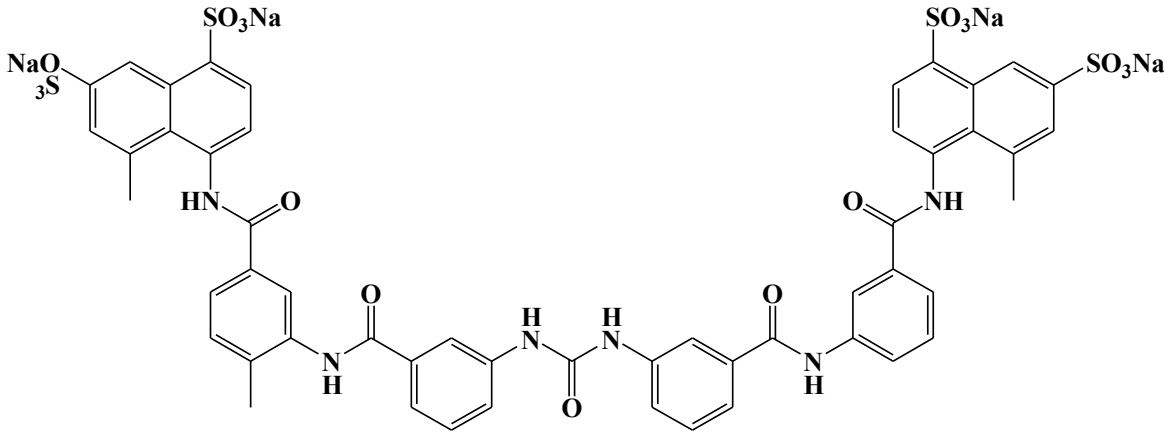

Suramin

2.1.4.1. Nicotinamde derivatives*:*

Nicotinamide and benzamide analogues were designed to develop inhibitors that occupy nicotinamide subpocket of NAD^+ binding site. Anilino benzamide represented below showed IC_{50} of 17 μM, which was non competitive with NAD^+, and was competitive with the acetylated lysine (Suzuki, T. K., *et al.,* 2006). Other analogues of aniline benzamide with meta substitutions, showed comparable SIRT1 inhibitory activity like parent lead. In addition, these analogues showed inhibitory activity on human colon HCT116 cancer cells. (Suzuki, T. K., *et al.,* 2009).

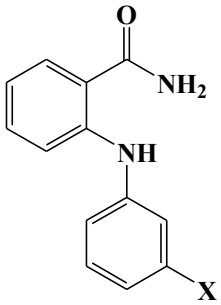

X = H, Ph, OPh

2-Anilinobenzamides

2.1.4.2. Sirtinol derivatives

Initially salermide, an analogue of sirtionol was rationally desiged to improve SIRT1 activity. When the amide was reversed and moved from 2' to 3' position of the phenyl ring, the carbonyl of amide showed better hydrogen bonding with glutamine in NAD^+ binding pocket. The IC_{50} of salermide (43 μM) was moderately more potent than sirtinol (123 μM). Further, salermide showed activity against cancer cells, especially leukemia and lymphoma by inducing apoptosis. Later, in-vivo studies were also performed in mice, revealing antitumor effects, most likely by reactivating pro-apoptotic genes, that were repressed in cancer cells by SIRT1-mediated K16H4 deacetylation (Lara, E., *et al.,* 2009).

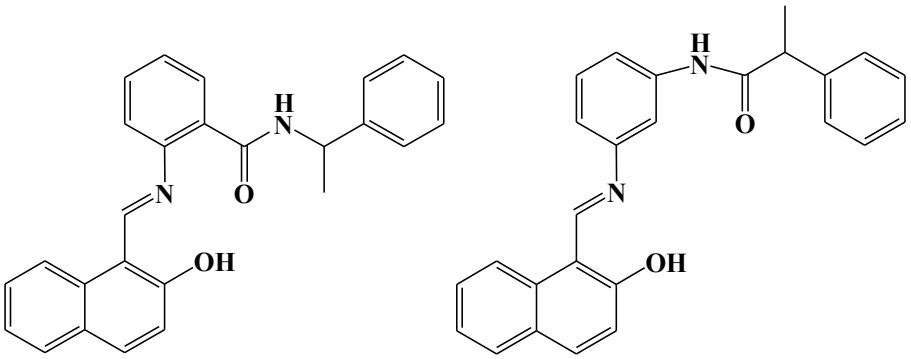

Sirtinol Salermide

2.1.4.3. Cambinol and Tenovin derivatives

Both cambinol and tenovin-6 are sirtuin inhibitors that showed antitumor activity in preclinical models (Heltweg, B., *et al.* 2006; Lain, S., *et al.,* 2008). However cambinol did not show much selectivity towards SIRT1, as the IC_{50} values against SIRT1 and SIRT2 were 56 μM and 59 μM respectively. Later it was found that selectivity could be achieved by modifying specific parts of the scaffold. Substitution on the phenyl ring produced modest improvement in SIRT1 activity (IC_{50} = 13 μM). In addition to that tenovin derivative was also synthesized, which showed optimized SIRT1 activity with SIRT1 IC_{50} of 13 μM over SIRT2 IC_{50} of 113 μM (Huhtiniemi, T., *et al.,* 2008)

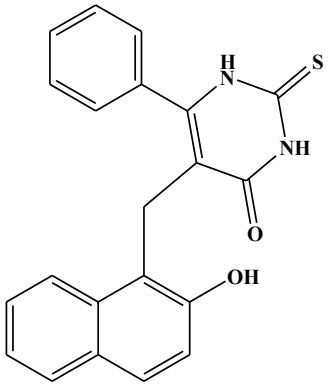

Cambinol

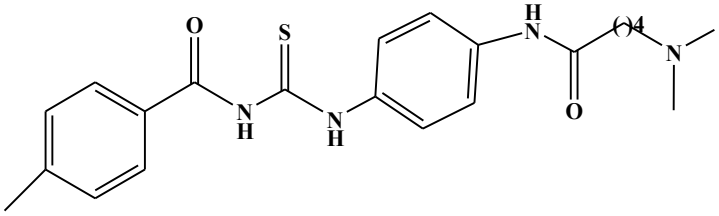

Tenovin-

2.1.4.4. Thiobarbiturates

A set of thiobarbiturates structures were identified by virtual screening using the crystal structure of SIRT2. Non-selective sirtuin inhibitors identified with both SIRT1 and SIRT2 inhibitions. The most potent thiobarbiturate showed SIRT1 IC_{50} of 13 μM and SIRT2 IC_{50} of 11 μM. Few other groups also carried high-throughput screening of 50,000 compounds that resulted in moderate non-selective compounds. Among them, aderivative of splitomicin was found potent against SIRT1 (SIRT1 IC_{50}=6 μM; SIRT2 IC_{50}=2 μM; SIRT3 IC_{50}=89 μM) (Sanders, B. D., *et al*., 2009)

2.1.4.5 Indole derivatives

Napper group performed high-throughput screening against human SIRT1, that lead to the discovery of a series of indoles as potent inhibitors. These indoles were selective for SIRT1 over other sirtuins and NAD processing enzymes (example EX527). Among these, the most potent compound inhibited SIRT1 with IC_{50} values of 60 –100 nM, which represented over 500 fold improvement over previously reported SIRT1 inhibitors. Further, kinetic analyses also suggested that these inhibitors bind after the release of nicotinamide from the enzyme and thus preventing the release of deacetylated peptide and O-acetyl-ADP ribose (Products of enzyme catalyzed reaction). These molecules were orally bioavialble and also metablically

stable. Currently these molecules were considered as benchmark for many groups working on discovery of SIRT1 inhibitors (Napper, A. D., *et al*., 2007)

2.2. Biosynthesis of NAD

Warburg, over 80 years ago, presumed that metabolism was significantly altered in cancer cells. But only recently, it was being exploited as a therapeutic strategy in cancer (Vander M. G., 2011). Among various pathways, the biosynthetic pathway leading to NAD synthesis has received considerable attention (Garten, A. S., *et al.,* 2009). Nevertheless, in cancer cells NAD synthesis was constantly required because of the high proliferation rate and high activity of NAD depleting enzymes like PARPs and sirtuins. As NAD function was conserved through evolution as an electron acceptor/donor, it was striking to know that there were differences between prokaryotes and eukaryotes on how these replenishment took place. Hence it was obvious that the enzymes of microbes involved in synthesis of NAD could be considered as druggable targets for the development of antibiotics (Bi, J., *et al.,* 2011). NAD was usually synthesized from various precursors containing pyridine moiety, which included nicotinic acid, nicotinamide, nicotinamide riboside and tryptophan. Lower eukaryotes and prokaryotes use nicotinic acid as a major NAD precursor, while mammal's predominantely use nicotinamide as a major precursor. It was in the de novo biosynthesis of NAD through aminoacid L-tryptophan, get converted into NAD through rate-limiting enzymes indole amine 2,3-dioxygenase and tryptophan 2,3-dioxygenase. However, in humans the main source of NAD was from salvage pathway. It was obvious that most NAD utilizing reactions liberated nicotinamide, and it was not surprising that mammals chose the most direct and economical route as their major NAD source (**Figure 2**). This pathways has two steps, one involve the synthesis of nicotinamide mono nucleotide (NMN) (Galli, U., *et al.,* 2013) from nicotinamide and 5-phosphoribosyl pyrophosphate (PRPP) by the enzyme nicotinamide phosphoribosyl transferase (NAMPT) and the second step involve conversion of NMN and ATP into NAD by nicotinamide mononucleotide adenylyltransferase (NMNAT). Among the two steps, the first step was rate limiting step and hence enzyme (NAMPT) catalyzing this reaction obtained considerable attention (Galli, U., *et al.* 2013).

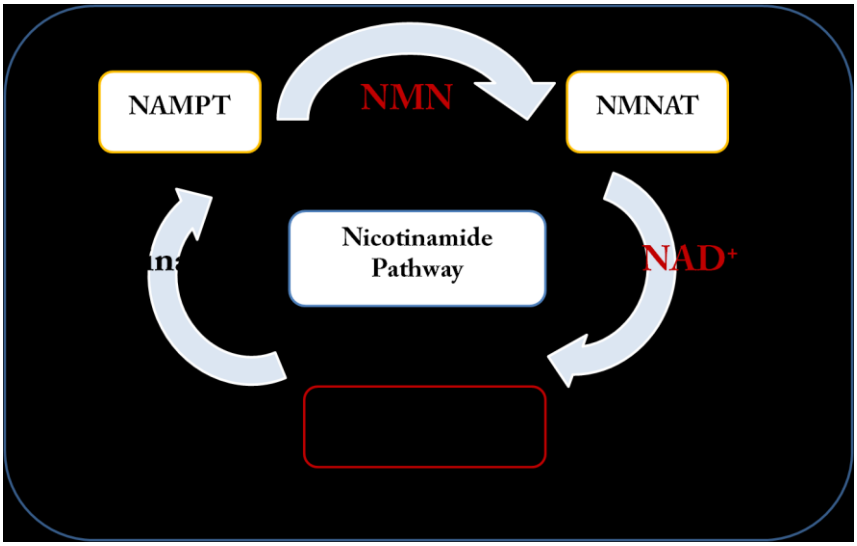

Figure 2: Illustrating the biosynthetic pathway of NAD synthesis

2.2.1. Nicotinamide phosphoribosyl transferase (NAMPT)

Preiss and Handler were the two scientists who pioneered the identification of enzymatic activity of NAMPT in 1957 (Preiss, J., *et al.,* 1958). Human has NAMPT is 491 aminoacids in length with molecular weight of 55k Da approximately. The x-ray crystal structure revealed that NAMPT was a dimeric protein, belonging to type II phosphoribosyl transferases (Wang, T., *et al.* 2006). It was interesting to know from mutagenesis experiments, that NAMPT without dimerization showed decreased enzymatic activity (Wang, T., *et al.* 2006; Revollo, J. R., *et al.* 2007). However, there were a number of splice variants and truncated proteins detected, but the physiological role of these peptides was not known and needed further investigation. Further, in humans number of single nucleotide polymorphisms (SNPs) has also been found, and some of these have been associated with increased risk of diseases like acute respiratory distress syndrome and diabetes. Interestingly, NAMPT activity was significantly affected by histidine

autophosphorylation at His 247 residue. The phosphorylated form showed at least 1000 fold higher activity compared to un-phosphorylated form. From this we could presume that enzyme phosphorylation cause stabilization of enzyme-phosphoribosyl pyrophosphate complex, which permit the efficient capture of nicotinamide (NAM) (Burgos, E., S., *et al*.,

2008). So far, no other post-translational modification has been discovered. However, bioinformatics suggested that the number of residues conserved across species could be phosphorylated, ubiquitinated or acetylated. The location of NAMPT was ubiquitous in the cell and was abundantly found in cytosol and also in nucleus (Pittelli, M., *et al.,* 2010). Besides, there were controversies on whether it might also be present in mitochondria (Yang, H., *et al.,* 2007; Pittelli, J., *et al.,* 2010). Interestingly, it was not exclusively intracellular, while many researchers also discussed about extracellular secreted forms. In literature it was usually reffered as visfatin (initially described as being secreted in adipose tissue) or PBEF as it function also as an enhancing factor for pre-B-cell maturation (Samal, B., *et al.,* 1994). More clarification with regard to the structural and functional differences between extracellular and intracellular forms should be known. Simultaneously, whether its extracellular effects were linked to an enzymatic function or not it's still need to be known. However, few scientists proposed that an unknown receptor existed, that was able to bind to eNAMPT, and transduced at least some of its effects. For example, extracellular application of NAMPT was able to trigger ERK and MAPK phosphorylation (Yammani R. R., *et al.,* 2012). Interestingly, a growing number of cell types have been shown to secrete NAMPT, which included adipocytes, hepatocytes, activated immune cells and LPS activated monocytes (Tanaka, M., *et al.,* 2007; Garten, A., *et al.,* 2010).

2.2.2 Physiological roles of NAMPT

Although role of NAMPT in NAD synthesis was well established, over the past decade, there has been a growing body of research that suggested NAMPT functions to be pleiotropic. Because of experimental limitations, it was not yet possible to assign specific functions to either intracellular form of NAMPT or extracellular form of NAMPT (Galli, U., *et al.,* 2013). Primarly, it has been shown by many research laboratories that NAMPT activity was a key regulator of NAD consuming enzymes. Among the enzymes which consumed NAD were poly ADP-ribose polymerases (PARPs), mono ADP-ribose transferases (ARTs) and sirtuins. Primarily, considerable attention was given recently to the ability of NAMPT to modulate the sirtuin activity. Studies showed that circadian machinery regulated the recruitment of SIRT1

to the NAMPT promoter to increase NAMPT expression. This was subsequently followed by the NAD biosynthesis, which inturn activated sirtuins and other enzymes which used NAD as co-substrate. Secondly, there existed a possibility that NMN, a direct product of NAMPT might have a role in signaling (Wang, P., *et al.,* 2008). Similarly, nicotinamide was an inhibitor of a number of NAD utilizing enzymes (SIRT1), which could be envisaged that NAMPT acted as a scavenger of nicotinamide itself. Thirdly, there was an increasing evidence suggesting that NAMPT could also act as cytokine and bind to unknown extracellular receptor. It has been shown to induce the function of stem cell factor (SCF) and interleukin-7 (IL-7). Further, it was also reported that NAMPT exerted proinflammatory effects on macrophages by increasing MMP expression and activity (Fan, Y., *et al.,* 2011).

2.2.3. NAMPT role in cancer

It was well known that the bioenergetics of cancer cells were different from that of healthy non-affected cells, which was proposed by Otto Warburg, a Nobel prize winner (Skokowa, J., et al., 2009). He suggested that the tumor cells switched from oxidative phosphorylation to aerobic glcyolysis for their energy conversion. Compared to oxidative phosphorylaiton, glycolytic pathway resulted in less number of ATP. Interestingly, the known importance of sirtuins and PARPs in cancer also suggested that NAMPT, one of its upstream regulators might be significantly involved. Primarly, it has been significantly shown that NAD turnover in cancer or proliferating cells was significantly increased over healthy cells. This statement was supported by various approaches in cancer cells or patients. Many of these observations were reported in many research articles (Galli, U., *et al.,* 2013). Furthermore, in most of the cancer tissues evaluated, the mRNA and protein levels of NAMPT have been found to be increased. Besides, the serum or blood levels of NAMPT were also shown to be increased. Interestingly, in a number of tumors a positive correlation has been reported. Recently, it was also reported that there was an elevated level of circulating NAMPT correlated with increased risk of developing postmenopausal breast cancer (Dalamaga M., *et. al.,* 2012).

2.2.4. Medicinal chemistry of NAMPT inhibitors

It was a great surprise to know that the first attempt to identify NAMPT inhibitors dated back to 1972, where a series of nicotinamide analogues were evaluated. However, these studies suffered a limitation of not having purified enzyme and detailed understanding of enzymatic mechanism (Dietrich, L., *et.al.,* 1972). Discovery of the first nanomolar inhibitor FK866, was considered as a turning point. Primarily, FK866 was shown to induce apoptosis by depleting NAD and ATP pool inside the cell. FK866 showed high affinity (K_i = 0.3 nM) for the binding site compared to the nicotinamide (K_m= 2 μM) (Khan, J. A., *et al.,* 2006). Interestingly, it was also established that nicotinamide or nicotinic acid could be viewed as antidotes for NAMPT inhibition. This result was also replicated by other potent NAMPT inhibitors such as CHS828.

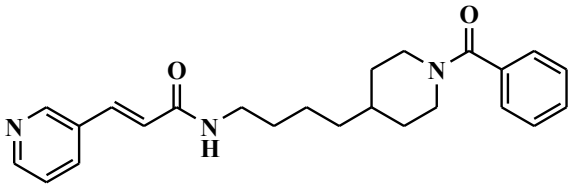

FK866

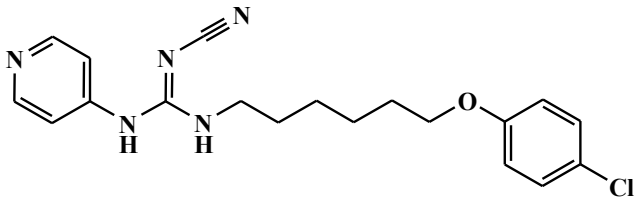

CHS828

Soon after, this the first crystal structure of NAMPT was obtained in complex with FK866 (PDB code 2GVJ), which clearly elucidated the structural information of NAMPT protein (Khan, J. A., *et al.,* 2006). The crystal structure revealed that FK866 bind in the narrow tunnel at the interface between two subunits of protein. Although, crystal structure revealed that two molecules of FK866 bind to the protein, whether both were required to inhibit the activity was never investigated. Pyridine ring of FK866 was sandwiched between the side chains of Phe 193 of monomer and Tyr18. The main binding interaction was a π-π offset stacking. Besides, the carbonyl oxygen atom of amide behaved as a hydrogen bond acceptor interacting with hydroxyl group of Ser275 residue of side chain, while the nitrogen atom of the amide was involved in hydrogen bonding with retained molecule of water (W1) (Khan, J. A., *et al.,* 2006). The tail group played an important role in holding the molecule in the hydrophobic cleft formed

by Ile309, Pro307, Val350, Ile378 and Ala379. FK866 molecule has alkyl chain, which interacted with the protein through van der Waals interactions in the tunnel. Interestingly, after couple of years crystallizing NAMPT protein in complex with FK866, many more crystal structures were reported with PDB codes 2G95, 2E5B, 4M6P, 2H3D, 4KFP and 4JR5 (Zheng, X., *et al.,* 2013). This suggested the importance of NAMPT in the world of drug discovery.

In addition to the discovery of FK866 as potent inhibitior, various other groups also discovered novel inhibitors. Among them discovery of GMX1778 elevated the therapeutic importance of NAMPT inhibitors. This molecule was a close analogue of antihypertensive potassium channel opener pinacidil, which was not a NAMPT inhibitor (Hjarnaa, P. J. V., *et al.,* 1999). This molecule was discovered in 1997, whose mechanism of action was not known. Its potent cytotoxic profile spurred research towards the identification of mechanism of action. Ten long years of pharmacological efforts, demonstrated NAMPT to be the main biological target for cytotoxic activity. Structure-activity relationship studies were carried on GMX1778, in understanding the role of pyridine ring. When pyridine was substituted in position 4 instead of 3, showed an increase in potency of 10 to 1000 fold. Furthermore, substitution of pyridine with phenyl ring yielded inactive compounds. It was interesting to know that, the length of alkyl chain was also important for improving the activity. Specifically, hexyl, heptyl and octyl were the best linkers, while the shorter chain linkers gave compounds with lower activity. Finally, bulky tail group that protruded towards the solvent exposed surface was important for determining the potency, most importantly, phenoxy group displayed the best potency (Lövborg, H., *et al.,* 2009). It was obvious that both FK866 and GMX1778 showed potent activity inhibition of NAMPT and thus entered clinical trials. However, no data were available regarding the preclinical toxicology. Furthermore, a number of research groups had further explored the possibility of developing novel NAMPT inhibitors. Using FK866 and GMX1778 as parent compounds various modifications were done to assess the biological activity. These modifications were grouped into three categories including replacement or chemical modification of pyridine ring, replacement of vinilogous amide group and replacement of tail groups (Figure 3). The results of the study are presented below in further sub sections.

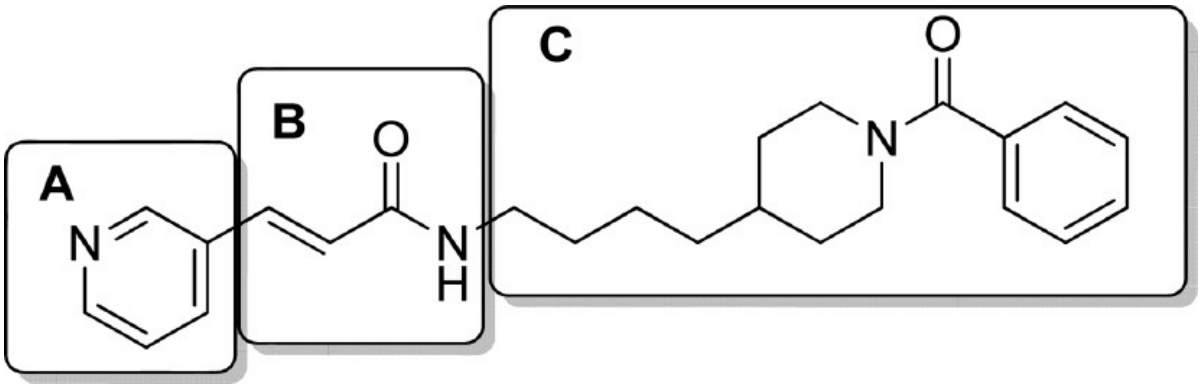

Figure 3: 2D structure of FK866, divided into three groups: A is pyridine group B. Vinylogus amide C. Tail group

2.2.4.1. Replacement or chemical modification of pyridine ring

Due to the rapid clearance of FK866, the scientists replaced the pyridine ring with other heterocyclic rings. This substitution resulted in loss of biological activity. Attempts were made to replace the pyridine ring with other heterocyclic rings containing at least one nitrogen atom or nitrobenzene and 2 and 3- substituted anilines that gave inactive compounds except for the pyrrole derivative. These compounds showed similar cytotoxic effects as compared to FK866 in breast cancer (MCF7) cell line. Recently, series of substituted pyridines, as well as pyridazine and pyrimidine analogues were shown to retain anti-NAMPT activity (Gunzner-Toste, J., *et al.,* 2013). Interestingly, some of them, while potent enzyme inhibitors, failed to elicit cytotoxic effects. From these studies, it could be concluded that to retain nanomolar NAMPT inhibitory activity, molecules should contain meta or para substituted pyridine, a heterocycle containing a pyridine moiety, or a pyridazine groups. In all these groups, π offset interaction with Tyr18 and Phe193 were common. This revealed the importance of π offset interaction for nanomolar activity (Gunzner-Toste, J., *et al.,* 2013).

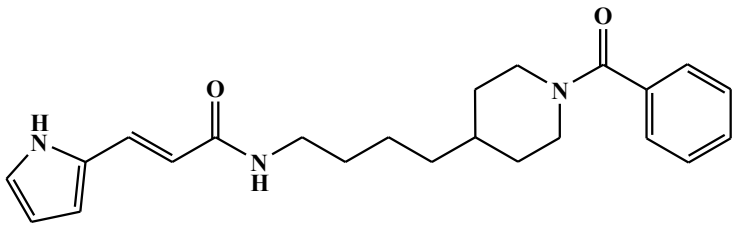

Example of replacement or chemical modification of pyridine group

4.2.4.2 Replacement of vinylogous amide group

When the amide of FK866 was replaced with sulfonamide, there was a total loss of activity (Colombano, G., *et al.,* 2009). When 1,4-disubstiuted triazole replaced the vinylogous amide of FK866, the compound exhibited cytotoxicity at IC_{50} of 3.0 μM, which was 3000 times lesser than FK866. On the other hand, molecule with pyridine ring directly attached to the triazole showed activity with 90 nM activity. However, the compound with amide directly attached to pyridine ring turned out to be inactive. This information could be infered that the hydrogen bond acceptor should be atleast three carbon atoms away from the pyridine. It was also important to know that the length of the alkyl linker chain was fundamental to allow perfect accommodation of both cap and tail group. The molecules with n = 6 showed IC_{50} of 56 nM, while with n = 7 and 8, showed IC_{50} 3.8 and 14.6 nM respectively. Recently, putative NAMPT inhibitors containing pyridinylurea or thiourea were synthesized and shown to have good cytotoxic activity against ovarian carcinoma cell line with IC_{50} of 0.89 nM (Colombano, G., *et al.,* 2009).

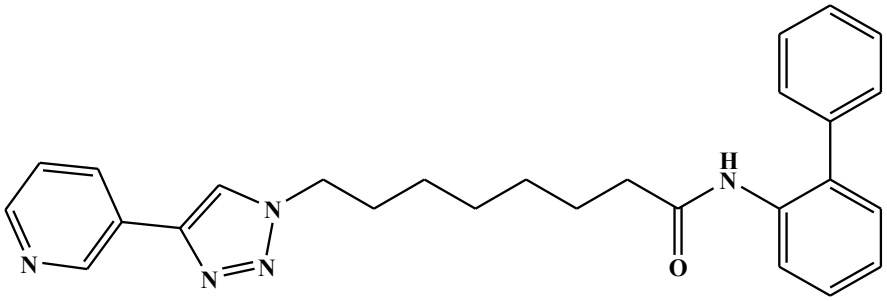

Example of lead showing the replacement of amide group

4.2.4.3. Replacement of tail group

Recently a new patent disclosed analogues of FK866 with different tail groups instead of benzoylpiperidine moiety. A series of nanomolar compounds active on A2789 ovarian carcinoma cell line was presented. Most active compound showed cytotoxic activity ot 0.16 nM. However no formal proof of NAMPT inhibitory activity was reported. In addition to that, replacement of long alkyl chain with benzene ring was also reported (Galli, U., *et al*., 2013). The most active compound of these substitutions resulted in nanomlar anti-NAMPT activity. From this lead compound, an impressive number of analogues displaying high cytotoxic activity has been reported (Zheng, Bauer *et al*., 2013). The same research group recently raised an issue that the pyridine in NAMPT inhibitors might be a structural determinant for CYP2C9 inhibition. Different pyridine substituted analogues were synthesized and tested, that led to the discovery of compounds with good antitutomoral activity (in xenografts), without showing any inhibition of CYP2C9.

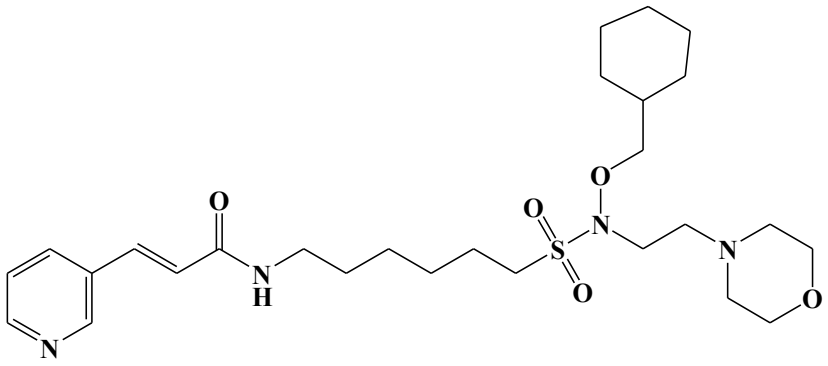

Example of tail group modification

Furthermore, in the year 2011, a research group from India for the first time used crystal structure information of FK866 and NMN bound to NAMPT and performed docking studies. This procedure yielded six compounds which were tested experimentally. Two of these compounds showed cytotoxicity on U87 cell line comparable with FK866 and one of them showed NAMPT inhibition (Chandra, N., *et al.,* 2011). However, this activity appeared to be 1000 fold lower than FK866.

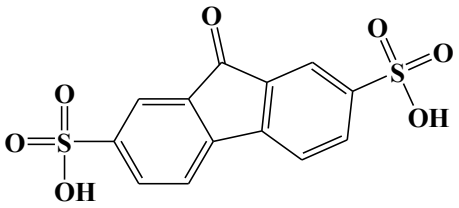

Example of compound identified from virtual screening

4.3. Relation between SIRT1 and NAMPT

As we had already discussed in the above sections, there exists a very close relationship between NAMPT and SIRT1. SIRT1, being a histone deacetylase, that alter the functions of various transcription factors and was also involved in chromatin remodeling. NAD^+, being a co-substrate for SIRT1, was a prerequisite for the activity of SIRT1 and other NAD^+ utilizing enzymes like PARPs. As NAMPT is involved in the synthesis of NAD, we could certainly infer that NAMPT activity, could regulate the function of SIRT1. However it was very interesting to know that, few researchers also proposed that SIRT1 being identified near the NAMPT promoter region, which meant SIRT1 could also regulate the expression of NAMPT, thereby signaling the synthesis of NAD^+, and subsequently helping in decetylation of various cellular substrates. Furthermore, in negative feedback loop mechanism, it was believed that SIRT1 repressed NAMPT expression (Nakahata,Y., *et al.,* 2009). It was through this mechanism, NAMPT and SIRT1 were considered to play crucial role in circadian regulation of metabolism.

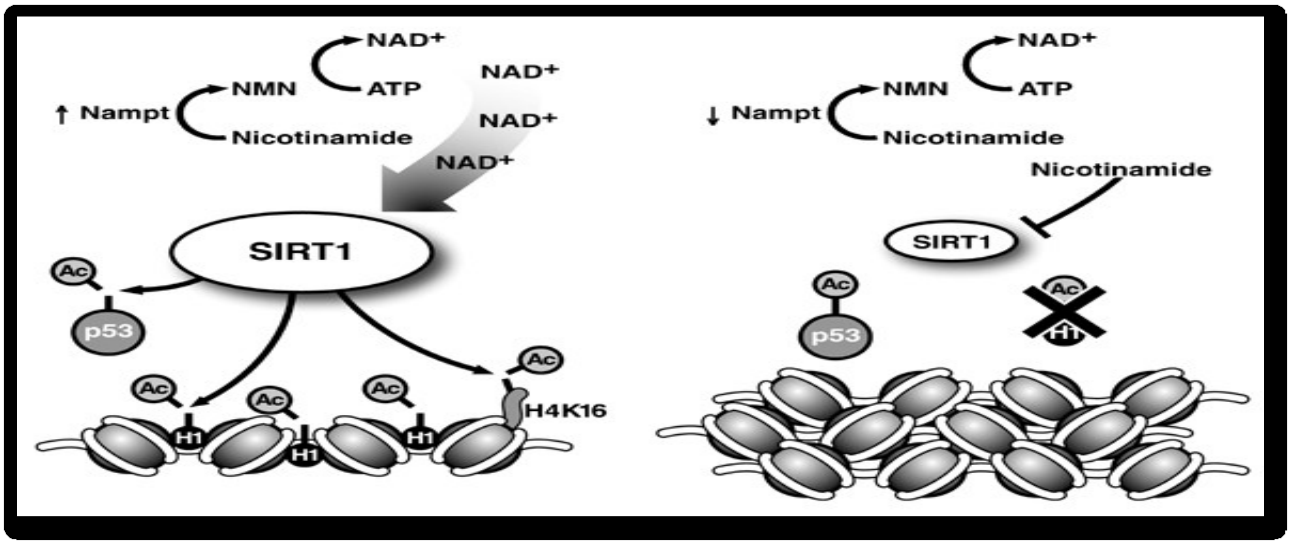

Figure 4: Illustrating the relation between SIRT1 and NAMPT

Chapter 3: Objectives and plan of work

3.1. Objectives

We know that cancer is an abnormal growth condition, resulting from various reasons, like DNA alterations (mutations), inhibition of tumor suppressors, reduction of DNA repair mechanisms, alterations in cell microenvironment or because of changes in metabolic activities. All these possible mechanisms have a significant relation to target proteins SIRT1 and NAMPT of our study. SIRT1 by deacetylating many transcription factors and histones, alters the function of various tumor suppressor genes, DNA repair mechanism and chromatin remodeling system. As SIRT1 has a wide range of substrates, it was obvious that it could show a myriad of functions in the cell. Specifically, it was overexpressed in many cancer cell lines including, colon, prostate and lymphomas. By inhibiting the function of SIRT1, we believe that cancer could be treated. NAD^+ being a prime regulator of SIRT1 activity, NAMPT as rate limiting enzyme involved in the synthesis of NAD^+, it was also significant to study NAMPT as target in disease conditions like cancer and inflammation. Though there were few small molecule inhibitors have discovered already against SIRT1 and NAMPT, still they are in various experimental testing's. Hence, there is wide room for identifying novel small molecule inhibitors, helpful in the treatment of cancer. Hence the prime objective of this study was to employ various strategies to discover novel small molecule inhibitors against SIRT1 and NAMPT as therapeutics targets.

I. Primary objective was to design novel small molecule inhibitors of SIRT1 and NAMPT

- Development of ligand and structure based pharmacophore models to explore new small molecule inhibitors against SIRT1 and NAMPT

- High throughput virtual screening of both in-house and asinex databases to select novel chemical entities with expected interaction pattern.

II. In-vitro screening of synthesized molecules for determining IC_{50} values.

III. In-vitro cell based studies to determine anticancer activity of novel leads

IV. In-vivo biological evaluation of novel leads in treating benign prostate hyperplasia condition.

V. Evaluating the role of SIRT1 and NAMPT inhibitors in treating inflammatory disease conditions

VI. Evaluating the role of SIRT1 and NAMPT inhibitors in tumorogensis

3.2 Plan of work

The plan of work was classified into following stages,

3.2.1. Design and development of novel SIRT1 and NAMPT inhibitors using computational methods depicted in the following **figure 5**.

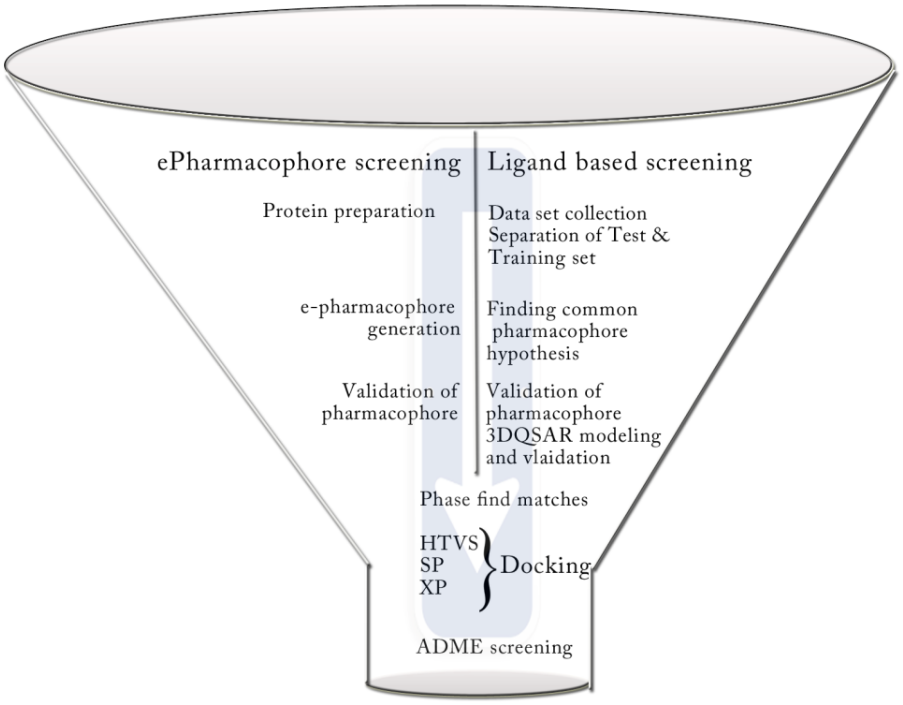

Figure 5: Illustrating the work strategies of computational work

3.2.2. In-vitro enzyme inhibition studies of SIRT1 and NAMPT proteins

3.2.3. Effect of leads in reducing cancer cell proliferation

3.2.3.1. In-vitro cell proliferation studies on various cancer cell lines including LnCAP, HT29 and MDAMB-231

3.2.3.2. Cell cycle analyses and apoptotic assay

3.2.4.In-vivo pharmacological evaluation

3.2.4.1. Development of testosterone induced benign prostate hyperplasia (BPH) animal model

3.2.4.2. Evaluation of the leads in reducing BPH condition by measuring prostate weight to body weight ratio

3.2.4.3. Histopathological studies

3.2.5. Effect of leads in treating inflammation

3.2.5.1 Effect of lead compounds in reducing the reactive oxygen species upon induction with LPS in U87 cell line

3.2.5.2 Evaluating the leads in-vitro reducing in acute carrageenan induced paw edema in male wristar rats.

Chapter 4 Material and Methods

4.1 Computational details

Computational work was carried out using Intel Core 2 Duo E7400 2.80GHz capacity processor with an internal memory of 2GB RAM, executing functions with RHEL 5.2 operating system. Schrodinger drug discovery software package consisting of modules for protein and ligand preparation and Glide for high-throughput virtual screening (docking) was employed in this study. Specialized application like LigPrep 2.5 (Schrödinger 2011) (Schrodinger LLC, New York, USA) was executed for building and minimizing the structures, and was also used to add hydrogens and generating various steroisomers at neutral pH (pH 7). To identify and select structurally diverse compounds from different clusters, Canvas 1.4 software package was utilized.

4.2 Design of SIRT1 inhibitors

4.2.1. Design of SIRT1 inhibitors by virtual screening

The crystal structure of SIRT1 bound with inhibitor (PDB ID: 4I5I) with affinity data and having resolution of 2.5 Å was retrieved from the RCSB Protein Data Bank (PDB) and prepared using protein preparation wizard, which was a part of the Maestro software package (Maestro, v9.2, Schrodinger, LLC, New York, NY). Bond orders and formal charges were added for heterogroups, and hydrogens were added to all atoms in the system. Water molecules in all structures were removed and the resulting structure was energy minimized. The commercial chemical database Asinex with about 6,00,000 compounds was processed for redundancy checking and Lipinski filters to select compounds that have better druggability. Database molecules were prepared using LigPrep (LigPrep v2.2, Schrodinger LLC, New York, NY) with Epik (Epik v1.6, Schro¨dinger, LLC, New York, NY) to expand protonation and tautomeric states at 7.0 ± 2.0 pH units. Conformational sampling was performed on all database

molecules using the ConfGen search algorithm (Friesner, R. A., *et al*., 2004). ConfGen sample conformations were based on a heuristic search algorithm and energetic evaluations to efficiently explore diversity around rotatable bonds, flexible ring systems, and nitrogen inversions. We employed ConfGen with OPLS_2005 force field and a duplicate pose elimination criterion of 1.0 Å rmsd to remove redundant conformers. A distance-dependent dielectric solvation treatment was used to screen electrostatic interactions. The maximum relative energy difference of 10.0 kcal/mol was chosen to exclude high-energy structures. Database ligands were docked into the binding site of the crystal structure with Glide 5.0 (Glide v5.0 Schrodinger, LLC, New York, NY). Glide energy grids were generated for each of the prepared complexes. Binding site was defined by a rectangular box surrounding the ligand in the x-ray structure. Ligands were refined using the "Refine" option in Glide, and the Glide SP (standard precision) and XP (extra precision) descriptors were chosen (Glide v5.7, Schrodinger, LLC, New York, NY). Default settings were used for refinement and scoring. Initially we utilized the high throughput virtual screening (HTVS) scoring function to estimate protein-ligand binding affinities. Glide HTVS was faster and more tolerant to suboptimal fits than Glide SP and XP, making it better for comparison in this work. The center of the Glide grid was defined by the position of the co-crystallized ligand. NAD+ was also included in the grid as there could be a possibility of vander Waals interaction with the inhibitors within the pocket (Zhao, X., *et al*., 2013). Default settings were used for both the grid generation and docking. Compounds with best docking and GLIDE scores were then subjected to GLIDE SP and further for XP screening.

4.2.2 Design of SIRT1 inhibitors using structure based drug designing strategy

4.2.2.1 Preparation of protein structure and generation of epharmacophore

Protein with PDB code 4I5I having 2.50 A^0 resolution was considered for this study and prepared using the protein preparation wizard (Maestro, 9.3). To the hetero groups of the protein, bond orders and formal charges were added along with addition of hydrogens. Water molecules in all the system were removed and energy was minimised using OPLS_2005 force field. Using Glide module (Maestro, 9.3) energy grids were generated for the prepared complex, and the binding site was defined by a rectangular box surrounding the crystal ligand.

Bound ligand (EX527 analogue) was refined using the refine tool in Glide module, and then option for output Glide XP descriptor information was selected. All the default settings were used for scoring and refinement. Pharmacophore features were by default using Phase module, which employed a default set of six chemical features containing hydrogen bond acceptor (A), hydrogen bond donor (D), hydrophobic (H), negative ionisable (N), positive ionisable (P) and aromatic ring (R). As per the hybridization of acceptor atom, hydrogen bond acceptor sites were depicted as vectors along the axis of hydrogen bond, whereas hydrogen bond donors were represented as projected points. Each pharmacophore feature was assigned a specific energy value equal to the sum of the Glide XP contributions of all the atoms in the site. As a result this allowed the sites to be quantified and ranked with respect to energy values

4.2.2.2 Pharmacophore validation

In order to validate the generated pharmacophore, enrichment calculation was performed. A decoy set of 1055 molecules, containing 1000 decoys and 55 known SIRT1 inhibitors were developed and the ability of the pharmacophore to retrieve known actives were determined using various parameters. Enrichment factor 1% (EF 1%)(Loving, K., *et al*., 2009) was one of the parameter considered, that determined the fraction of actives recovered after 1% of decoy database (1055 molecules) was screened. Further to calculate statistical significance of the predicted parameter called Boltzmann-enhanced discrimination of receiver operating characteristic (BEDROC) (Truchon, J.F., *et al.,* 2007) parameter was obtained using Maestro (Schrödinger). In addition to this, enrichment factor (EF manual) and goodness of hit (GH) were calculated using following equations 1 and 2

$$EF = \frac{(H_a \times D)}{(H_t \times A)} \quad (1)$$

$$GH = \left(\left(\frac{H_a}{4H_tA}\right) \times (3A + H_t)\right) \times \left(1 - \left(\frac{H_t - H_a}{D - A}\right)\right) \quad (2)$$

Where

'Ht' was the total number of compounds in the hit list; 'Ha' was the total number of active molecules in the hit list; 'A' was the total number of actives in the decoy set and 'D' was the total number of molecules in the decoy set.

4.2.3. Design of SIRT1 inhibitors using ligand based drug design strategy and 3D QSAR mapping

4.2.3.1 Data set and molecular modeling

Dataset of 79 molecules reported as SIRT1 inhibitors in various literatures were considered for ligand based modeling. The scaffolds used in development of ligand based pharmacophore model consisted of derivatives of indole (Napper, A.D., *et al*., 2007), aurones(Manjulatha, K., *et al*., 2012), thioacetyl lysine (Suzuki, T., *et al*., 2009), pyrimidine carboxamide (Disch, J.S., *et al*., 2013) and sirtinol (Mai, A., *et al*., 2005) . All the dataset compounds were initially drawn in Maestro graphical user interface using 2D sketcher tab, and later they were prepared using LigPrep 2.529 module (Schrodinger) by adding hydrogens and stereoisomers at neutral pH 7 to build energetically minimized structures. Canvas 1.4 module was then used to cluster the dataset based on Tanimoto similarities to determine the structural diversity and PHASE was employed to develop ligand based pharmacophore model. In order to achieve linear relationship in QSAR equation the IC_{50} values of the dataset compounds were converted into pIC50 (-logIC50).

4.2.3.2 Molecular alignment and development of pharmacophore model for 3D-QSAR approach

Before alignment, various conformers were generated using ConfGen tool in Maestro 9.4. These conformers were generated using macro model torsion angle search approach, which was then followed by minimization of each conformer using OPLS_2005 force field. The high energy and redundant conformers were eliminated with a cut-off criterion of 1 Å root mean square deviation (RMSD) and an energy difference of 10 kcalmol-1. Upon generation of conformers, pharmacophore sites were generated on the corresponding atoms of ligand showing noncovalent interaction with receptor (protein). Scoring hypothesis was performed to

rank various hypotheses and to make a rational choice for further steps. Later best common pharmacophores were identified by aligning the pharmacophore with active ligands. Further, inactive lignads were also scored to observe the difference between the alignment scores of actives and inactives. More the difference, the better was the hypothesis, which could differentiate actives from inactives in any test set.

4.2.3.3. 3D-QSAR modelling

All the 79 molecules in the dataset were used to develop 3D-QSAR model and were divided into test and training set randomly by automated random selection tool in PHASE module. PHASE relied on partial lease square (PLS) regression applied to the large set of binary valued variables. Each independent variable in the model originated from the grid of cubic volume elements spanning the space occupied by the training set ligands. Each training ligand in training set was represented by binary code consisting of set of bit values (0 or 1) indicating the volume of elements occupied by vander Waals model of the ligand. QSAR models containing one to seven PLS factor were generated and the model with five PLS factors was considered as a best suitable statistical model. This model was further validated by predicting the activities of the test molecules in data set. Leave one out (LOO) method was used to cross validate the predictive ability of QSAR model as per the procedure and equation reported in (Truchon, J. F., *et al.,* 2007) (Loving, K., *et al.,* 2009) (Pratim Roy, P., *et al.,* 2009). QSAR model with best predictive ability was then considered for finding new leads

4.2.3.4. Pharmacophore validation

A similar procedure was followed as mentioned earlier in the section **4.2.2.2**.

4.2.3.5. Partial least squares (PLS) analysis and validation

The leave one-out (LOO) cross-validation analysis was applied to evaluate the predictive value of the models. The cross validated coefficient, $\boldsymbol{r_{cv}^2}$ (also called as LOO-q^2) was calculated using the following equation:

$$r_{cv}^2 = 1 - \frac{\Sigma(Y_{obs} - Y_{pred})^2}{\Sigma(Y_{obs} - Y_{mean})^2} \quad (3)$$

Where

Y_{obs}, Y_{pred}, and Y_{mean} were the observed, predicted, and mean values of the target property (PIC_{50}) of the training set, respectively. $(Y_{obs} - Y_{mean})^2$ was the predictive residual sum of squares (PRESS). The predictive correlation coefficient (r^2_{pred}), based on molecules of test set indicating the predictive power of the models for the external test set was derived as follows,

$$r^2_{pred} = \frac{SD - PRESS}{SD} \quad (4)$$

Where SD was the sum of the squared deviations between the actual activities of the test sets and mean activities of the training set molecules and PRESS was the sum of squared deviation between predicted and actual activity values for each molecule in test set.

4.2.3.6. External statistical validation.

External validation was necessary to evaluate the true predictive abilities of the established models. Based on the preceding inventions and developments, the properties of external validation of a 3D QSAR model could be acceptable when the 3D QSAR model satisfied fallowing statistical parameters.

$r^2_{cv} > 0.5$, $r^2 > 0.6$, R^2_0 or R'^2_0 should close to r^2, i.e. $((r^2 - R^2_0)/ r\ ^2) < 0.1$ or $((r^2 - R'^2_0)/ r^2) < 0.1$, whereas here the corresponding values of k and k′ should be, $0.85 \leq k \leq 1.15$ or $0.85 \leq k' \leq 1.15$, $r^2_m > 0.5$, and $R^2_p > 0.5$.

The r^2 value was calculated by the following formula:

$$R = \frac{\sum(Y_i - \bar{Y}o)(\tilde{Y}_i - \bar{Y}p)}{\sqrt{\sum(Y_i - \bar{Y}o)^2 \sum(\tilde{Y}_i - \bar{Y}p)^2}} \quad (5)$$

Where, Y_i and $\tilde{Y}_i$ were the observed and predicted activities, $\bar{Y}o$ and $\bar{Y}p$ were the average values of the observed and predicted pIC_{50} values of the test set molecules.

Regressions in scatter plots of Y_i against $\tilde{Y}_i$ or $\tilde{Y}_i$ against Y_i through the origin, where $Y^{ro} = k\tilde{Y}$ and $\tilde{Y}^{ro} = k'Y$ (with the intercept set to 0) respectively (Golbraikh, A., *et al*., 2002), Slopes k and k′ were calculated as follows:

$$k = \frac{\sum Y_i \tilde{Y}_i}{\sum \tilde{Y}_i^2} \quad (6a)$$

$$k' = \frac{\sum Y_i \tilde{Y}_i}{\sum Y_i^2} \quad (6b)$$

Both the correlation coefficients for the regression lines through the origin (Y^{ro}) could be defined by R_0^2 and R'^2_0, which were calculated as follows (Golbraikh, A., *et al.,* 2002):

$$R_0^2 = 1 - \frac{\sum(\tilde{Y}_i - Y_i^{ro})^2}{\sum(\tilde{Y}_i - \bar{Y}_p)^2} \quad (7a)$$

$$R'^2_0 = 1 - \frac{\sum(Y_i - \tilde{Y}_i^{ro})^2}{\sum(Y_i - \bar{Y}_o)^2} \quad (7b)$$

For better external predictive potential of the model, a parameter of modified r^2 (r_m^2) was used for the whole set considering LOO-predicted values for the training set and predicted values of the test set compounds. The r_m^2 statistic equation for overall test and training set values, were generally used for selection of the best predictive models (Pratim Roy, P., *et al*., 2009). Substantiation of particular QSAR models with r_m^2 value could be defined by the following equation:

$$r_m^2 = r^2 \left(1 - \sqrt{|r^2 - R_0^2|}\right) \quad (8)$$

Where r^2 was the non-cross-validated correlation coefficient obtained from the PLS process, and the R^2_0 was calculated from eqn. 7a.

A parameter R_p^2 (Pratim Roy, Paul., *et al*., 2009) was used to penalize the model R^2 accounting for the difference between squared mean correlation coefficient (R_r^2) of randomized models and squared correlation coefficient (R^2) of the non-randomized model. R_p^2 was thus calculated:

$$R_p^2 = R^2 \left(\sqrt{R^2 - R_r^2}\right) \quad (9)$$

4.2.4. Screening of 3D databases

Phase module was used to search the databases for compounds with similar pharmacophore features. The basic method of matching was by applying a user defined tolerance to each inter pharmacophoric site distances in a given hypothesis. This approach was used to search the 3D databases (Asinex and in-house). The molecules must match at least 3 sites for the hypotheses with 3 or 4 sites and at least a minimum of 4 sites for hypotheses of 5 or more sites. Upon screening the database, hits were ranked as per the fitness score. The Higher the fitness score more was the alignment of the matched ligand with the hypotheses. This scoring was based on the RMSD, site matching, vector alignments and volume terms. The fitness scores were from 0 to 3, where fitness score of 3 implied for ligands with maximum alignment with hypotheses. Database compounds with best fitness scores were then subjected to molecular docking. Initially high throughput virtual screening (HTVS) was performed to estimate ligand-protein binding affinities. HTVS docking was quick and more tolerant to suboptimal fits than the standard precision (SP) and extra precision (XP) docking, making it better for comparison in this work. The position of glide grid was defined based on the co-crystalized ligand. Post docking minimization was executed to optimize the ligand geometries. Best fit compounds with good docking score and glide score were then subjected to Glide SP (Standard precision) and XP (extra precision) docking. Compounds resulting with good docking scores were selected from Asinex and in-house databases (3D database) for in-vitro screening.

4.3 Design of NAMPT inhibitors

4.3.1 Design of NAMPT inhibitors using structure based drug design strategy

4.3.1.1 Preparation of protein structure and generation of e-pharmacophore model

The crystal structure of NAMPT bound with inhibitor (PDB ID: 2GVJ) with good affinity data and having resolution of 2.1 Å was retrieved from the protein data bank (PDB) and prepared using protein preparation wizard, which was a part of the Maestro software package (Maestro, v9.2, Schrodinger, LLC, New York, NY). Bond orders and formal charges were added for heterogroups, and hydrogens were added to all atoms in the system. After removing water molecules in all the structures, energy was minimized to achieve a low energy

stable state using OPLS-2005 force field and the minimization was terminated when the rmsd (root mean square deviation) reached a maximum cutoff value of 0.30Å. Using Glide module, energy grids were generated for the prepared protein complexes. Surrounding the crystal ligand, binding site was defined as a rectangular box. Using Refine option in Glide module, crystal ligand was refined and docked and the option to output Glide XP descriptor information was chosen for future steps. For refinement and scoring default settings were used.

Receptor Grid Generation tool in Maestro software package was used to generate energy grids for all prepared protein structures. We docked the crystal ligands using None (refine only) option in the XP (extra precision) docking in Glide 4.2 X. Default settings were employed to minimize and optimize the structure. Based on the XP descriptor information pharmacophore features were generated using PHASE 3.4. Pharmacophore sites were automatically generated with Phase (Phase, v3.0, Schrodinger, LLC, New York, NY) using the default set of six chemical features: hydrogen bond acceptor (A), hydrogen bond donor (D), hydrophobe (H), negative ionizable (N), positive ionizable (P), and aromatic ring (R). Hydrogen bond acceptor sites were represented as vectors along the hydrogen bond axis in accordance with the hybridization of the acceptor atom. Hydrogen bond donors were represented as projected points, located at the corresponding hydrogen bond acceptor positions in the binding site. Projected points allow the possibility for structurally dissimilar active compounds to form hydrogen bonds to the same location, regardless of their point of origin and directionality. Each pharmacophore feature site was first assigned an energetic value equal to the sum of the Glide XP contributions of the atoms comprising the site, allowing sites to be quantified and ranked on the basis of the energetic terms. Glide XP descriptors include terms for hydrophobic enclosure, hydrophobically packed correlated hydrogen bonds, electrostatic rewards, π-π stacking, π-cation, and other interactions. ChemScore, hydrogen bonding and lipophilic atom pair interaction terms are included when the Glide XP terms for hydrogen binding and hydrophobic enclosure is zero.

4.3.2 Design of NAMPT inhibitiors using ligand based drug design strategy and 3DQSAR mapping

4.3.2.1. Data set and molecular modelling

Dataset of 111 molecules reported as NAMPT inhibitors in various literatures were considered for ligand based modeling. The scaffolds used in development of ligand based pharmacophore model consisted of derivatives of ureas (Zheng, B., *et al*., 2013), azides and other molecules synthesized by click chemistry(Colombano, T., *et al*., 2009). All the dataset compounds were initially drawn in Maestro graphical user interface using 2D sketcher tab, and later they were prepared using LigPrep 2.529 module (Schrodinger) by adding hydrogens and stereoisomers at neutral pH7 to build energetically minimized structures. Canvas 1.4 modules were then used to cluster the dataset based on Tanimoto similarities to determine the structural diversity and developed ligand based pharmacophore model. In order to achieve linear relationship in QSAR equation the IC50 of the dataset compounds were converted into pIC50 (-logIC50). The data set included few highly active and inactive molecules along with moderately active compounds.

4.3.2.2 Molecular alignment and development of pharmacophore model for 3D-QSAR approach

Before alignment, various conformers were generated using ConfGen tool in Maestro 9.4. These conformers were generated using macro model torsion angle search approach, which was then followed by minimization of each conformer using OPLS_2005 force field. The high energy and redundant conformers were eliminated with a cut-off criterion of 1 Å root mean square deviation (RMSD) and an energy difference of 10 $Kcalmol^{-1}$. Upon generation of conformers, pharmacophore sites were generated on the corresponding atoms of ligand showing noncovalent interaction with receptor (protein). Scoring hypothesis were performed to rank various hypotheses and to make good rational choice for next steps. Later best common pharmacophores were identified by aligning the pharmacophore with active ligands. Further

inactive lignads were also scored to observe the difference between the alignment scores of actives and inactives. More the difference, the better was the hypotheses, which could differentiate actives from inactive in any test set.

4.3.2.3. 3D-QSAR modeling

All the 111 molecules in the dataset were used to develop 3D-QSAR model and they were divided into test and training set randomly by automated random selection tool in Phase module. PHASE relied on partial lease square (PLS) regression applied to a large set of binary valued variables. Each independent variable in the model originated from the grid of cubic volume elements spanning the space occupied by the training set ligands. Each training ligand in training set was represented by a binary code consisting of set of bit values (0 or 1) indicating the volume of elements occupied by vander Waals model of the ligand. QSAR models containing one to seven PLS factors were generated and the model with five PLS factors was considered as best suitable statistical model. This model was further validated by predicting the activities of the test molecules in data set. Leave one out (LOO) method was used to cross validate the predictive ability of QSAR model as per the procedure and equation explained previously (Truchon and Bayly 2007) (Loving, S., *et al*., 2009) (Pratim Roy, P., *et al*., 2009). QSAR model with best predictive ability was then considered for finding new leads

4.3.2.4 Pharmacophore validation

Similar procedure was followed as mentioned in the section **4.2.2.2**

4.3.2.4.1 Partial least squares (PLS) analysis and validation

Similar procedure was followed as mentioned in the section **4.2.3.4.**1

4.3.2.4.2 External statistical validation

Similar procedure was followed as mentioned in the section **4.2.3.4.2**

4.3.3 Screening of 3D Databases

Commercially available chemical database (Asinex) consisting of over 600,000 compounds and in-house database compounds (20,000) were processed through redundancy check and the resulting chemical compounds were further processed through Lipinski filters to select

compounds with better druggable properties. Similar procedure was followed as mention in the section **4.2.4.**

4.4 Enzyme inhibition studies

4.4.1. SIRT1 enzyme inhibition studies

Enzyme inhibition studies were performed using SIRT1 fluorimetric drug discovery kit (Cayman) (Nayagam, V.M., *et al*., 2006). As per the protocol, all the reactions were performed in reaction buffer provided in the kit. Initially, test drugs were diluted in varying concentrations with reaction buffer to a total volume of 25 µL and the reaction was then initiated with addition of 25 µL of substrate solution containing peptide (Arg-His-Lys-Lys.(Ac)) and NAD+. The reaction was incubated for 45 min at 37^0C and then developer containing nicotinamide was added to end the reaction. Later fluorescence reading was measured using Spectramax (M4) multiplate reader with excitation and emission at 355 nm and 460 nm respectively. Before calculating percentage of inhibition, the background noise and autofluorescence of test compounds were normalized. Later IC_{50}s were calculated using GraphPad prism software

4.4.2. NAMPT enzyme inhibition studies

4.4.2.1 Cloning of human NAMPT gene in bacterial host systems

The Human NAMPT gene was amplified using forward primer 5'CACCCATATG AATCCTGCGGCAGAAG3' and reverse primer 5'AGCTAAGCTT CTAATGATGTGCTGCTTCC 3' (Sigma-aldrich) from cDNA produced after reverse transcribing the mRNA isolated from MDAMB231 cell line. Subsequently, the amplified PCR products were digested with NdeI and HindIII and cloned into NdeI and HindIII sites of pQE2 vector (Qiagen) under T5 promoter with His tag at N-terminal domain and the clone was later authenticated by sequencing. Eventually for expression, this clone was transformed into BL21 (DE3) codon PLUS cells of *E. coli* and grown in Lauria- Bertani (LB) broth at 37^0C at rotation per minute (RPM) 140, in the presence of ampicillin (100 µg/mL) (Sigma). The exponentially

growing cultures with OD 0.4 – 0.6 were induced with 0.2 mM IPTG, and further grown overnight for protein induction at 18^0C. Cells were then harvested and lysed by sonication. Further the His-tag fusion proteins were purified using Ni-NTA resin (Bio-Rad) and confirmed by SDS-PAGE and Coomassie staining.

4.4.2.2 In-vitro NAMPT enzyme assay

Fluorometric in-vitro enzyme inhibition studies were performed as per the procedure proposed earlier (Zhang, R.Y., *et al*., 2011). Briefly, the purified NAMPT protein and the test compounds were incubated for 5 min in the reaction buffer containing 0.4 mM phosophoribosylpyrophosphate (PRPP), 2 mM ATP, 0.02% BSA (Bovine serum albumin), 2 mM DTT (dithiothreitol), 12mM $MgCl_2$ and 50 mM Tris-HCl (pH 7.5). Eventually the enzyme reaction was initiated by adding NAM (1.6 µM) and allowed to precede the reaction for 20 minutes. Later to the reaction mixture 10 µL of 20% acetophenone (in DMSO) and 10 µL of 2M KOH were added. Then the mixture was incubated on ice for 2min and 45 µL of formic acid (88%) was added and incubated at 37^0C for another 10 minutes. After the end of reaction, the solution was transferred into flat bottom opaque 96 well plates and fluorescence reading was measured in multi-plate reader (Spectramax M4, Molecular devices) at excitation and emission wavelengths of 382 and 445 nM respectively. Each reaction was performed in triplicates and percentage of activity was determined using the formula (F-Fco)/(F100%-FO). where Fo represented the fluorescence of reaction containing enzyme with no NAM (substrate) and test compound, F100% was the fluorescence of the positive control having enzyme and substrate but no compound and Fco was the fluorescence of reaction with enzyme and test compound but no NAM and finally F was the fluorescence of the reaction containing enzyme, NAM and test compound. The enzyme activity was measured by calculating NMN (product) concentration. NMN by itself did not show any fluorescent properties, hence after treating with KOH, acetophenone and formic acid formed derivatives which could exhibit fluorescence at excitation and emission of 385 and 445 nM respectively.

4.4.2.3. Differential Scanning fluorimetry (DSF)

Differential scanning fluorimetry (DSF) was performed by measuring the fluorescence of the native protein and the protein in complex with ligand in the presence of a fluorescent dye (Sypro orange, Sigma Aldrich). Fluorescence increased when the dye was exposed to non-polar residues of the protein and it reached the maximum when protein gets completely denatured. Briefly, the native protein (7.5 µl of protein 2mg/ml) + 4.5 µl of buffer (2 mM DTT, 12mM $MgCl_2$ and 50 mM Tris-HCl (pH 7.5)) was subjected to stepwise heating in a PCR instrument (Bio-Rad, CFX connect) from 25^0C to 100^0C with an increment of 0.6^0C/min in presence of the fluorescent dye SYPRO orange (3 µl) dissolved in dimethyl sulfoxide (1:100). As the temperature was increased the proteins slowly got denatured and reached equilibrium, where the concentration of the folded and unfolded proteins were equal, and this temperature was considered as melting temperature (TM) (Niesen, F.H., *et al*., 2007). When the melting temperature of the protein-ligand complex was higher than the native protein, it signified stable binding of the inhibitor to the protein.

4.5. Cell based studies

4.5.1 Cell culture and MTT assay

Cell lines used in the present study were procured from the American Type Culture Collection (ATCC, USA). MDAMB231 (breast) HT29 (colon), LnCap (Prostate), and U87 (Glioblastoma) were grown in Dulbecco's modified Eagles's medium (containing 10% FBS in a humidified atmosphere of 5% CO_2 at 37^0C). Cells were trypsinized when confluent from T75 flasks and seeded in 96-well plates in 200 µL aliquots at plating densities of 5000 cells/well. MTT (3-(4,5-Dimethylthiazol-2-yl)-2,5-diphenyltetrazolium bromide) assay was then performed to determine the cell viability. The designed compounds were tested for cytotoxicity in above three cell lines. The microtiter plates were incubated at 37^0C, 5% CO_2, 95% air and 100% relative humidity for 24 h prior to addition of experimental drugs. Aliquots of different drug dilutions were added to the appropriate microtiter wells resulting in the required final drug concentrations. Plates were later incubated for another 48 h; later 10 µL of 10 mg/ml concentration of MTT was added and incubated for 3 h at 37^0C. At the end of incubation period

formazon crystals were formed, and the plates were centrifuged and the media from microtiter plates were removed and the plates were air dried. The bound crystals were subsequently dissolved by adding 100 μL DMSO. The absorbance was then read on ELISA plate reader at a wavelength of 560 nm. Relative to the control wells the percent growth was calculated for each well. Sensitivity of the cells to the drug treatments was expressed in terms of GIC_{50} which was the concentration of a compound at which 50% growth reduction was observed when compared to the control. The percentage of cells killed was obtained from the formula

4.5.2. Cell cycle analyses

Cell cycle analyses was performed using Guava Cell Cycle Assay kit (Zhang, Y., *et al*. 2012) . After incubation with the test compound, cells were harvested and freezed at -20^0C with ethanol for overnight. Then DNA was stained with propidium iodide and the cell cycle gates were set to a position in dot plot which corresponded to four markers, marker 1: G1 phase, marker 2: S phase, marker 3: G2/M phase and marker 4: sub-G0/G1.

4.5.3. Annexin V apoptosis assay

Approximately 5 X 10^6 cells were plated in 6 well plates and incubated 48 h with test compounds at 37^0C. Cells were harvested after trypsinization and apoptotic cells were assayed with an annexin V-FITC apopotosis detection kit (Millipore). Briefly 4 X 10^5 cells were incubated with an annexin V-FITC for 30 min at room temperature in the dark. Later after centrifugation at 1200 X g for 7 minutes, the medium was removed and was suspended in 0.5 ml of binding buffer. Later, propidium iodide was added before flow cytometry analyses (Amnis imaging flow cytometers, Merck Millipore). Early apoptotic cells were stained exclusively with annexin V-FITC and late apoptotic stages were labelled with both annexin V-FITC and propidium iodide.

4.5.4. Measurement of NAD

All the chemicals unless stated were procured from Sigma Aldrich. Cells were seeded in 12 well plates 24 h prior to drug incubation and after the incubation time 300 µL of 1N $HClO_4$ was added and incubated in ice for 30 min, and then the supernatant was carefully collected in 1.5 ml eppendorf and neutralized with 100 µL of 3M K_2CO_3. This was incubated for 10 min on ice and later centrifuged at 15,000 rpm for 10 minutes. The supernatant was collected and used to determine NAD levels (Formentini, L., *et al*., 2009). 75 µl of supernatant and 25 µl NAD cycling mix was added, which contained assay buffer (50 mM triethylamine pH 8.0 and 1mM $MgCl_2$) ADH (Alcohol dehydrogenase) 0.18 U/ml, diaphorase 0.5 U/ml, resazurin 10 µM, ethanol 2 mM) and the reaction mixtures were incubated at room temperature for 20 min, and the fluorescence was measured at excitation and emission of 544 and 590 nm respectively. All the reactions were performed in triplicates and the resultant fluorescence signal was normalized with background signal.

4.5.5. Measurement of reactive oxygen species

Reactive oxygen species (ROS) was measured using fluorescent dye called 2′,7′-dichlorofluorescin diacetate (DCFDAE, Sigma Aldrich). The DCFDAE get deacetylated after penetrating into the cells because of cellular esterases, which was later oxidised by ROS into DCF (2', 7' dichlorofluorescin) a fluorescent compound measured using multiplate reader at excitation and emission of 495 NMN and 529 nm respectively. U87 cell lines were grown in media and seeded in opaque (black) 96 well plates at cell density of 2.5 X 10^5 cells/well. The cells were then incubated for 24 h at 37^0C, once the cells were adhered to the bottom of the plate, the test compounds were incubated and cells were stained with DCFDAE for 40 min at 37^0C. Eventually all the wells were washed with PBS, to minimize the background signal, and then fresh media was added to measure fluorescence in multiplate reader (Spectramax-M4) at excitation and emission of 495 nm and 529 nm respectively. Each reaction was done in 6 wells, with background signal normalised by considering fluorescence of unstained cells.

4.5.6. RNA extraction and qRT-PCR

LnCAP cells were seeded in 6 well plates at cell density of 2 X 10^6 cells/ml and incubated with LPS (10 µg/ml) and test compound for 6 hr. Thereafter cells were harvested and RNA was extracted using Tri reagent (Sigma Aldrich). RNA purity and concentration was determined by measuring absorbance at 260, 280 and 320 nm using spectrophotometer. Later mRNA was reverse transcribed using verso cDNA synthesis kit (Thermo scientific). Further using specific primer for each gene, quantification was done by using Sybr green master mix (SensiMix SYBR no-ROX, Bioline) in PCR machine (Bio-Rad, CFX connect). The qRT-PCR was performed using following parameters: 95^0C for 10 min, then denaturation at 95^0C for 15 s followed by annealing at 60^0C for 15 s and amplification at 72^0C for 15 s. Further denaturation, annealing and amplification steps were repeated 40 times. Optimal primer concentrations were determined before all the qPCR experiments. The sequence of forward and reverse primers of TNF-α and IL-6 were CCCTCACACTCAGATCATCTTCT (forward), GCTACGACGTGGGCTACAG (reverse) and GACAACTTTGGCATTGTGG (forward), ATGCAGGGATGATGTTCTG (reverse) respectively. To determine apoptosis in LnCAP cells, test compounds were incubated for 24 h and eventually RNA isolation and cDNA synthesis were performed. The following sequence of forward and reverse primers of p53 and caspase 3 were used to know the mRNA expression. CCGTCCAGGGAGCAGGTAGC (forward, p53), GCCAATCCAGGGAAGCGTGTC (reverse, p53) and GCTGAGCTGCCTGTAACTTGAGAG (forward,Caspase-3) , GCCCTTCCTGCGTGGTCCA (reverse, Caspase-3) respectively.

4.6. In-vivo studies

4.6.1. Benign prostate hyperplasia

Male wistar rats weighing 180 to 220 g were used. All the animal experiments were approved by the Institutional Animal Ethical Committee of our Institute. Testosterone propionate with a dosage of 3 mg/Kg was injected subcutaneously to induce benign hyperplasia for 14 continuous days (Gossell-Williams, M., *et al*., 2006). Simultaneously along with testosterone, the effect of the test drug in reducing hyperplasia was determined by administering intraperitoeally. Initially

the animals were divided into three groups, each group has 5 animals. Group A served as negative control, Group B served as positive control, which received only testosterone propionate suspended in 5% methyl cellulose and 0.5% Tween 80. Group C received both testosterone and test compound suspended in 5% methyl cellulose. After 14 days of dosing, animals were sacrificed using light ether anesthesia and subsequently prostate glands were carefully removed and weighed. Ratio of body weight to prostate weight was calculated to determine the percentage of inhibition (%I) using below formula

%I = (100 –(treated group-negative control)/(positive control-negative control) X 100)

Isolated prostate gland was fixed in Bouin's solution and then stained with hematoxylin and eosin stain. Later histology of stained tissues were observed under light microscope and recorded.

4.6.2. Carrageenan induced inflammation model

Acute anti-inflammatory activity was measured using carrageenan induced paw inflammation assay (Morris, C.J., 2003). Male wistar rats of 180 g were used for the current study, and animals were acclimatized for one week before the experimental session. All the animal experiments were done following the guidelines of the Institutional Animal's Ethics committee (IEAC). Acute inflammation was induced by subplantar injection of 100 µL of 1% freshly prepared solution of carrageenan in normal saline. Animals were divided into three groups. Group A received only carrageenan (control), Group B received carrageenan and indomethacin (10 mg/Kg suspended in 5% methyl cellulose, known drug to treat acute inflammation) and Group C received both carrageenan and test drug (30 mg/Kg suspended in 5% methyl cellulose). Groups B and C were treated with the drug 30 min prior to carrageenan injection. Paw volume was measured using plethysmometer (Ugobasile) before administering carrageenan, which was considered as 0 h reading, and then after every 1 h paw volume was measured with carrageenan treatment. Increase or decrease in the paw volume was recorded and graph was plotted against time (hours).

Chapter 5 Results and Discussion

5.1. Design and biological evaluation of SIRT1 inhibitors identified by virtual screening

Sirtuins are the mammalian orthologues for the yeast Sir2 proteins, which is implicated in chromatin silencing. SIRT1 (EC 3.5.1.98) is the major member of sirtuin deacetylase family of enzymes that removes acetyl group from lysine residues in histones and other proteins. Human SIRT1 belongs to class III HDACs, uniquely depend on NAD for activity. Enzyme catalytic reactions require the cleavage of glycosidic bonds between ADP ribose and nicotinamide moieties of NAD with simultaneous release of nicotinamide. This is followed by transfer of acetyl group from lysine to O-acetyl ADP ribose. Numerous studies have suggested a role of SIRT1 in tumorogenesis. Transient knock-down of SIRT1 leads to increase apoptotic response to DNA damage or oxidative stress. To date, there were very few potent inhibitors identified. Thus, we employed computer aided drug design strategies to develop novel small molecule inhibitors showing potent anticancer activities.

5.1.1 Design and identification of leads

Inhibitors were identified using high-throughput virtual screening. Crystal structure of human SIRT1 with PDB ID 4I5I was used to screen the Asinex database (commercially available). To understand docking pose of inhibitor, the known inhibitor (EX527) in crystal structure was redocked flexibly and the rmsd (root mean square deviation) was compared with the pose of inhibitor in the crystal structure. The rmsd was found to be 0.8479 A^0, which inferred that the docking pose and grid conditions were well within the range and could be considered to virtually screen any ligand database. The protocol followed for inhibitor design included,

HTVS (high throughput virtual screening) docking and then secondary SP docking was performed, by which the survivors from these docking studies were further validated through XP docking along with known reported ligands, by which we could understand the hydrogen-bond interactions, electrostatic interactions, π-π stacking interactions and hydrophobic enclosures. The top five ligands as SIRT1 inhibitors (**I1-I5**) were shortlisted and their structures are presented in **Figure 6**

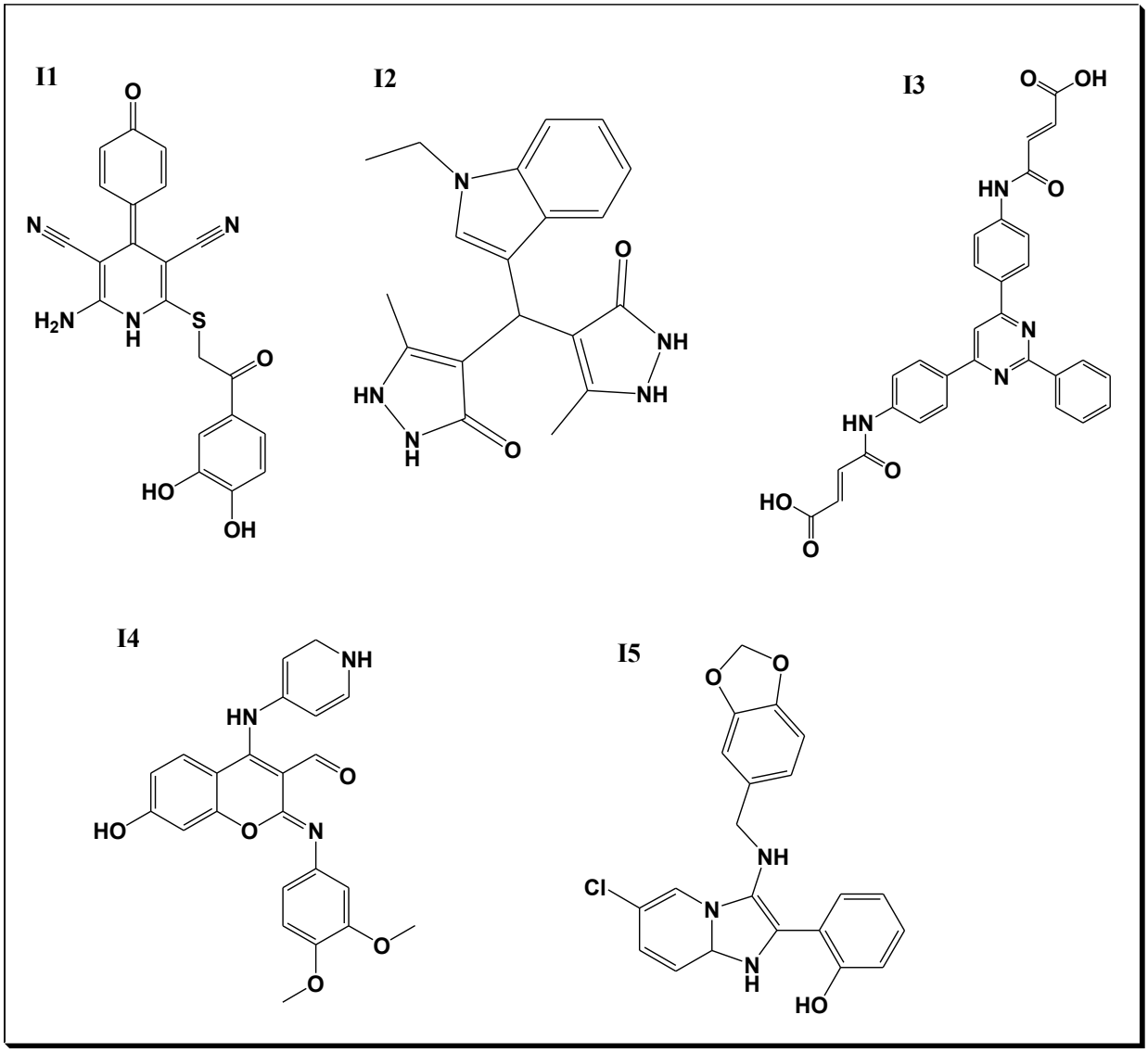

Figure 6: Two dimensional structures of top leads

The short listed ligands along with hydrogen bond interactions of inhibitors are depicted in **Table 1**. Known inhibitors were utilized to validate and compare the results for better understanding. Most of the hits were found to show similar interactions (Phe-293, Phe-297, Gln-345 and Asp-348) as that of crystal ligand (**CL**) and were also found to show similarity with regard to known inhibitors like salerimide, splitomycin, EX-527 and sirtinol. Comparing the docking score, it is interesting to know that EX-527 showing highest docking score with -9.132 Kcal/mol, followed by crystal ligand (-8.979 Kcal/Mol). Though, the lead compound I4 has shown least score -3.298 Kcal/mol, it very much comparable with a sirtinol (known SIRT1 inhibitor) docking score (-3.298Kcal/mol). Hence molecules with docking score above 3.0 Kcal/mol was considered for this study and presented in Table 1. All the top shortlisted inhibitors showed π bonding with Phe-297 or Phe-273, which strongly supported the statement of Zhao., *et al*., 2013 that inhibitors interact with SIRT1 primarily through hydrophobic interaction and fixed deep in the active site behind the nicotinamide and the ribose of NAD^+ (Zhao., *et al*., 2013).

Considering the docking position of the crystal ligand (**CL**) (Zhao., *et al*., 2013), it could be inferred that it interacted well with the available H-bond acceptor and donor sites. The hydrophobic site of catalytic pocket was found to interact with the aliphatic and aromatic parts of the inhibitor as presented in Figure 7. From the docking pose it was clear that catalytic pocket bound with inhibitor showed extensive H-bonding. As the amide ($-NH_2$) moiety of inhibitor faced the carboxyl group of Asp-348 that donate hydrogen and in addition to that the carbonyl oxygen of inhibitor showed hydrogen bonds with the NH of Asp-348 and Ile-347. Further to this, NH group of indole ring acted as H-bond donor to the carbonyl oxygen of Gln-345. Down to this H-bond network, a flexible loop lined the catalytic pocket in a conformation which was triggered by the NAD^+ binding. From the figure it could be seen that Phe-273 oriented into the pocket and prevented or restricted the binding of large sized ligands. Towards the other side, chlorine group in the aromatic ring of inhibitor lied adjacent to Phe-297. This binding conformation was exactly similar to the model proposed by Huhtiniemi *et al*., (Huhtiniemi, T., *et al*., 2006).

Table 1: Glide docking score, important amino acids and gold fitness of shortlisted inhibitors

Inhibitors	Glide gscore	H bond	Amino acid involved in interactions with ligand
I1	-7.56	2	Gln-345, Val-412, Gln-320, Phe-297 (π bonding)
I2	-6.41	2	Asn-346, Asp-348, Pro-271, Phe-293 (π), Phe-297 (π)
I3	-5.04	1	Gln-345, Phe-297 (π), Phe-273 (π)
I4	-3.78	0	Phe-297 (π)
I5	-4.61	0	Gln-345, Phe-273 (π)
Saleremide	-4.51	0	Phe-297 (π)
Splitomycin	-8.26	0	Phe-297 (π)
Sirtinol	-3.29	0	Phe-273 (π)
CL[a]	-8.97	3	Asp-348, Ile-347, Gln-345, Phe-273 (π) , Phe-297 (π)
EX-527	-9.13	4	Asp-348 (2), Ile-347, Gln-345

[a] CL represents crystal ligand from PDB ID: 4I5I.

We compared the docking pose of the crystal inhibitor (**CL**) with the finest hits filtered through docking studies. It was observed that hydrophilic moieties were adjacent to the hydrogen bond donor and acceptor residues (**Figure 7**). In case of **I1,** the two hydroxyl groups were precisely fixed and oriented adjacent to the Gln-345 and Val-412, whereas the hydrophobic head group of phenyl ring was facing towards the Phe-297. The other two rings of this compound were not allowing these rigid planar rings to move or rotate flexibly. This prevented proper fixing of the hydrophilic moieties (oxo, cyano and amine groups) adjacent to Asn-346 and Ile-347. In the case of **I2,** we could see two identical 2,3 diazole rings which acted as hydrogen acceptors or donor moieties. Hence, in these moieties, one of the diazole rings were freely bound with Asn-346 and Asp-348, while benzopyrrole, the hydrophobic moiety was oriented away from the hydrophilic pocket. With regard to **I5**, chlorine substituted pyridine ring was oriented similar to chlorine on the crystal inhibitor (**CL**) adjacent to Phe-297. Further the hydroxyl group at ortho position, was away from Gln-345 and Asn-346. If it would have been in the para position there was a chance for the inhibitor to make bonding firmly with Gln-345 and Asn-346 residues. Hence we observed only π bonding with Phe-273. The designed inhibitors showed π bonding with Phe-297 or Phe-273, thus resulting in an extended conformation of NAD^+ binding length wise across the mouth of the binding site, which sterically obstructed the productive binding of substrate.

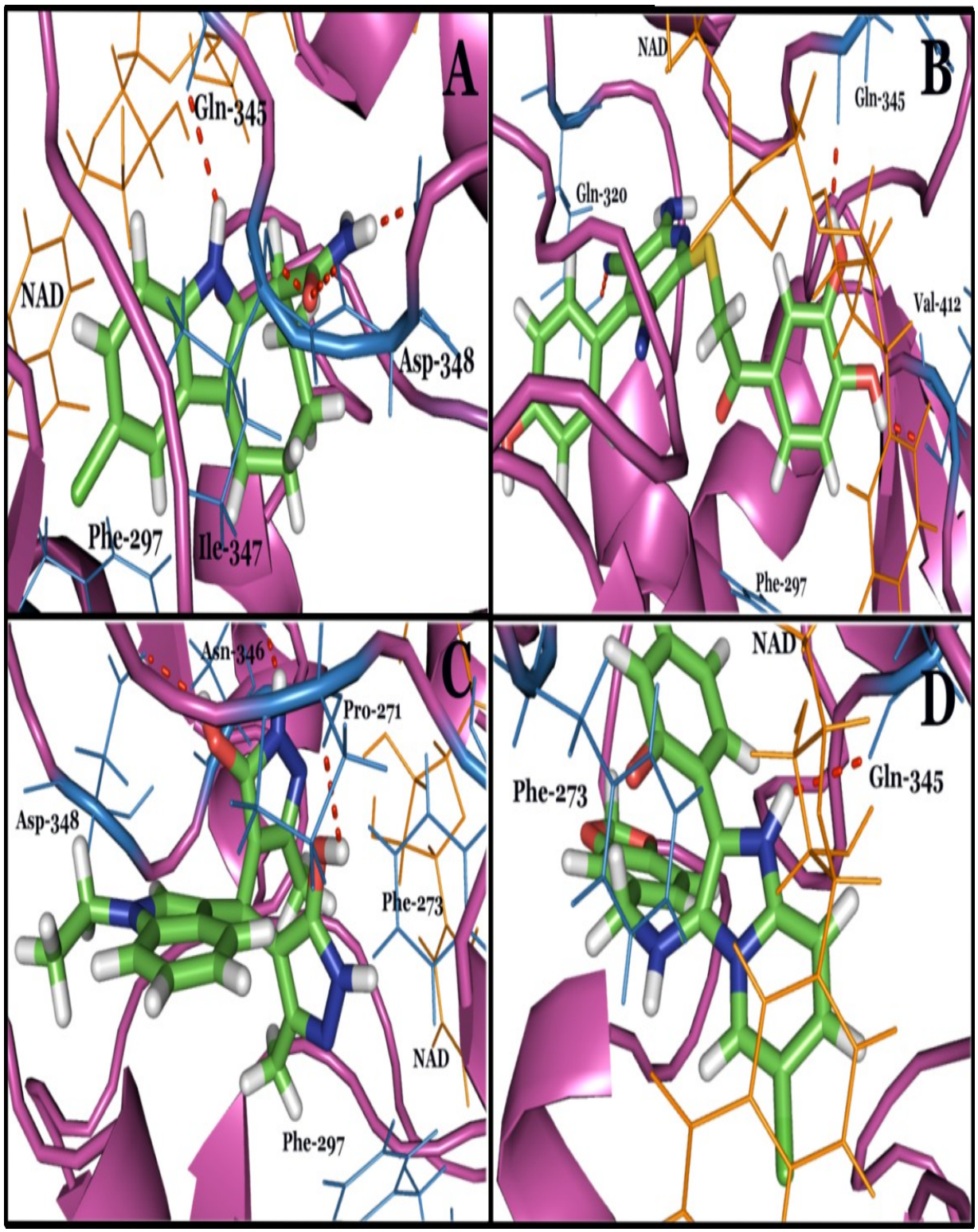

Figure 7 Binding pose of inhibitors in the active site pocket. A B C and D represent CL, I1, I2 and I5 respectively. The red colour bonds indicate the hydrogen bonds between ligand (in sticks) and amino acids (in blue lines). The NAD in the active pocket was represented in orange

5.1.2 In-vitro SIRT1 enzyme inhibition studies

Thus, based on the HTVS technique, the shortlisted fine ligands were procured from commercial sources and were subjected to biological assays to prove the concept of design. During the in-vitro enzyme assay, we employed different controls in experiments, with and without substrate to reduce the background signals. Five compounds from the inhibitor class were found to be promising and hence quantified to determine IC_{50} of these compounds. For comparison, we had included the IC_{50} data of known inhibitors like suramin, sirtinol and EX-527 **(Table 2)**. Dose depended curves for all the shortlisted inhibitors were given in the **Figure 8**.

Table 2: IC_{50} values resulted from in-vitro hSIRT1 inhibition

Compounds	IC_{50} µM
I1	16.35±0.975
I2	19.59±2.347
I3	22.15± 3.563
I4	52.92±4.270
I5	32.03±11.907
CL	0.067[a]
EX-527	2.7[a]
Sirtinol	130[b]
Suramin	2.5[c]

[a]The IC_{50} values of CL and EX-527 were from (Napper, A.D., *et al*., 2007)
[b]The IC_{50} value of Sirtinol was from: (Mai, A., *et al.,* 2005)
[c]The IC_{50} value of Suramin was from (Mai, A., *et al*., 2005

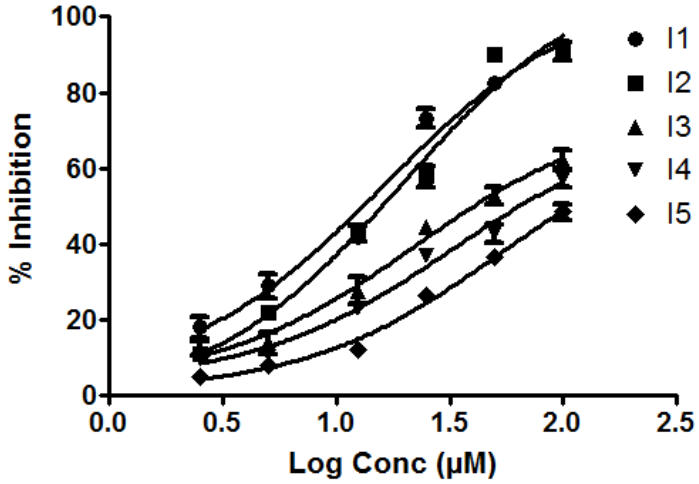

Figure 8: Percentage inhibition at different concentration of test compounds

5.1.3. Cell proliferation studies

As we know that SIRT1 has been reported to be over expressed in many cancers, it was proven before that SIRT1 inhibitors could specifically be used in cancer treatment; Hence the anticancer activity was studied using MTT on four cell lines. All the 5 designed ligands with IC_{50} values were considered for this study and the results are presented in **Table 3**. For comparison, we utilized standard drug gemcitabine in various concentrations and the GI_{50} are reported in **Table 3**. From the results it could be inferred that most of the compounds were showing GI_{50} of less than 5µM in almost two of the cell lines and all the compounds showed GI_{50} less than 1µM in prostate cancer cell line. From this we could intrigue that these molecules act best on prostate cancer.

Table 3: Showing the GI_{50} of top five inhibitors on four different cell lines

Compounds	GI_{50} values in µM				%Inhibition at 30 µM
	U937	MDAMB	LnCap	CaCO2	HEK-293
I1	4.71±2.36	0.79±0.19	0.24±0.07	0.02±0.01	22.67±2.37
I2	5.78±2.34	16.69±5.12	0.53±0.01	3.71±1.12	20.69±3.94
I3	51.53±1.32	50.3±1.43	0.07±0.01	0.07±0.01	25.87±1.94
I4	18.42±1.12	15.1±2.76	0.003±0.01	0.51±0.01	10.97±2.89
I5	4.31±0.12	1.24±0.08	0.09±0.03	3.32±1.23	30.47±2.02 (CC_{50}:40.12)
Gemcitabine	0.66±0.02	0.05±0.03	0.50±0.02	0.04±0.02	ND

We further performed cell cycle analysis at five different concentrations for two compounds (**I4** and **I5**). We selected these compounds as they showed GI_{50} less than 100 nM in prostate cancer. There were three compounds that showed GI_{50} value less than 100 nM (**I3, I4** and **I5**), among which, **I3** showed less potency against MDAMB-231 cell line with GI_{50} of 50 µM, whereas the other two showed 1.2 µM and 15.1 µM respectively. The other reason for comparing the GI_{50} values of LnCap and MDAMB-231 was based on the literature evidence of SIRT1 being specifically overexpressed in these two cells lines and were well characterized.

5.1.4. Cell cycle analyses

Cell cycle analyses were performed to further analyze the growth inhibition of lead compounds. In this method cells were incubated with propidium iodide to stain the DNA. Later cells were passed through flow cytometer.to measure the fluorescence. It is known fact that the cells which are dividing are in G0/G1 and M phase and least observed in sub G0 phase. If there is growth inhibition of test compound because of either apoptosis or necrosis, the cells will enter into subG0 phase. Based on this objective, different phases of cell cycle can be measured using flow cytometer after staining the DNA with propidium iodide.

From the cell cycle analysis data **(Figure 9)** we could understand the percentage of cells in each phase and from the results it could be inferred that cells treated with compound **I4** showed a similar percentage of cells as that of control (untreated) at different cell phases, while

compound **I5** showed significant difference at 1 µM and 10 µM concentrations. It was also clear that cells entering into sub G0 phase were increased from 1 µM to 10 µM, which clearly indicated that cell undergoing apoptosis had increased. Thus, from this study **I5** could be considered as the most potent promising anticancer drug candidate. To understand the cytotoxic characteristic of compound **I5**, we tested on HEK-293T cell line (Human embryonic kidney cell line) at different concentrations. We observed that its CC_{50} (cytotoxic concentration 50) was 40.12 µM, which was comparatively higher (10-100 times) than the GIC_{50} obtained against 5 cancerous cell lines. This could be inferred that it was not toxic on normal cell lines and was more specific to cancerous cell lines.

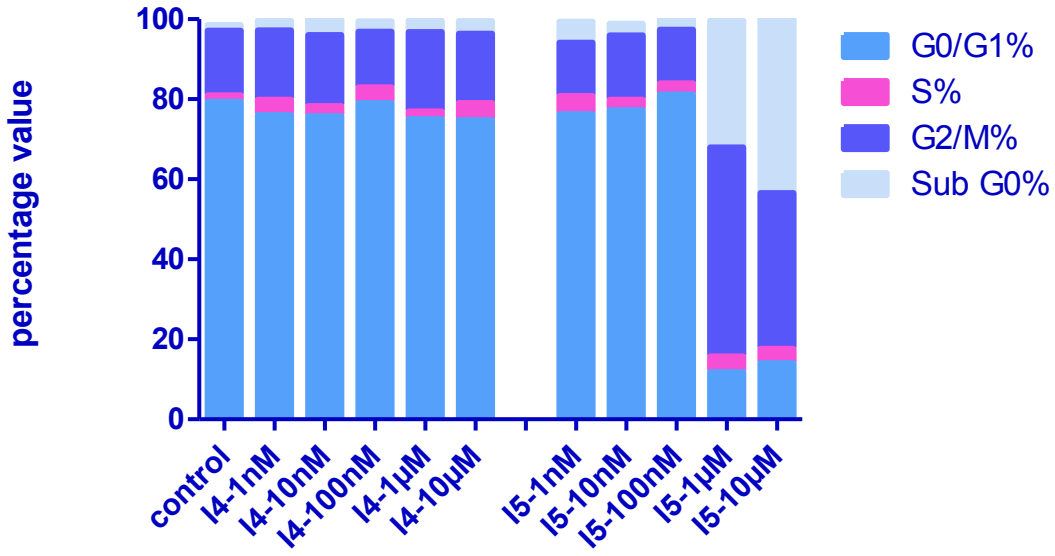

Figure 9: Showing the percentage of different cell phases after treating LnCap with two test compounds (I4 and I5) at five different concentrations**.**

If we compare the results from docking, *in vitro* enzyme assay and cell based assays, we could understand that the compound **I5** showed moderate parameters in docking studies (docking score -4.617) and *in vitro* enzyme activity (IC_{50}-32 µM) when compared to the compound **I1** which was found to show good interactions (docking score -7.568) and better IC_{50} (16.35µM)

among the rest. The promising anticancer activity of **I5** could be due to the fact that the compound might be acting through other mediators including SIRT1.

5.1.5 Conclusion

SIRT1 being the most important regulator of metabolism, inhibitors are important in treating various metabolic disorders. The present work focuses on discovering novel inhibitors, which would help with further development of future drugs. In conclusion, the study involving HTVS of commercial database yielded a new inhibitor **I1** with IC_{50} values of 16.35 μM and moderate activity in cancer cell lines. Further to this, in the process of discovery, we also discovered a new compound **I5** with moderate activity on SIRT1 enzyme, but potentially promising effect on prostate cancer cell line with GI_{50} value of 96 nM, which was supported by cell cycle analysis studies. It was interesting to know that **I5,** with structural scaffold of dihydro imidazole had shown 5 times more potent activity (96 nM) in LnCAP cells compare to gemicitabine (500 nM). In addition to that, **I5** did not show any toxicity when tested in human embryonic kidney cell (HEK-293) cell line, showing the CC_{50} of 40 μM. It is several fold higher in concentration compared to the inhibition shown in LnCAP cell line. Thus, infers the specificity of this compound in treating cancer condition.Further work to increase the affinity of these lead molecules through structural modification and developing structure-activity relationship could be fruitful.

5.2. Design and biological evaluation of SIRT1 inhibitors identified using structure and ligand based pharmacophore modelling

Design of durgs using the available knowledge about the structural properties of the target proteins and inhibitors would be very useful and could also give some directions in the discovery process. Computer aided drug designing strategies are specially meant for this and were employed for the current work. It was categorized into two methods. One is ligand based drug design and other is structure-based drug design. Structure-based drug design relies on high resolution crystallized structural data, to calculate interaction energies between the ligand molecule and protein active site. In the current work, co-crystallized molecules in the active site were subjected to re-interact with the protein active site virtually and energy descriptors were utilized to recognize important pharmacopore features responsible for binding. This method was fruitful to attain novel chemical analogues which can bind to the protein active site.

Ligand based drug design exploits the knowledge of known active and inactive molecules obtained through chemical similarity searches and utilizes this information while generating the pharcophore features. The pharmacophore features obtained in this strategy will have median features of all the known active molecules. Later employing various pharmacophore validation methods and 3D-QSAR mapping gives the choice to finalize the best pharmacophore hypothesis with high predictive molecular searching capacity.

5.2.1. EPharmacophore modeling

Human SIRT1 crystal structure with PDB ID 4I5I bound to an inhibitor (EX527 analogue) was retrieved from protein data bank. Although there were other crystal structures (4KXQ, 4IG9 and 4IF6) reported for human SIRT1, there were no known inhibitors bound in the catalytic pocket and hence not utilized in our study. Energy based pharmacophore modelling was carried out on the crystal structure (4I5I) with 2.5 A^0 resolution. The protein was prepared to correct missing hydrogen, ambiguous protonation states and flapped residues. After removing water molecule the protein structure was minimized and refined using OPLS_2005 force field. The crystal ligand EX527 analogue (CL) was redocked onto the prepared protein. Using the docked pose, five

pharmacophoric features containing two donors (D), two rings (R) and one acceptor (A) features were generated. Thus the e-pharmacophore features were generated based on the structural and interacting energy parameters between the protein and ligand. The five feature pharmacophore was divided into various combinations of 4 and 3 features as shown in **Table 4**. To evaluate and select best pharmacophore feature for virtual screening, parameters like EF1%, BEDROC, RIE and ROC were compared. These parameters directly depended on the recovery rates of known actives against the ranked decoy databases. About 55 of known inhibitors were included in the decoy set of 1000 compounds making into 1055 compounds. Further to this enrichment factor (manual) and goodness of hits were calculated. These parameters depended not only on true actives but also on false actives. From the **Table 4** we could understand that both pharmacophore features set of D4R8R7 and D4A1R8R7 showed similar valuation with BEDROC, RIE, and ROC but there were small deviations in terms of enrichment factor (manual) and goodness of hit (GH). This difference was due to the retrieval of more false positives by D4R8R7 than that of D4A1R8R7 pharmacophore model. Hence we considered enrichment factor and goodness of hit was also calculated manually for the selection of best pharmacophore models to be utilized for 3D database screening. Finally, we selected one best pharmacophore set from each of 5 feature, 4 feature and 3 feature pharmacophore models (**Figure 10**) and they were R8D4R7A1D3 (two rings, two donors and 1 acceptor), D4A1R8R7 (two rings, one donor and acceptor) and D4R8R7 (two rings and one donor). Interestingly D3 (donor) feature was found lacking in the 4 feature pharmacophore model as it had less energy score than other pharmacophore features (**Table 5**). Similarly A1 (acceptor) feature was found missing in the 3 feature pharmacophore model. This illustrated the significance of energy scores of epharmacophore features. More the negative energy score the pharmacophore feature had, more was the impact on retrieving true actives.

Table 4: Depicting the energy score of energy based pharmacophore features

Pharmacophore features	Energy scores (Kcal/ml)
R8	-1.73
D4	-0.96
R7	-0.87
A1	-0.57
D3	0.33

Table 5: Validation of epharmacophore and ligand based hypothesis

Pharmacophore	EF 1%	RIE	ROC	BEDROC (α=20.0)	EF (Manual)	GH
D4A1R8R7D3	26	4.65	1.02	0.361	0.864	0.207
D4A1R8R7	78	11.01	1	0.854	1.976	0.229
D4A1D3R7	38	6.38	1.01	0.494	1.670	0.137
D4A1D3R8	34	5.81	1.02	0.451	1.732	0.137
D4R8R7	78	11.01	1	0.854	1.935	0.168
D4A1D3	42	6.92	1.01	0.537	1.443	0.122

EF	Enrichment factor at 1% of the decoy data set.
RIE	Robust initial enhancement.
ROC	Receiver operating characteristic curve value.
BEDROC	Boltzmann-enhanced discrimination of receiver operating characteristic.
EF	Overall enrichment factor.
GH	Goodness of fit.

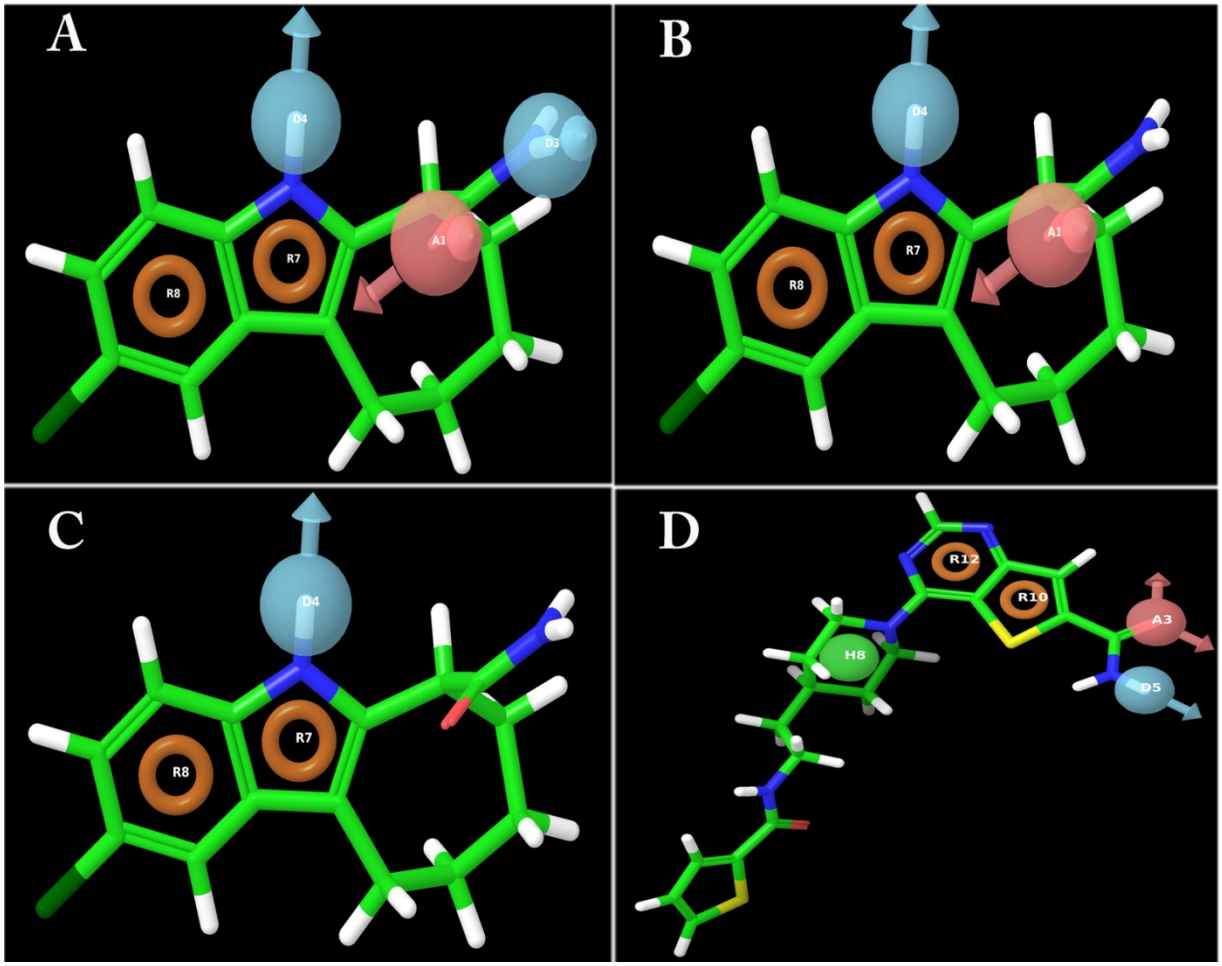

Figure 10: Depicting the pharmacophore hypothesis generated from both energy based (A,B and C) and ligand based pharmacophore hypothesis (D). A. 5 feature pharmacophore hypothesis with two ring (R), two donar (D) and 1 acceptor (A) features. B. 4 feature pharmacophore hypothesis with two ring (R), one donar (D) and 1 acceptor (A) feature. C. 3 feature pharmacophore hypothesis with two ring (R), and one donar (D) feature. D. Hyopothesis generated from ligand based pharmacophore with two rings (R), one acceptor (A), one donar (D) and one hydrophobic (H) feature

5.2.2 Ligand-based pharmacophore modeling

In addition to the energy based pharacophore modelling we also attempted to screen 3D databases by using ligand based pharmacophore modeling. By employing PHASE module (Schrodinger) either we could generate QSAR model of atom based or pharmacophore based. As

the training set molecules were rigid and congeneric we attempted to generate common pharmacophore hypotheses. Data set of 79 molecules was divided into active, moderately active and inactive sets. The scaffolds used in the development of ligand based pharmacophore model consisted derivates of indole (Napper, A.D., *et al*., 2007), aurones (Manjulatha, K., *et al*., 2012), thioacetyl lysine (Suzuki, T., *et al*. 2009), pyrimidine carboxamide (Disch, J.S., *et al*., 2013) and sirtinol (Mai, A., *et al*., 2005). Compounds with pIC_{50} values higher than 8.1 were considered as actives and those with less than 4.11 were considered as inactives. Molecules with pIC_{50} values between active and inactives were considered as moderately active.

Based on different steps of scoring procedure like survival, survival inactive and post hoc, twenty five hypotheses were generated. Further, we selected five best hypotheses which satisfied internal parameters like survival activity, vector, volume and most active alignment. These five hypotheses were further validated, determining enrichment factor and goodness of fit as done with epharmacophore validation. Hypothesis ADHRR 782 with one hydrogen bond acceptor (A), one hydrogen bond donor (D), one hydrophobic group (H) and two rings (R) displayed good enrichment factor and goodness of hit compared to other hypotheses **Table 6**. Hence we could infer that hypothesis ADHRR 782 (**Figure 11**) could predict most of the active molecules than the rest of the hypotheses. In addition to this, these five hypotheses were further validated for QSAR predictability and subjected to partial least square (PLS) analyses.

Table 6: Ligand based pharmacophore hypothesis and their scores

Hypothesis	Survival score	Survival-inactive score	Vector scores	Volume Score	Score site
ADHRR.782	3.404	1.984	0.917	0.707	0.78
ADHRR.771	3.302	1.848	0.916	0.615	0.77
ADHRR.756	3.255	1.743	0.908	0.655	0.69
ADHRR.769	3.083	1.503	0.92	0.586	0.58
ADHRR.802	2.301	1.023	0.615	0.323	0.36

Table 7: Pharmacophore validation of ligand based pharmacophore model

Pharmacophore	EF 1%	RIE	ROC	BEDROC (α=20.0)	EF (Manual)	GH
ADHRR 782	39	5.60	1.04	0.608	3.056	0.276
ADHRR 802	41	5.79	1.04	0.628	2.525	0.238
ADHRR 771	40	5.69	1.04	0.618	2.451	0.231
ADHRR 756	35	5.19	1.04	0.563	2.276	0.211
ADHRR 769	37	5.39	1.04	0.585	2.335	0.218

EF	Enrichment factor at 1% of the decoy data set.
RIE	Robust initial enhancement.
ROC	Receiver operating characteristic curve value.
BEDROC	Boltzmann-enhanced discrimination of receiver operating characteristic.
EF	Overall enrichment factor.
GH	Goodness of fit.

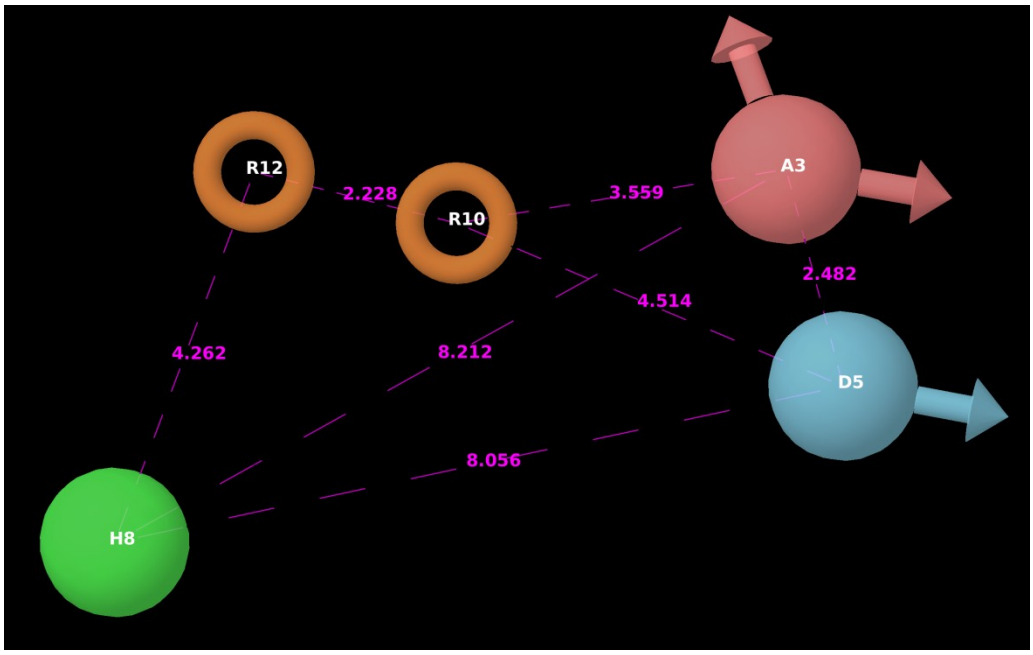

Figure 11: Pharmacophore hypothesis (Hypothesis 782) and the distance between the pharmacophoric sites are in pink dotted lines. All the distances are in A^0 unit.

5.2.4. Generation of 3D-QSAR model and PLS analyses

All the five pharmacophore hypothesis were further validated for the best QSAR predictability by generating pharmacophore based 3D-QSAR models and subjected to PLS analysis. As the purpose was to generate a common 3D-QSAR map for the most active structurally diverse compounds. Hence, we chose the method of pharmacophore based 3D-QSAR developmet rather than atom-based method. Herein, pharmacophore based 3D-QSAR models all atoms would take into account or the pharmacophore sites would be matched to the entire ligand alignment pattern respectively. If the ligand structures are relatively small and it has a small number of rotatable bonds with some common structural framework, then, an atom based pharmacophore would work quite well. For the generation of 3D-QSAR model, a data set of known SIRT1 inhibitors was split into training and test set. 3D alignments of the data set molecule were assessed by statistical validation methods, where the shift of test and training set compounds leads to the proper alignment of molecules. All the data set compounds used for pharmacophore generation and 3D-QSAR study were given in **Figure 12** with their structural information, experimental and predicted biological activity and dataset positions.

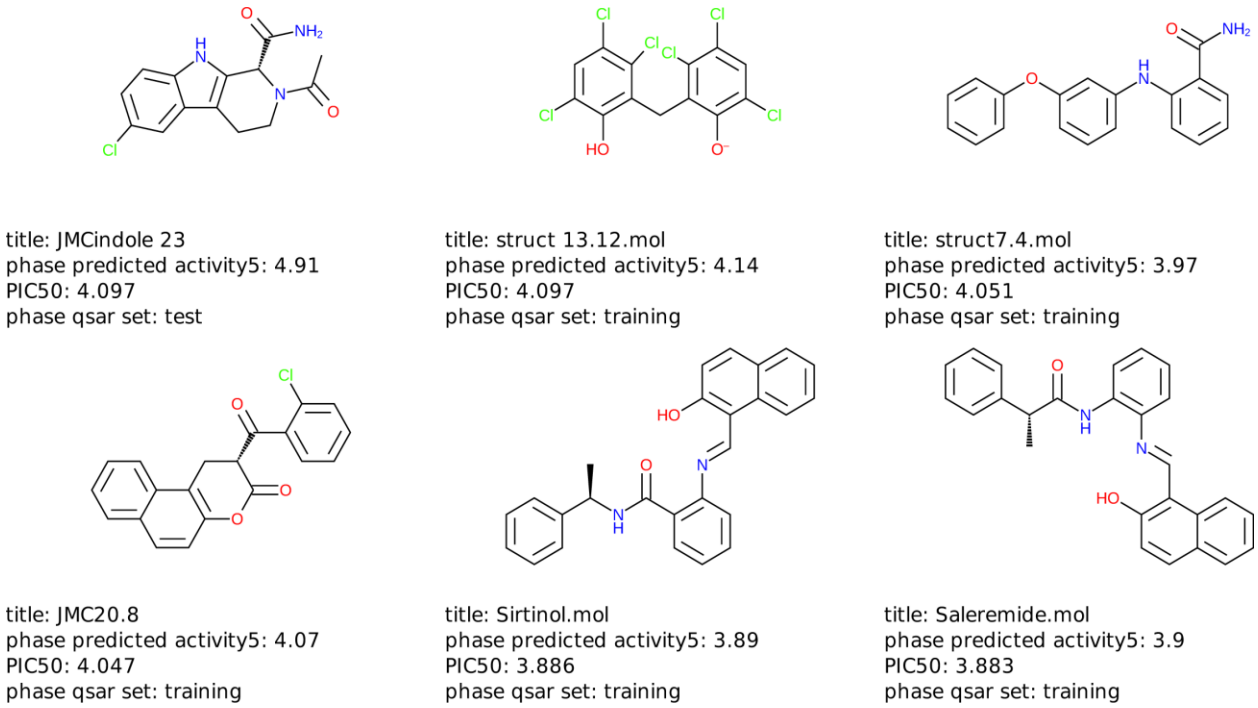

Figure 12 : Two dimensional structures of data set used to develop pharmacophore model

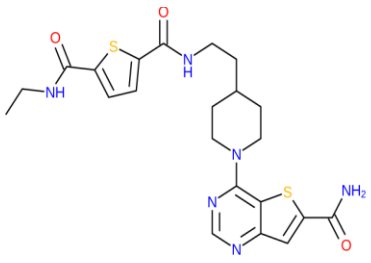

title: JMCpyrimid 11c
phase predicted activity5: 8.52
PIC50: 8.444
phase qsar set: training

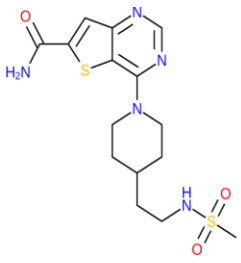

title: JMCpyrimid 31
phase predicted activity5: 8.37
PIC50: 8.367
phase qsar set: training

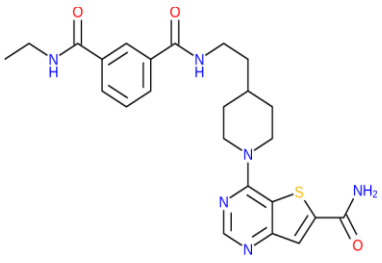

title: JMCpyrimid 11a
phase predicted activity5: 8.27
PIC50: 8.276
phase qsar set: training

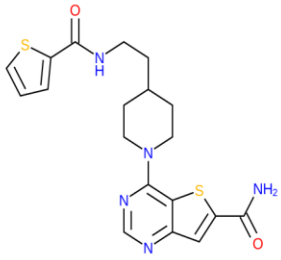

title: JMCpyrimid 19
phase predicted activity5: 8.15
PIC50: 8.237
phase qsar set: training

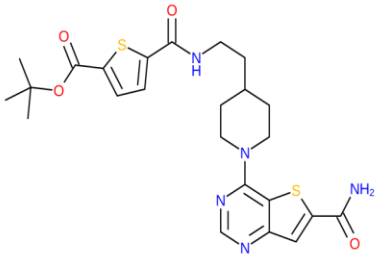

title: JMCpyrimid 17
phase predicted activity5: 8.5
PIC50: 8.174
phase qsar set: test

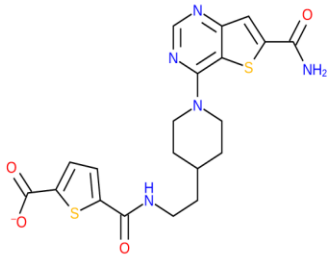

title: JMCpyrimid 18
phase predicted activity5: 8.02
PIC50: 7.854
phase qsar set: test

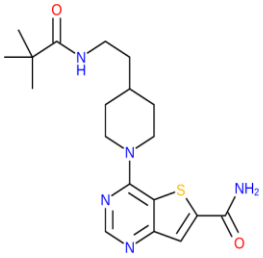

title: JMCpyrimid 28
phase predicted activity5: 7.27
PIC50: 7.824
phase qsar set: test

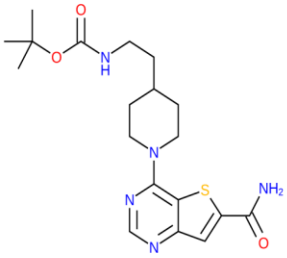

title: JMCpyrimid 15a
phase predicted activity5: 7.41
PIC50: 7.77
phase qsar set: test

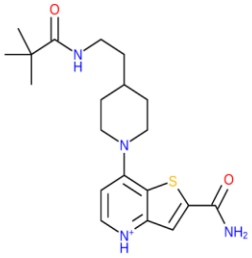

title: JMCpyrimid 37
phase predicted activity5: 7.52
PIC50: 7.553
phase qsar set: training

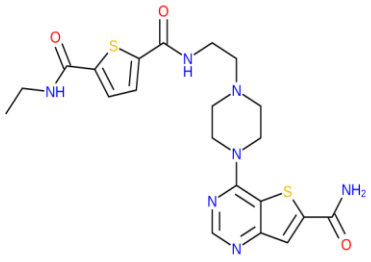

title: JMCpyrimid 11d
phase predicted activity5: 7.53
PIC50: 7.509
phase qsar set: training

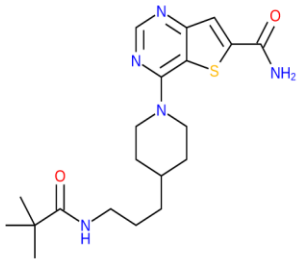

title: JMCpyrimid 29
phase predicted activity5: 6.93
PIC50: 7.377
phase qsar set: test

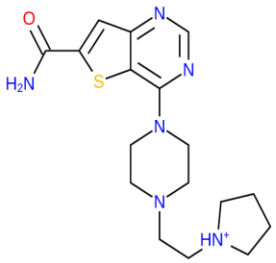

title: JMCpyrimid 35
phase predicted activity5: 7.3
PIC50: 7.276
phase qsar set: training

Figure 12 : Two dimensional structures of data set used to develop pharmacophore model

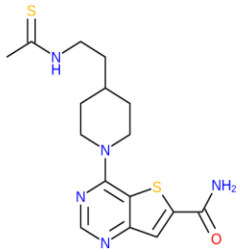

title: JMCpyrimid 25
phase predicted activity5: 6.61
PIC50: 7.252
phase qsar set: test

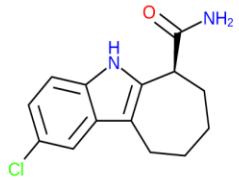

title: JMCindole 35-S
phase predicted activity5: 7.17
PIC50: 7.201
phase qsar set: training

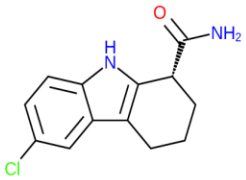

title: JMCindole 1
phase predicted activity5: 6.49
PIC50: 7.009
phase qsar set: test

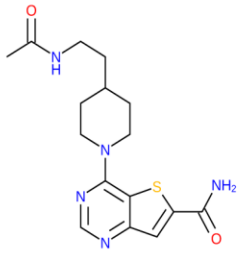

title: JMCpyrimid 20
phase predicted activity5: 6.56
PIC50: 6.959
phase qsar set: test

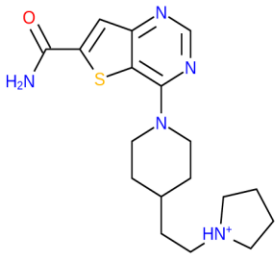

title: JMCpyrimid 34
phase predicted activity5: 7.0
PIC50: 6.959
phase qsar set: test

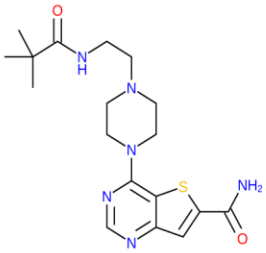

title: JMCpyrimid 30
phase predicted activity5: 6.72
PIC50: 6.921
phase qsar set: training

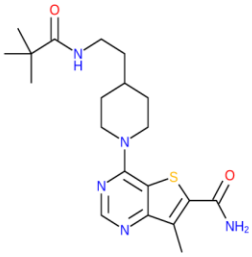

title: JMCpyrimid 39
phase predicted activity5: 6.86
PIC50: 6.886
phase qsar set: training

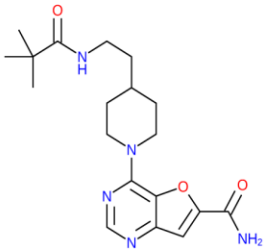

title: JMCpyrimid 36
phase predicted activity5: 6.84
PIC50: 6.824
phase qsar set: training

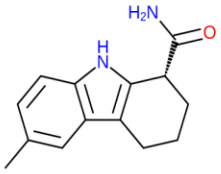

title: struct 13.9.mol
phase predicted activity5: 6.69
PIC50: 6.745
phase qsar set: training

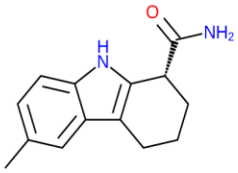

title: JMCindole 2
phase predicted activity5: 6.7
PIC50: 6.688
phase qsar set: training

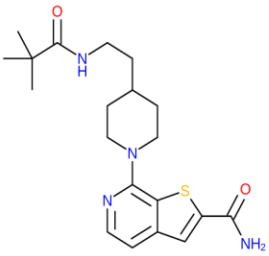

title: JMCpyrimid 38
phase predicted activity5: 6.68
PIC50: 6.523
phase qsar set: training

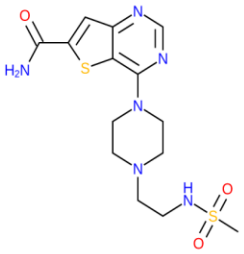

title: JMCpyrimid 32
phase predicted activity5: 6.69
PIC50: 6.42
phase qsar set: test

Figure 12 : Two dimensional structures of data set used to develop pharmacophore model

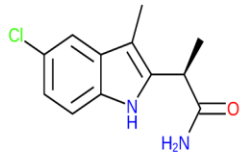

title: JMCindole 30
phase predicted activity5: 6.45
PIC50: 6.388
phase qsar set: training

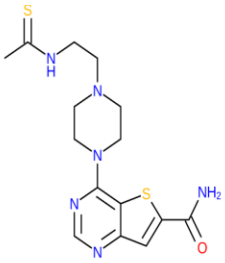

title: JMCpyrimid 26
phase predicted activity5: 6.29
PIC50: 6.31
phase qsar set: test

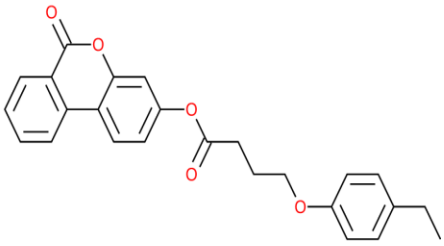

title: struct 13.10.mol
phase predicted activity5: 6.1
PIC50: 6.194
phase qsar set: training

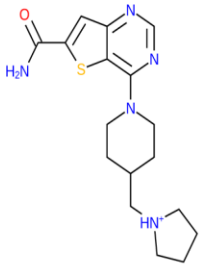

title: JMCpyrimid 33
phase predicted activity5: 6.43
PIC50: 6.137
phase qsar set: test

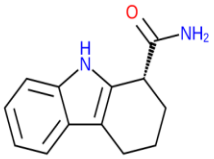

title: JMCindole 3
phase predicted activity5: 5.82
PIC50: 5.833
phase qsar set: training

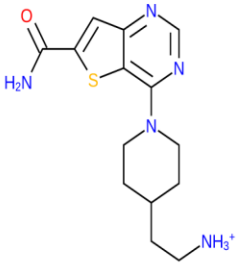

title: JMCpyrimid 16a
phase predicted activity5: 5.86
PIC50: 5.796
phase qsar set: training

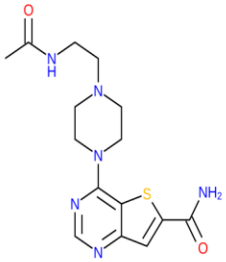

title: JMCpyrimid 24
phase predicted activity5: 5.91
PIC50: 5.796
phase qsar set: training

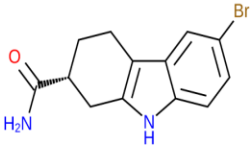

title: JMCindole 27
phase predicted activity5: 5.11
PIC50: 5.613
phase qsar set: training

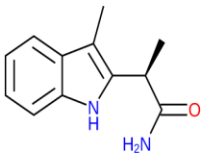

title: JMCindole 31
phase predicted activity5: 5.54
PIC50: 5.573
phase qsar set: training

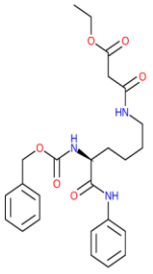

title: struct 14.1.mol
phase predicted activity5: 5.59
PIC50: 5.569
phase qsar set: training

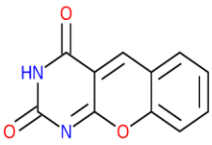

title: JMC20.10
phase predicted activity5: 5.22
PIC50: 5.276
phase qsar set: training

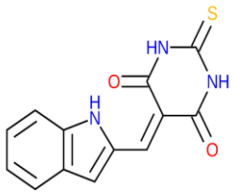

title: JMC 19.18.mol
phase predicted activity5: 5.34
PIC50: 5.222
phase qsar set: training

Figure 12 : Two dimensional structures of data set used to develop pharmacophore model

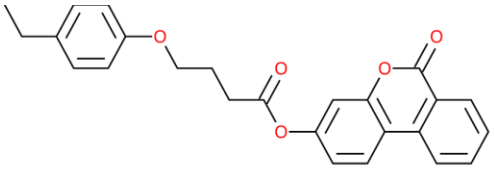

title: JMC 19.20.mol
phase predicted activity5: 5.13
PIC50: 5.222
phase qsar set: training

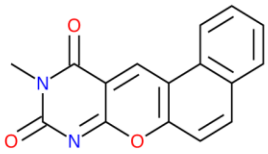

title: JMC21.2a
phase predicted activity5: 5.19
PIC50: 5.155
phase qsar set: training

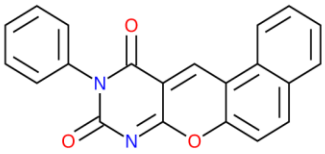

title: JMC20.9
phase predicted activity5: 4.95
PIC50: 5.076
phase qsar set: test

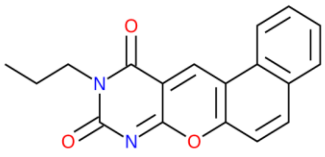

title: JMC21.2c
phase predicted activity5: 5.03
PIC50: 5.027
phase qsar set: training

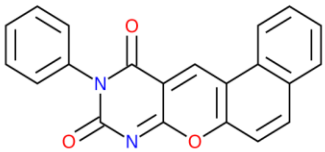

title: JMC21.1
phase predicted activity5: 4.95
PIC50: 5.009
phase qsar set: test

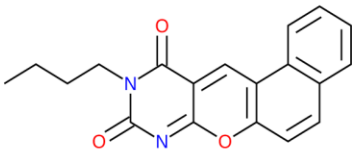

title: JMC21.2e
phase predicted activity5: 5.02
PIC50: 4.983
phase qsar set: test

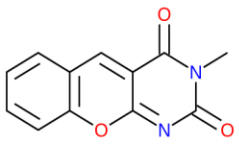

title: JMC21.3a
phase predicted activity5: 5.14
PIC50: 4.979
phase qsar set: test

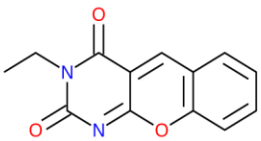

title: JMC21.3b
phase predicted activity5: 5.0
PIC50: 4.928
phase qsar set: test

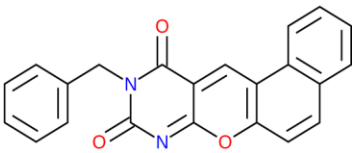

title: JMC21.2g
phase predicted activity5: 4.94
PIC50: 4.921
phase qsar set: test

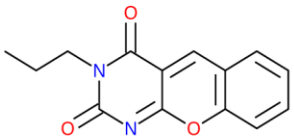

title: JMC21.3c
phase predicted activity5: 4.97
PIC50: 4.903
phase qsar set: test

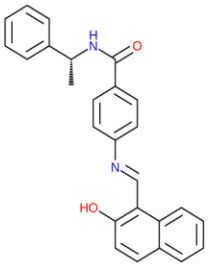

title: p_sirtinol
phase predicted activity5: 4.93
PIC50: 4.886
phase qsar set: training

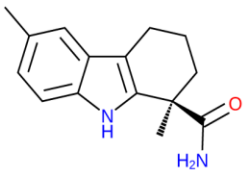

title: JMCindole 41
phase predicted activity5: 4.95
PIC50: 4.886
phase qsar set: training

Figure 12 : Two dimensional structures of data set used to develop pharmacophore model

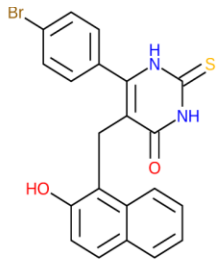

title: JMC 19.13d.mol
phase predicted activity5: 4.8
PIC50: 4.886
phase qsar set: training

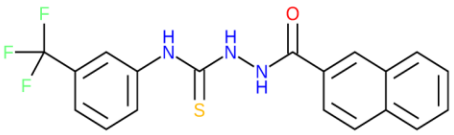

title: JMC 19.15.mol
phase predicted activity5: 4.99
PIC50: 4.886
phase qsar set: training

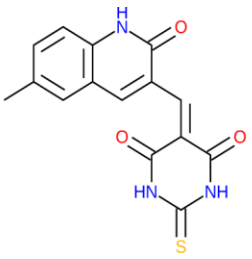

title: JMC 19.16.mol
phase predicted activity5: 4.81
PIC50: 4.886
phase qsar set: training

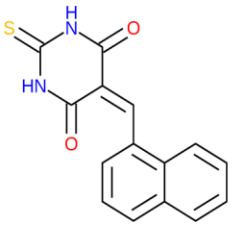

title: JMC 19.17.mol
phase predicted activity5: 4.97
PIC50: 4.886
phase qsar set: training

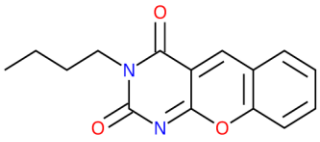

title: JMC21.3d
phase predicted activity5: 4.96
PIC50: 4.851
phase qsar set: test

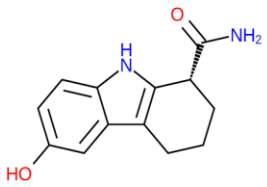

title: JMCindole 12
phase predicted activity5: 4.67
PIC50: 4.824
phase qsar set: test

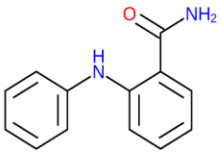

title: JMC 19.7a.mol
phase predicted activity5: 4.26
PIC50: 4.77
phase qsar set: test

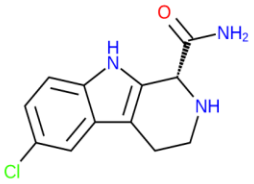

title: JMCindole 20
phase predicted activity5: 4.77
PIC50: 4.745
phase qsar set: training

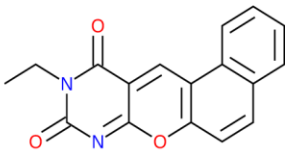

title: JMC21.2b
phase predicted activity5: 5.07
PIC50: 4.695
phase qsar set: test

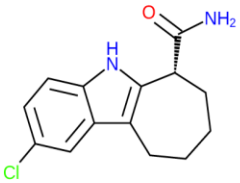

title: JMCindole 35-R
phase predicted activity5: 4.63
PIC50: 4.638
phase qsar set: training

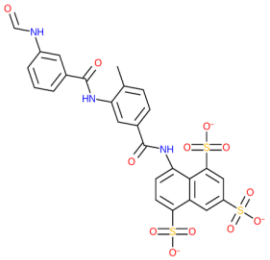

title: struct 13.6.mol
phase predicted activity5: 4.89
PIC50: 4.602
phase qsar set: test

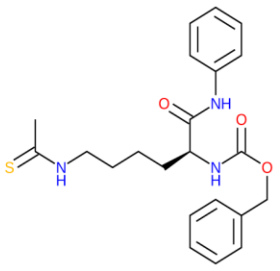

title: struct 13.13.mol
phase predicted activity5: 4.45
PIC50: 4.469
phase qsar set: training

Figure 12 : Two dimensional structures of data set used to develop pharmacophore model

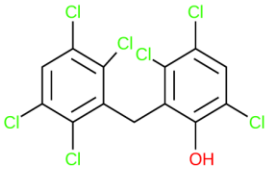

title: JMC 19.21.mol
phase predicted activity5: 4.48
PIC50: 4.469
phase qsar set: training

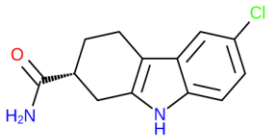

title: JMCindole 26
phase predicted activity5: 5.01
PIC50: 4.462
phase qsar set: training

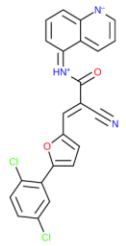

title: JMC20.AGK2
phase predicted activity5: 4.48
PIC50: 4.42
phase qsar set: training

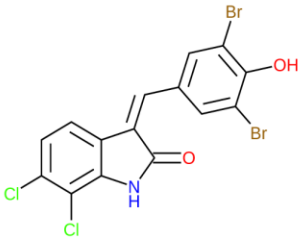

title: JMC 19.22.mol
phase predicted activity5: 4.28
PIC50: 4.398
phase qsar set: test

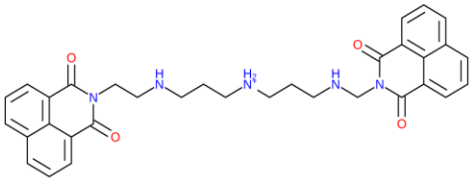

title: JMC 19.23.mol
phase predicted activity5: 4.13
PIC50: 4.367
phase qsar set: test

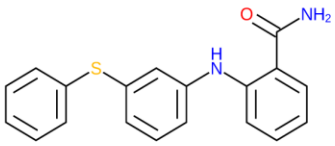

title: struct7.3.mol
phase predicted activity5: 4.12
PIC50: 4.284
phase qsar set: test

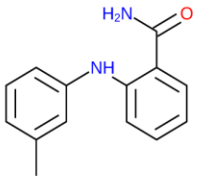

title: struct7.1.mol
phase predicted activity5: 4.14
PIC50: 4.252
phase qsar set: training

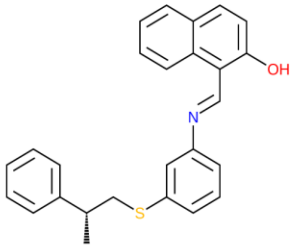

title: JMC20.6
phase predicted activity5: 4.24
PIC50: 4.232
phase qsar set: test

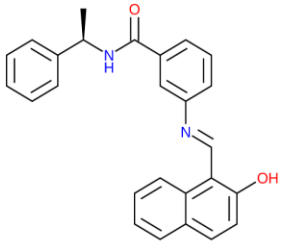

title: JMC20.meta-sirtino
phase predicted activity5: 4.22
PIC50: 4.229
phase qsar set: training

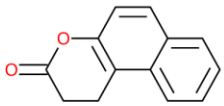

title: JMC20.splitomycin
phase predicted activity5: 4.27
PIC50: 4.222
phase qsar set: training

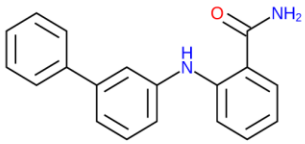

title: struct7.2.mol
phase predicted activity5: 4.3
PIC50: 4.167
phase qsar set: test

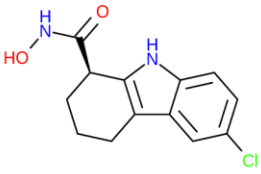

title: JMCindole 15
phase predicted activity5: 3.96
PIC50: 4.11
phase qsar set: training

Figure 12: Two dimensional structures of data set used to develop pharmacophore model

As mentioned above data set of known SIRT1 inhibitors compounds was split into training and test sets, where the shift of test and training set positions leads to the proper alignment of molecules. Generated 3D-QSAR model simultaneously generates predicted pIC_{50} values for each compound that involved in model building. Their predicted pIC_{50} values, training and test set allocation was presented in **Figure 12**. A good QSAR model should exhibit reliable predictions, with validation by both internal and external statistical tools. The predictive power of the model (ADHRR 782) was tested with test set of 31 molecules. For useful insights, statistical significance of the model was achieved using partial least square (PLS) factor of five. The robustness model in predicting the active molecules was considered based on various numerical parameters, including leave one out cross validation for training set (Q^2), leave one out cross validation for test set (R^2), pearson correlation coefficient (r) standard deviation (SD), root mean square error (RMSE) and variance ratio (F). The standard value of Q^2 should be more than 0.55; however 3D-QSAR model obtained with ADHRR 782 showed value much higher than the standard value, which was 0.9395. This indicated high predictive ability of the model. In addition to this, other parameters like R^2 showed numerical values higher than the standard value, which was 0.9906, almost near to 1 (**Table 8)**. The goodness in predictive ability and robustness of the model could be inferred from the low value of SD (0.1371) whereas the statistical significance of the model exhibited by high F value (782). If we compare the statistical parameters of 782 model with other pharmacophore models, all of them displayed R^2 value above 0.9. However, if we consider Q^2, 782 model has showed highest value 0.939 compare to any any other model. Similarly with respect to RMSE, pharmacophore model 782 has displayed less value. Hence, ADHRR 782 model could be more reliable in predicting the activity. Scatter plot was constructed between the observe and predicted activity of all the compounds in the data set **Figure 13**. It can be inferred that the best fit line was close to the R^2 value of 1, which further confirms the reliability of the model.

Table 8: PHASE 3D-QSAR and PLS Statistics for Internal Validation of the Dataset

Statistical parameters	ADHRR.782	ADHRR.771	ADHRR.756	ADHRR.769	ADHRR.802
Number of molecules in training set	48	48	48	48	48
Number of molecules in test set	31	31	31	31	31
R^2	0.991	0.991	0.988	0.988	0.991
Q^2	0.939	0.859	0.851	0.837	0.844
SD	0.137	0.127	0.151	0.148	0.136
F-value	882	1023	732.1	749	894.5
Pearson-R	0.971	0.945	0.931	0.921	0.934
RMSE	0.322	0.491	0.505	0.528	0.516

R2	For the regression
Q	Squared (Q2) value for the predicted activities
SD	Standard deviation of the regression..
F	Variance ratio.
Pearson R	Correlation between the predicted and observed activities for the test set.
RMSE	Root-mean-square error.

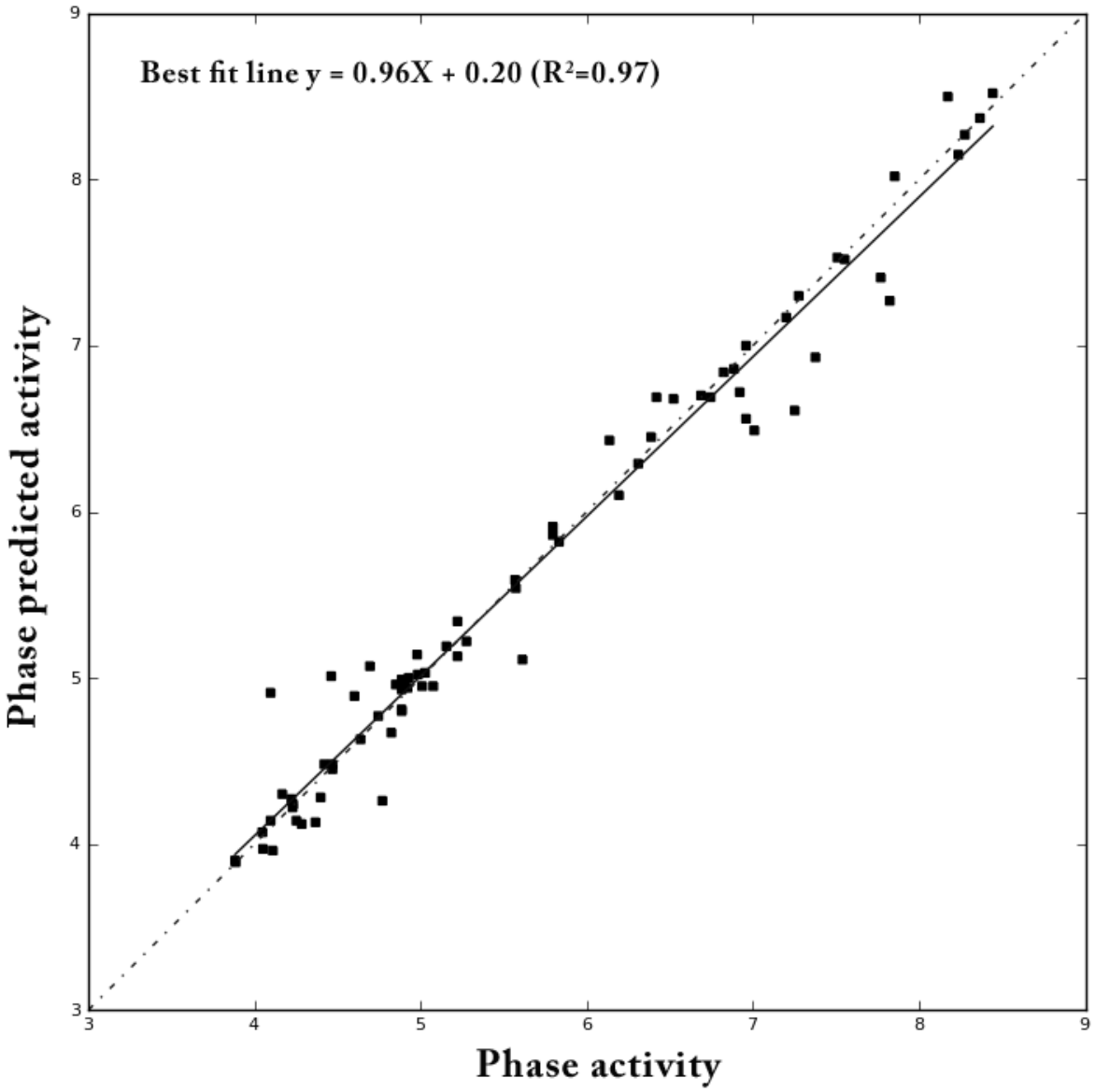

Figure 13: Scatter plot of the observed vs. predicted activity of SIRT1 inhibitors generated by the best model obtained employing 50 compounds as the training set and validated using 31 compounds as the test set. Best fit line is very close to 1 with R2 of 0.97.

5.2.4. External statistical validation of 3D-QSAR model

Reliable 3D-QSAR model should also poses high correlation between the predicted and observed activities, which was referred with correlation coefficient R (or r^2). The best predictive ability of the QSAR model from ADHRR 802 was supported by correlation coefficient R with 0.956 (r^2= 0.914) and high slope of regression lines with K and K' values of 1.009 and 0.986 respectively. Using K and K' values R_0^2 and $R_0'^2$ were calculated using the regression lines in scatter plot of actual activity *versus* predicted activity and vice versa respectively. R_0^2 and $R_0'^2$ being 0.997 and 0.996, were further used to calculate the relation between r, R_0^2 and $R_0'^2$, which gave (($r^2 - R_0^2$)/ r^2) and (($r^2 - R_0'^2$)/ r^2) value of -0.046 and -0.044 respectively, which were within the statistical limits **(Table 9)**. In addition to this a parameter of modified r^2 (r_m^2) and R_P^2 were calculated, where r_m^2 was considered for better external predictive potential for the whole set of compounds which were found to be 0.6508 and R_P^2 = 0.5129 was well within the statistical limits **(Table 9).** Thus the overall external numerical parameters confirmed the robustness of the developed 3D-QSAR model in predicting the active molecules.

Table 9: External Statistical Validation of Quantitative Structure-Activity Relationship (QSAR) for Hypothesis ADHRR 782

External validation	Parameter calculated	Limitations
r_{cv}^2	0.989	$r_{cv}^2 > 0.5$
R	0.956	Close to 1
r^2	0.914	$r^2 > 0.5$
K	1.009	$0.85 \leq k \leq 1.15$
K'	0.986	$0.85 \leq k' \leq 1.15$
R_0^2	0.997	R_0^2 or $R_0'^2$ close to r2
$R_0'^2$	0.996	R_0^2 or $R_0'^2$ close to r2
$((r^2 - R_0^2)/r^2)$	-0.046	$((r^2 - R_0^2)/r^2) < 0.1$
$((r^2 - R_0'^2)/r^2))$	-0.044	$((r^2 - R_0'^2)/r^2)) < 0.1$
r_m^2 (LOO)	0.903	r_m^2 (LOO) > 0.5
r_m^2	0.650	$r_m^2 > 0.5$
R_p^2	0.512	$R_p^2 > 0.5$

r_{cv}^2 Cross validated coefficient.

R (or r2) Correlation coefficient between the actual and predicted activities.

k and k′ Slope values of regression lines.

R_0^2 and R_0^2: Correlation coefficients for the regression lines through the origin.

$((r^2 - R_0^2)/r^2)$ and $((r^2 - R_0'^2)/r^2)$ To calculate the relation between r^2, R_0^2 , and $R_0'^2$.

r_m^2 (LOO) Modified squared correlation coefficient for the "Leave One Out" method.

5.2.5. Contour map analyses

The validated 3D-QSAR model (ADHRR 782) was further analysed using contour maps, which could help in understanding the importance of functional groups at specific positions towards biological activity. Comparing the contour maps of most and least active compounds as shown in Figure 14, could be useful in the further design. The blue and red cubes (**Figure 14**A and B) indicated the favourable and unfavourable regions respectively of hydrogen bond donor effect, while light red and yellow (**Figure 14** C and D) indicated favourable and unfavourable regions respectively of hydrophobic effect. Whereas the cyan and orange cubes (**Figure 14** E and F) indicated favourable and unfavourable regions respectively of electron withdrawing effect. From the **Figure 14A** we could infer that the blue favourable regions of hydrogen bond donor effect were nearer to the donor feature (D5) of active molecule and also concentrated at the amide group beside thiophene, thus illustrating importance of donor groups at these regions to increase biological activity. However in the inactive molecule, red unfavourable boxes were seen around the donor feature (D5) inferring the biological inactiveness of the molecule. In the case of hydrophobic effect the light red color cubes were seen surrounding the hydrophobic feature (H8, piperidine) of the active molecule, whereas the presence of few yellow unafavourable cubes indicated that these hydrophobic groups were not in right position for inactive molecule, illustrating the weak biological activity Whereas in the case of electron withdrawing effect of active molecule, the favourable cyan cubes were seen around the acceptor feature (A3), besides cyan cubes were also seen near the pyrimidine ring. It inferred that the acceptor features near pyrimidine ring could further increase the bioactivity of the molecule. However in the case of inactive molecule (**Figure 14** F) mostly unfavourable orange cubes were seen around acceptor feature (A3), illustrating the importance of electron withdrawing group in the activity of lead molecules.

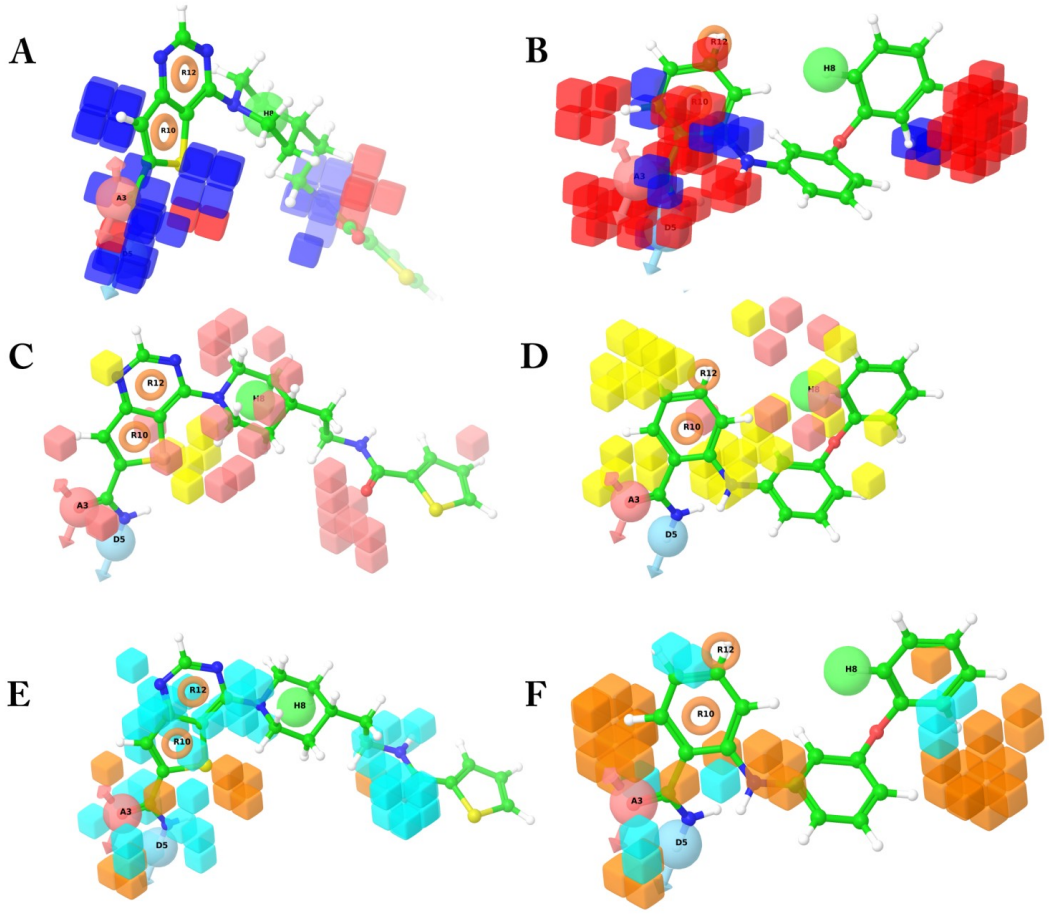

Figure 14: Contour maps of the most active and inactive molecule A, H-bond donor effect: Most active; B, Least active (Blue- favorable, Red- unfavorable); C, Hydrophobic effect: Most active; D, Least active (Light red- favorable, Yellow- unfavorable); E, Electon with-drawing effect: Most active; F, Least active (Cyan-favorable, Orange –unfavorable)

5.2.6. Virtual screening and docking

Novel lead identification was our primary objective in the current study which could be achieved by virtual screening of all available 3D databases (Asinex 5,00,000 and In-house 971 molecules). Based on the epharmacophore validation parameters various pharmacophore features were compared and the best pharmacophores were selected for virtual screening, which included 3 feature pharmacophore D4R8R7 (one donor and two rings), 4 feature pharmacophore D4A1R8R7 (one donor, one acceptor and two rings) and 5 feature pharmacophore D4A1R8R7D3 (two donors, one acceptor and two rings). In addition to the epharmacophore

features we also considered pharmacophore model obtained from ligand-based 3D-QSAR, which was ADHRR 802 (One acceptor, one donor, one hydrophobic and two rings). All the selected pharmacophore features were initially subjected to phase find matches. Molecules were required to match a minimum of 4 sites for a hypothesis with 5 features and minimum of 3 sites for hypothesis with 3 or 4 sites. All the hits from phase find matches were ranked based on fitness score. Fitness score was a measure of how good the ligand conformer features matched with hypotheses. The top hits with good fitness value (>1.0) were selected for docking. To speed up the screening of large databases, docking was done in three stages; initially high throughput virtual screening (HTVS) of 5,231 compounds was done, based on docking score and hydrogen bonding interactions 400 molecules were considered for standard precision (SP) docking. From the results only 100 molecules were considered for extra precision (XP) docking and the best hits with good docking score were selected as presented in **Table 10** and **Figure 15**, compounds from Lead1 to Lead12 were retrieved from asinex database and Lead17 was retrieved from in-house dataset.

Table 10: Docking score, important aminoacids, hydrogen bonds and %enzyme inhibition at 40µM concentration of lead compounds

S.NO	Compound	Important aminoacids	Fitness	Docking score	Hydrogen bonds	%Inhibition at 40µM[a]
1	Cry lig	Gln-345, Ile-347, Asp-348 , Phe-297	2.77	-9.02	4	92.24± 5.25
2	Lead 1	Gln-345, Asp-348, Ile-347, Phe-297, Phe-273	1.09	-13.69	4	20.73±1.82
3	Lead 2	Gln-345, Ile-347, Asp-348, Phe-321, Phe-297	1.21	-9.23	4	11.63±0.86
4	Lead 3	Ile-347, Asp-348 , Phe-273	1.76	-9.18	4	29.88±2.61
5	Lead 4	Ile-347, Asp-348, Gln-345, Phe-297	2.61	-11.12	4	10.25±0.85
6	Lead 5	Asp-348, Ile-347, Phe-273, Phe-297	2.68	-10.66	4	50.22±3.11
7	Lead 6	Ile-347, asp-348, Gln-345, Phe-297	2.17	-11.97	4	57.14±1.14
8	Lead 7	Ile-347, Asp-348, Asn-346, Gln-345, Phe-273, Phe-321	2.04	-11.53	6	48.69±1.32
9	Lead 8	Gln-320, Asp-348, Ile-347, Gln-345, Phe-31, Phe-297	1.94	-10.21	6	59.88 ±1.46
10	Lead 9	Asp-348, Ile-347, Gln-345, phe-297	2.01	-13.45	4	77.32 ± 3.42
11	Lead 10	Ile-347, Asp-348, Asn-346, Gln-345, Phe-273	1.91	-12.04	6	81.87 ± 2.51
12	Lead 11	Ile-347, Asp-348 , Gln-345 , Phe-294	1.71	-10.28	5	83.71 ± 4.14
13	Lead 12	Asp-348, Ile-347, Gln-345, Ile-316, Phe-273, Phe-297	1.62	-9.51	6	85.9 ± 2.84
14	Lead 17	Gln345, Arg282, Phe273	1.61	-8.11	2	91.13 ± 3.12

[a] Enzyme inhibitions studies were initially performed at 40µM concentration. Leads showing more 60% inhibition were further diluted to lower concentration to calculate IC_{50} values. Each reaction was performed in triplicates and standard deviation values are represented.

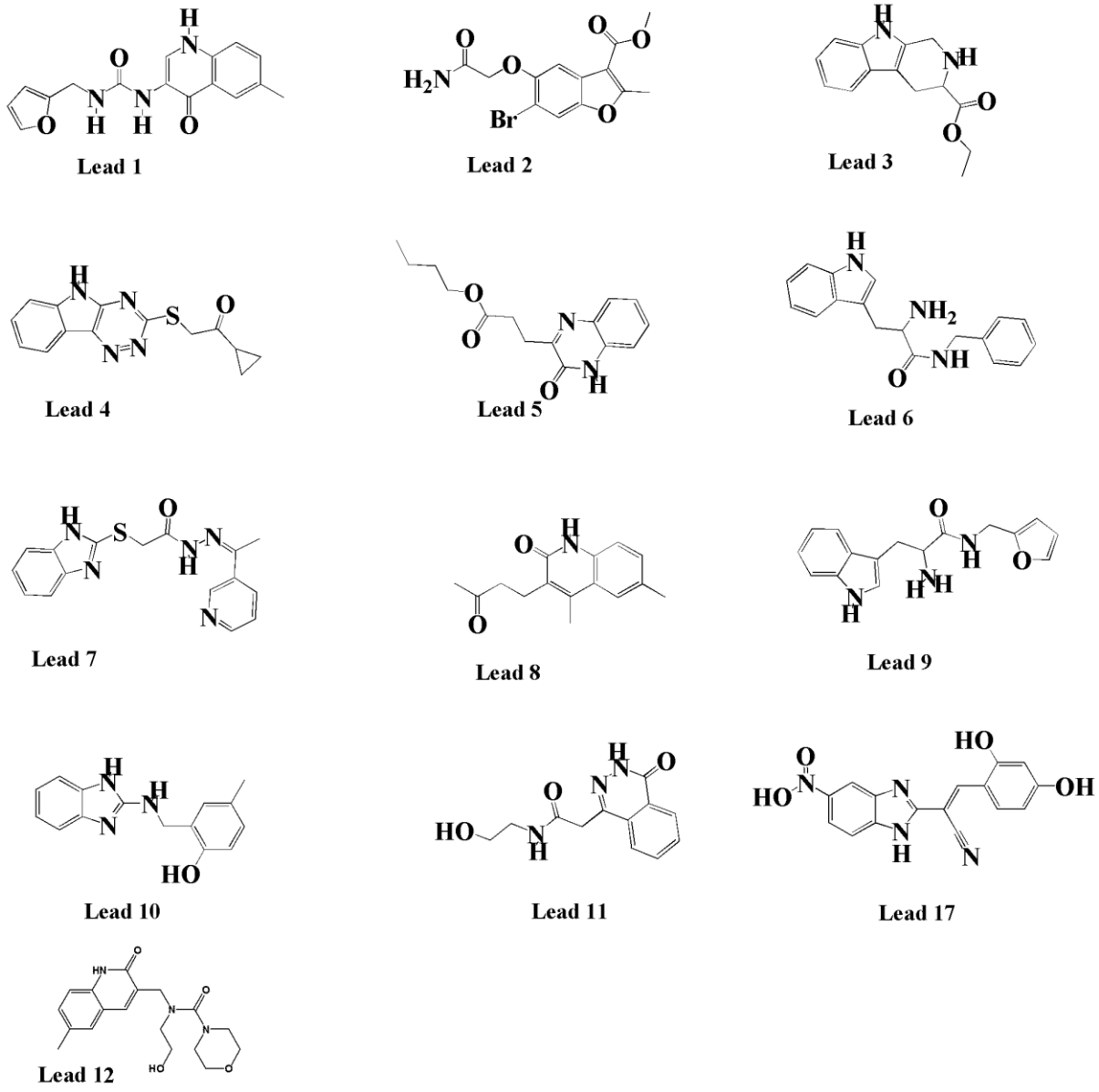

Figure 15: Two dimensional structures of top leads. Lead17 was retrieved from in-house database and rest others were from Asinex database

5.2.7. In-vitro SIRT1 enzyme screening

Asinex molecules which showed good docking score and hydrogen bond interactions were purchased and the molecules from in-house database showing good interaction pattern were collected for in-vitro fluorescence based SIRT1 assay. All the molecules were diluted in dimethyl sulfoxide (DMSO) and SIRT1 enzyme assay was initially performed at 10 μM concentration. Lead compounds displaying more than 60% inhibition were further diluted to lower concentrations to calculate IC_{50} (concentration at which there was 50% inhibition). Among all the compounds screened from in-house database (**Lead 17**) (**Figure 16**) showed the promising activity with IC_{50} of 4.434 μM. However the IC_{50}s of other molecules screened from Asinex database were more than 10 μM. Considering the structural novelty of lead **17** and its bio activity, it was considered as good lead for further exploitation.

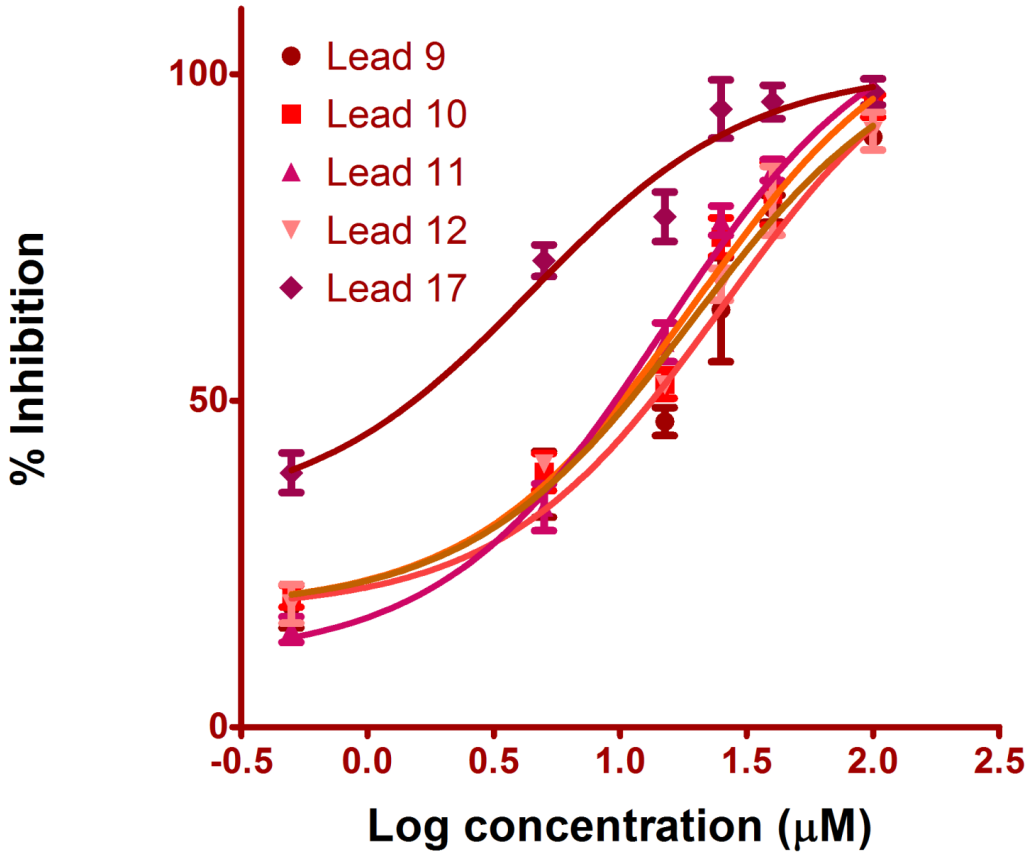

Figure 16: IC_{50} curves determined in triplicate fitted in logistic dose response curve. Hill slopes of SIRT1 enzyme inhibition assay. Lead 9 (IC_{50} = 25.21± 3.23μM), Lead10 (IC_{50} = 19.56 ± 1.82μM), Lead 11 (IC_{50} = 14.80 ± 3.56 μM), Lead 12 (IC_{50} = 19.14 ± 3.71μM) and Lead 17 (IC_{50} = 4.34± 0.86 μM).

5.2.8. ADME properties

The top hits with good docking scores and in-vitro enzyme inhibition were verified for the drug likeliness properties (ADME) using QikProp module of Schrödinger. All the lead compounds showed good octanol/water partition coefficient (QPlogPo/w) ranging from -0.26 to 2.1, which were in permeable range (**Table 11**). The parameter defining the caco-2 cell permeability was represented as QPPCaco which was in permissible range of 32 to 1352. QPPCaco coefficient was considered important in understanding the cell permeability in biological membranes. The percentage of oral absorption for the leads were in the range of 58 to 100, which was generally believed to be satisfying, hence all the leads were within the drugable range. Further to these predictions, violations in Lipinski's rule of 5 were also considered and all the lead compounds did not show any violations **(Table 11)**. From these predictions it could be inferred that the lead compounds may exhibit good pharmacokinetic and drug likeliness properties

Table 11: Illustrating the predicted ADME properties of lead compounds

Molecules	Molecular weight [a]	QPlogP o/w[b]	QPPCaco[c]	Percent human oral absorption [d]	Rule of five[e]
Lead9	243.30	2.18	1052.43	93.83	0
Lead10	283.32	1.41	155.851	74.41	0
Lead11	253.29	2.78	1352.41	100	0
Lead12	247.24	-0.26	65.82	57.96	0
Lead17	322.20	1.14	32.21	58.66	0

[a] Molecular weight (acceptable range <500).

[b] Predicted octanol /water partition coefficient log p (acceptable range from −2.0 to 6.5).

[c] Predicted Caco-2 cell permeability in nm/s (acceptable range: <25 is poor and >500 is great).

[d] Percentage of human oral absorption (<25% is poor and >80% is high).

[e] Rule of five (no. of violations of Lipinski's rule of five: 0 is good and 4 is bad).

5.2.9. Ligand interaction analyses

All the shortlisted inhibitors showed similar interaction pattern as that of the crystal ligand (EX527 analogue), with pharmacophore fitness more than 1.5 and docking score less than -8.0 Kcal/mol. This inferred that all the lead compounds interacted within the active site pocket of SIRT1 protein. The interaction profile of the best molecule, **lead17** was compared with crystal ligand and is presented in **Figure 17**. From the Figure we could infer that the crystal ligand interacted with all the available hydrogen bond acceptor and donor sites in the pocket (Asn-346, Ile-347 and Asp-348), besides the hydrophobic pocket (Phe-273 and Phe-297) showed hydrophobic interaction with aliphatic and aromatic parts of the inhibitor. Interestingly the molecule **lead17** also revealed similar interactions, especially the free hydroxyl group at one end showed hydrogen bond interaction with Gln-345. In addition to this the other end with nitro group aligned adjacent to Arg-282 showing another hydrogen bond interaction. As the **lead 17** was bigger in size than the crystal ligand it was deeply fixed in the pocket showing additional interaction (Arg-282) not observed with crystal ligand. Besides, the **lead17** also exhibited hydrophobic interaction with aromatic amino acids (Phe-273 and Phe-297) as observed with crystal ligand (**Figure 17**).

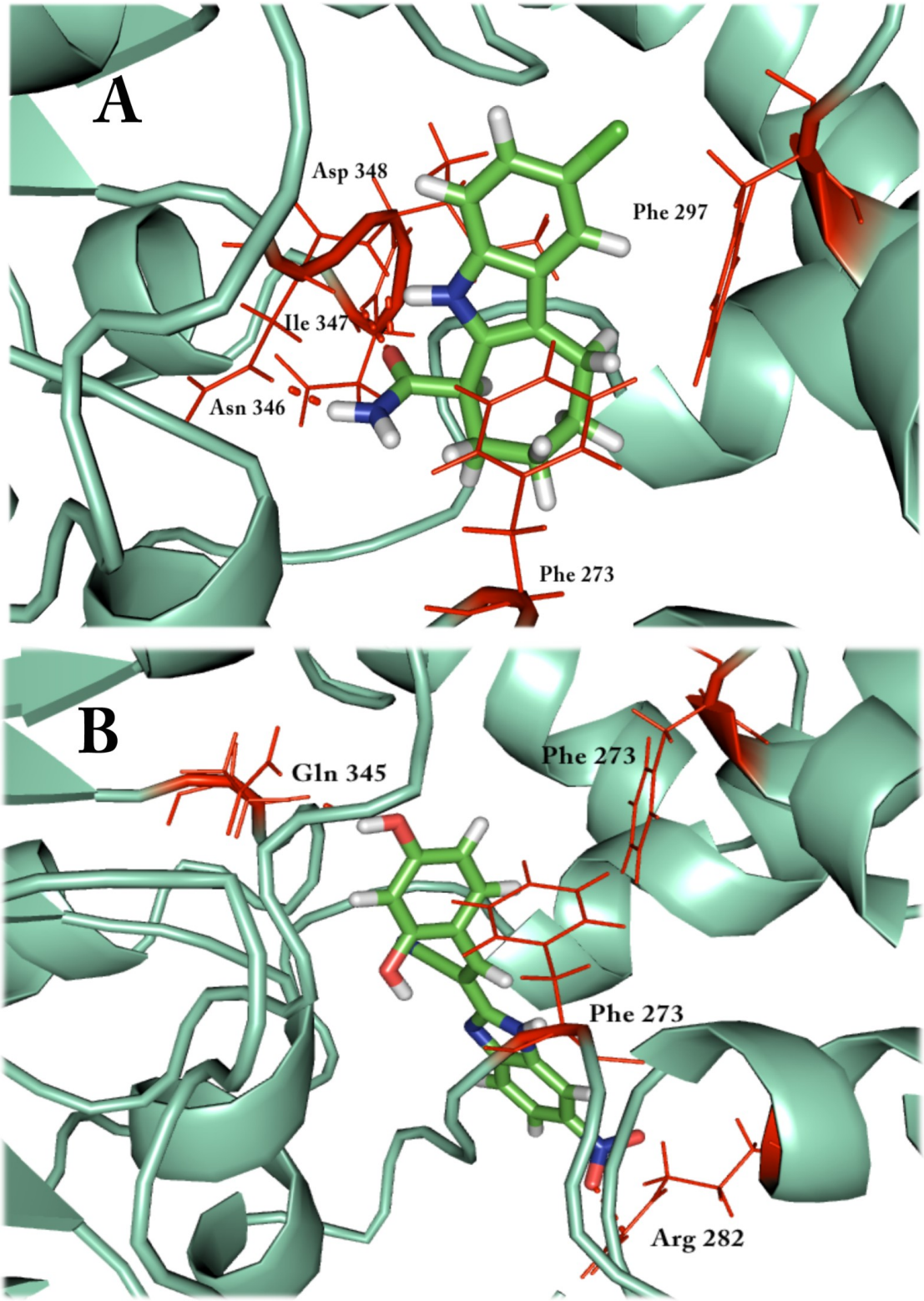

Figure 17: Ligand interaction presentation of crystal ligand (A) and lead 17 (B), within which red color sticks indicates the aminoacids surrounding the bound ligand and green cyan indicates indicate the binding site of a protein.

5.2.10. Growth inhibition studies

SIRT1 being an important deacetylase enzyme expressed abundantly in various cancers, it was important to test the lead molecules in cancer cell proliferation assay. Cell proliferation assay was conducted on three cancer cell lines, like MDAMB231 (breast), HT29 (colon) and LnCAP (prostate). From the results it could be inferred that **Lead 17** exhibited better activity across all the three cell lines compared to other leads **(Table 12)**. Besides, it was also important to know that all the leads showed lowest GIC_{50} (Concentration at which 50% growth was inhibited) in LnCAP cell line. This inferred that SIRT1 inhibitors could act as novel leads in treating cancers, specifically prostate cancer condition.

Table 12: Growth inhibitory concentration -50 (GIC_{50}) of lead compounds tested at various cancer cell lines Each experiment was performed in triplicates and the standard deviation values were given in the table (±)

	Lead 9	Lead 10	Lead 11	Lead 12	Lead 17	Gemcitabine
HT29	2.01±0.06	1.38±0.71	1.35±0.14	4.51± 1.95	0.59± 0.52	0.062 ± 0.02
MDAMB231	1.56±0.15	4.56±0.61	3.94±0.75	3.13±1.00	1.02±0.09	0.050 ± 0.03
LnCAP	0.95±0.15	1.17±0.54	1.00±0.26	1.35±0.17	0.36±0.08	0.500 ± 0.02

5.2.11. Apoptosis assay

To further establish how **Lead17** was acting on prostate cancer cell line (LnCAP), apoptosis assay was performed. Here in this assay, cells were stained with annexin-V and propidium iodide (counter stain) and the results as graph is represented in the **Figure 18A**. As the dye annexin-v specifically stained the apoptotic cells, it was easy to estimate the amount of apoptosis, beside propidum iodide was used as counter stain, which stained the DNA of necrotic and late apoptotic cells. From the graph it was clear that there was an increase in the percentage of apoptotic cells when treated with **lead 17** as compared to the control. This indicated that the **lead17** exhibited growth inhibition by inducing apoptosis.

5.2.12. Quatification of apoptotic genes (p53 and caspase3)

To further illustrate that **Lead17** induce apoptosis in LnCAP cells, apoptotic genes p53 and caspase 3 were quantified using real time PCR **(Figure 18B)**. Results revealed that the p53 and caspase 3 genes were upregulated when cells were incubated with **lead17**. From the Figure it could be ascertained that as both p53 and caspase 3 genes were increased approximately two times compared to the control cells, induction of apoptosis by lead 17 could be through SIRT1 inhibition.

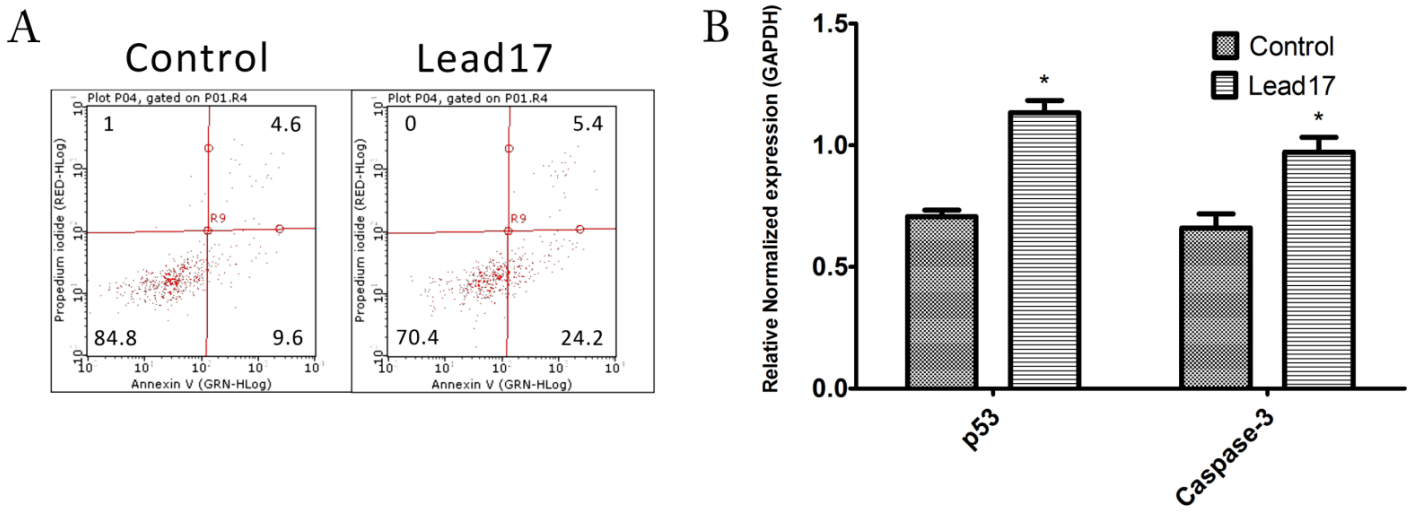

Figure 18: A. Illustrating the percentage of cells stained with Annexin-V drawn against propidum iodide and numbers in each square indicate the percentage of cells in different phase of cell cycle. B. Depicts the mRNA levels of p53 and caspase 3 genes (pro apoptotic Genes) drawn after normalizing the expression with GAPDH (mean ± SEM, *P<0.05 unpaired T test)

5.2.13. Benign prostate hyperplasia

From in-vitro SIRT1 and cell proliferation assays, it was clear that SIRT1 inhibitors could be used to treat cancer conditions. As the **lead17** showed better activity in LnCAP, it was intriguing to evaluate the activity in benign prostate hyperplasia condition. Here in the animal studies

prostate hyperplasia was induced by administering testosterone. In the development of benign prostate hyperplasia, enzyme 5α-reductase catalysed the rate of conversion of testosterone to dihydrotestosterone, which resulted in increase of dihydrotestosterone in prostate cells which acted on stromal and epithelial cells causing prostate enlargement. From the studies it was clear that prostate gland to body weight ratio was increased 1.8 times in animal administered with testosterone compared to the control animal, however when administered with finasteride (known 5α reductase inhibitor) and **Lead17** it was found to be more than 50% reduction in weight (**Table 13**). These results were also supported with histopathological studies, which suggested that normal tissue architecture of the prostate tissue was disrupted (**Figure 19**), which was characterised by glandular hyperplasia with epithelial proliferation and nuclear stratification. However when treated with Finastiride and **Lead17,** there were significant reductions in tissue disruption **(Figure 19)**. It was also observed that the cell morphology of the prostate tissue isolated from Groups C and D (**Figure 19)** were convincingly comparable with that of the tissue isolated from control group (Group A). This confirmed the efficacy of **Lead17** in prostate hyperplasia.

Table 13: Ratio of prostate weight to body weight of different groups studied in benign prostate hyperplasia animal model.

Animal group	P.Wt[a]	S.V Wt[b]	P. Wt /B wt ratio[c]	%Inhibition	Bwt (Initial)	Bwt (Final)
Group A[d]	0.37985±0.006	0.349±0.139	1.805 ± 0.149		173.75±12.44	218.66±16.62
Group B[e]	0.707± 0.256	0.944±0.166	3.314 ± 0.787[h]		214.66±15.43	240.3 ± 15.2
Group C[f]	0.526 ± 0.126	0.843±0.103	2.497 ± 0.713[j]	54.76	203.12±10.148	206.85 ± 8.96
Group D[g]	0.513 ± 0.112	0.812±0.121	2.286 ±0.682[i]	68.012	218.12 ± 3.21	220.12 ± 2.12

Each group consist of five animals and the values presented in the table is average ± Standard error mean. Statistical analysis was done by one-way ANOVA followed by Bonferroni's multiple comparison tests. [a] PWt: prostate weight.
[b] SVWt: seminal vesicle weight,
[c] P.Wt/Bwt: prostate weight/ body weight ratio.
[d] Group A: negative control (untreated rat).
[e] Group B: positive control (only testosterone treated rat).
[f] Group C: Lead 17 (10 mg/kg) treated rat
[g] Group D: Finasteride (5 mg/kg) treated rat..
[h] $P < 0.001$ when compared with normal control.
[i] $P < 0.01$ when compared with testosterone treatment.
[j] $P < 0.001$ when compared with testosterone treatment.

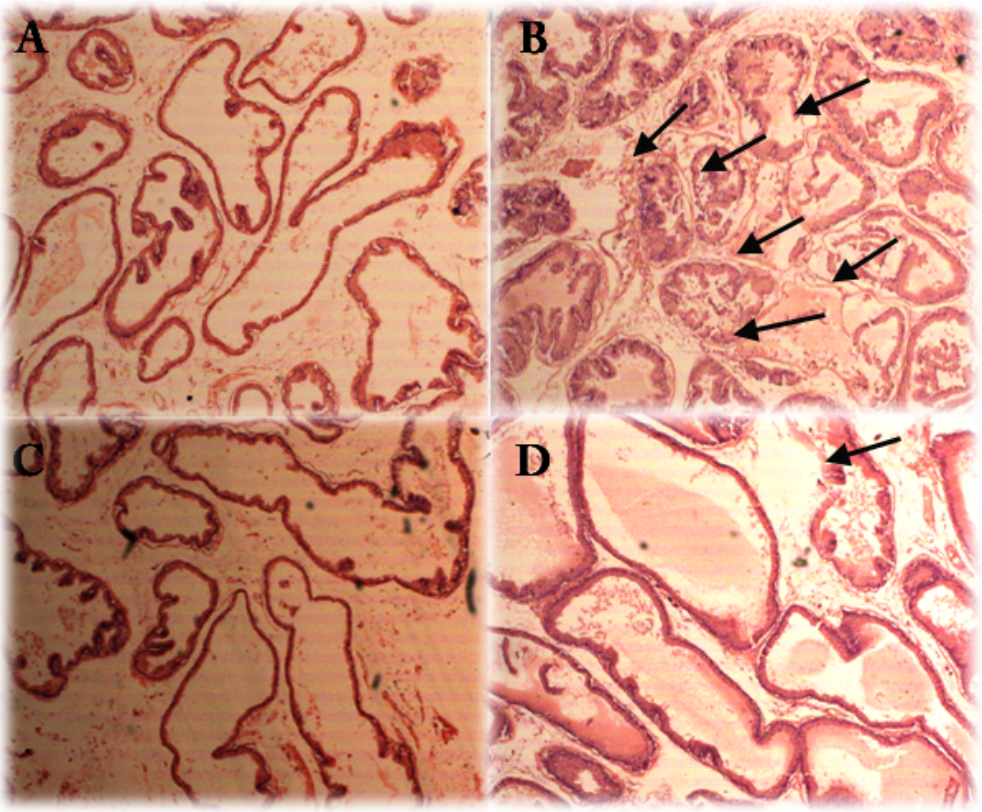

Figure 19: Histopathology pictures of prostate tissue stained with haematoxylin and eosin stain A. control group (untreated) B. Testosterone treated group (3mg/Kg) C. Finasteride treated group (Testosterone 3mg/Kg and finasteride 10 mg/Kg) D. Lead 17 treated group (Testosterone 3mg/Kg and Lead 17 10mg/Kg). The arrows indicate tissue disruption, observed mostly in testosterone treated group. One representative section is shown at original magnification X100

5.2.14. Estimation of inflammatory mediators

It was interesting to know from various literatures that SIRT1 inhibitors were useful in treating rheumatoid arthritis and other inflammatory disorders. Inflammation has large number of mediators, which include reactive oxygen species. The levels of reactive oxygen species were shown to be increased in inflammatory conditions. Hence, in our present study, levels of reactive oxygen species were determined after induction of U87 cells with lipopolysacharides. From the **Figure 20A** it was clear that there was significant increase in the reactive oxygen species when treated with lipopolysacharides. However when treated with **Lead17** and curcumin (known drug)

the levels of reactive oxygen species were reduced to that of control cells (untreated with lipopolysaccharides). This inferred that **Lead17** could be used in treating inflammatory condition; however it would be interesting to know the effect of **Lead17** on inflammatory mediators like tumor necrosis factor-α (TNF-α) and interleukin-6 (IL-6). Gene levels of TNF-α and IL-6 were determined after incubation with test compounds using real time PCR. There was a significant increase in inflammatory mediators when incubated with lipopolysaccharides (**Figure 20B**), however, when incubated with **Lead17** the levels of TNF-α and IL-6 were in comparison with control cells. This further illustrated that the **Lead17** could be useful in treating inflammatory disorders.

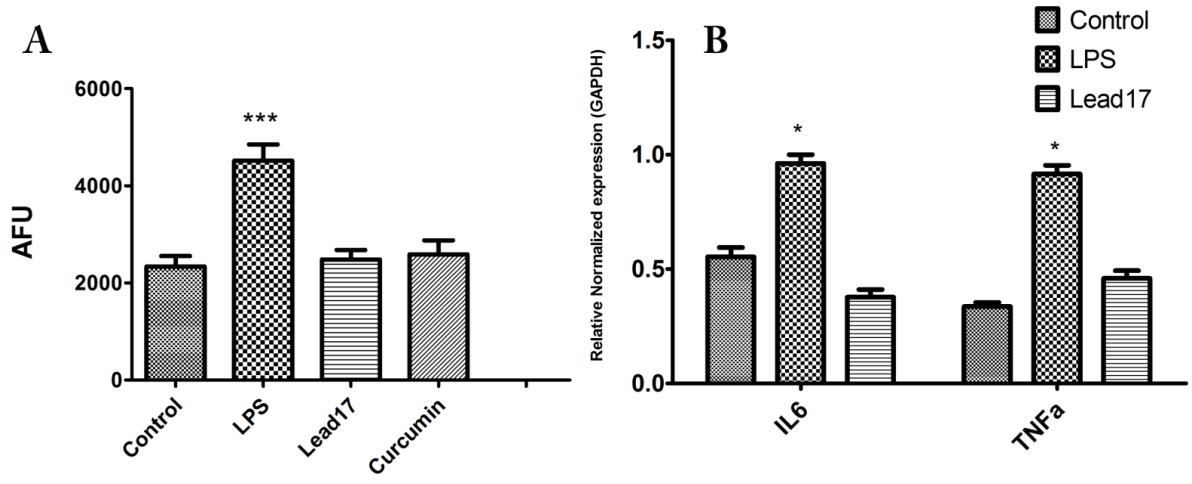

Figure 20: A. detection of Reactive oxygen species in various groups stained with 2′,7′-dichlorofluorescin diacetate (mean ± SEM, ***P<0.001 unpaired T test) B. Illustrates the mRNA levels of pro inflammatory mediators such as IL6 and Tnf-α genes, normalized with GAPDH expression (mean ± SEM, *P<0.05 unpaired T test)

5.2.15. Carrageenan induced paw inflammation

As cell based studies showed positive results, we undertook in-vivo assays to understand the activity of **Lead17** in animals. To further illustrate the potency of **Lead17** in inflammation, carrageenan induced paw inflammation model was employed. Carrageenan, a seed weed when administered at the subplantar region, increased the paw volume. Paw volume was determined using plethysmometer and it was observed that there was an increase in the paw volume

consistently for 4 h after administration of carrageenan (Figure 21). However the effect of carrageenan was reverted when treated with standard non-steroidal anti-inflammatory drug indomethacin. Similar effect was observed when **lead17** was administered to Wistar rats confirming their effect as observed in-vitro. This proved that SIRT1 inhibitor **lead17** could be considered as an effective lead in treating inflammatory disorders as well.

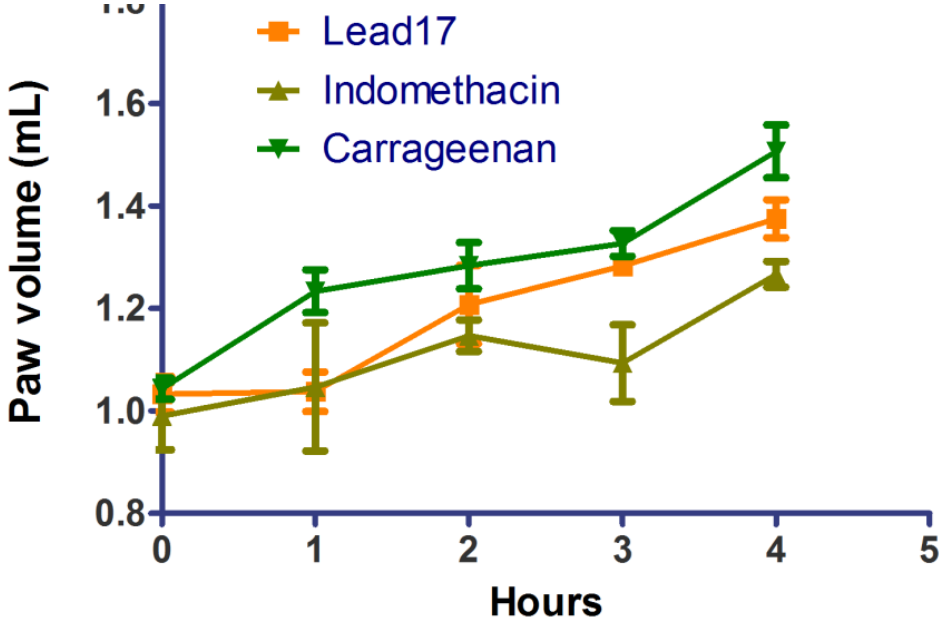

Figure 21: Paw volumes at different time points of various groups after sub plantar injection of Carrageenan (100µL of 1% freshly prepared carrageenan).

5.2.16. Conclusion

SIRT1 crystal structure bond with known SIRT1 inhibitor was used to design novel small molecule inhibitors based on structure and ligand based drug discovery strategies. Pharmacophore features developed were validated by various parameters and the best models were selected for screening both Asinex and in-house databases. Molecules with good docking scores were evaluated for their in-vitro enzyme inhibition activity. **Lead17** was found to be most

active with IC_{50} of 4.3 μM. As SIRT1 was involved in various functions, **Lead17** effect in reducing the cell proliferation and inflammation was evaluated. From the results, we confirmed that **lead17** being SIRT1 inhibitor was found promising in reducing the cancer cell proliferation, *via* apoptosis. This was further supported by the increased levels of proapoptotic genes like p53 and caspase3. It was also interesting to observe that animal administered with l**ead17** exhibited significant reduction of prostate to body weight ratio compared to control. This inferred that SIRT1 inhibitor **lead17** could be utilized in benign prostate hyperplasia conditions. In addition to the role in hyperplasia **lead17** also exhibited significant attenuation of ROS and the expression of inflammatory cytokines like TNF-α and IL-6. Besides **lead17** also showed good activity in reducing the carrageenan induced paw inflammation as compared with indomethacin. Thus, this study illustrated that **lead17** could be a candidate prototype worth exploring further for cancer and inflammatory diseases. In future using 3D-QSAR developed in this study, further leads could be optimized that would be helpful in treating various disease conditions.

5.3. Design and biological evaluation of NAMPT inhibitors using structure based drug design

5.3.1. Epharmacophore modeling

NAMPT crystal structure with PDB id 2GVJ was retrieved from protein data bank for this study. Though there were many crystal structures available in PDB 2GVJ with resolution 2.1 A^0 was considered for having bound with most potent ligand (FK866, K_i 0.3 nM) (Khan, J.A., *et al*., 2006). Protein was prepared using protein preparation wizard with the addition of hydrogens and energy minimization using OPLS_2005 force field. By redocking the crystal ligand onto the prepared protein, e-pharmacophore was generated using PHASE with three pharmacophoric features containing two rings (R8 and R7) and one acceptor (A3). Although, while generating maximum of 7 features as default option were given, it resulted in only 3 pharmacophore features (**Figure 22**). In principle the e-pharmacophores generated based on structural and energy interacting parameters between protein and ligand, were different to that of ligand based methods.

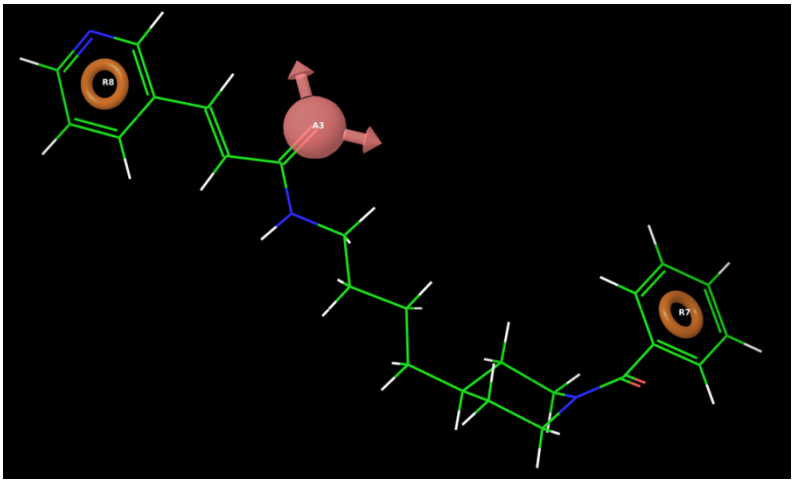

Figure 22: Three point pharmacophore generated using energy based pharmacophore strategy, which consists of two Ring features (R8 ad R7) and one acceptor feature (A3)

The 3-point e-pharmacophore was then subjected to PHASE find matches to screen Asinex database (commercial) containing 600,000 unique compounds. Based on fitness values, initial leads were identified, in which fitness was a value that measured how well the ligand fitted with the pharmacophore hypothesis. Greater the fitness score, inferred the molecule to have greater chance of similarity to reference ligand (FK866) and had greater chance of being active. The molecules with good fitness values were selected and further subjected to molecular docking. Docking was done in three stepes as followed in previous experiments, initially HTVS (High-throughput virtual screening) then SP (standard precision) and finally XP docking (extra precision). Survivors at each step were further taken to next subsequent steps. To understand precisely the hydrogen bond interactions, electrostatic and hydrophobic interactions, XP docking was performed and the finest ligands among all were shortlisted and procured from commercial chemical database (Asinex). The fitness values, docking score, hydrogen bonds and important aminoacids are depicted in **Table 14**. Two dimensional structure of the top leads are depicted in

Figure 23. From the **Table 14**, it was clear that the crystal ligand (FK866) has shown only one hydrogen bond with Ser-275 of the protein. Interestingly, all the shortlisted inhibitors have also shown interaction with Ser-275, which illustrates the importance of Ser-275 in active site pocket. From the docking studies, it was also inferred that the shortlisted compounds interact with Arg-311, Arg-196 and Ala-245. The docking score of the crystal ligand (-6.341Kcal/mol) was comparatively lower than the most of the shortlisted compounds. It could be because of a single hydrogen bond interaction with an enzyme.

Table 14: Crystal ligand binding aminoacids, docking score, hydrogen bonds, fitness and important interactions of all shortlisted inhibitors identified through virtual screening and enzyme inhibition data

S.No	Compounds	Docking Score	Hydrogen bonds	Fitness	Percentage of inhibition (40µM)	Important interactions
1	Lead 1	-11.49	6	2.11	53.06±3.1	Tyr-188, Ser-275, Arg-311, His-247 (2)
2	Lead 2	-9.37	3	1.79	27.35±2.4	Ser-275, Ala-245, Arg-196
3	Lead 3	-8.89	3	1.61	17.65±2.3	Ser-275, Ala-245, Arg-196
4	Lead 4	-8.87	2	2.08	29.75±3.3	Arg-196, Ser-275
5	Lead 5	-6.674	3	2.05	82.18±8.1	Asp-219, Ser-241, Ser-242
6	Lead 6	-8.71	3	1.62	24.96±3.4	Ser-275, Arg-311, Arg-196
7	Lead 7	-8.6	3	1.63	11.24±1.2	Ser-275, Ala-245, Arg-196
8	Lead 8	-8.56	3	1.62	33.55±4.6	Ser-275, Ala-245, Arg-196
9	Lead 9	-8.48	5	1.64	45.42±6.1	Ser-275
10	Lead 10	-8.43	4	1.83	9.88±0.9	Ala-245, Val-242, Ser-275, Arg-196
11	Lead 11	-8.36	3	1.64	8.25±1.6	Arg-311, Arg-196, Ser-275
12	Lead 12	-8.28	5	1.62	39.48±3.7	Arg-311, Arg-196, Ser-275
13	Lead 13	-7.158	4	1.7	98.59±4.7	Gly-383, Phe-193, Tyr-188, Arg-349
14	Lead 14	-8.13	3	1.76	29.14±4.6	Ser-275, Val-242, Arg-196
15	Lead 15	-7.94	3	1.54	18.45±0.9	Ser-275, Arg-311, Arg-196
16	Lead 16	-7.64	1	1.72	37.52±5.8	Ser-275
17	Lead 17	-7.56	2	1.9	22.08±4.1	Ala-245, Ser-275
18	Lead 18	-7.51	4	1.64	14.32±2.9	Ser-275, Lys-189, Arg-349
19	**Cryligand**	-6.341	1	2.27	99.91±4.7	Ser-275

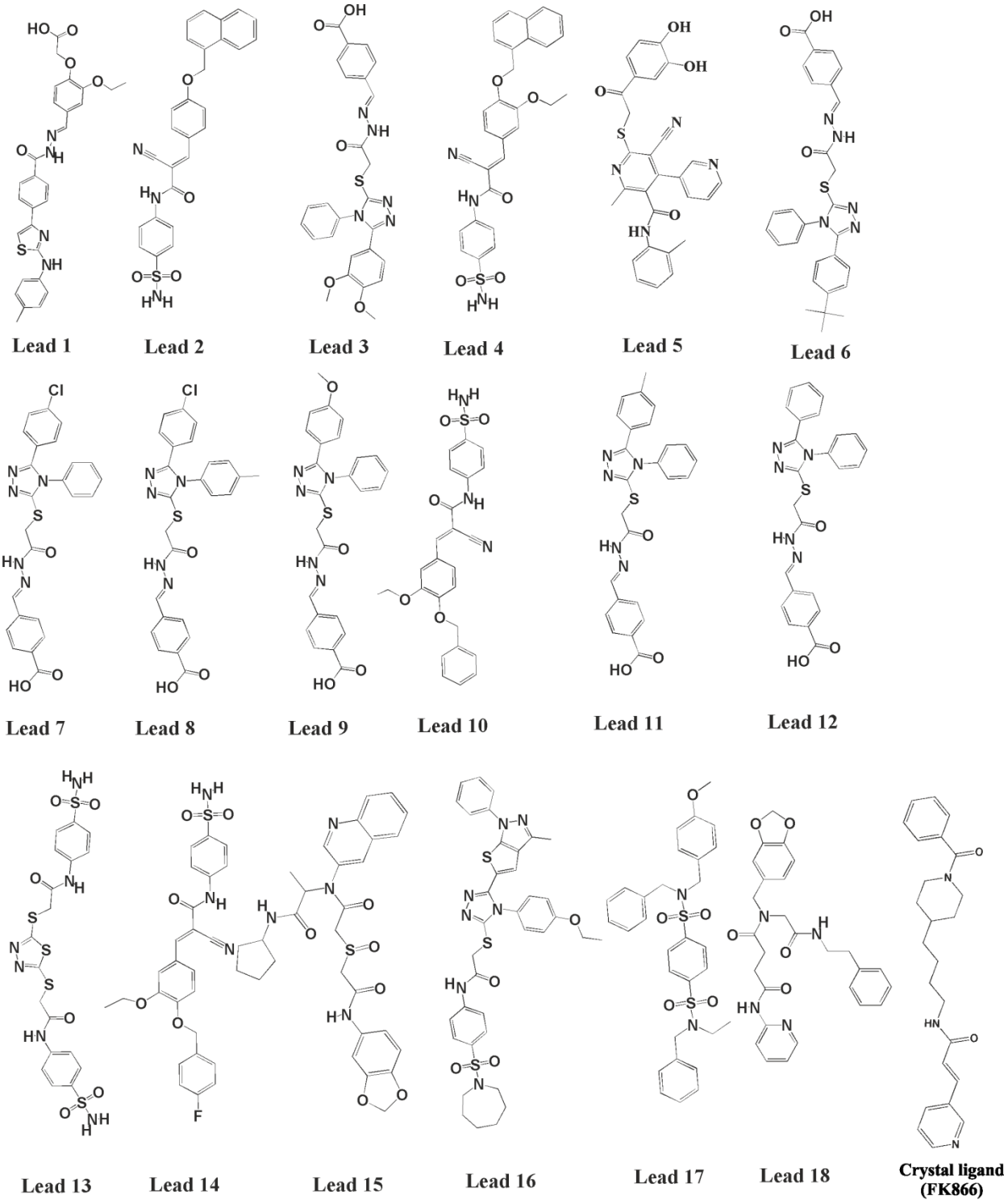

Figure 23: Two dimensional structures of the top leads obtained after docking

5.3.2. In-vitro enzyme inhibition

Shortlisted compounds from commercial source were procured and in-vitro enzyme studies were carried out. The substrate of the enzyme being nicotianmide, can be easily procured from commercial source. In order to carry out the enzyme inhibition studies, pure enzyme was necessay. To get the purified NAMPT enzyme, human NAMPT gene was cloned in the bacterial host system with histidine tag. After inducing the protein expression with IPTG, proteins were purified employing affinity (Ni-NTA based) chromatography. As the cloned gene consists of histidine tag, has the highest affinity to the coluumn. Later using imidazole of various concentrations, NAMPT protein was eluted and confirmed using polyacrylamide gel electrophoresis. Protein quantification was made using Bradford reagent after constructing standard curve with BSA. Later enzyme kinetics studies were performed to find the optimum concentration of substrate and enzyme As per the method developed earlier by Zhang et al (Zhang, R-Y., et al., 2011), NAMPT (Nicotinamide phosphoribosyl transferase) enzyme activity was determined by quantifying the product NMN (Nicotinamide mononucleotide). NMN was converted into a fluorescent derivative after reacting with acetophenone, potassium hydroxide in excess of acid (Formic acid). The resultant fluorescent derivate of NMN was quantified using multiplate reader measuring the fluorescent intensity at excitation and emission of 382 nm and 445 nm respectively. To further validate the method, a standard curve of NMN was constructed using concentrations ranging from 10 nM to 100 μM (**Figure 24A,** AFU: Arbitrary fluorescence units). Later using sufficient quantity of the substrate (nicotinamide, 5μM), the enzyme activity of the purified protein was tested with increasing concentrations ranging from 1 to 20 μg/ml and the fluoroscence intestity was found to be increased and was apparently linear (**Figure 24B**),

demonstrating that the method employed was well suited for enzyme inhibition studies. In addition to that, considering enzyme concentration to be constant at 2 µg/ml, substrate concentration was increased up to 125 µM. and the resulting curve was fitted in Michaelis Menten equation to obtain K_m value (**Figure 24C**), which was found to be 1.5 µM. Thus, by considering the substrate concentration close to K_m value of 1.2 µM and enzyme concentration of 2 µg/ml, enzyme inhibition studies for designed compounds were performed and the percentage inhibitions were calculated at different concentrations of test compounds, and finally using Graph pad prism, IC_{50}s were calculated. Initially, all the procured compounds were screened at 40 µM concentration and compounds that showed more than 65 % inhibition were further screened at lower concentrations.

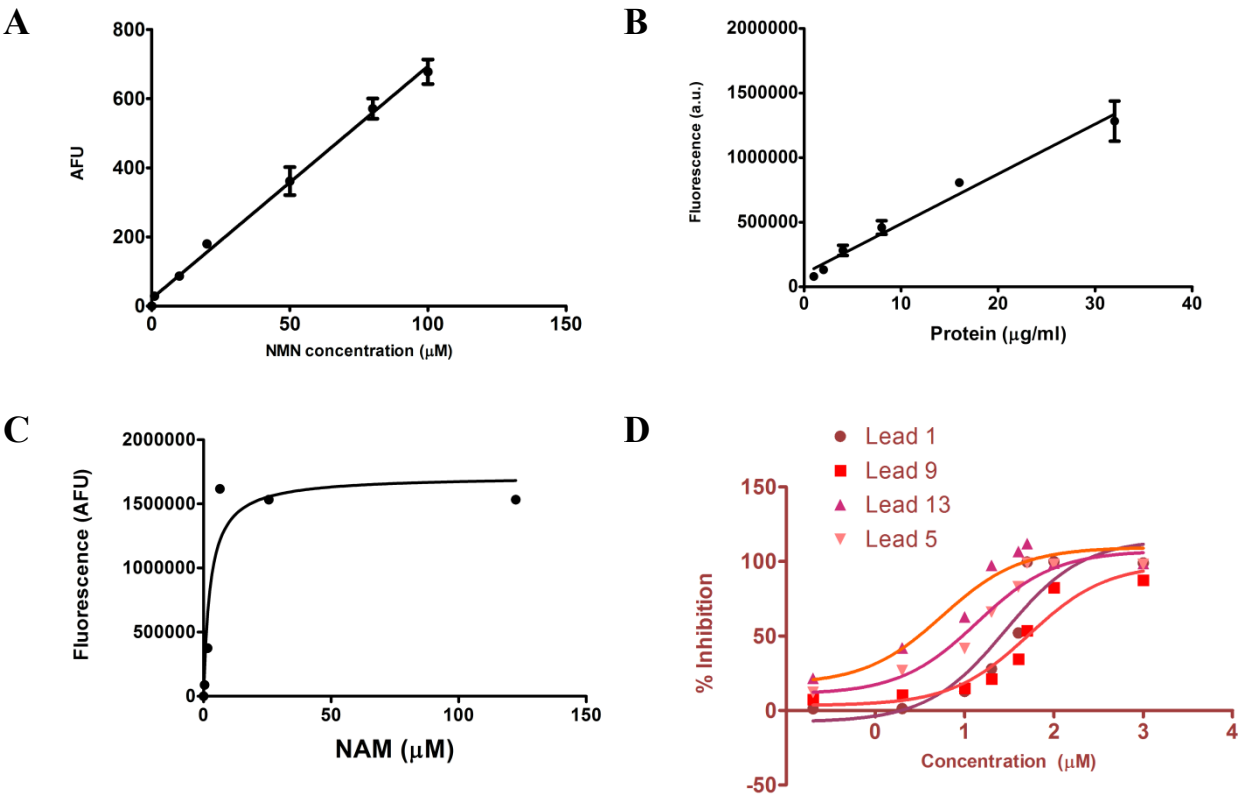

Figure 24: Enzyme optimization and inhibition assay. A: Standard curve of NMN (nicotinamide mononucleotide) constructed with various concentrations ranging from 1 µM to 100 µM; B: Enzyme assay performed at various concentration of protein ranging from 1 µg to 32 µg at constant substrate concentration of 5 µM (NAM); C: Graph fitted in Michaelis Menten equation, enzyme assay was performed at various concentration of substrate ranging from 0.4 µM to 120

μM at constant concentration of enzyme; D: Hill- slopes obtained through enzyme assay at various concentrations of potent inhibitors discovered in this study

Among all the compounds, **Lead13** was found to be the most potent with IC_{50} of 5.617±0.983 μM, and the second most potent compound was **Lead5** with IC_{50} of 13.77±2.391 μM. Along with this, IC_{50}s of the other two moderately active compounds were also determined and hill slopes are depicted in the **Figure 24D .** The structures of the top hits are presented in **Figure 25**.

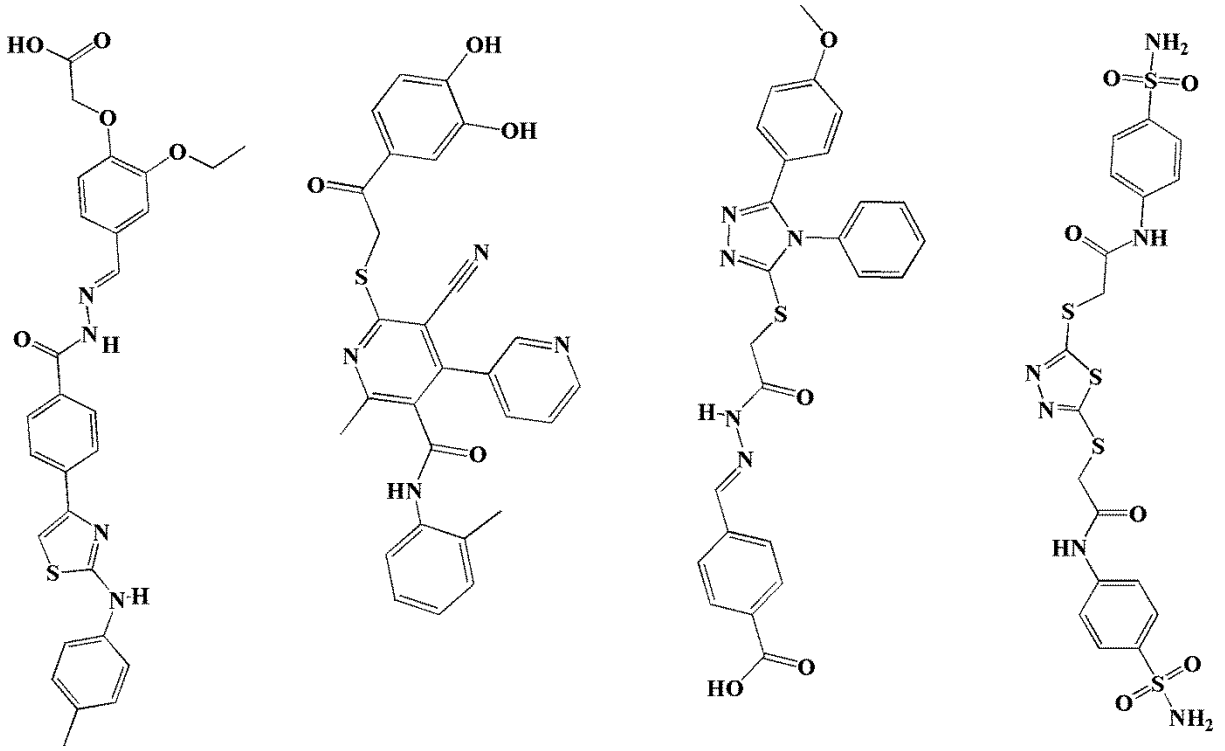

Figure 25: Important lead compounds identified using e-pharmacophore

5.3.3. Ligand interaction pattern

From the Figure 26 we could infer that the crystal ligand (FK866) was comfortably fixed in the tunnel formed by the core of parallel β-sheet in domain B. Specifically the pyridyl ring was sandwiched between Phe-193 and Tyr-188. The carbonyl oxygen at the centre of the inhibitor aligned besides the side chain of Ser-275 resulting in hydrogen bonding. Further to this, the aliphatic carbons interacted with hydrophobic residues in the tunnel, hence it did not allow the molecule to escape. On the other hand, the interaction and orientation of **Lead 13** was found to be very much similar to that of the crystal ligand (**Figure 26**), which occupied the whole hydrophobic tunnel. **Lead13** being a symmetrical compound, sulphonamide group at both ends interacted with Gly-383 at one end and Arg-349 at the other end. In addition to that the carbamido NH at each side of the molecule oriented towards the two aromatic amino acids (Phe-193 and Tyr-188) resulting in strong hydrogen bonding. This could have helped the molecule a grip inside the pocket. Looking into the chemical structure of **Lead5,** it was found to be branched unlike the **Lead13** and **FK866,** and the docking score was found to be higher than the crystal ligand (-6.674 Kcal/mol) with three hydrogen bonding interactions. From the docking results of **Lead5** we could infer that the two hydroxyl groups represented as hydrophilic head groups were oriented outside the hydrophobic pocket, close to the hydrophilic amino acids like Asp-219, Ser-241 and Ser-242. However toluene and pyridyl rings at the other end, aligned onto the hydrophobic groove to be involved in hydrophobic interactions.

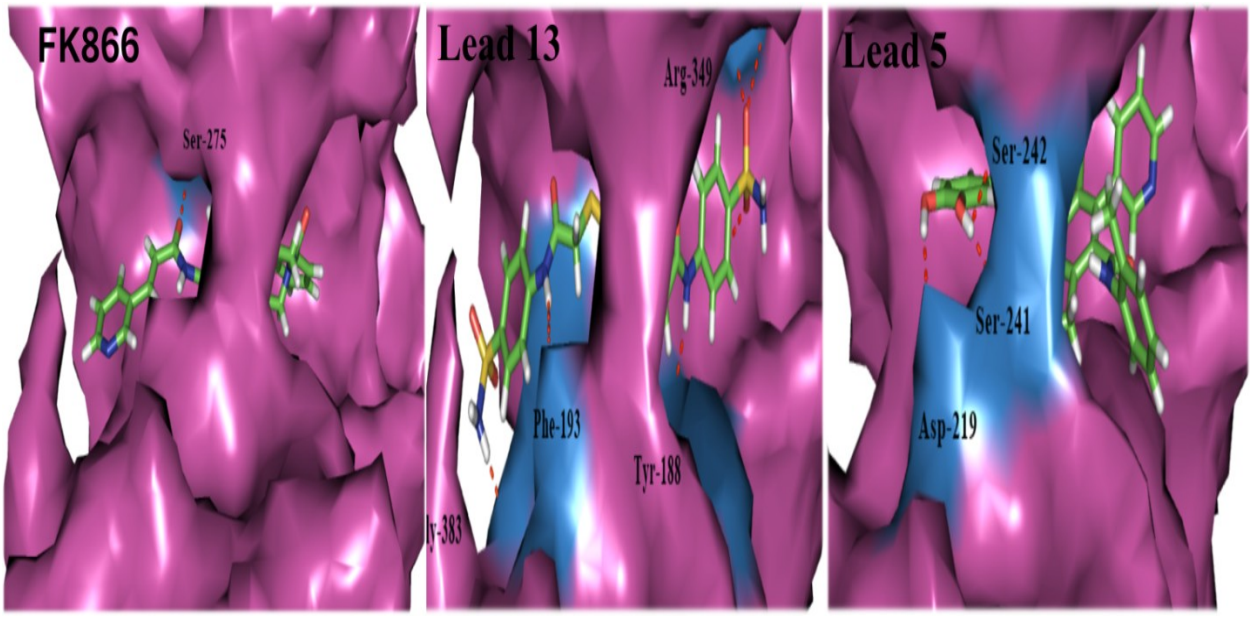

Figure 26: Illustrating the docking pose of the crystal ligand in comparison with potent inhibitors (Lead5 and Lead13) along with crystal ligand FK866.

5.3.4. Quantification of NAD

After evaluating in-vitro enzyme activities of the lead compounds, their ability in reducing the cellular NAD (Nicotinamide adenine dinucleotide) pool was tested upon incubation with U87 cell line for 6 hr, and the cytosol was extracted to measure the NAD concentration. U87 cell line was considered for this study because NAMPT has been reported to be overexpressed. Initially this method of NAD determination was validated by constructing a standard curve with increasing concentrations of pure NAD (Sigma) from 10 µM to 80 µM and the resulting curve was found to be linear (**Figure 27A**). As expected, incubating U87 cell line with nicotinamide (NAM) and nicotinic acid (NA) resulted an increase in NAD levels (**Figure 27B**), and when the potential inhibitors (**Lead13**, **Lead5 and FK866**) were incubated with U87 cell line, resulted in decreased in NAD levels more than half compared to the untreated (control) cells. Further, we also tried to know the effect of nicotinic acid in opposing the activity of lead compounds

(**Lead13** and **Lead5**). Surprisingly, it was observed that the decreases in NAD levels were reverted and became similar to that of control. There were no significant differences observed between the NAD levels of untreated cells with treated groups (**Lead5**/**13** + NA (100 μM)). Similarly, when the cells were incubated with known inhibitor (FK866) there was decrease in the NAD levels as observed with the test compounds. NAD levels were regained when the cells treated with nicotinic acid along with FK866. This infers that the lead compounds and known inhibitors (FK866), mode of action was same and also illustrates that the lead compounds were specifically inhibiting NAMPT function. As nicotinic acid acted as an alternate source of NAD, the NAD synthesis could have been directed to alternate pathways *via* nicotinic acid in presence of NAMPT inhibitors.

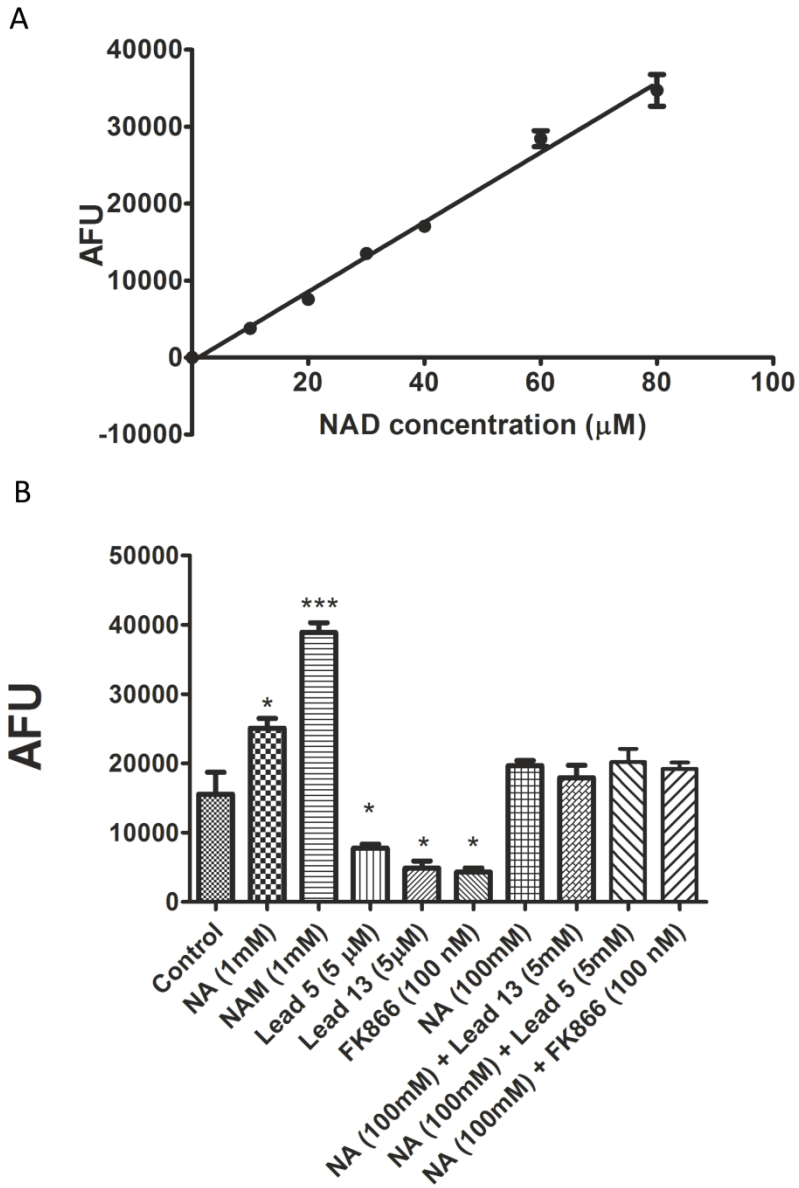

Figure 27: Optimization of NAD determination and estimation of NAD levels. A: Standard curve for NAD, concentration ranging from 10 μM to 80μM of NAD; B. Depicting NAD concentration obtained from different groups of U87 cell line incubated with different test compounds. NA refers to nicotinic acid and NAM refers to nicotinamide. *P<0.05, ***P<0.001 vs Control (untreated) (Annova + Turkey's post hoc test). Each bar represents the mean±SEM of two independent experiments in six well conditions.

5.3.5. In-vitro anticancer and cell cycle analysis

As NAMPT inhibitors like FK866 was reported to exhibit good anticancer properties, and is in clinical trials, we also tested the inhibitors identified from our study against different cancer cell lines. Cell proliferation studies were performed to understand the anticancer properties in four cell lines (MCF7, HT29, MPC and LNCAP). Initially, all the four compounds (**Lead1, Lead5, Lead9**, and **Lead13**) were tested at 10 μM concentrations, and the compounds that showed more than 50% inhibition were subsequently tested in 5 more lower concentrations to calculate their GIC_{50}s (growth inhibition IC_{50}). From the **Figure 15 & Figure 28A**, it was clear that among the compound tested, **Lead5** was the only compound that showed significant anticancer activity in all the three of the 4 cancer cell lines (HT29 (colan), MPC (mylenoma), LNCAP (prostate)) and their GIC_{50} values were calculated and found to be 3.12 μM, 1.82 μM and 3.4 μM respectively. Based on in-vitro enzyme inhibition studies, it can be known that, Lead13 was more potent than Lead5. However, in the cell proliferation studies, it was not effective. This could be attributed for its chemical and physical characteristics. As we see from the two dimensional structure that the Lead5 was less bulky than Lead13. Hence it could easily penetrate into the cell and do its job.

To further understand the specificity of **Lead 5**, The GIC_{50} was calculated in the presence of NAD (Nicotinamide adenine dinucleotide) in LnCAP cell line. Interestingly the GIC_{50} increased considerably. This increase was also observed with known inhibitor (FK866). This infers that both **Lead 5** and FK866 inhibit the cell growth by inhibiting NAD production. Hence, by supplementing NAD externally, inhibition in the production of NAD was reverted significantly, thus an increase in cell viability and GIC_{50} (**Figure 29**).

Table 15: Percentage inhibition of growth at 10 µM was tested in four different cell lines

Compound	Percentage inhibition at 10 µM[a]			
	MCF7 (Breast cancer)	HT29 (Colon cancer)	MPC (Mylenoma)	LNcaP (Prostate Cancer)
Lead1	18.43±1.873	13.45±0.142	22.62±1.273	35.06±2.463
Lead5	23.08±2.452	68.86±2.238	91.19±5.757	95.24±5.709
Lead9	18.35±0.492	35.04±2.671	8.31±0.783	12.30±0.0963
Lead13	33.11±3.721	39.66±4.624	25.81±3.283	32.03±2.893

[a]Compounds showing more than 50% inhibition were further screened at different concentration. GIC_{50} values of Lead5 in HT29, MPC and LNcaP was 3.12±0.823 µM, 1.825±0.212 µM and 3.4±0.972 µM respectively. Graphpad prism software was used to calculate GIC_{50}.

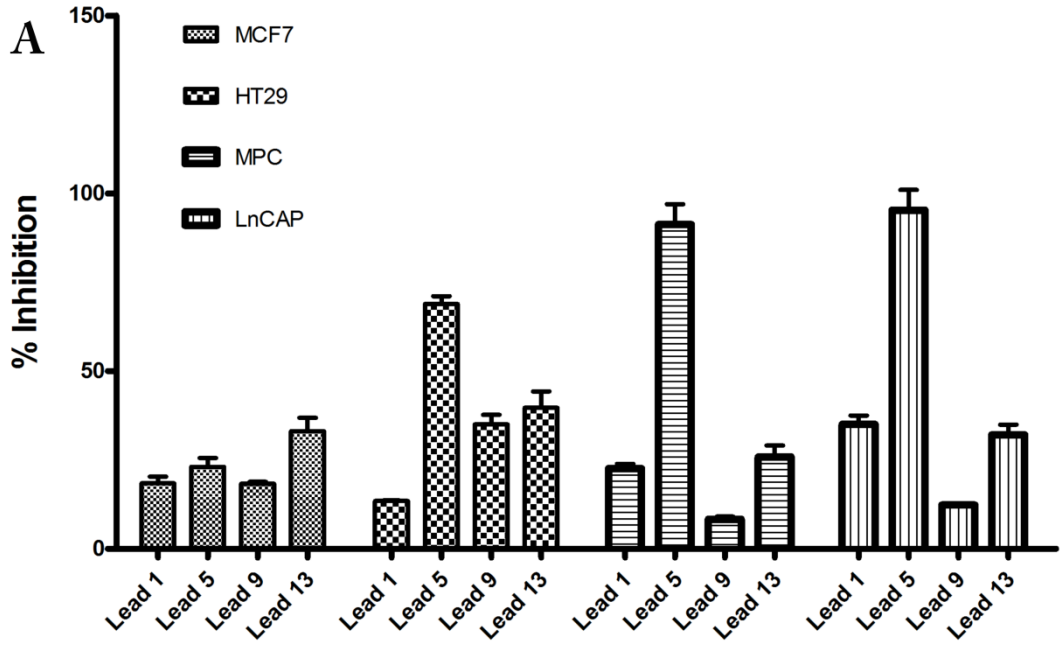

Figure 28: the percentage of inhibition of cell growth at 10µM on four human cancer cell lines (MCF7, HT29, MPC, LnCAP).

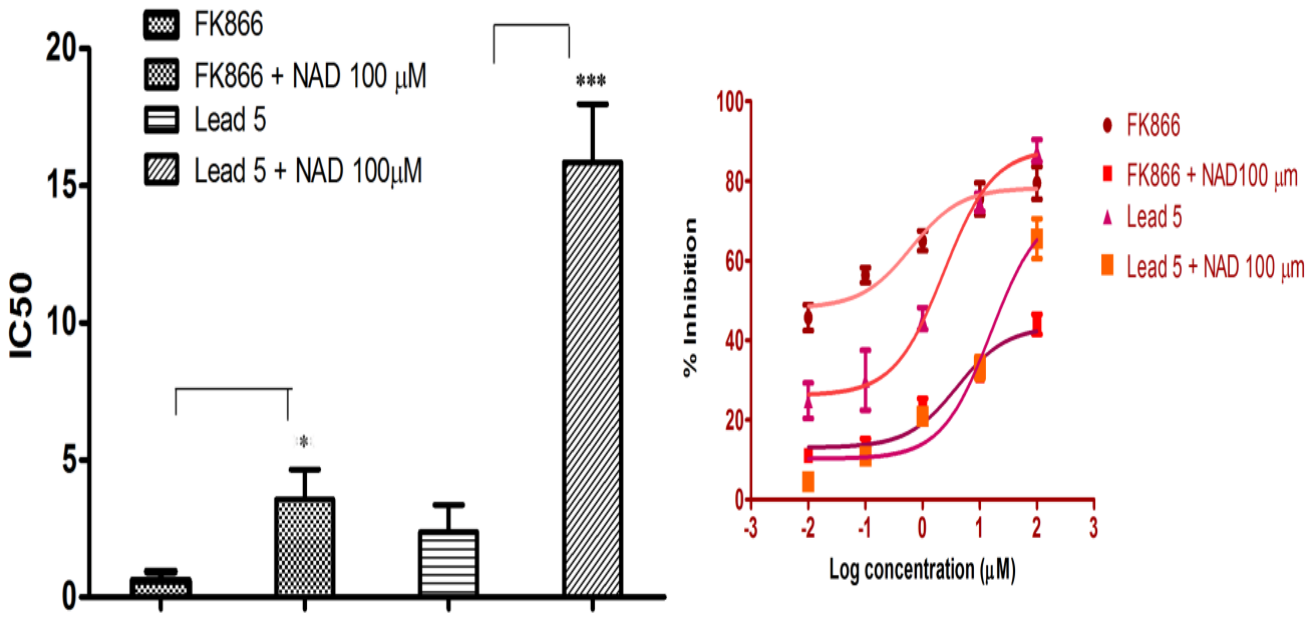

Figure 29: IC50 of known NAMPT inhibitor (FK866) and lead 5 on LnCAP cell line in absence and presence of NAD (Nicotinamide adenine dinucleotide) respectively. The hill slopes used to determine GIC50 of FK866 and lead 5 on LnCAP in absence and presence of NAD (Nicotinamide adenine dinucleotide). *P<0.05, ***P<0.001 vs Control (untreated) (Annova + Turkey's post hoc test). Each bar represents the mean±SEM of three independent experiments

To further understand the effect of **Lead5** on cell division, cell cycle analysis was carried out. As there were previous reports that NAMPT was overexpressed in prostate cancer, we specifically used LNCAP cells for our study. From the **Figure 30A**, it was clear that percentage of cells entering into the G0 phase were significantly increased after treating with **Lead5** as compared to the control, which inferred that there was an increase in cell death. To find out the cause of cell death, LnCAP cells were stained with annexin-V and propidium iodide. The reagent Annexin-V would detect specific biochemical changes in the cell surface membrane (exposure of phophosphatidylserine), which was considered to be a signature event for early apoptotic detection. The counter stain propidium iodide used in this assay helped in distinguishing the

apoptotic cells with intact membranes (early apoptotic cells) from necrotic cells. From the **Figure 30B** it could be inferred that the percentage of early apoptotic cells increased considerably (24.6%) when treated with **Lead 5** compared to that of control cells (9.6%). Further, when the cells were treated with **Lead 5** and NAD (Nicotinamide adenine dinucleotide, 100µM), there was a considerable decrease in the early apoptotic cells (9.6%). This inferred that the **Lead 5** induced apoptosis by decreasing the NAD pool inside the cell due to inhibition of NAMPT. However replenishment of NAD (Nicotinamide adenine dinucleotide) externally decreased the apoptosis.

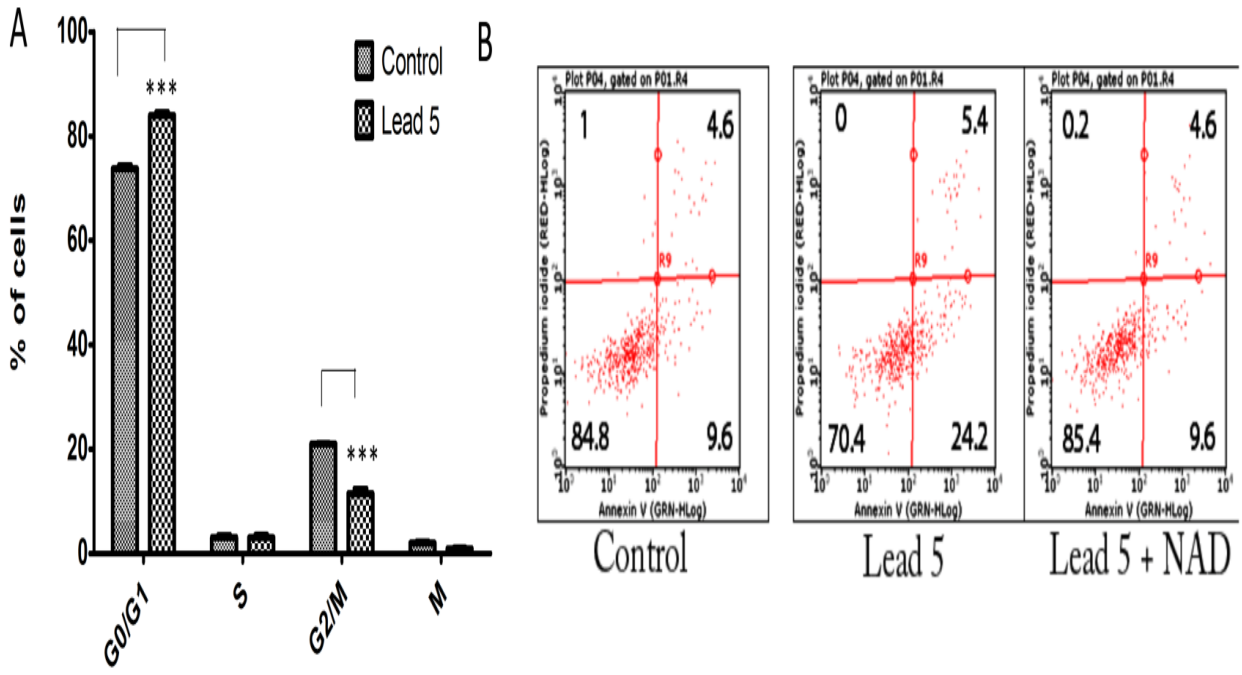

Figure 30: A: Illustrating percentage of cells in each phase when LnCAP cells were incubated with test compound (Lead5) for 24 hr and then stained with propidium iodide, later subjected to flow cytometry analysis to determine the percentage of cells in each phase. ***P<0.001 vs Control (untreated) (Two way Annova + bonferroni post test) B: Depicting LnCAP cells stained with Annexin-V FITC and propidium iodide to determine the percentage of cells in early and late apoptosis

5.3.6. Quantification of mRNA levels

After understanding the effect of **Lead5** on LnCAP cells, mRNA levels of p53 and caspase-3 were relatively quantified using SYBR green. Interestingly, both p53 and caspase-3 mRNA levels were increased significantly compared to the control (untreated) (**Figure 31**). As these proteins were involved in apoptosis, it could be confirmed that **Lead5** induced cell death *via* apoptosis. It is also known from the figure that, Fk866 (known inhibitor) also increased the proapoptotic genes significantly. This illustrates that Lead5 induces apoptosis in the same way as FK866.

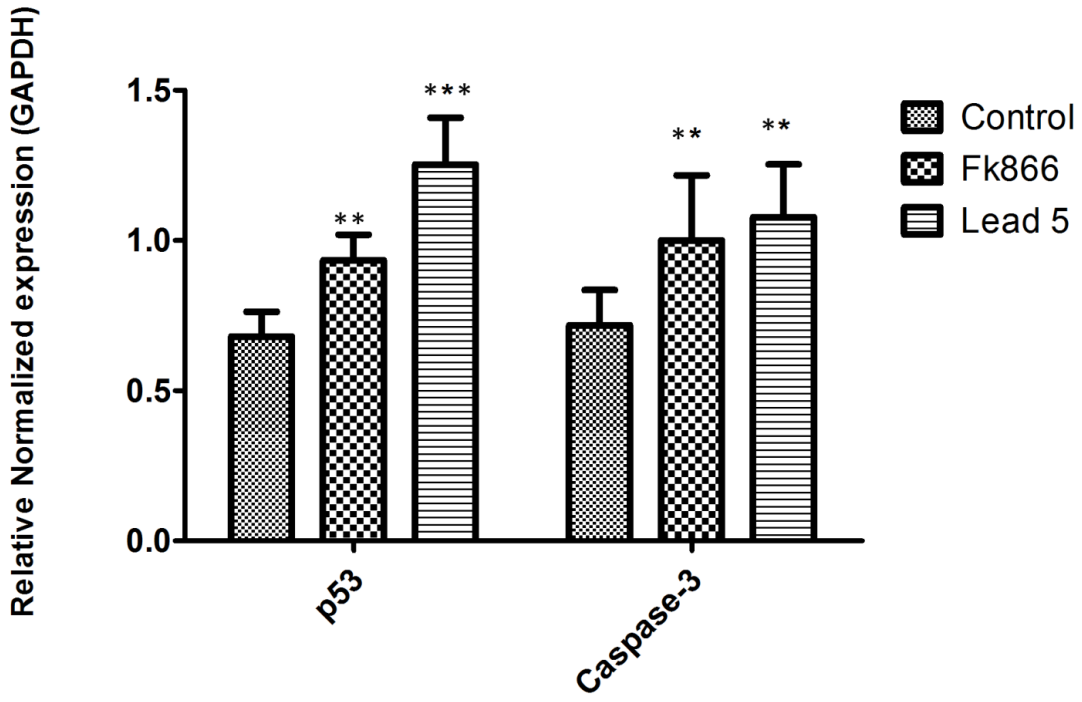

Figure 31: Illustrating the mRNA levels of p53 and caspase-3 of LnCAP cells incubated with FK866 and Lead 5. **P<0.01, ***P<0.001 vs Control (untreated) (Annova + Turkey's post hoc test). Each bar represents the mean±SEM of three independent experiments

5.3.7. Measurement of ROS

It has been reported that NAMPT inhibitors were useful in treating inflammatory disorders like rheumatoid arthritis, periodontitis, and it would be interesting to know the effect of NAMPT inhibitors in regulating inflammatory mediators like ROS. As we know that cellular ROS increase during oxidative stress, and could be mimicked by treating cells with hydrogen peroxide (150 μM) and/or lipopolysacharides (LPS 1 μg/ml). **Lead5** and **Lead13** being the most promising NAMPT enzyme inhibitors, their effects in reducing the ROS were determined using a fluorescent dye DCFDAE (2′,7′-Dichlorodihydrofluorescein diacetate**)** based method. Before the induction of ROS *via* H_2O_2, test compounds (**Lead5 and Lead13**) were pre-incubated for 2 h, and then DCFDAE was added and incubated for another 1 h. Later, the media was removed and fresh media were added along with H_2O_2. As the maximum ROS was produced at 35 min time point, it was considered as the end point reading. Here in this study the wells with only DCFDAE were considered as negative control. Statistically, there were significant differences observed between the induced (H_2O_2 treated) group) and un-induced cells (only DCFDAE treated group). Comparing the fluorescent readings of cells treated with test compounds, we estimated that **Lead5** had shown significant reduction in the ROS levels in both IMR32 and U87 cell lines (**Figure 32A & B**). Simultaneously the activity of the lead compounds in reducing the ROS response after induction with LPS (1 μg/ml) was also studied. The ROS levels were maximum at 6 h time point and hence the readings at 6 h time point was analyzed and the graph was plotted between compounds and AFU (**Figure 32C**). In this study the cells treated with LPS were considered as positive control and the cells treated with only DCFDAE was considered as negative control. Statistically, there were significant differences in the ROS responses between positive and negative controls. Surprisingly **Lead13** was found to show good activity in reducing

the ROS response after induction with LPS compared to the H_2O_2 (**Figure 32 A & B**). However the activity of **Lead5 and FK866** (Known inhibitor) in reducing the ROS was consistent in both H_2O_2 and LPS-induced cells.

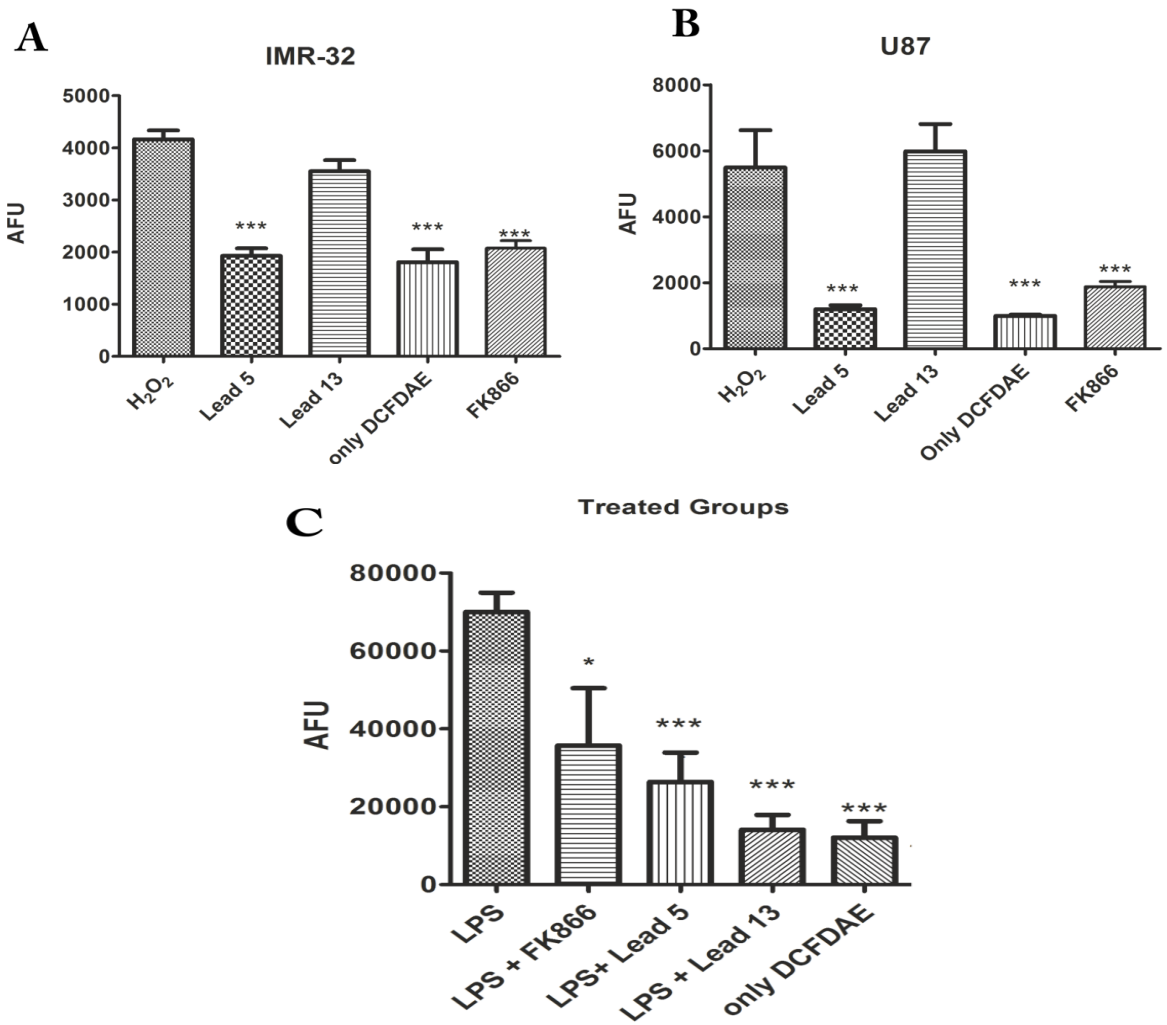

Figure 32: Cell-based assays on ROS inflammation. Reactive oxygen species detected using DCFDAE fluorescent assay in two cell lines (IMR32: 8A U87: 8B) after inducing with H_2O_2. ***P<0.001 vs H_2O_2 (Positive control (Annova + Dunnett's Test). Each bar represents the Mean±SEM of two independent experiments in six well conditions; C: Reactive oxygen species measured using DCFDAE based fluorescent assay in U87 cell line after inducing with lipopolysacharide (1µg/ml). ***P<0.001 vs negative control (only DCFDAE) (Annova + Dunnett's Test). Each bar represents the mean±SEM of three independent experiments in six well conditions;

5.3.8. mRNA quantification of inflammatory cytokines

To further know the effect of **Lead5** on the inflammatory mediators like TNF-α and IL-6, mRNA levels of these inflammatory mediators were determined. Total RNA was isolated after 6 h incubation with LPS from all the three groups (FK866, **Lead5**, and control) in U87 cells. Then mRNA levels of inflammatory genes (IL-6, TNF-α) were relatively quantified using Sybr green. All the expression levels were normalised with GAPDH, plotted and represented in **Figure 33**. As expected, the LPS treated group showed a significant increase in the mRNA levels of the two inflammatory mediators under study (IL6, TNF-α). While **Lead5** treatment after induction with LPS showed a significant reduction in the mRNA levels TNF-α and IL-6 similar to that of FK866, which indicated that NAMPT inhibitors could have significant implication in treating inflammatory disorders.

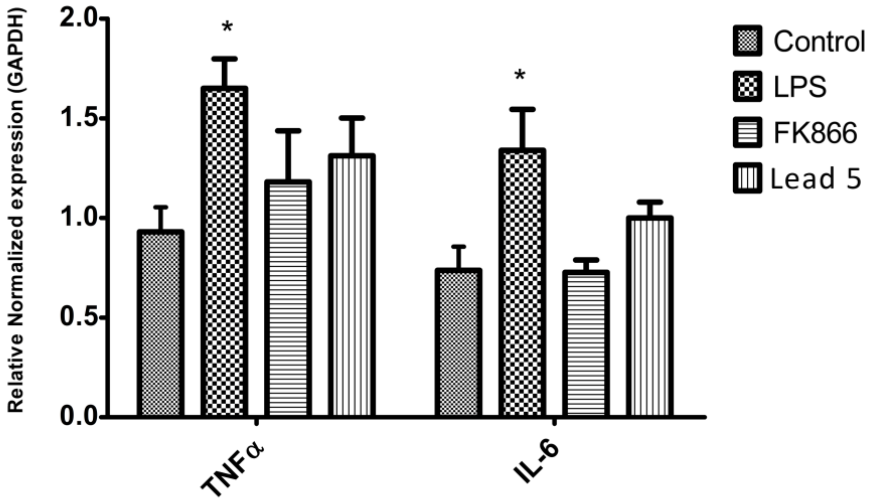

Figure 33: Relative normalized expressed of IL6 and TNFα genes extracted from U87 cell lines after incubation with different test compounds, FK866 was considered as reference compound. *P<0.1 vs control (untreated), each bar represents the mean±SEM of two independent experiments

5.3.9. Differential scanning fluorimetry

To understand ligand interaction and protein stability, differential scanning fluorimetry (DSF) was employed as a biophysical technique. It was considered as an inexpensive screening method to understand the interaction of low molecular weight ligands that could bind and stabilize the proteins. In this method, protein unfolding was measured with increase in the fluorescence of dye (Sypro orange), which showed high affinity to the hydrophobic residues of the protein. It was important to know that stability of the proteins decreased with an increase in temperature; and it was also linked with Gibb's free energy of unfolding. As the temperature was increased, the Gibbs free energy of unfolding was found to be decreased. At the equilibrium point, both the folded and unfolded proteins remained same, and the temperature at which the complex reached equilibrium was noted as the melting temperature denoted as T_m. The difference in $T_{m,}$ in the presence and absence of a ligand (low molecular weight) inferred on the interaction of a ligand with the protein. From the **Figure 34,** it could be seen that the melting temperature of the native protein was found to be 46.3^0C and the melting point of the protein with ligand (**Lead5**) was found to be 48.4^0C, which indicated that the ligand-protein complex was more stabilized as it had resulted a two degree shift in T_m.

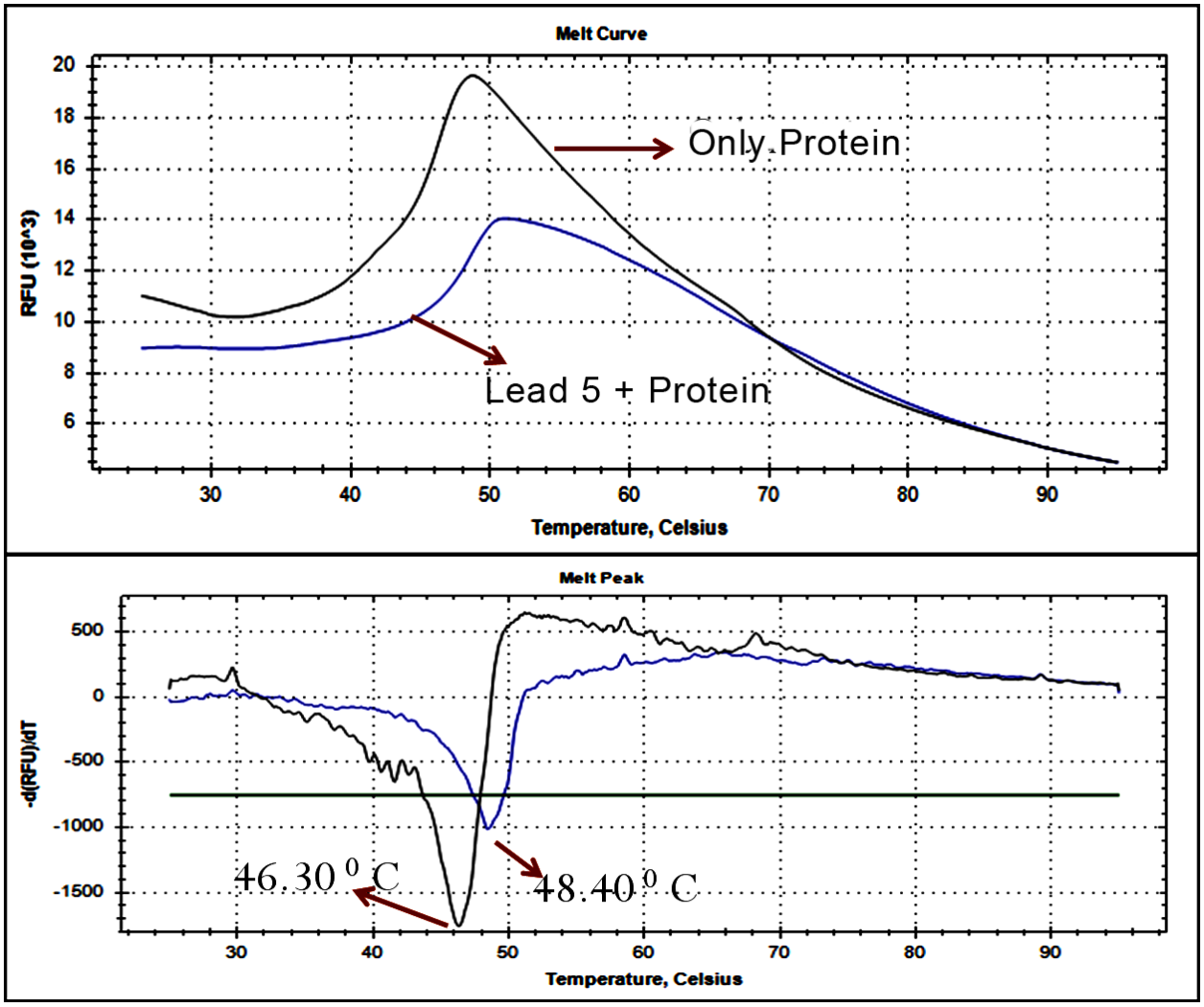

Figure 34: Differential scanning fluorimetry with Sypro orange dye, T_m of native protein was compared with the complex having protein and test compound (Lead5).

5.3.10. Conclusion

NAD (Nicotinamide adenine dinucleotide) acts as a central metabolite in many metabolic pathways, especially in both redox and non-redox reactions. Interestingly the role played by NAD in non-redox reactions had attracted considerable attention in recent years. The most common product of the non-redox reactions was NAM (Nicotinamide), which would be formed from the breakdown of NAD. Hence mammalian cells using NAM as the chief source of NAD

via salvage pathway were the most economical one when compared to other de-nova pathways. It was interesting to know that NAMPT (Nicotinamide phosphoribosyl transferase) has pleiotropic functions. Initially the function of NAMPT was presumed to be limited for bioenergetics, but as many enzymes such as PARPs (poly ADP-ribose polymerases), ARTs (mono ADP ribose transferases) and sirtuins were depended on NAD. Hence it was obvious that NAMPT has wider functions in cellular metabolism. Considering the importance of NAMPT in producing NAD, a detailed structural analysis was reported previously. In this process various crystal structures were proposed in association with inhibitors. In addition, it was also known that NAMPT played a major role in circadian clock, in which circadian machinery regulated the recruitment of SIRT1 to the NAMPT promoter, which activated NAD utilizing enzymes. Later through negative feedback inhibition, SIRT1 in turn would repress the function of NAMPT. Thus from all the above reports, it could be inferred that the role of NAMPT was not restricted to one function, but was complicated and linked to various metabolic pathways. NAMPT inhibitors showed considerable implications recently in treating various disorders like cancer and inflammation. As NAMPT protein was overexpressed in these conditions, reducing the activity using small ligands had kindled interest in many researchers. Here in this study we employed a novel strategy involving e-pharmacophore (Energy based pharmacophore) modelling to discover novel inhibitors against NAMPT. Based on the interaction of ligand at the active site of proteins, three pharmacophoric features including two rings (R8 & R7) and one acceptor (A3) was generated. As the crystal ligand (FK866) had big alkyl chain between the A3 and R7, this molecule was fitted into a deep hydrophobic tunnel. As expected the tunnel in which FK866 was fixed had favourable hydrophobic interactions. Thus using this three-point pharmacophore model, molecules from Asinex database were virtually screened and the finest ones were

procured for in-vitro enzymatic screening. From in-vitro screening, compounds **Lead5** and **Lead13** were identified to be more potent in the study with IC_{50}'s of 13.77±2.391 and 5.617±0.983 μM respectively. In order to estimate the inhibition of NAD synthesis in U87 cell line, these potent compounds were incubated for 12 h and found that there was a significant decrease in the NAD pool which were reverted when the cells were treated with NMN (Nicotinamide mono nucleotide) along with test compounds (**Lead5** and **Lead13)**. This reasertained, that these compounds were specifically inhibiting NAMPT. As NAMPT had been earlier implicated in inflammation, we tested the ROS (Reactive oxygen species) response against H_2O_2 and LPS induction. It was interesting to know that **Lead5** had significantly reduced the ROS response in both LPS and H_2O_2 induced groups, indicating the link between NAD synthesis and ROS response. Further to evaluate their effect on inflammation, mRNA levels of various genes (IL6, TNFα) were determined and interestingly were found reduced significantly with **lead5** (lead5+LPS) and **FK866** (FK866 + LPS) treated groups, when compared with LPS (LPS alone) groups. This also clarified the fact that there was a link between the NAD synthesis and ROS response. We could also infer that the NAMPT inhibitors were helpful in treating inflammation *via* reduction of ROS response and various cytokines like IL6, and TNFα. As NAMPT inhibitors were reported with anticancer activities previously, we evaluated the anticancer activities of potent compounds in four different cell lines. Once again, **Lead5** was found to be more potent than other compounds. To understand the specificity of **Lead5,** GI_{50} was calculated in presence of NAD (Nicotinamide adenine dinucleotide). Interestingly there was a significant increase in GIC_{50} from 3.4±0.97 μM to 12.32±1.23 μM. This explained that Lead5 inhibited the cell proliferation by inhibiting the synthesis of NAD. The annexin-V/propidium iodide staining studies confirmed that there was an increase in the early apoptotic cells after

incubation with **Lead5**, however there was decrease in the apoptosis when NAD replenished externally. This further explained that **Lead5** induced cell death *via* apoptosis and the increase in percentage of cells in G0/G1 phase (cell cycle analysis) was due to increase of apoptotic cells. mRNA levels of few apoptosis markers (p53 and Caspase-3) were also found to be increased in both **Lead5** and FK866 treated cells. Thus we could clearly infer that **Lead5** decreased NAD synthesis by acting on NAMPT, which further led to apoptosis by increasing the apoptotic markers (p53 and Caspase-3). Though these compounds discovered in this study were less potent than the previous reported compounds, but certainly these compounds has the potential to be considered as prototypical leads for further development as drug candidates with better pharmacodynamic and kinetic properties.

5.4. Design of NAMPT inhibitors using multiple pharmacophore models from structure ligand-based methods.

5.4.1. Design of novel small molecule inhibitors using multiple e-pharmacophore modelling strategy

At the beginning of the project in the year 2011, only one crystal structure of NAMPT (PDBID 2GVG) was available in the protein data bank. By the year, 2014 there were 30 crystal structures reported. Thus, employing multiple epharmacophore models was considered for discovering novel small molecule inhibitors (**Table 16**). The sudden increase in the crystal structures infers that the therapeutic importance of NAMPT would have attracted many crystallographers attention. From all the available PDB's only human NAMPT crystal structues with co-crystal small molecule inhibitors were employed in the design of epharmacophore models, which were thirteen crystal structures in number. As energy based drug design primarly depend on ligand and protein interaction, considering crystal structures having small molecule inhibitors could only bring the best pharmacophore features for screening compound library. Hence, crystal structures which does not have ligands and small molecule inhibitors were ignored. Based on the interaction between crystal ligand and protein, pharmacophore features are developed for each crystal structure. Crystal structures resulting with more than two pharmacophore features were only selected for further screening (**Table 17**). It was believed that, two pharmacophore features does not bring diversity in the compounds retrieved from virtual screening. Hence, pharmacophores with two features were ignored. As a result we had 8 PDB ID's, which has more than two pharmacophore features, which includes 4KFN, 4KFO, 4JNM, 4KFP, 4LVG, 4M6Q and 4M6Q.

Table 16: Available PDB crystal structures of NAMPT protein.

PDB code	Resolution A^0	ligand	Organism	Year
2gvg	2.2	NMN	Human	2006
2gvj	2.1	fk866	Human	2006
2h3b	1.95	S04	Mouse	2006
2h3d	2.1	NMN	Mouse	2006
2GVL	2.1	0	Mouse	2006
2G95	1.9	0	Rat	2006
2G96	2.9	NMN	Rat	2006
2G97	2.9	FK866	Rat	2006
2E5B	2	0	Human	2010
2E5C	2.2	5 phosphoribosyl 1 pyrophosphate	Human	2010
2E5D	2	nicotinamide	Human	2010
3DGR	2.1	ADP analogue	Human	2009
3DHD	2	NMN + pyrophosphate	Human	2009
3DHF	1.8	NMN + pyrophosphate	Human	2009
3DKJ	2	benzamide + Phosphoribosyl pyrophosphate	Human	2009
3DKL	1.89	benzamide + Phosphoribosyl pyrophosphate	Human	2009
3G8E	3	FK866 analogue	Rat	2009
4JR5	1.91	1LS	Human	2013
4KFN	1.6	1QR	Human	2013
4KFO	1.6	1QS	Human	2013
4JNM	2.2	1LJ	Human	2013
4KFP	1.84	1R7	Human	2013
4LV9	1.81	20J	Human	2013
4LVA	1.55	20M	Human	2013
4LVB	1.84	20N	Human	2013
4LVD	1.75	1EB	Human	2013
4LVF	1.5	20P	Human	2013
4LVG	1.7	20O	Human	2013
4M6P	1.75	20R	Human	2013
4M6Q	2.41	2OT	Human	2013

Table 17: Human NAMPT PDB ID, with their pharmacophore features, resolution and PDB codes. Bold font represents the PDBID with more than two pharmacophore features.

PDB code	Resolution A0	ePharcophores	Features
4JR5	1.91	2 point	2R
4KFN	1.6	5point	3R, 2D
4KFO	1.6	5 point	4R, 1D
4JNM	2.2	4 point	3R, 1A
4KFP	1.84	4 point	3R, 1D
4LV9	1.81	1 point	1R
4LVA	1.55	2 point	2R
4LVB	1.84	2 point	1A, 1R
4LVD	1.75	2 point	1R, 1D
4LVF	1.5	3 point	2R, 1A
4LVG	1.7	4 point	3R, 1A
4M6P	1.75	5 point	4R, 1D
4M6Q	2.41	7 point	3D, 2A, 1R, 1N

Enrichment calculation and goodness of hit were calculated using 131 known NAMPT inhibitors, and five best pharmacophore features were selected for virtual screening (Table 18), which includes 4JNM, 4KFP, 4LVG, 4KFO and 4M6P. Among them both 4M6P and 4KFO were selected based on enrichment factor and good ness of fit calculated manually and other four were selected based on machine calculated enrichment factor (Schrodinger module was used). The significance of highest enrichment factor and good ness of fit was that the possibility of retrieving active leads from a large database was high compared to the one with lower scores. As discussed above we have employed two different strategies to select the best pharmacophore. One was using schrodinger platform and another was through manual calculation. As our objective was to screen and select the best compounds from library, selection of pharmacophore models was a critical step. Using manual calculation we also obtained good ness of fit along with enrichment factor value. The significance of this method was that it calculates the EF and GH values based on the number of true actives and false actives. To get the highest possible score, there should be the highest number of true actives and lowest number of false actives. Thus considering this aspect, 4M6P and 4KFO has better scores compared to other, hence they were considered for screening. Similarly, Schrodinger platform also calculates the enrichment factor

using different algorithms. Herein, we also get other parameters such as bedrock α-20. Pharmacophores which show highest EF and bedrock were considered for virtual screening. By analyzing the scores it can be inferred that Schrodinger algorithm considers mainly the true actives. Even the number of false actives was more, it could give good score based on a number of true actives. However, we considered this scores to not rule out many pharmacophore features.

Table 18: Enrichment factor and good-ness of fit obtained after manual calculation (EF and GH highlighted were high in score and considered for virtual screening). Enrichment factor 2% obtained after employing schrodinger module. (The Bedroc values highlighted with low score are highlighted in bold and they were ignored for virtual screening)

PDB	Ht	Ha	A	D	EF	GH	Bedroc α-20	EF 2%
4JNM	741	131	131	1131	1.52	0.14	0.83	28
4KFN	513	101	131	1131	1.69	0.21	0.78	29
4KFO	346	88	131	1131	**2.19**	**0.26**	0.74	21
4KFP	832	122	131	1131	1.26	0.09	0.731	19
4LVF	577	120	131	1131	1.79	0.22	**0.34**	**3.1**
4M6P	340	89	131	1131	**2.26**	**0.27**	0.73	21
4M6Q	126	15	131	1131	1.02	0.10	**0.09**	**0**
4LVG	714	131	131	1131	1.58	0.16	0.79	25

After comparing the pharmacophore features resulted from various PDB IDs, it can be interesting to know that pharmacophore features of 4M6P and 4KFO were very similar. Both of them have four rings and one donar feature. The distance between these pharmacophore features were similar in both the cases. This illustrates that the two co-crystal ligands have similar scaffold. Thus, resulting in similar pharmacophore features (Figure 35). Similarly, if we compare the pharmacophore features of 4KFP and 4KFN, they resemble similar features. However, PDB ID 4KFN has resulted one extra donar feature compare to 4KFP having three ring and one donar feature. In addition to this, 4LVG and 4JNM also resulted similar features. Both the PDB's gave three rings and one acceptor features with similar distances and angles between the pharmacophore features. By analyzing this, it would be redundant to use two similar pharmacaophore features for virtual screening. Interestingly, both 4LVG and 4JNM gave similar

EF and GH values. This was even observed between 4KFP and 4KFN . Hence, for virtual screening, we have considered 4M6P, 4LVG and 4KFN. Because, these pharmacophore features show high EF and GH values than their analogous patners.

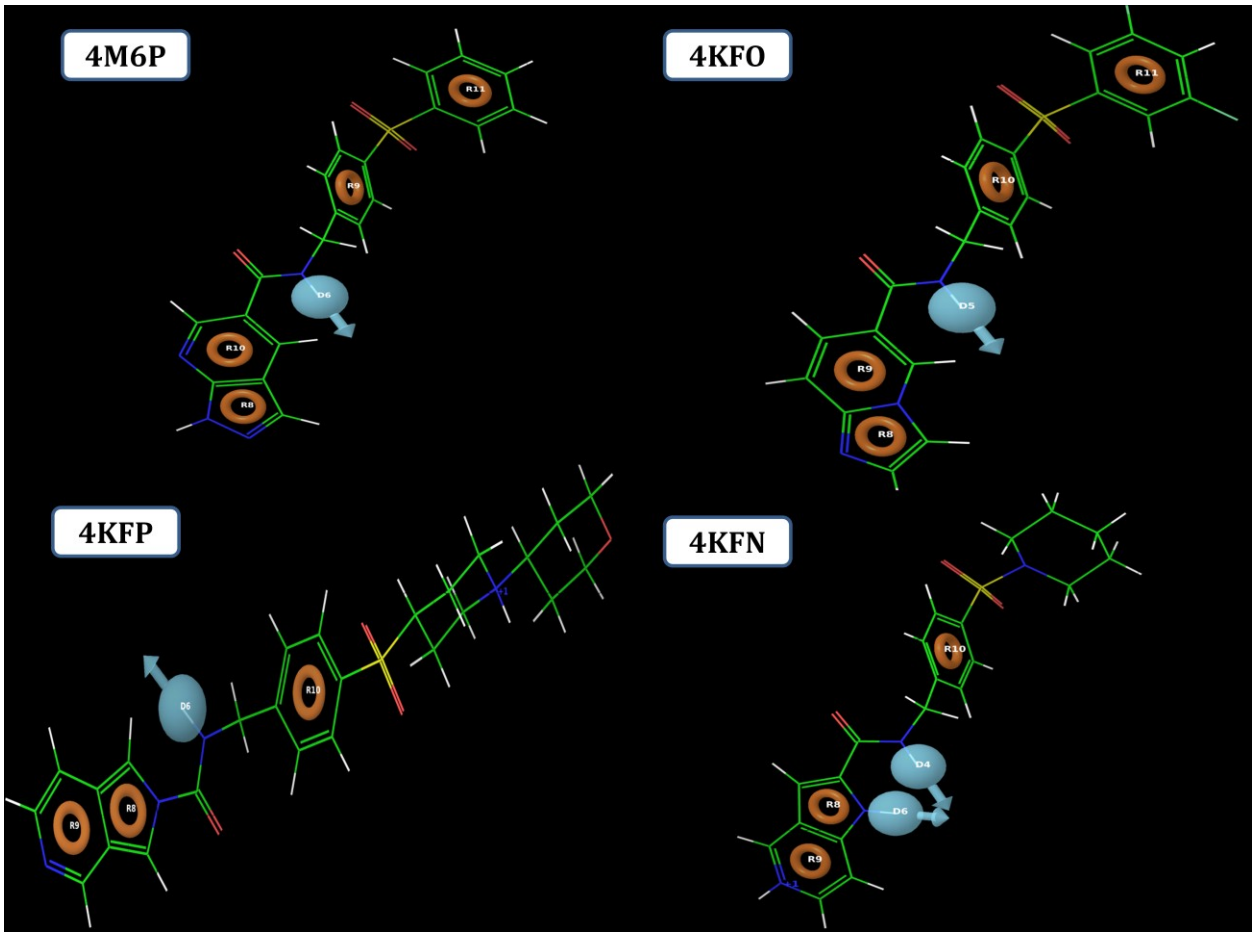

Figure 35 : Multiple pharmacophore features obtained from multiple crystal structures of NAMPT protein. A , D, R and H pharmacophore features indicate acceptor, donor, ring and hydrophic features respectively.

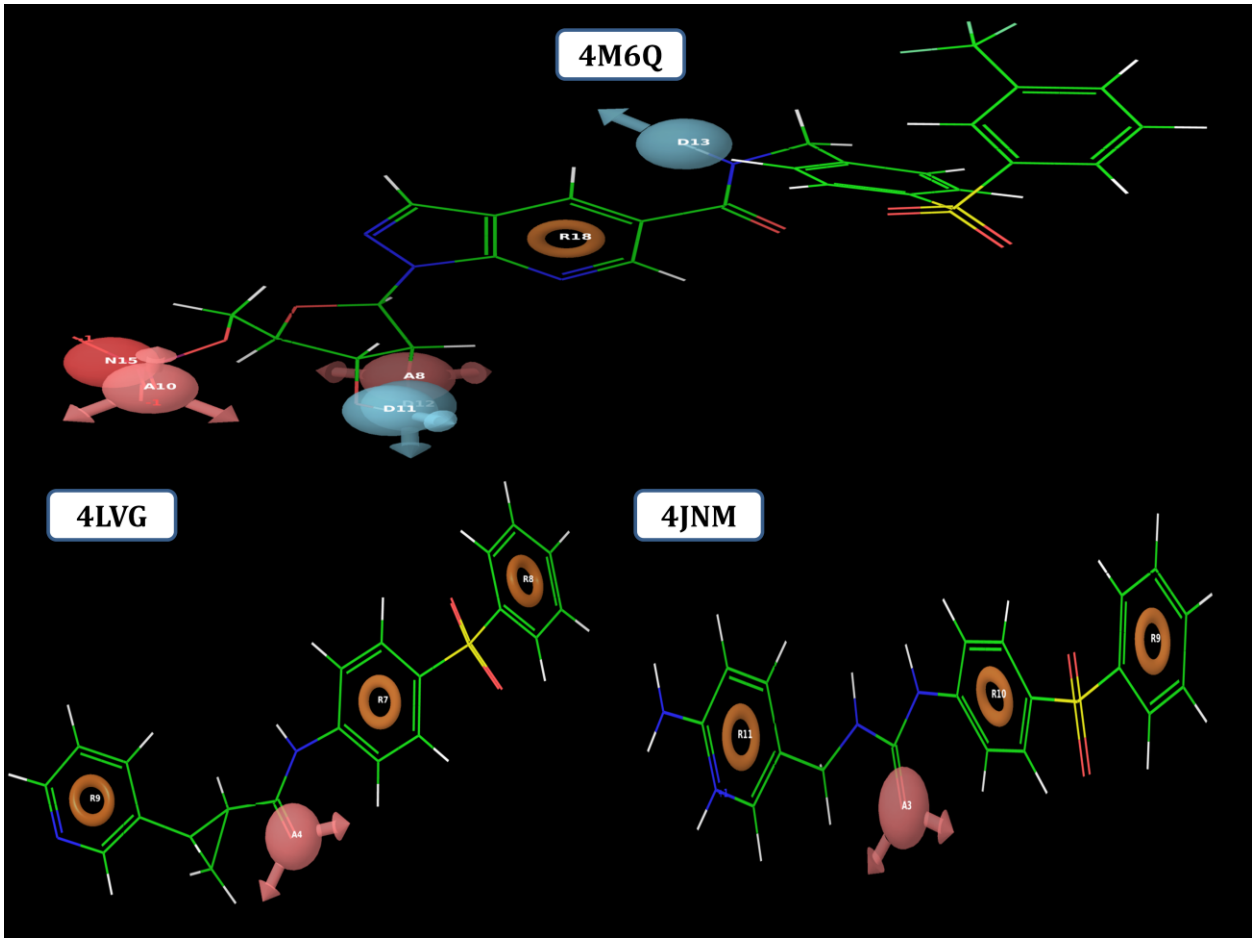

Figure 35: Multiple pharmacophore features obtained from multiple crystal structures of NAMPT protein. A , D, R and H pharmacophore features indicate acceptor, donor, ring and hydrophic features respectively.

5.4.2. Ligand based pharmacophore model

In addition to the energy based multiple pharmacophore modeling we also attempted to develop ligand based pharmacophore models. By employing PHASE module (Schrodinger) either we could generate a QSAR model of the atom based or pharmacophore based. As the training set molecules were rigid and congeneric we attempted to generate common pharmacophore hypotheses. Data set of 111 molecules reported as NAMPT inhibitors from various research articles were considered for ligand based modeling. The scaffolds used in development of ligand based pharmacophore model consisted of derivates of ureas (Zheng., etal., 2013), azides and molecules synthesized by click chemistry (Colombano, Travelli., etal., 2009) were divided into active, moderately active and inactive sets. Compounds with pIC_{50} values higher than 8.5 were considered as actives and those with less than 5 were considered as inactive. Molecules with pIC_{50} values between active and inactive were considered as moderately active. Based on different steps of scoring procedure like survival, survival inactive and post hoc, twenty hypotheses were generated. Further we selected four best hypotheses which satisfied internal parameters like survival activity, vector, volume and most active alignment (**Table 19**). Among all the hypothesis AADR 194 showed better vector and volume score. Thus, infers that AADR194, could be better pharmacophore model. However, they were further validated using enrichment and goodness of fit calculations (**Table 20**). Interestingly, hypothesis AADR 194 with two hydrogen bond acceptor (A), one hydrogen bond donor (D) and one rings (R) displayed good enrichment factor (2.904) and goodness of hit (0.33) markedly higher compared to other hypotheses. Hence we employed hypothesis AADR.194 to predict active molecules for data base screening. In addition to this, these five hypotheses were also further validated for QSAR predictability and subjected to partial least square (PLS) analyses.

Table 19: Survival scores of pharmacophore hypothesis (NAMPT)

Hypothesis	Survival score	Survival-inactive score	Vector score	Volume Score	Score site
AADR.25	2.681	1.37	0.76	0.425	0.25
ADRR.29	2.674	1.34	0.758	0.427	0.49
AADR.194	2.971	1.124	0.891	0.459	0.59
AADR.195	2.567	1.319	0.751	0.313	0.35

Table 20: Enrichment (EF) and Goodness of fit (GH) calculation for ligand based drug design models

PDB	EF	GH
ADRR 4	2.176158	0.263372
AADR 195	2.496151	0.295596
AADR 194	**2.9049**	**0.33728**
ADRR 28	1.148444	0.124931
AADR 25	2.314342	0.278135
ADRR 29	1.516425	0.164751

5.4.3. Generation of 3D-QSAR model and PLS analyses

QSAR models for reliable predictions were validated by both internal and external statistical tools. The predictive power of the models was tested with test set of 41 molecules. For useful insights, the statistical significance of the model was achieved using partial least square (PLS) factor of five. The robustness of models in predicting the active molecules were considered based on various numerical parameters, including leave one out cross validation for training set (R^2), leave one out cross validation for test set (Q^2), Pearson correlation coefficient (r) standard deviation (SD), root mean square error (RMSE) and variance ratio (F). The standard value of Q^2

should be more than 0.55; however QSAR model generated from AADR.194 exhibited much higher value than the standard, which was 0.704. This indicated high predictive ability of the model. In addition to this, other parameters like R^2 showed numerical values higher than the minimum standard, which was 0.945, almost near to 1. The goodness in predictive ability and robustness of the model was inferred from the low value of SD (0.1371) whereas the statistical significance of the model was inferred by the high F value (221.3). All the internal statistical parameters from PLS analyses were well within the range. However, external statistical validation was also important for more reliability. The significance of AADR 194 model was further illustrated in the scatter plot, which shows the correlation of phase activity and phase predicted activity close to the value1 (0.91) (**Figure 37**). The picture of pharmacophore (AADR 194) was shown in the picture , which has two hydrogen bond acceptors, one hydrogen bond donar and one ring features. The picture also depicts the distances between various features. This, illustrated pharmacophore could be used to screen the library of the compounds.

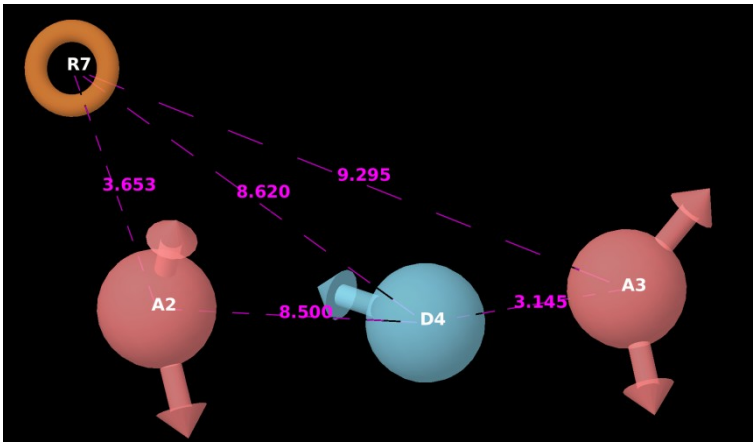

Figure 36: Pharmacophore features of ligand based pharmacophore model (AADR.194), with two hydrogen bond acceptors, one hydrogen bond donar and one ring features. The pink dotted lines represents the distances between the pharmacophore features.

Table 21: Internal statistical validation of ligand based pharmacophore models

Statistical Parameters	AADR. 25	ADRR.29	AADR 195	AADR. 194	ADRR. 4
Number of molecules in training set	70	70	70	70	70
Number of molecules in test test	41	41	41	41	41
R2	0.874	0.834	0.749	**0.945**	0.815
Q2	0.058	0.604	0.28	**0.704**	0.066
F-Value	87.6	63.6	38.4	221.3	56.7
Pearson-R	0.444	0.165	0.583	0.845	0.509
RMSE	0.892	1.164	0.781	0.501	0.888

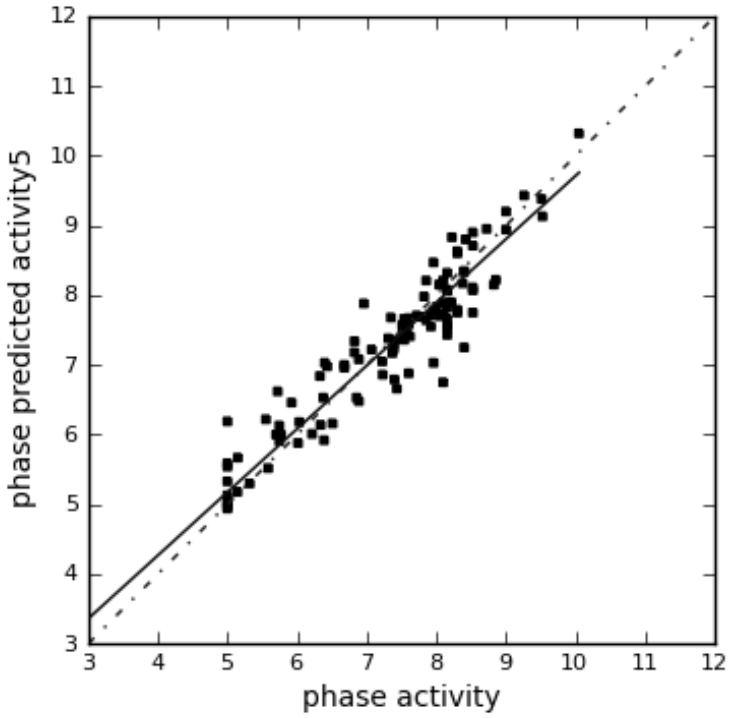

Figure 37: Scatter plot of the observed vs predicted activity of NAMPT inhibitors generated by the best model (AADR 194) obtained employing 70 compounds as the training set and validated using 41 compounds as the test set. Best fit line is very close to 1 with R2 of 0.91 (Straight line equation Y= 0.91x + 0.64)

5.4.4. External statistical validation

Reliable model should also posses' high correlation between the predicted and observed activities, referred with correlation coefficient R (or r^2). The best predictive ability of the QSAR model from AADR 194 was supported by correlation coefficient R with 0.935 (r^2= 0.925) and high slope of regression lines with K and K' values of 1.004 and 0.992 respectively. Using K and K' values R_0^2 and $R_0'^2$ were calculated using the regression lines in scatter plot of actual activity *versus* predicted activity and vice versa respectively. R_0^2 and $R_0'^2$ being 0.987 and 0.982, were further used to calculate the relation between r, R_0^2 and $R_0'^2$, which gave (($r^2 - R_0^2$)/ r^2) and (($r^2 - R_0'^2$)/ r^2) value of -0.129 and -0.054 respectively, which were within statistical limits **(Table 22)**. In addition to this a parameter of modified r^2 (r_m^2) and R_P^2 were calculated, where r_m^2 was considered for better external predictive potential for the whole set of compounds which was found to be 0.566 and R_P^2 = 0.674 was well within the statistical limits **(Table 22).** Thus from all the external numerical parameters we confirmed the robustness in predicting the active molecules by the 3D-QSAR model. Data set all the 111 compounds two dimenational structures along with experimental activity (PIC_{50}) and predicted activity (Phase predicted activity) was presented in the **Figure 38**. It could be inferred that for all the compounds the predicted and phase activity were closely associated. This illustrates further that the model developed was reliable in predicting the activity of test compounds.

Table 22: External statistical validation parameters

External validation	Parameter calculated	Limitations
r^2_{cv}	0.924917	$r^2_{cv}2 > 0.5$
R	0.935115	Close to 1
r^2	0.874439	$r^2 > 0.5$
K	1.0044626	$0.85 \leq k \leq 1.15$
K'	0.992326	$0.85 \leq k' \leq 1.15$
R^2_0	0.987793	R^2_0 or R'^2_0 close to r2
R'^2_0	0.982925	R^2_0 or R'^2_0 close to r2
$((r^2- R^2_0) /r^2)$	-0.1296308	$((r^2- R^2_0) /r^2) < 0.1$
$((r^2- R'^2_0) /r^2))$	-0.0546796	$((r^2- R'^2_0) /r^2)) < 0.1$
r^2_m (LOO)	0.750443	r^2_m (LOO) > 0.5
r^2_m	0.566815	r^2_m>0.5
R^2_p	0.674814	R^2_p>0.5

r^2_{cv}	Cross validated coefficient.
R (or r2)	Correlation coefficient between the actual and predicted activities.
k and k'	Slope values of regression lines.
R^2_0 and R^2_0:	Correlation coefficients for the regression lines through the origin.
$((r^2- R^2_0) /r^2)$and $((r^2- R'^2_0) /r^2)$	To calculate the relation between r^2, R^2_0 , and R'^2_0.
r^2_m (LOO) method.	Modified squared correlation coefficient for the "Leave One Out"

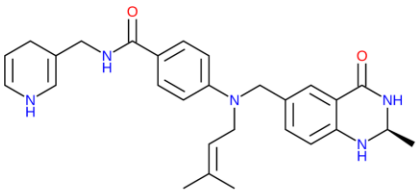

title: 22o.1
phase predicted activity5: 8.22
PIC50: 8.854
phase qsar set: test

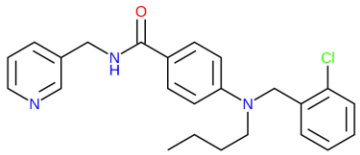

title: 20j.1
phase predicted activity5: 8.15
PIC50: 8.824
phase qsar set: test

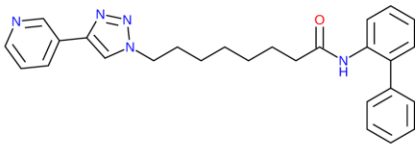

title: 5.1
phase predicted activity5: 8.11
PIC50: 8.523
phase qsar set: test

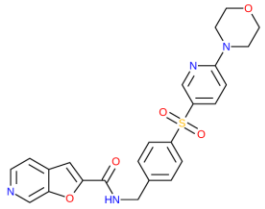

title: 54E K2
phase predicted activity5: 8.9
PIC50: 8.523
phase qsar set: test

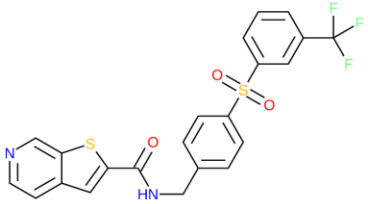

title: 56D K2
phase predicted activity5: 8.07
PIC50: 8.523
phase qsar set: test

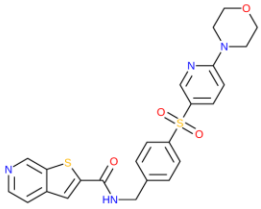

title: 57E K2
phase predicted activity5: 8.71
PIC50: 8.523
phase qsar set: test

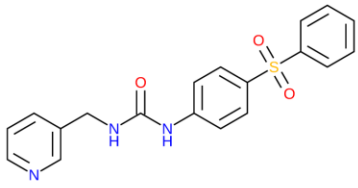

title: 11B K3
phase predicted activity5: 8.34
PIC50: 8.398
phase qsar set: test

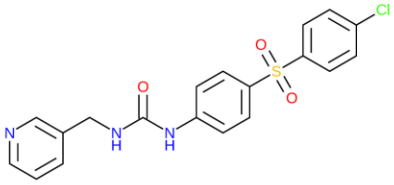

title: 13 K3
phase predicted activity5: 8.63
PIC50: 8.301
phase qsar set: test

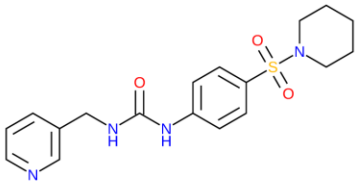

title: 9 K3
phase predicted activity5: 7.82
PIC50: 8.155
phase qsar set: test

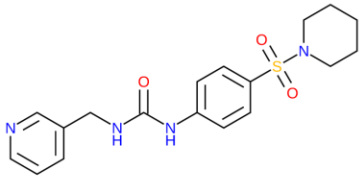

title: 9 A K3
phase predicted activity5: 7.54
PIC50: 8.155
phase qsar set: test

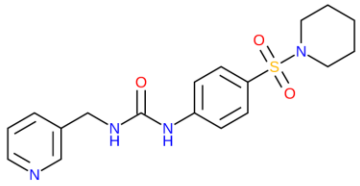

title: 9 K3
phase predicted activity5: 7.57
PIC50: 8.155
phase qsar set: test

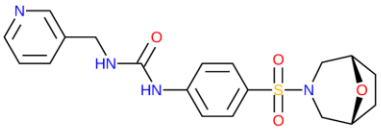

title: 50 K3
phase predicted activity5: 7.66
PIC50: 8.155
phase qsar set: test

Figure 38: Two dimensional structures of test and training set compounds along with experimental and predicted PIC50 values.

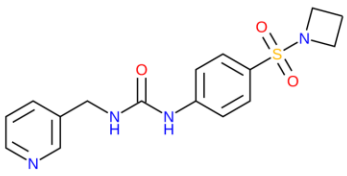

title: 41 K3
phase predicted activity5: 7.05
PIC50: 7.222
phase qsar set: test

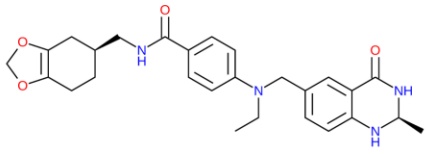

title: 22h.1
phase predicted activity5: 7.22
PIC50: 7.071
phase qsar set: test

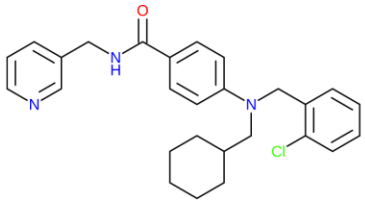

title: 20k.1
phase predicted activity5: 7.88
PIC50: 6.959
phase qsar set: test

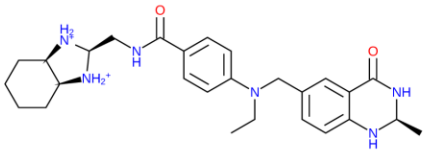

title: 22f.1
phase predicted activity5: 7.08
PIC50: 6.886
phase qsar set: test

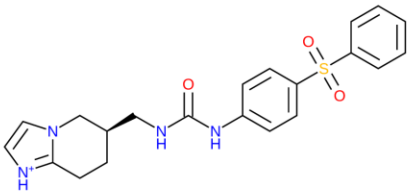

title: 25 B K3
phase predicted activity5: 6.48
PIC50: 6.886
phase qsar set: test

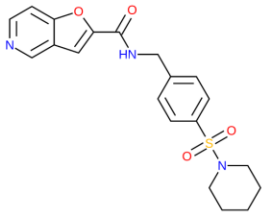

title: 16A K2
phase predicted activity5: 6.53
PIC50: 6.854
phase qsar set: test

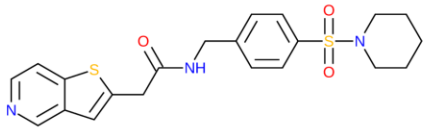

title: 21A K2
phase predicted activity5: 7.34
PIC50: 6.824
phase qsar set: test

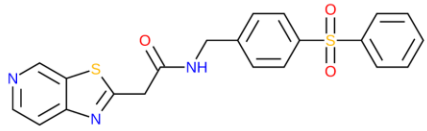

title: 24B K2
phase predicted activity5: 7.0
PIC50: 6.678
phase qsar set: test

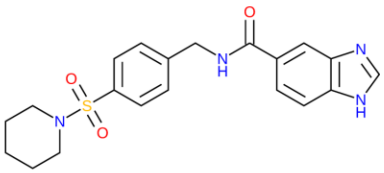

title: 26A K2
phase predicted activity5: 6.16
PIC50: 6.509
phase qsar set: test

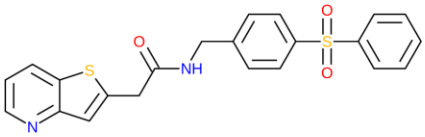

title: 23B K2
phase predicted activity5: 7.03
PIC50: 6.398
phase qsar set: test

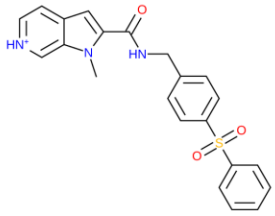

title: 14B K2
phase predicted activity5: 5.92
PIC50: 6.387
phase qsar set: test

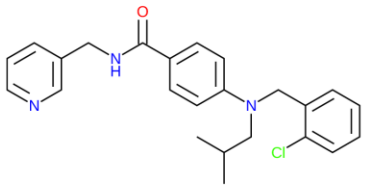

title: 20e.1
phase predicted activity5: 6.53
PIC50: 6.377
phase qsar set: test

Figure 38: Two dimensional structures of test and training set compounds along with experimental and predicted PIC50 values.

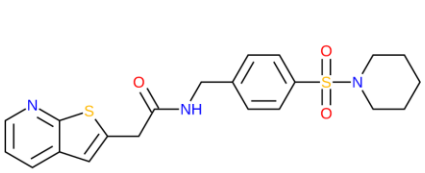

title: 22A K2
phase predicted activity5: 6.75
PIC50: 8.097
phase qsar set: test

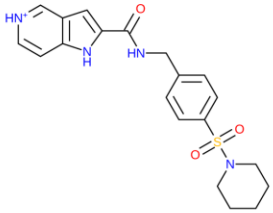

title: 7a k2
phase predicted activity5: 8.15
PIC50: 8.046
phase qsar set: test

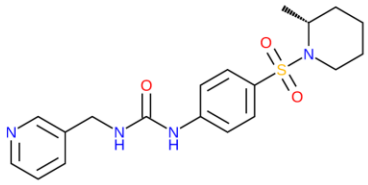

title: 45' K3
phase predicted activity5: 7.03
PIC50: 7.959
phase qsar set: test

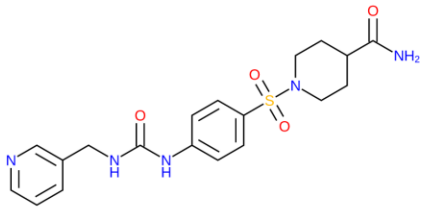

title: 48 K3
phase predicted activity5: 7.71
PIC50: 7.921
phase qsar set: test

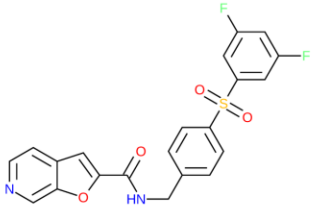

title: 52C K2
phase predicted activity5: 8.21
PIC50: 7.854
phase qsar set: test

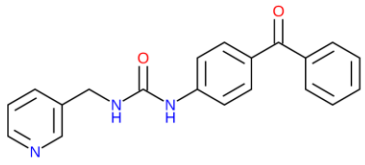

title: 16 K3
phase predicted activity5: 7.69
PIC50: 7.77
phase qsar set: test

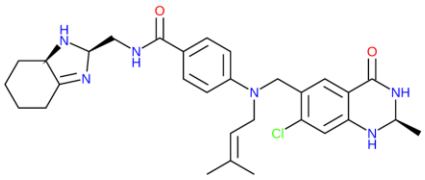

title: 22d.1
phase predicted activity5: 7.58
PIC50: 7.602
phase qsar set: test

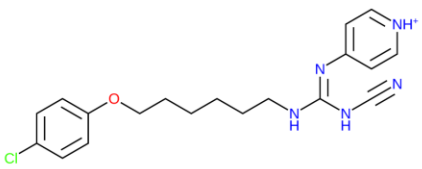

title: GMX1778.1
phase predicted activity5: 7.67
PIC50: 7.602
phase qsar set: test

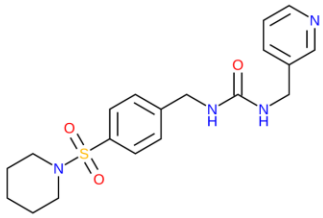

title: 37 A K3
phase predicted activity5: 6.88
PIC50: 7.602
phase qsar set: test

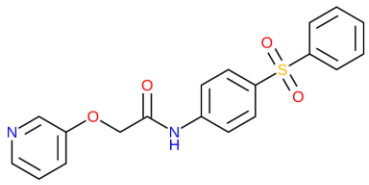

title: 30 B K3
phase predicted activity5: 7.46
PIC50: 7.569
phase qsar set: test

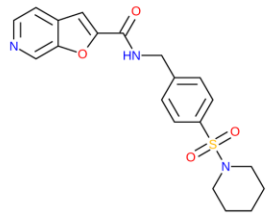

title: 17A K2
phase predicted activity5: 6.79
PIC50: 7.398
phase qsar set: test

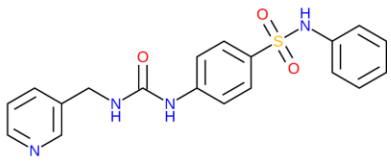

title: 43 K3
phase predicted activity5: 6.86
PIC50: 7.229
phase qsar set: test

Figure 38: Two dimensional structures of test and training set compounds along with experimental and predicted PIC50 values.

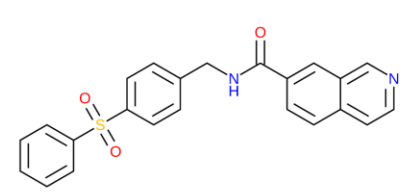

title: 37B K2
phase predicted activity5: 6.01
PIC50: 6.215
phase qsar set: test

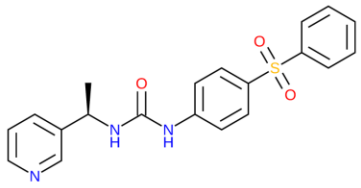

title: 33 B K3
phase predicted activity5: 6.18
PIC50: 6.032
phase qsar set: test

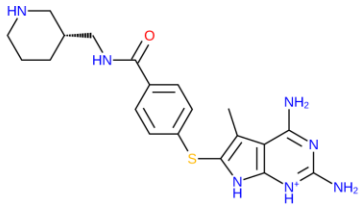

title: 37.1
phase predicted activity5: 6.46
PIC50: 5.921
phase qsar set: test

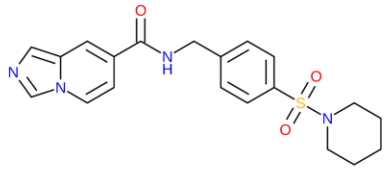

title: 30A K2
phase predicted activity5: 6.0
PIC50: 5.77
phase qsar set: test

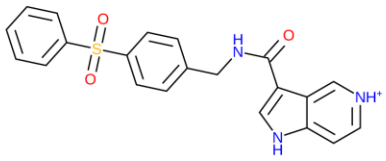

title: 15B K2
phase predicted activity5: 6.62
PIC50: 5.721
phase qsar set: test

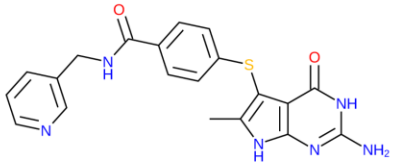

title: 35.1
phase predicted activity5: 6.22
PIC50: 5.553
phase qsar set: test

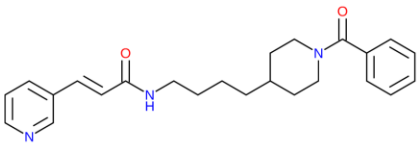

title: crystallig.1
phase predicted activity5: 10.32
PIC50: 10.046
phase qsar set: training

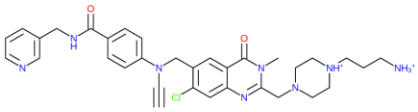

title: 27.1
phase predicted activity5: 9.13
PIC50: 9.523
phase qsar set: training

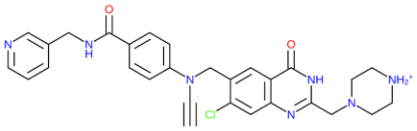

title: 2.1
phase predicted activity5: 9.38
PIC50: 9.509
phase qsar set: training

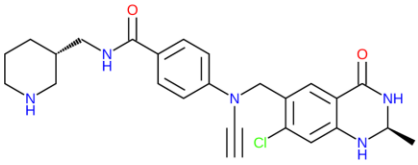

title: 22b.1
phase predicted activity5: 9.43
PIC50: 9.26
phase qsar set: training

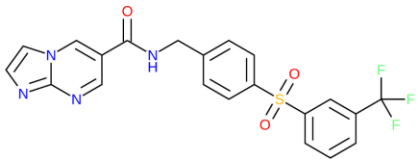

title: 62D K2
phase predicted activity5: 9.2
PIC50: 9.0
phase qsar set: training

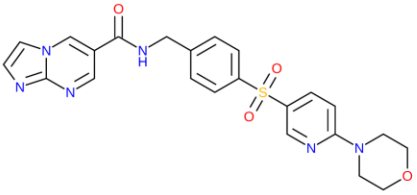

title: 63E K2
phase predicted activity5: 8.94
PIC50: 9.0
phase qsar set: training

Figure 38: Two dimensional structures of test and training set compounds along with experimental and predicted PIC50 values.

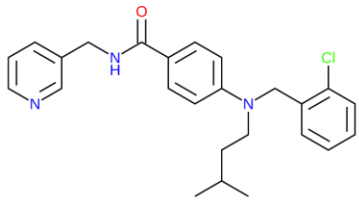

title: 20i.1
phase predicted activity5: 8.95
PIC50: 8.721
phase qsar set: training

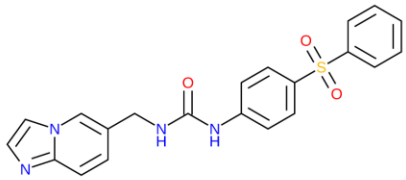

title: 24 B K3
phase predicted activity5: 7.75
PIC50: 8.523
phase qsar set: training

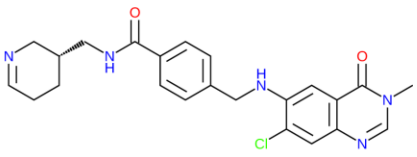

title: 31.1
phase predicted activity5: 8.8
PIC50: 8.42
phase qsar set: training

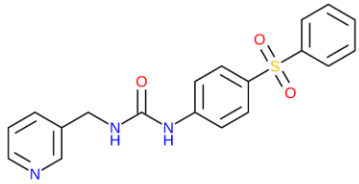

title: 11 K3
phase predicted activity5: 8.34
PIC50: 8.398
phase qsar set: training

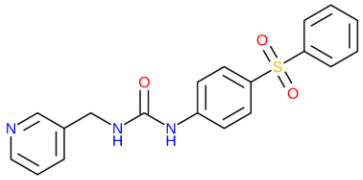

title: 11 B K3
phase predicted activity5: 7.25
PIC50: 8.398
phase qsar set: training

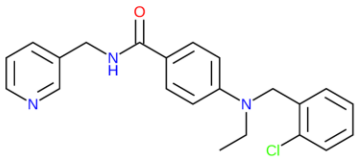

title: 20g.1
phase predicted activity5: 8.17
PIC50: 8.377
phase qsar set: training

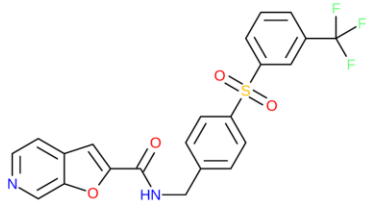

title: 53D K2
phase predicted activity5: 7.75
PIC50: 8.301
phase qsar set: training

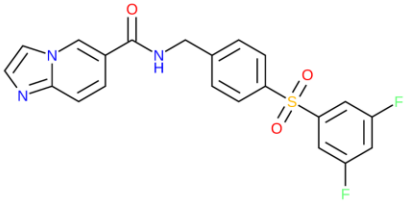

title: 58C K2
phase predicted activity5: 7.79
PIC50: 8.301
phase qsar set: training

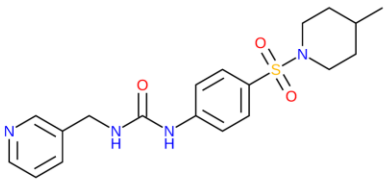

title: 47 K3
phase predicted activity5: 8.6
PIC50: 8.301
phase qsar set: training

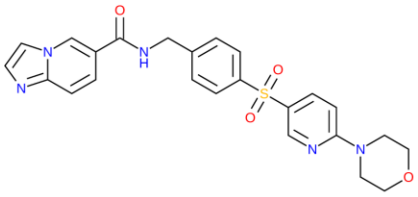

title: 60E K2
phase predicted activity5: 8.83
PIC50: 8.222
phase qsar set: training

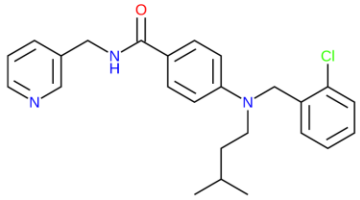

title: 20f.1
phase predicted activity5: 7.9
PIC50: 8.215
phase qsar set: training

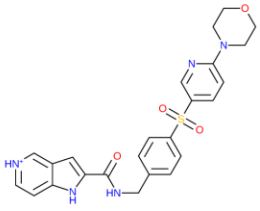

title: 51E
phase predicted activity5: 8.06
PIC50: 8.155
phase qsar set: training

Figure 38: Two dimensional structures of test and training set compounds along with experimental and predicted PIC50 values.

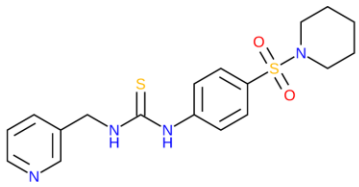

title: 5 K3
phase predicted activity5: 8.32
PIC50: 8.155
phase qsar set: training

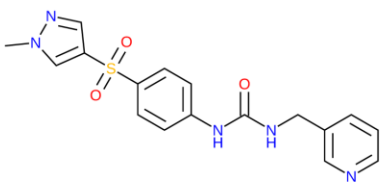

title: 12 K3
phase predicted activity5: 7.43
PIC50: 8.155
phase qsar set: training

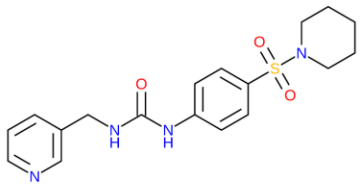

title: 9A K3
phase predicted activity5: 8.08
PIC50: 8.155
phase qsar set: training

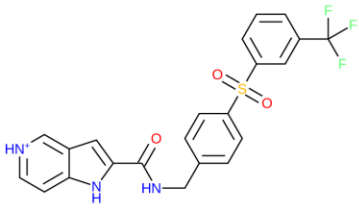

title: 44D K2
phase predicted activity5: 8.21
PIC50: 8.097
phase qsar set: training

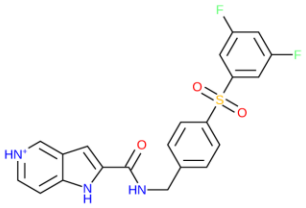

title: 49C
phase predicted activity5: 7.89
PIC50: 8.097
phase qsar set: training

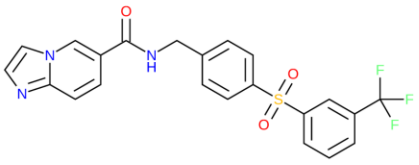

title: 59D K2
phase predicted activity5: 7.73
PIC50: 8.097
phase qsar set: training

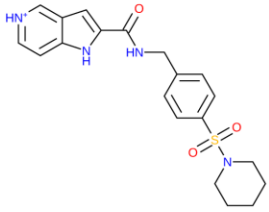

title: 7A K2
phase predicted activity5: 8.15
PIC50: 8.046
phase qsar set: training

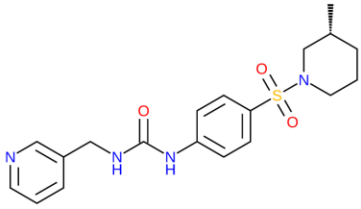

title: 46'' K3
phase predicted activity5: 7.7
PIC50: 8.046
phase qsar set: training

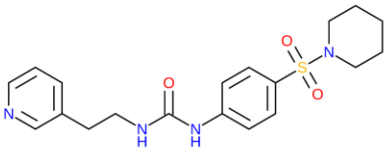

title: 35 A K3
phase predicted activity5: 7.83
PIC50: 8.0
phase qsar set: training

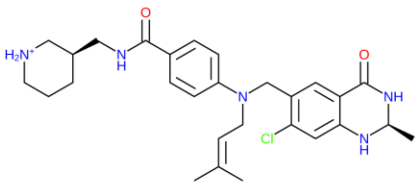

title: 22c.1
phase predicted activity5: 8.47
PIC50: 7.959
phase qsar set: training

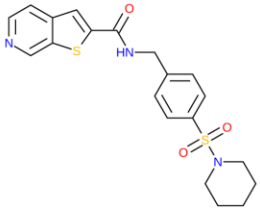

title: 19A K2
phase predicted activity5: 7.77
PIC50: 7.959
phase qsar set: training

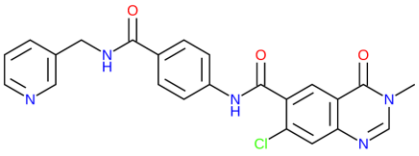

title: 29.1
phase predicted activity5: 7.55
PIC50: 7.921
phase qsar set: training

Figure 38: Two dimensional structures of test and training set compounds along with experimental and predicted PIC50 values.

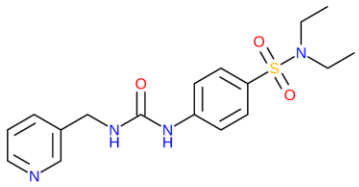

title: 44 K3
phase predicted activity5: 7.64
PIC50: 7.854
phase qsar set: training

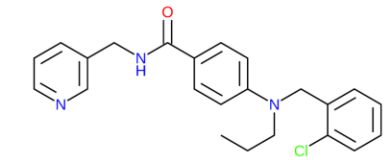

title: 20c.1
phase predicted activity5: 7.98
PIC50: 7.824
phase qsar set: training

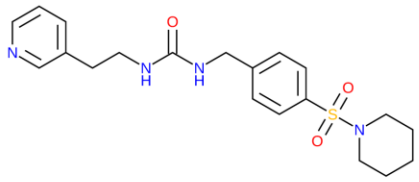

title: 36 A K3
phase predicted activity5: 7.71
PIC50: 7.721
phase qsar set: training

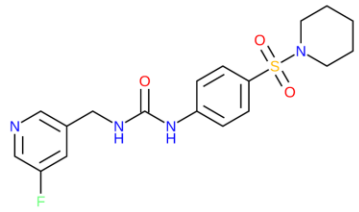

title: 23 A K3
phase predicted activity5: 7.41
PIC50: 7.62
phase qsar set: training

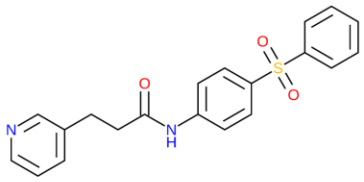

title: 32 B K3
phase predicted activity5: 7.53
PIC50: 7.553
phase qsar set: training

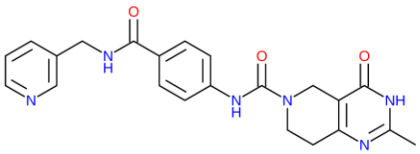

title: 44.1
phase predicted activity5: 7.36
PIC50: 7.538
phase qsar set: training

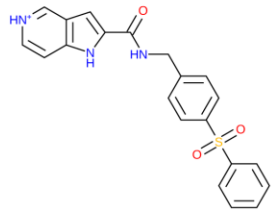

title: 8b k2
phase predicted activity5: 7.66
PIC50: 7.538
phase qsar set: training

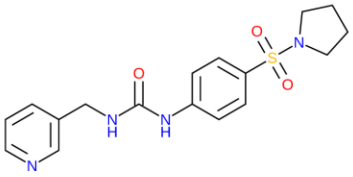

title: 40 K3
phase predicted activity5: 7.48
PIC50: 7.523
phase qsar set: training

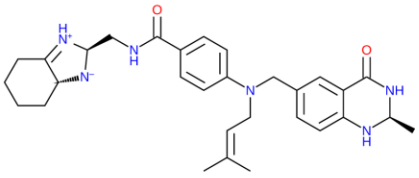

title: 22p.1
phase predicted activity5: 7.57
PIC50: 7.509
phase qsar set: training

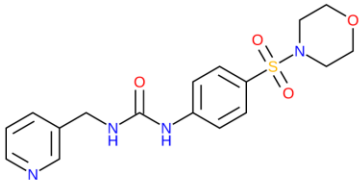

title: 49 K3
phase predicted activity5: 7.43
PIC50: 7.509
phase qsar set: training

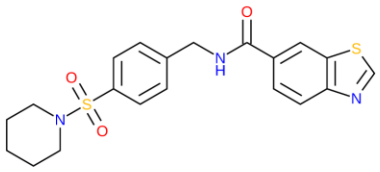

title: 25A K2
phase predicted activity5: 6.66
PIC50: 7.432
phase qsar set: training

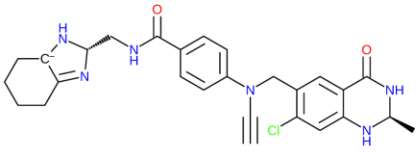

title: 22a.1
phase predicted activity5: 7.35
PIC50: 7.398
phase qsar set: training

Figure 38: Two dimensional structures of test and training set compounds along with experimental and predicted PIC50 values.

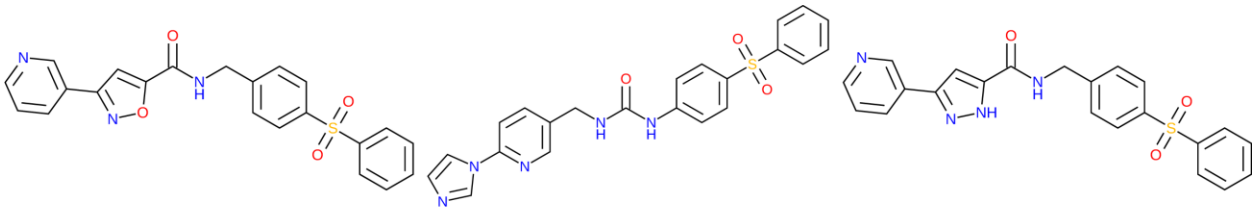

title: 40B K2
phase predicted activity5: 7.23
PIC50: 7.387
phase qsar set: training

title: 26 B K3
phase predicted activity5: 7.29
PIC50: 7.387
phase qsar set: training

title: 39B K2
phase predicted activity5: 7.17
PIC50: 7.367
phase qsar set: training

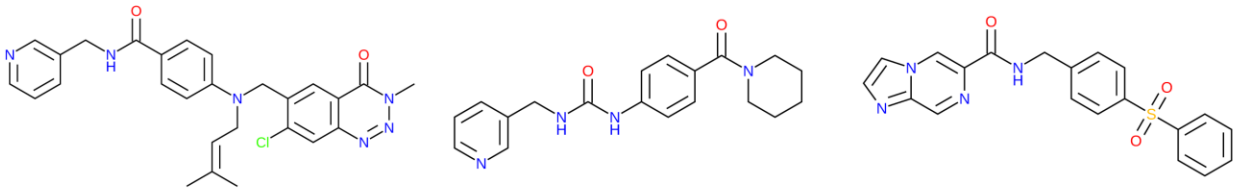

title: 22q.1
phase predicted activity5: 7.68
PIC50: 7.347
phase qsar set: training

title: 17 K3
phase predicted activity5: 7.38
PIC50: 7.31
phase qsar set: training

title: 34B K2
phase predicted activity5: 7.18
PIC50: 6.824
phase qsar set: training

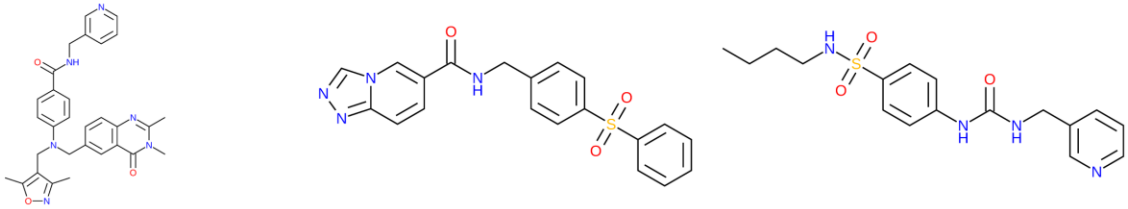

title: 23h.1
phase predicted activity5: 6.96
PIC50: 6.678
phase qsar set: training

title: 35B K2
phase predicted activity5: 6.98
PIC50: 6.432
phase qsar set: training

title: 42 K3
phase predicted activity5: 6.14
PIC50: 6.337
phase qsar set: training

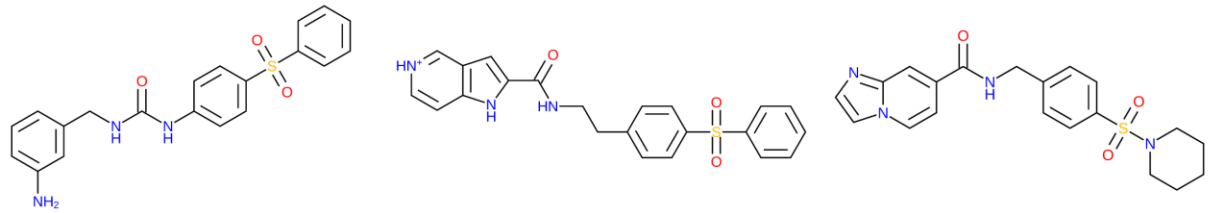

title: 18 A K3
phase predicted activity5: 6.84
PIC50: 6.328
phase qsar set: training

title: 10BK2
phase predicted activity5: 5.88
PIC50: 6.013
phase qsar set: training

title: 31A K2
phase predicted activity5: 6.13
PIC50: 5.745
phase qsar set: training

Figure 38: Two dimensional structures of test and training set compounds along with experimental and predicted PIC50 values.

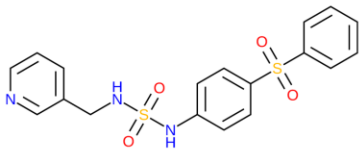

title: 38 B K3
phase predicted activity5: 5.91
PIC50: 5.745
phase qsar set: training

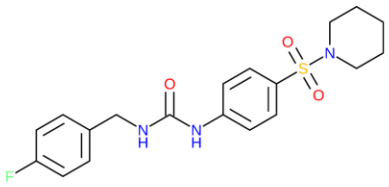

title: 22 A K3
phase predicted activity5: 6.0
PIC50: 5.699
phase qsar set: training

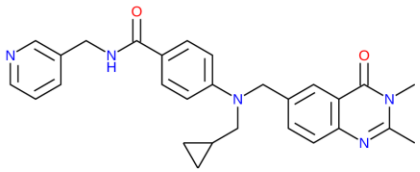

title: 23k.1
phase predicted activity5: 5.52
PIC50: 5.585
phase qsar set: training

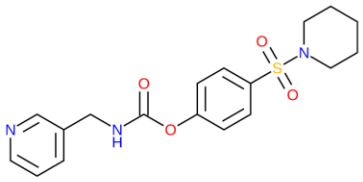

title: 28 A K3
phase predicted activity5: 5.3
PIC50: 5.319
phase qsar set: training

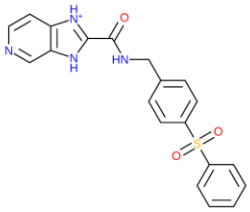

title: 12BK2
phase predicted activity5: 5.67
PIC50: 5.149
phase qsar set: training

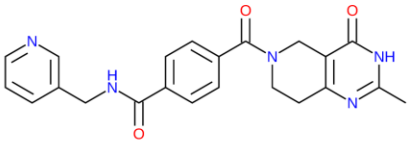

title: 45.1
phase predicted activity5: 5.18
PIC50: 5.143
phase qsar set: training

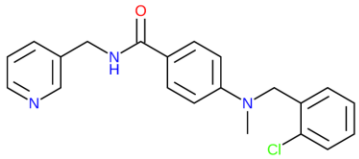

title: 20a.1
phase predicted activity5: 4.97
PIC50: 5.0
phase qsar set: training

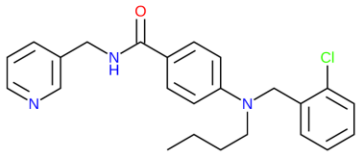

title: 20d.1
phase predicted activity5: 5.33
PIC50: 5.0
phase qsar set: training

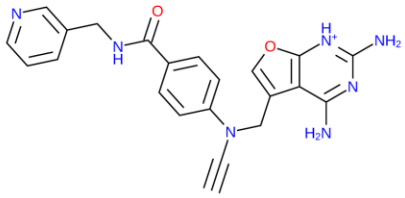

title: 40.1
phase predicted activity5: 4.94
PIC50: 5.0
phase qsar set: training

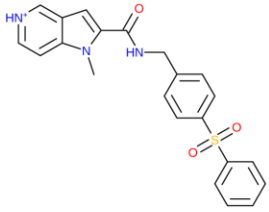

title: 13BK2
phase predicted activity5: 5.13
PIC50: 5.0
phase qsar set: training

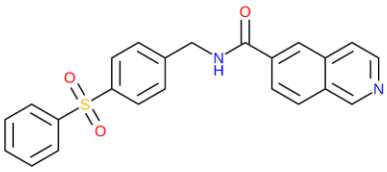

title: 36B K2
phase predicted activity5: 5.59
PIC50: 5.0
phase qsar set: training

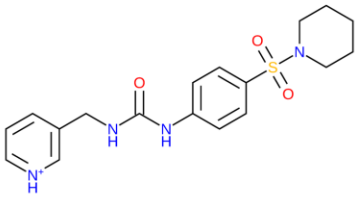

title: 10 K3
phase predicted activity5: 5.01
PIC50: 5.0
phase qsar set: training

Figure 38: Two dimensional structures of test and training set compounds along with experimental and predicted PIC50 values.

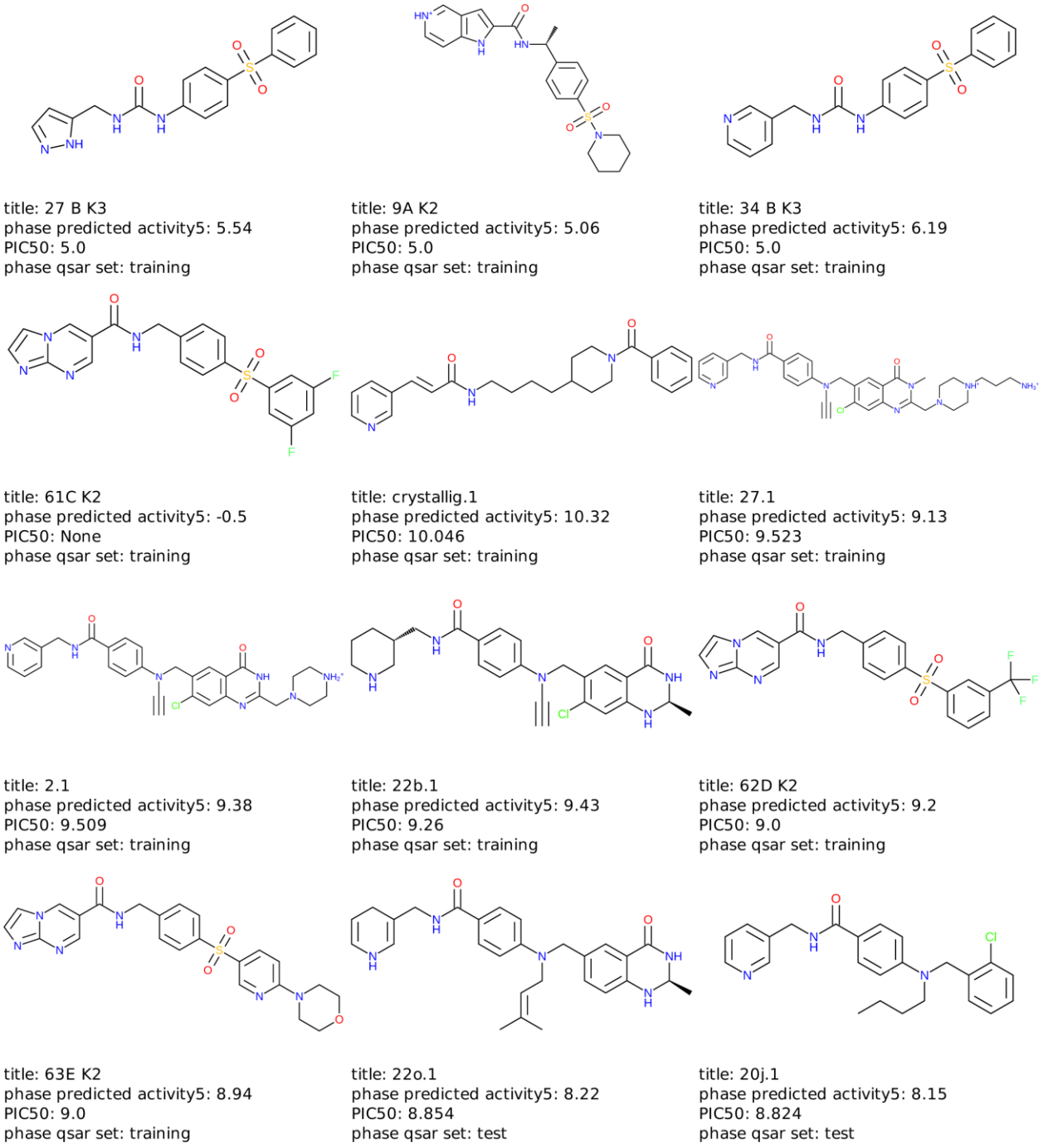

Figure 38: Two dimensional structures of test and training set compounds along with experimental and predicted PIC50 values.

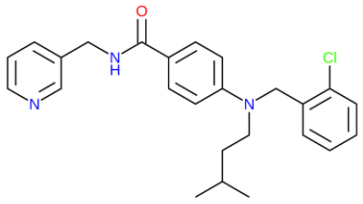

title: 20i.1
phase predicted activity5: 8.95
PIC50: 8.721
phase qsar set: training

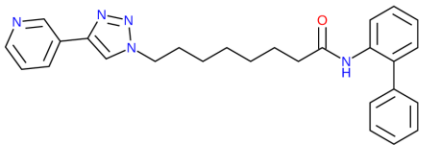

title: 5.1
phase predicted activity5: 8.11
PIC50: 8.523
phase qsar set: test

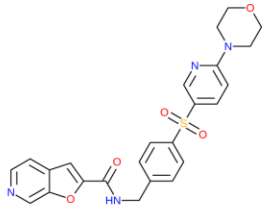

title: 54E K2
phase predicted activity5: 8.9
PIC50: 8.523
phase qsar set: test

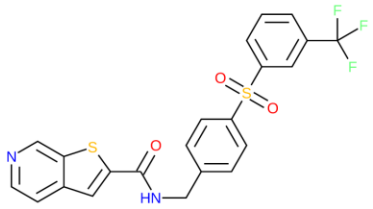

title: 56D K2
phase predicted activity5: 8.07
PIC50: 8.523
phase qsar set: test

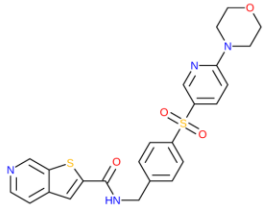

title: 57E K2
phase predicted activity5: 8.71
PIC50: 8.523
phase qsar set: test

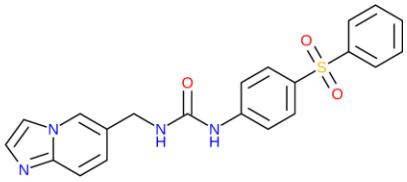

title: 24 B K3
phase predicted activity5: 7.75
PIC50: 8.523
phase qsar set: training

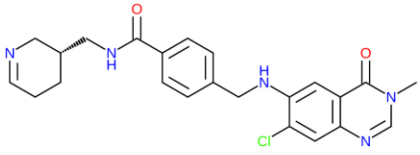

title: 31.1
phase predicted activity5: 8.8
PIC50: 8.42
phase qsar set: training

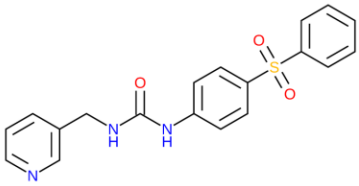

title: 11 K3
phase predicted activity5: 8.34
PIC50: 8.398
phase qsar set: training

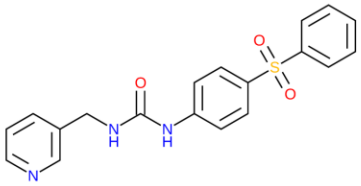

title: 11B K3
phase predicted activity5: 8.34
PIC50: 8.398
phase qsar set: test

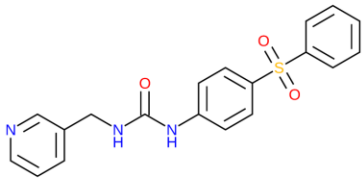

title: 11 B K3
phase predicted activity5: 7.25
PIC50: 8.398
phase qsar set: training

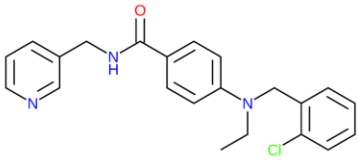

title: 20g.1
phase predicted activity5: 8.17
PIC50: 8.377
phase qsar set: training

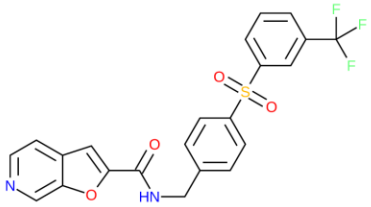

title: 53D K2
phase predicted activity5: 7.75
PIC50: 8.301
phase qsar set: training

Figure 38: Two dimensional structures of test and training set compounds along with experimental and predicted PIC50 values.

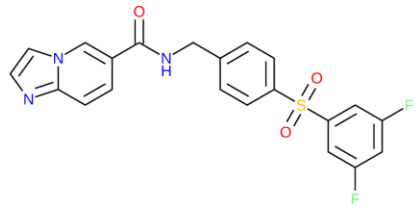

title: 58C K2
phase predicted activity5: 7.79
PIC50: 8.301
phase qsar set: training

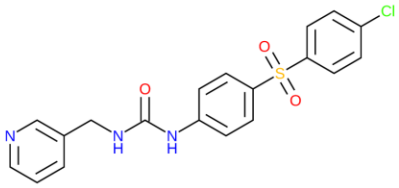

title: 13 K3
phase predicted activity5: 8.63
PIC50: 8.301
phase qsar set: test

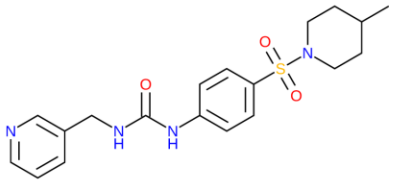

title: 47 K3
phase predicted activity5: 8.6
PIC50: 8.301
phase qsar set: training

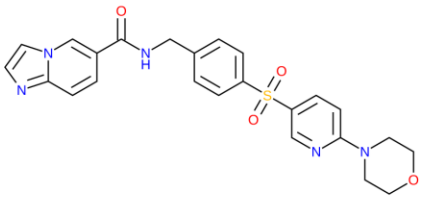

title: 60E K2
phase predicted activity5: 8.83
PIC50: 8.222
phase qsar set: training

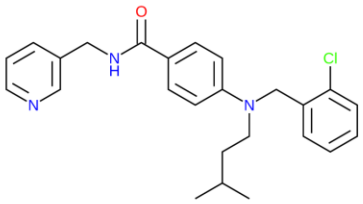

title: 20f.1
phase predicted activity5: 7.9
PIC50: 8.215
phase qsar set: training

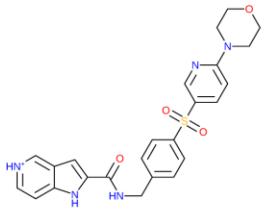

title: 51E
phase predicted activity5: 8.06
PIC50: 8.155
phase qsar set: training

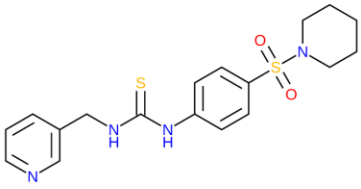

title: 5 K3
phase predicted activity5: 8.32
PIC50: 8.155
phase qsar set: training

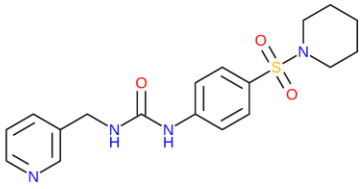

title: 9 K3
phase predicted activity5: 7.82
PIC50: 8.155
phase qsar set: test

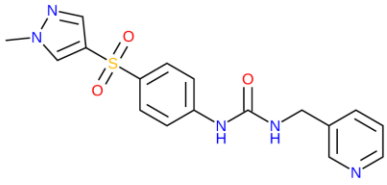

title: 12 K3
phase predicted activity5: 7.43
PIC50: 8.155
phase qsar set: training

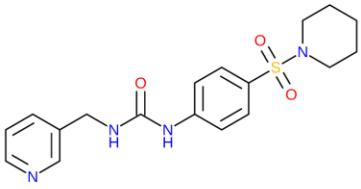

title: 9A K3
phase predicted activity5: 8.08
PIC50: 8.155
phase qsar set: training

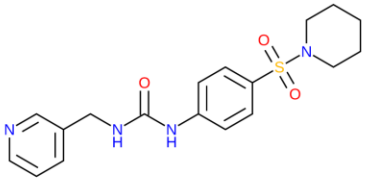

title: 9 A K3
phase predicted activity5: 7.54
PIC50: 8.155
phase qsar set: test

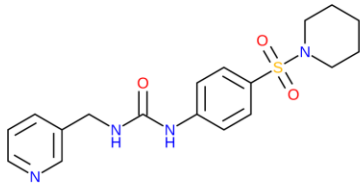

title: 9 K3
phase predicted activity5: 7.57
PIC50: 8.155
phase qsar set: test

Figure 38: Two dimensional structures of test and training set compounds along with experimental and predicted PIC50 values.

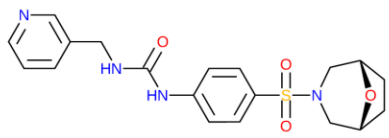

title: 50 K3
phase predicted activity5: 7.66
PIC50: 8.155
phase qsar set: test

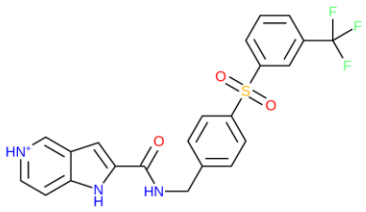

title: 44D K2
phase predicted activity5: 8.21
PIC50: 8.097
phase qsar set: training

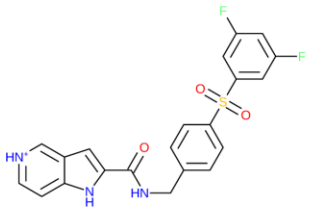

title: 49C
phase predicted activity5: 7.89
PIC50: 8.097
phase qsar set: training

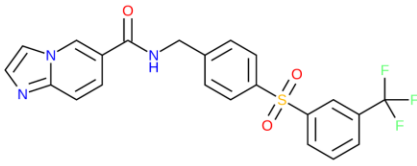

title: 59D K2
phase predicted activity5: 7.73
PIC50: 8.097
phase qsar set: training

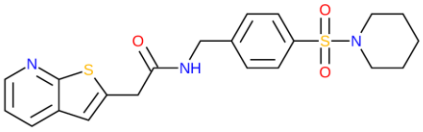

title: 22A K2
phase predicted activity5: 6.75
PIC50: 8.097
phase qsar set: test

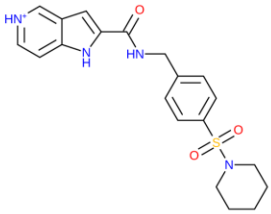

title: 7A K2
phase predicted activity5: 8.15
PIC50: 8.046
phase qsar set: training

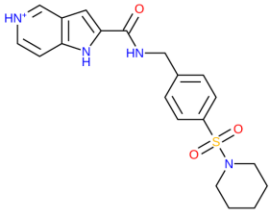

title: 7a k2
phase predicted activity5: 8.15
PIC50: 8.046
phase qsar set: test

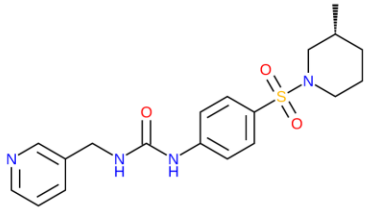

title: 46'' K3
phase predicted activity5: 7.7
PIC50: 8.046
phase qsar set: training

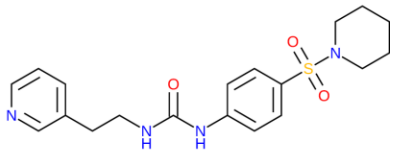

title: 35 A K3
phase predicted activity5: 7.83
PIC50: 8.0
phase qsar set: training

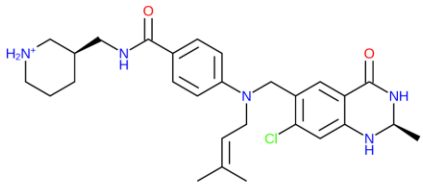

title: 22c.1
phase predicted activity5: 8.47
PIC50: 7.959
phase qsar set: training

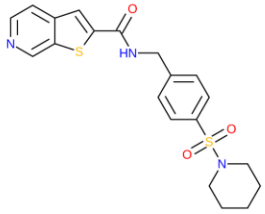

title: 19A K2
phase predicted activity5: 7.77
PIC50: 7.959
phase qsar set: training

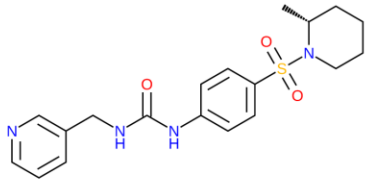

title: 45' K3
phase predicted activity5: 7.03
PIC50: 7.959
phase qsar set: test

Figure 38: Two dimensional structures of test and training set compounds along with experimental and predicted PIC50 values.

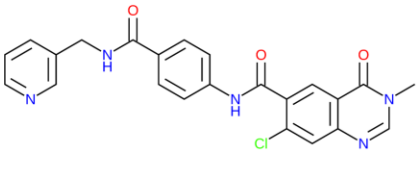

title: 29.1
phase predicted activity5: 7.55
PIC50: 7.921
phase qsar set: training

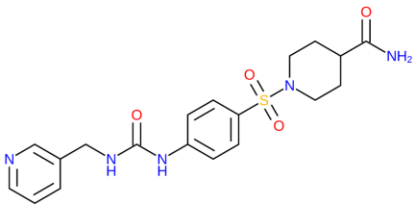

title: 48 K3
phase predicted activity5: 7.71
PIC50: 7.921
phase qsar set: test

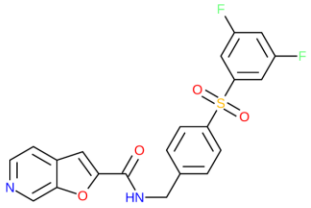

title: 52C K2
phase predicted activity5: 8.21
PIC50: 7.854
phase qsar set: test

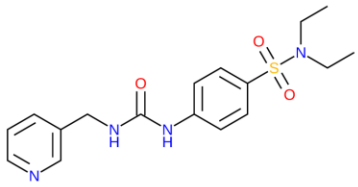

title: 44 K3
phase predicted activity5: 7.64
PIC50: 7.854
phase qsar set: training

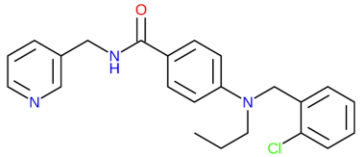

title: 20c.1
phase predicted activity5: 7.98
PIC50: 7.824
phase qsar set: training

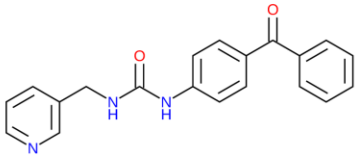

title: 16 K3
phase predicted activity5: 7.69
PIC50: 7.77
phase qsar set: test

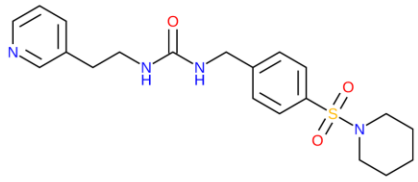

title: 36 A K3
phase predicted activity5: 7.71
PIC50: 7.721
phase qsar set: training

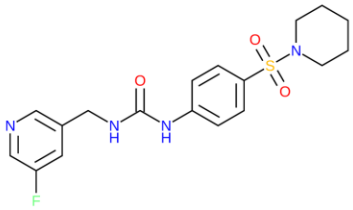

title: 23 A K3
phase predicted activity5: 7.41
PIC50: 7.62
phase qsar set: training

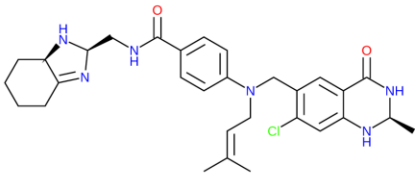

title: 22d.1
phase predicted activity5: 7.58
PIC50: 7.602
phase qsar set: test

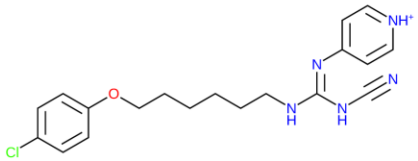

title: GMX1778.1
phase predicted activity5: 7.67
PIC50: 7.602
phase qsar set: test

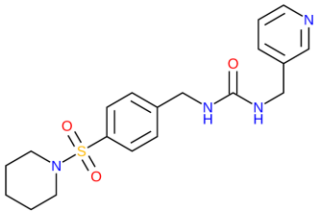

title: 37 A K3
phase predicted activity5: 6.88
PIC50: 7.602
phase qsar set: test

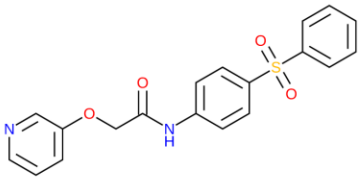

title: 30 B K3
phase predicted activity5: 7.46
PIC50: 7.569
phase qsar set: test

Figure 38: Two dimensional structures of test and training set compounds along with experimental and predicted PIC50 values.

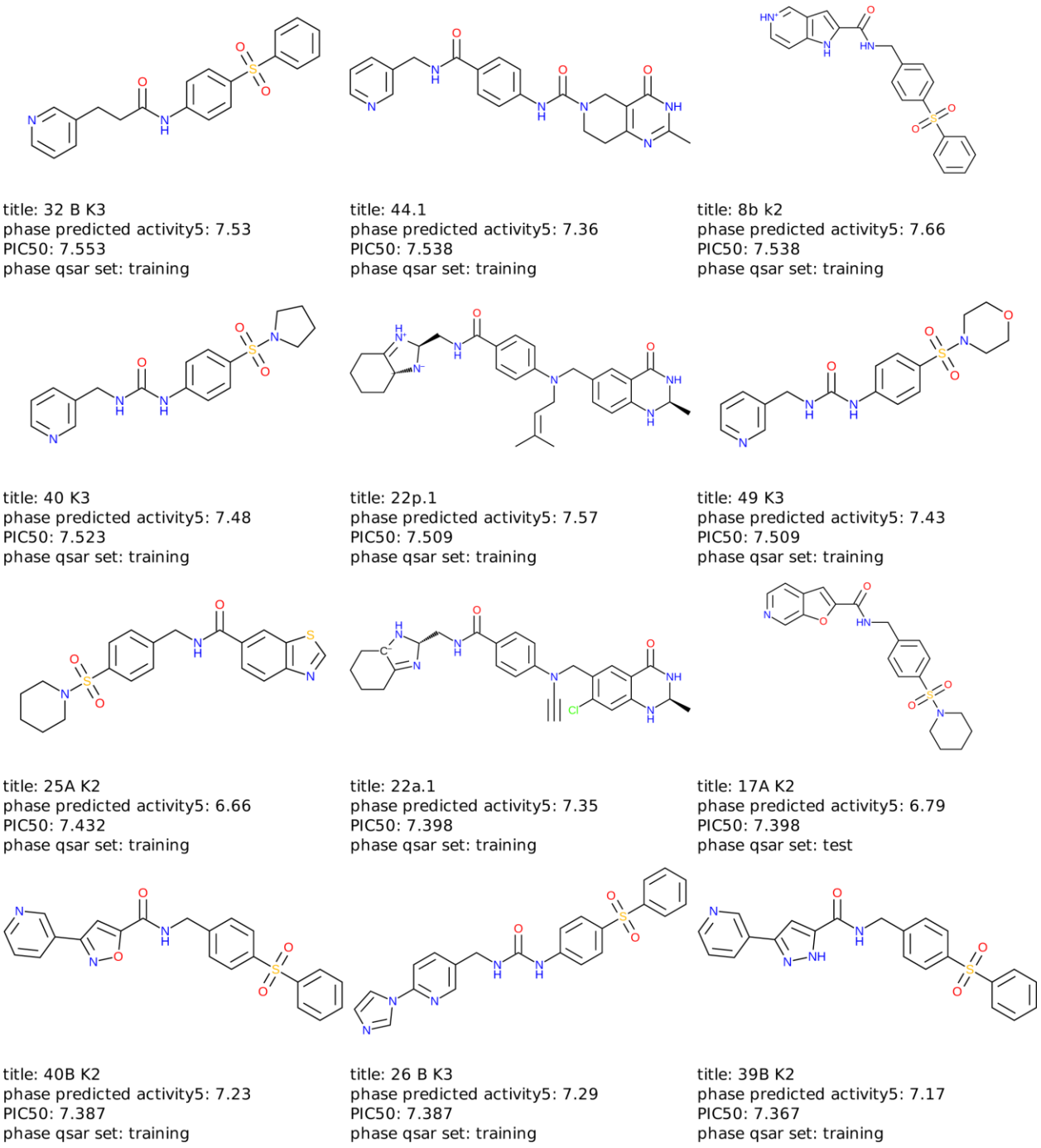

Figure 38: Two dimensional structures of test and training set compounds along with experimental and predicted PIC50 values.

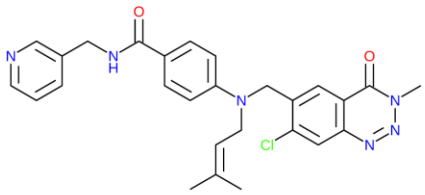

title: 22q.1
phase predicted activity5: 7.68
PIC50: 7.347
phase qsar set: training

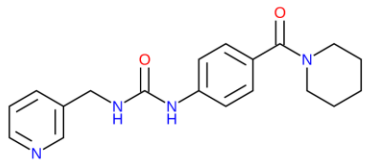

title: 17 K3
phase predicted activity5: 7.38
PIC50: 7.31
phase qsar set: training

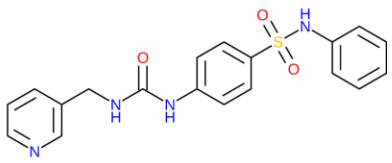

title: 43 K3
phase predicted activity5: 6.86
PIC50: 7.229
phase qsar set: test

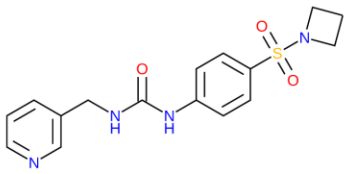

title: 41 K3
phase predicted activity5: 7.05
PIC50: 7.222
phase qsar set: test

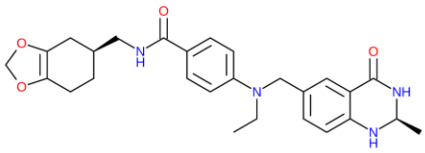

title: 22h.1
phase predicted activity5: 7.22
PIC50: 7.071
phase qsar set: test

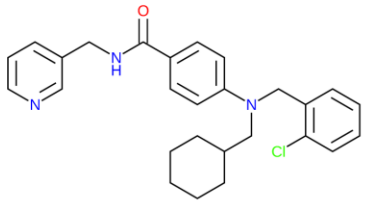

title: 20k.1
phase predicted activity5: 7.88
PIC50: 6.959
phase qsar set: test

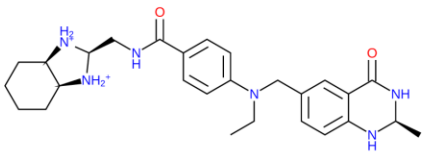

title: 22f.1
phase predicted activity5: 7.08
PIC50: 6.886
phase qsar set: test

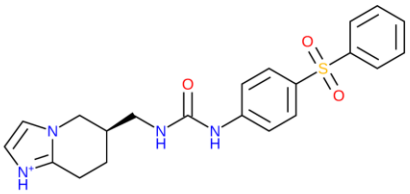

title: 25 B K3
phase predicted activity5: 6.48
PIC50: 6.886
phase qsar set: test

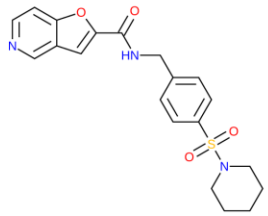

title: 16A K2
phase predicted activity5: 6.53
PIC50: 6.854
phase qsar set: test

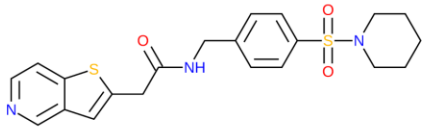

title: 21A K2
phase predicted activity5: 7.34
PIC50: 6.824
phase qsar set: test

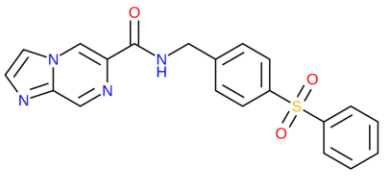

title: 34B K2
phase predicted activity5: 7.18
PIC50: 6.824
phase qsar set: training

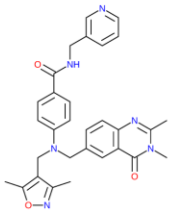

title: 23h.1
phase predicted activity5: 6.96
PIC50: 6.678
phase qsar set: training

Figure 38: Two dimensional structures of test and training set compounds along with experimental and predicted PIC50 values.

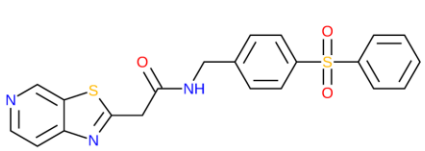

title: 24B K2
phase predicted activity5: 7.0
PIC50: 6.678
phase qsar set: test

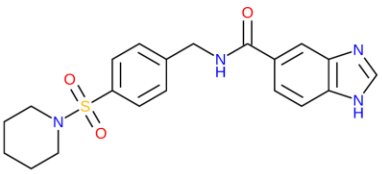

title: 26A K2
phase predicted activity5: 6.16
PIC50: 6.509
phase qsar set: test

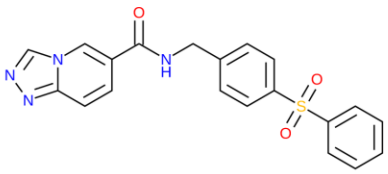

title: 35B K2
phase predicted activity5: 6.98
PIC50: 6.432
phase qsar set: training

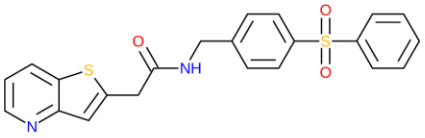

title: 23B K2
phase predicted activity5: 7.03
PIC50: 6.398
phase qsar set: test

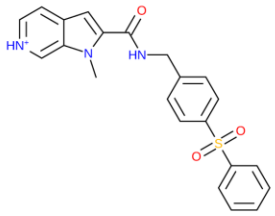

title: 14B K2
phase predicted activity5: 5.92
PIC50: 6.387
phase qsar set: test

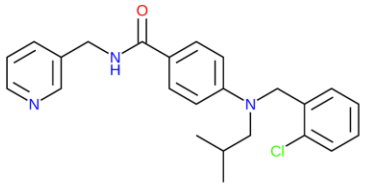

title: 20e.1
phase predicted activity5: 6.53
PIC50: 6.377
phase qsar set: test

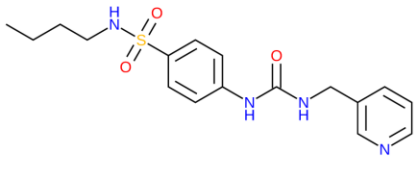

title: 42 K3
phase predicted activity5: 6.14
PIC50: 6.337
phase qsar set: training

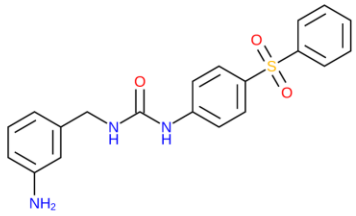

title: 18 A K3
phase predicted activity5: 6.84
PIC50: 6.328
phase qsar set: training

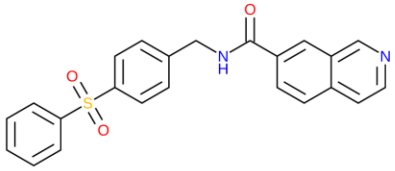

title: 37B K2
phase predicted activity5: 6.01
PIC50: 6.215
phase qsar set: test

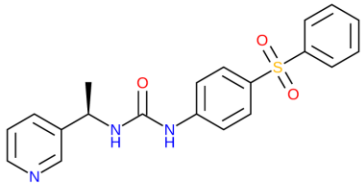

title: 33 B K3
phase predicted activity5: 6.18
PIC50: 6.032
phase qsar set: test

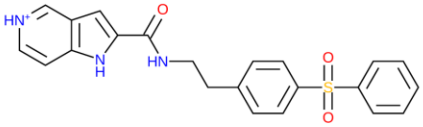

title: 10BK2
phase predicted activity5: 5.88
PIC50: 6.013
phase qsar set: training

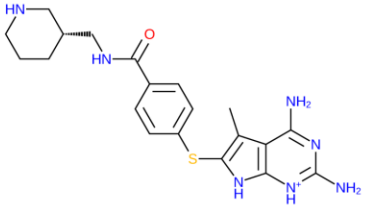

title: 37.1
phase predicted activity5: 6.46
PIC50: 5.921
phase qsar set: test

Figure 38: Two dimensional structures of test and training set compounds along with experimental and predicted PIC50 values.

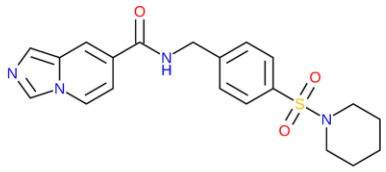

title: 30A K2
phase predicted activity5: 6.0
PIC50: 5.77
phase qsar set: test

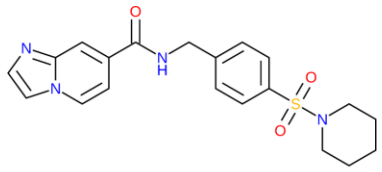

title: 31A K2
phase predicted activity5: 6.13
PIC50: 5.745
phase qsar set: training

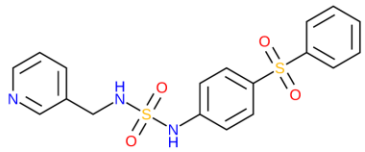

title: 38 B K3
phase predicted activity5: 5.91
PIC50: 5.745
phase qsar set: training

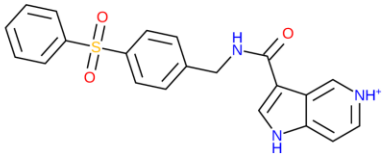

title: 15B K2
phase predicted activity5: 6.62
PIC50: 5.721
phase qsar set: test

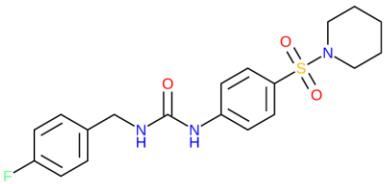

title: 22 A K3
phase predicted activity5: 6.0
PIC50: 5.699
phase qsar set: training

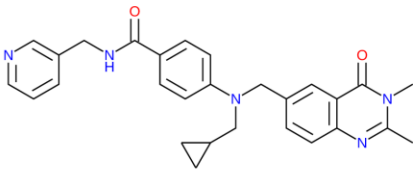

title: 23k.1
phase predicted activity5: 5.52
PIC50: 5.585
phase qsar set: training

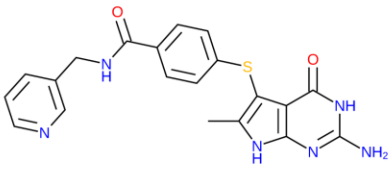

title: 35.1
phase predicted activity5: 6.22
PIC50: 5.553
phase qsar set: test

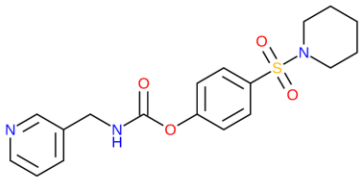

title: 28 A K3
phase predicted activity5: 5.3
PIC50: 5.319
phase qsar set: training

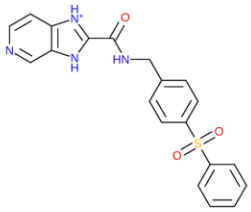

title: 12BK2
phase predicted activity5: 5.67
PIC50: 5.149
phase qsar set: training

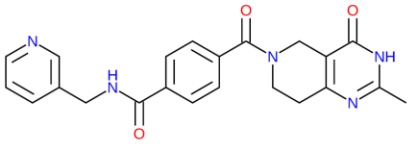

title: 45.1
phase predicted activity5: 5.18
PIC50: 5.143
phase qsar set: training

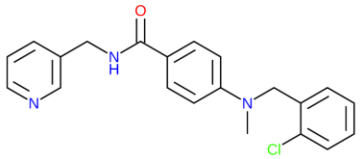

title: 20a.1
phase predicted activity5: 4.97
PIC50: 5.0
phase qsar set: training

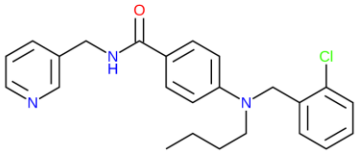

title: 20d.1
phase predicted activity5: 5.33
PIC50: 5.0
phase qsar set: training

Figure 38: Two dimensional structures of test and training set compounds along with experimental and predicted PIC50 values.

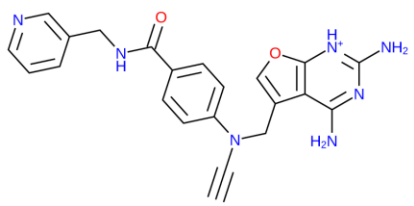

title: 40.1
phase predicted activity5: 4.94
PIC50: 5.0
phase qsar set: training

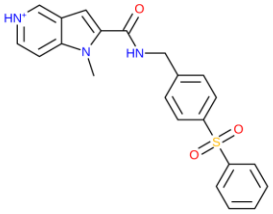

title: 13BK2
phase predicted activity5: 5.13
PIC50: 5.0
phase qsar set: training

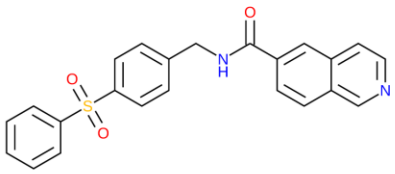

title: 36B K2
phase predicted activity5: 5.59
PIC50: 5.0
phase qsar set: training

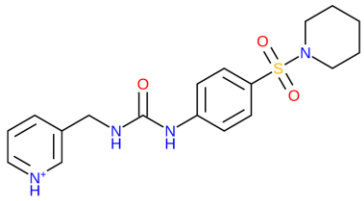

title: 10 K3
phase predicted activity5: 5.01
PIC50: 5.0
phase qsar set: training

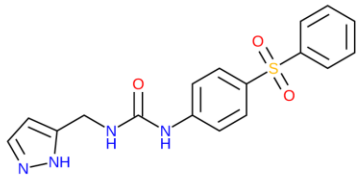

title: 27 B K3
phase predicted activity5: 5.54
PIC50: 5.0
phase qsar set: training

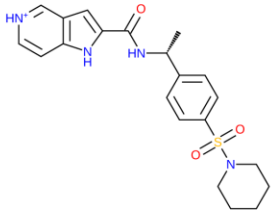

title: 9A K2
phase predicted activity5: 5.06
PIC50: 5.0
phase qsar set: training

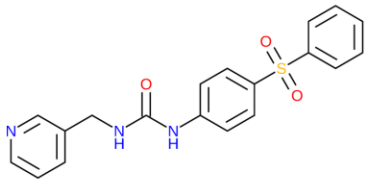

title: 34 B K3
phase predicted activity5: 6.19
PIC50: 5.0
phase qsar set: training

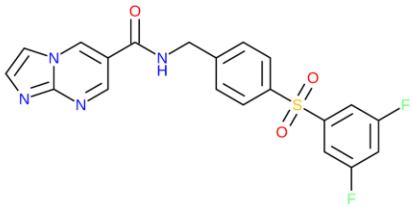

title: 61C K2
phase predicted activity5: -0.5
PIC50: None
phase qsar set: training

Figure 38: Two dimensional structures of test and training set compounds along with experimental and predicted PIC50 values.

5.4.5. In-vitro enzyme inhibition

As discussed in the earlier section, various pharmacophore models were generated employing both ligand (AADR 194) and structure based (4KFO, 4M6P, 4KFN, 4M6Q and 4JNM) drug designing strategies. Later they were subjected to enrichment calculation; the best pharmacophores showing good enrichment factor and goodness of fitness were selected for virtual screening of in-house database. These hits, showing good docking score and hydrogen bonding interactions were shortlisted and presented in **Table 23**.

Most of the compounds shortlisted were from the thiadiazole series of compounds, which were named ND1-10. Interestingly, the scaffold of the molecule identified from the earlier studies was also similar (**Lead 13)**. Hence, considering all the 10 compounds in the series could also help in analyzing structure activity relationship. Almost all the compounds showed hydrogen bond interaction with Asp219, Ser275 and Phe193. Besides, all the compounds also showed pie-pie interactions, signifying the presence of hydrophobic pocket in the protein. All the compounds were initially screened at 40μM concentration (**Table 23**), and molecules that showed more than 50% inhibition were tested at lower concentrations to calculate the IC_{50} values. Among all the compounds **RR2**, **ND2, PS21** have showed more than 50% inhibition IC_{50} of top leads were calculated. Among all RR2 was more potent with IC_{50} of 2.3 μM (**Figure 39**). Further novelty search was carried using various tools like pubchem and scifinder, from which it can be clearly inferred that the molecule (RR2) (**Figure 40**) identified as novel chemical molecule.

Table 23: Top hits resulted from virtual screening

S. No	Ligand name	Hydrogen bonds	Docking score	Important amino acids	%Inhibition at 40 µM
1	**FK866**[a]	1	-6.91	Ser275, Phe193 (P)	82.30 ± 6.62
2	**Lead13**[b]	5	-6.91	Arg349, Lys 189, Arg 196, Asp 219, Tyr 188 and Phe 193	98.59±4.7
3	ND1	2	-6.53	Arg196, Tyr188, Arg 311 (P)	25.29 ± 3.25
4	ND2	3	-6.94	Ala244, Asp219, His191, Phe193 (P), Phe169 (P)	60.92 ± 3.14
5	ND3	1	-6.03	Asp219	32.3 ± 3.96
6	ND4	2	-4.76	Gln305, Asp219, Phe193 (P), Arg196 (P)	31.77 ± 2.52
7	ND5	3	-7.46	His191, Gly385, Gly384, Tyr188 (P), Phe193 (P)	47.22 ± 3.15
8	ND6	0	-6.81	Phe193 (P)	34.81 ± 9.15
9	ND7	1	-6.31	His247, Arg311 (P), tyr188 (P)	22.76 ± 71
10	ND8	1	-6.21	Asp354, Phe193 (P)	2.87 ± 0.6
11	ND9	3	-5.17	Ser275, Lys389, Val356, Arg196 (P), His191 (P)	24.90 ± 9.1
12	ND10	3	-6.11	Arg311, Tyr195, Lys189, Arg196 (P)	33.31 ± 3.62
13	RR2	4	-6.19	Arg349, Asp219, His191 (P), Tyr188, Phe193 (P), Lys189	78.60 ± 8.24
14	PS21	3	-6.80	Arg196, Asp219, Ser275, Phe193 (P)	53.24 ± 6.23
15	PS35	1	-6.78	Phe193, Phe193 (P)	49.43 ± 7.38

[a] FK866 (crystal ligand), [b] Lead 13 (compound from asinex database identified in earlier studies)

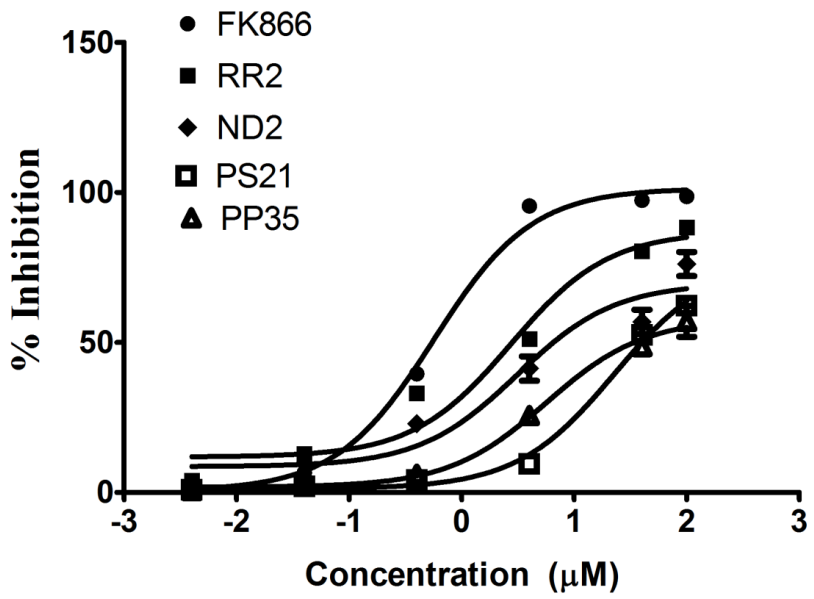

Figure 39: Hill slopes of lead compounds plotted concentration vs % inhibition to determine IC_{50} values

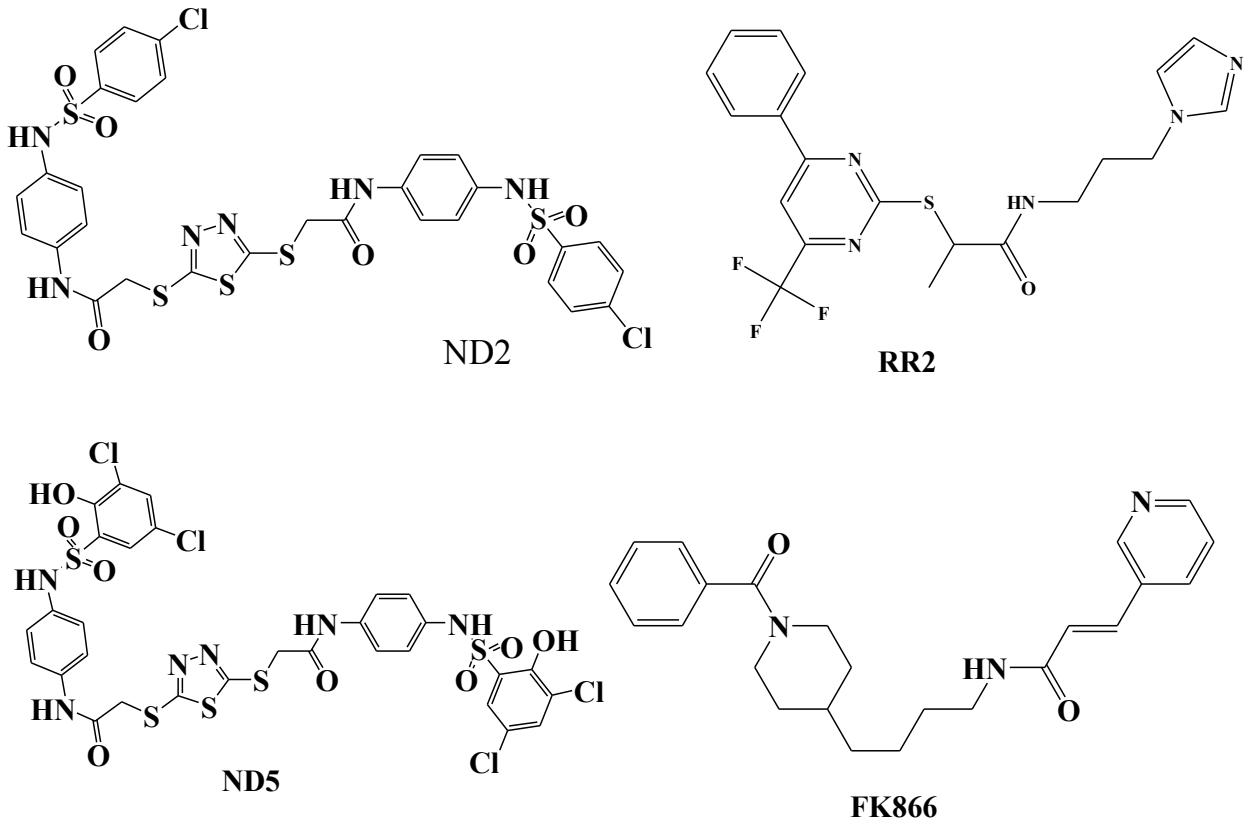

Figure 40: Two dimensional structures of identified leads along with reference compound FK866

5.4.6. Cell proliferation and apoptosis studies

The objective of the current work is to design small molecule inhibitors to treat cancer. Effect of novel leads on cell proliferation of various cancer cell lines best explain the anticancer activity. Due to this reason, growth inhibition concentration 50 (GIC_{50}) was determined on three cancer cell lines. In all the cell lines used in this study reported that NAMPT was over expressed. Hence GIC_{50} would also tell the potency of the compounds inhibiting cell growth by reducing NAD pool inside the cell. In this study FK866 was used as reference control. Among all the compounds FK866 was most potent in all the three cell lines, it could be because of nano molar activity in inhibiting the function of NAMPT, thereby reducing the cellular pool. Besides, no other compound was effective in inhibiting NAMPT activity at such a lower nanomolar concentration, hence all other compounds were inhibiting the growth of the cell lines in micro molar concentration. Among all the cell lines, LnCAP (Prostate cancer) cell line was most inhibited by all the compounds. It could be because of increased expression of NAMPT, compare to other cell lines. ND2 has shown high potency in inhibiting the growth of LnCAP, MDAMB231 and HT29 with GIC_{50} of 173, 398 and 198 nano molar (**Table 24**).

Table 24: GIC_{50} of top leads along with enzyme IC_{50} concentration

	GIC50 (µM)			
Compounds	**LnCAP**	**MDAMB231**	**HT29**	**IC50 (µM)(enzyme)**
RR2	0.142 ± 0.03	4.213 ± 1.21	2.128 ± 0.92	2.73 ± 0.98
ND2	0.173 ± 0.04	0.398 ± 0.07	0.198 ± 0.05	3.11 ± 1.01
PS21	1.453 ± 0.01	5.213 ± 1.21	10.38 ± 2.52	22.81 ± 3.82
PP35	2.783 ± 0.03	3.125 ± 1.03	1.289 ± 0.07	15.04 ± 2.73
FK866	0.059 ± 0.01	0.043 ± 0.01	0.126 ± 0.08	0.561 ± 0.09

Although, from the **Table 24** it was clear that ND2 was potent, yet the mechanism of action in killing the cancer cell line was not understood. Usually any small molecule would inhibit the growth of the cell line either through necrosis or apoptosis. Apoptosis is programmed cell death, which has advantageous in terms of energy with the necrosis. Hence, using annexin-V apoptosis assay was carried out. In the assay, propidum iodide was used a counter stain, staining necrotic cells. From the annexin-V apoptosis assay, it was confirmed that ND2 has reduced the healthy cells and induced apoptosis, which can be known by observing the increase in the apoptotic cells in the second quadrant (25.8%) and decrease in the cells in the first quadrant (**figure 41**). Further, it is interesting to know that the induction of apoptosis is reduced by the addition of NAM. This illustrates that the NAMPT inhibitors inhibit the growth of the cells by reducing NAD pool. After knowing the mechanism of action it is interesting to know the potency of lead ND2 in treating benign prostate hyperplasia.

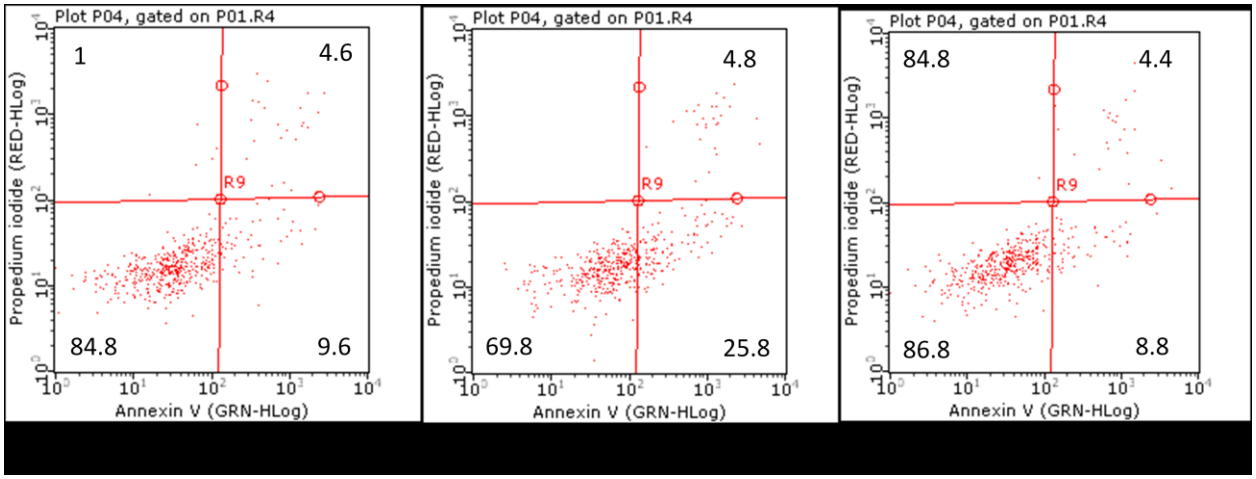

Figure 41: Annexin-V apotosis assay incubated with ND2 and ND2 with Nicotinamide. First quadrant refers to healthy cells, second quadrant refers to early apoptotic cells, third quadrant refers to late apoptotic cells and fourth refers to necrosis.

5.4.7. Testosterone induced benign prostate hyperplasia

From in-vitro enzyme inhibition studies and cell proliferation assays, it was clear that NAMPT inhibitors could be used to treat cancer conditions. As the **lead ND2** showed better activity in LnCAP, it was intriguing to evaluate the activity in benign prostate hyperplasia condition. Here in the animal studies prostate hyperplasia was induced by administering testosterone. In the development of benign prostate hyperplasia, enzyme 5α-reductase catalysed the rate of conversion of testosterone to dihydrotestosterone, which resulted in an increase of dihydrotestosterone in prostate cells which acted on stromal and epithelial cells causing prostate enlargement. From the studies it was clear that prostate gland to body weight ratio was increased 4.7 times in animal administered with testosterone compared to the control animal, however when administered with finasteride (known 5α reductase inhibitor) and **Lead ND2** it was found to be more than 50% reduction in weight (**Table 25**). These results were also supported with histopathological studies, which suggested that normal tissue architecture of the prostate tissue was disrupted (**Figure 42**), which was characterized by glandular hyperplasia with epithelial proliferation and nuclear stratification. However, when treated with Finastiride and **ND2** showed significant reduction in tissue disruption **(Figure 42)**. It was also observed that the cell morphology of the prostate tissue isolated from Group C and D (**Figure 42)** were convincingly comparable with that of the tissue isolated from control group (group A). This confirmed the inhibitory action of the **ND2** on prostate hyperplasia.

Table 25: Weights of prostate gland and associated structures like seminal vesicles, to assess the potency of lead compound prostate weight to body weight ratio was calculated and percentage of inhibition was calculated.

Animal group	P.Wt[a]	S.V Wt[b]	P. Wt /B wt ratio[c]	%Inhibition	Bwt (initial)	Bwt (Final)
Group A[d]	0.950 ± 0.121	0.816 ± 0.092	3.432 ± 0.21		294.34 ± 23.43	287.63 ± 12.34
Group B[e]	2.11 ± 0.304[h]	2.804 ± 0.132[h]	7.353 ± 0.98[h]		273.3 ± 24.83	287.93 ± 26.89
Group C[f]	1.331 ± 0.221[i]	1.427 ± 0.211[i]	4.761 ± 0.67[i]	66.094	279.66 ± 50.63	279.66 ± 32.45
Group D[g]	1.123 ± 0.112[i]	0.812±0.121[j]	4.01 ± 0.54[j]	85.263	278.12 ± 4.21	280.2 ± 3.12

Each group consist of five animals and the values presented in the table is average ± Standard error mean. Statistical analysis was done by one-way ANOVA followed by Bonferroni's multiple comparison tests. [a]
PWt: prostate weight.
[b] SVWt: seminal vesicle weight,
[c] P.Wt/Bwt: prostate weight/ body weight ratio.
[d] Group A: negative control (untreated rat).
[e] Group B: positive control (only testosterone treated rat).
[f] Group C: ND2 (10 mg/kg) treated rat
[g] Group D: Finasteride (5 mg/kg) treated rat..
[h] $P < 0.001$ when compared with normal control.
[i] $P < 0.01$ when compared with testosterone treatment.
[j] $P < 0.001$ when compared with testosterone treatment.

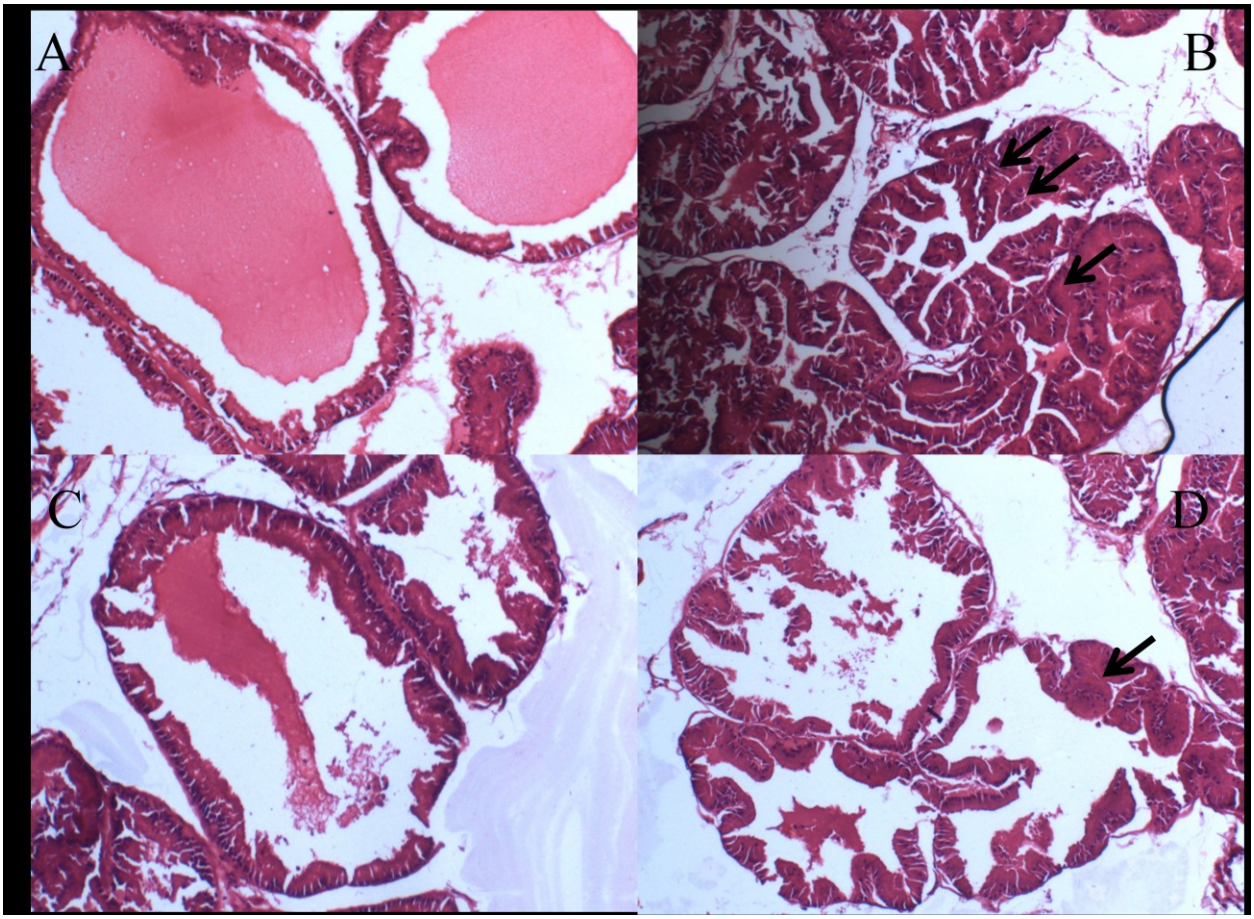

Figure 42: Histopathology of prostate gland stained with haematoxilin and eosin stain. After the tissue fixation and staining, they were magnified 100 times, eventually pictured was captured. The arrow marks indicates the disruption of tissue architecture of prostate tissue because of testosterone induction. A: Control group, B: Testosterone treated group, C: Finasteride treated group and D: ND2 treated group

5.4.8. Carrageenan induced paw inflammation

As discussed in the literature review that NAMPT inhibitors were showed good potency in reducing inflammatory disorders, we have determine to understand the effect of lead ND2 in reducing carragenan induced acute paw inflammation. Carrageenan, a seed weed when administered at the subplantar region, increased the paw volume. Paw volume was determined using plethysmometer and it was observed that there was an increase in the paw volume consistently for 4 h after administration of carrageenan **(Figure 43**). However the effect of

carrageenan was reverted when treated with standard non-steroidal anti-inflammatory drug indomethacin. Interestingly, similar effect was observed when **ND2** was administered to Wistar rats. This proved that NAMPT inhibitor lead ND2 could be considered as an effective lead in treating inflammatory disorders as well.

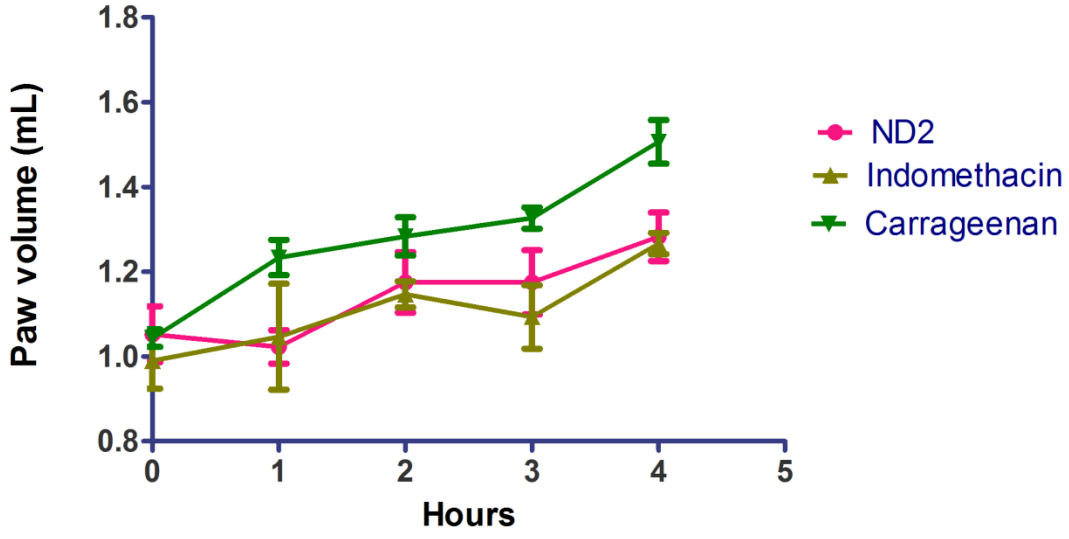

Figure 43: Paw volume measured using plethismometer before and after injection of carrageenan and test compounds at the sub plantar surface of paw

5.4.9 Conclusion:

The objective of this study was to explore new structural moieties inhibiting the function of NAMPT. Employing both structure based and ligand based drug designing strategies identified novel leads. Among all the identified leads obtained after virtual screening lead RR2 was most potent showing IC_{50} of 2.3 µM. The identified molecule was novel and was not reported before showing the inhibitory function of NAMPT. Besides, from in-house database ND2 has shown highest activity in cell proliferation and docking studies. ND2 also showed significant induction of apoptosis after treating LnCAP cells with 10µM concentration for 72 hours. However, when treated with NAM, the apoptosis activity was reduced. This infers that the ND2 acts specifically on NAMPT, thereby reducing the function of NAMPT in reducing the NAD pool. Further, when tested in treating benign prostate hyperplasia, it has shown significant reduction of prostate to

body weight ratio. Thus, signifying the therapeutic importance of ND2 in treating benign prostate hyperplasia. As previous NAMPT inhibitors were used in treating inflammatory disorders, we have tested the effect of ND2 in treating carrageenan induced acute inflammation. In comparisons to treated rats, ND2 has shown reduction in paw volume, which further confirms the effect of ND2 in treating several disorders associated with increase of NAMPT expression.

Chapter 6

6.1 . Drug combination analysis

To further understand the relation between the identified inhibitors (SIRT1 and NAMPT inhibitors) and NAD, GIC_{50} was calculated in the presence and absence of nicotinic acid (**Figure 43**4). There is no significant difference in GIC_{50}, both in the presence and absence of nicotinic acid after incubation with Lead17 (SIRT1 inhibitor), however, there is a significant difference ($P<0.001$) in the presence and absence of nicotinic acid after incubation with NAMPT inhibitors (Lead ND2 and FK866). This infers that nicotinic acid could act as antidote for NAMPT inhibitors, but not for SIRT1 inhibitors.

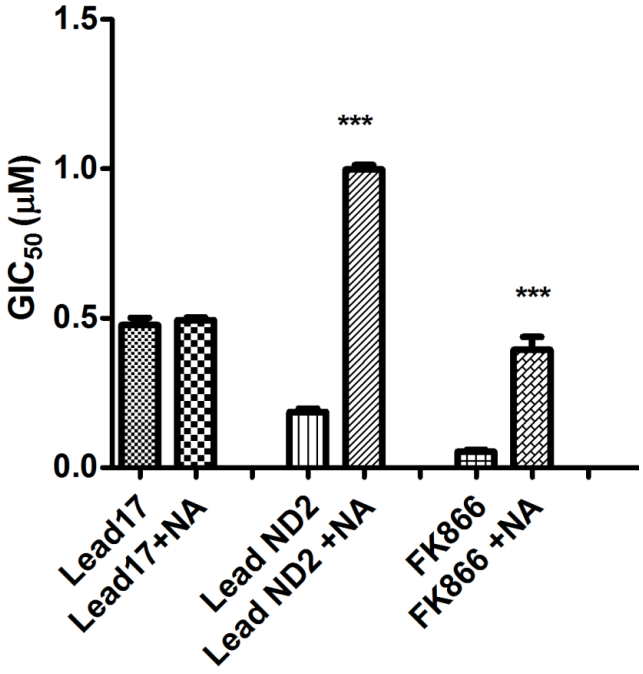

Figure 434: GIC_{50} calculated in presence and absence of nicotinic acid (NA) after incubated with test compounds for 72 hours. Each experiment was done in triplicates (Bonferonni comparision test was performed,(***p value <0.001)

To further understand the relation between SIRT1 and NAMPT, GIC_{50} was calculated with various combinations of SIRT1 and NAMT inhibitors (EX527 and FK866 respectively). Initially GIC_{50} of FK866 was calculated (12nM), however ,after incubation with EX527 (10µM) after 24 hr and 48 hr there is no significant difference in the GIC_{50}. Similar experiments were carried after incubation with nicotinic acid (NA), there is a significant difference in the GIC_{50} when nicotinic acid was added after 24hr. It could be because, nicotinic acid has increased the NAD concentration, thereby increasing the GIC_{50}. It is surprising to know that there is no significant increase in the GIC_{50} when nicotinic acid was added after 48 hr (**Figure 45** A). This may be because of maximum cell death after 24 hr of FK866 incubation. Similar studies were carried with EX527, the GIC_{50} of EX527 is 48µM. There is a significant reduction in GIC_{50} after incubation with FK866 (1µM) at both 24 and 48hr incubation. This could because of nanomolar potency of FK866 compare to micromolar potency of EX527. It infers that the synergic effect of EX527 and FK866 is much more potent than EX527 alone. However, after incubation with nicotinic acid, there is no change in the GIC_{50} (**Figure 45B**). This infers that nicotinic acid does not have any effect on SIRT1 inhibitors.

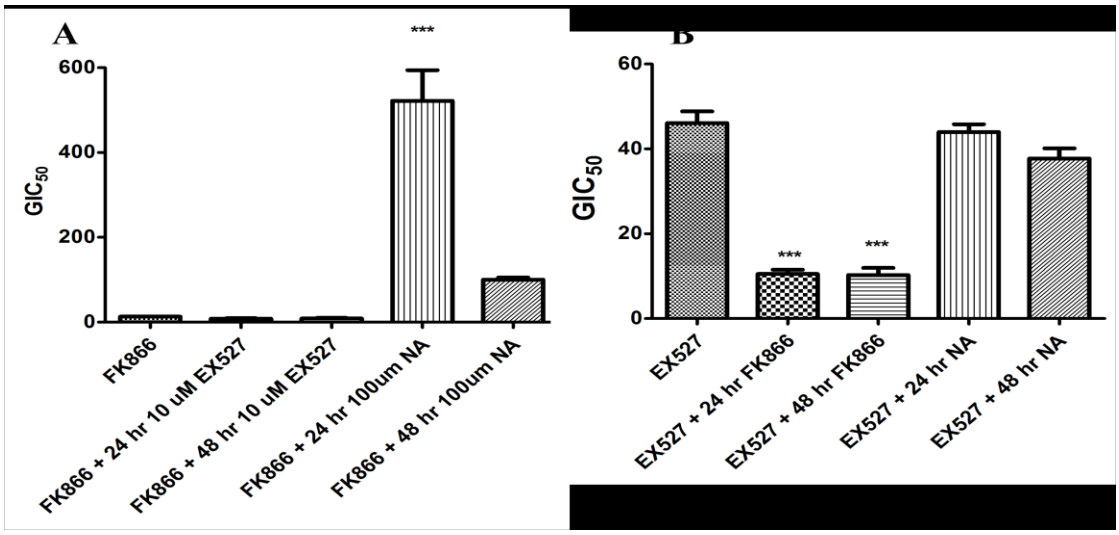

Figure 445: GIC_{50} of FK866 and EX527 in presence and absence of Nicotinic acid (NA). Each experiment was done in triplicates. Dunnet post hoc test was done for statistical validation (***P<0.001)

It is known that AICAR activates the AMPK, which further induce NAD synthesis through NAMPT. It is interesting to know the effect of AICAR on GIC_{50} of FK866. Similarly from the previous reports it is known that myc protein sequesters DBC1, thereby activating SIRT1 and NAMPT. To understand the relation both myc inhibitor and AICAR was used, surprisingly, there is no significant increase in the GIC_{50} of FK866 in addition of AICAR . Similarly, myc inhibition does not cause significant difference. Neverthelss, after incubation with both AICAR and Myc there is a significant increase in the GIC_{50} (**figure 46**A), which was not significant when incubated individually. The possible reason was unknown, it could be because of cross talk between AICAR and myc, or there could be various other mediators between myc and SIRT1. Besides, similar studies were carried in the presence of AICAR and myc , the GIC_{50} of EX527 has significantly increased ($P<0.05$) in the presence of AICAR (Increase in GIC_{50}) and myc inhibitor (Decrease of GIC_{50}) . However, when incubated together, there is a significant decrease in the GIC_{50} (**Figure 46B**). The reason could be better known after understanding the molecular relation between myc, SIRT1 and NAMPT. From all the studies, it was clear that nicotinic acid has an important role in modulating the GIC_{50} of NAMPT inhibitors but not SIRT1 inhibitors. However, from this studies there was no clear relation shown between AICAR, Myc and NAMPT proteins. Further molecular biological techniques need to be employed in future to elucidate the cross talk between these proteins.

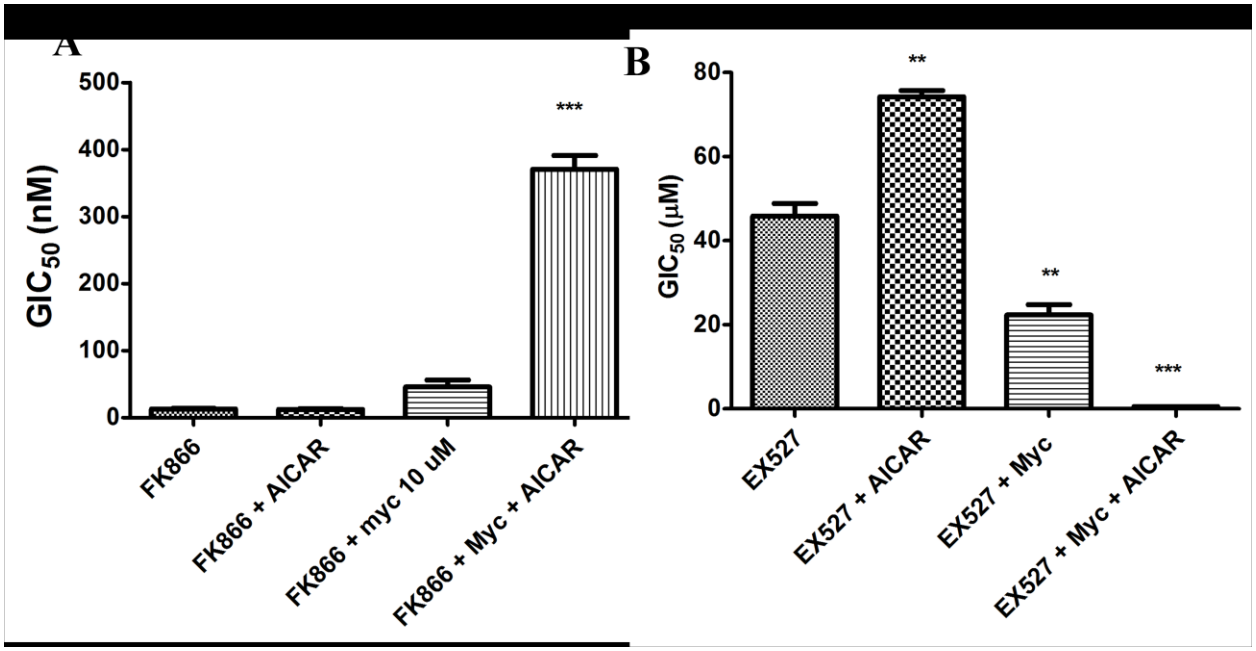

Figure 456: GIC_{50} of FK866 and EX527 in presence and absence of AICAR and myc inhibitor Each experiment was done in triplicates. Dunnet post hoc test was done for statistical validation (** P<0.05; ***P<0.001)

Chapter 7

7.1 Summary and conclusion

The prime objective of entire thesis work is to identify novel SIRT1 and NAMPT inhibitors in treating cancer. In achieving the objective we have employed various strategies including simple virtual screening, epharmacophore and ligand based drug design strategies. Although, docking studies infer the interaction pattern between the small molecules and proteins, it may not always resemble the live condition. However, to save time and money it is considerd being correct strategy in identifying novel leads. Nevertheless, in improving the potency various lead optimization strategies and high-throughput enzyme screening should be carried out. The known inhibitors of SIRT1 and NAMPT were EX527 and FK866 respectively, which were identified a decade ago. As mentioned in the literature review, both the leads showing nanomolar enzyme inhibitory activity were in clinical trials phase II. No other molecule with different structural moiety was identified with higher potency than the above said molecules (EX527 and FK866). As there is room to identify novel structural molecules we have perceived this task and achieved identifying novel leads.

After identifying the leads, effort was also made to understand the mechanism of action. For each set of compounds apoptosis assay was performed to test the mode of growth inhibition. Further, mRNA levels of apoptotic genes were quantified for confirmation. However, specificity of lead molecules acting on a target protein cannot be understood by growth inhibition or apoptosis assay. After effects of inhibition could be linked to apoptosis, but drug specific action can be known quantifying the metabolites or products of the target enzyme reaction. In consideration to NAMPT, NAD levels were quantified after incubation with test compounds; accordingly simultaneous incubation with nicotinic acid along with test compound has reverted

the function. This infers that the designed molecules were specifically binding to NAMPT, thereby shutting down the NAD synthesis.

Besides, as explained in the literature review, inflammation and cancer has close relation. It is been reviewed earlier that chronic inflammation provokes cancer by secreting cytokines and inhibiting the function of DNA repair enzymes. That means leads which inhibit the enzyme function over-expressed in inflammatory disorders have add on advantage. In this perspective the identified leads (I5, Lead17, Lead5, Lead13 and LeadND2) has shown significant inhibition of reactive oxygen species. Further Lead 17 (SIRT1 inhibitor) and Lead ND2 (NAMPT) were tested in carrageenan induced acute paw inflammation and showed reduction in paw volume as compared with indomethacin (NSAID). Thus, confirming the role of both SIRT1 and NAMPT inhibitiors in treating both cancer and inflammatory disorders.

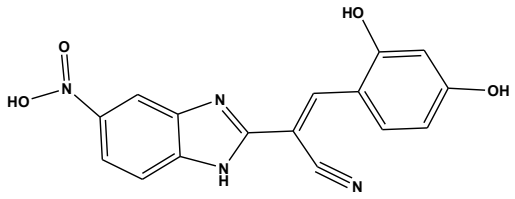

Lead 17

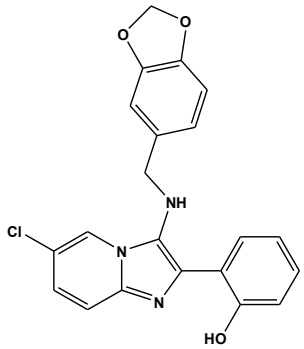

I5

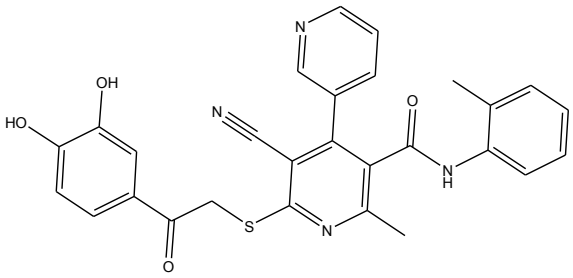

Lead 5

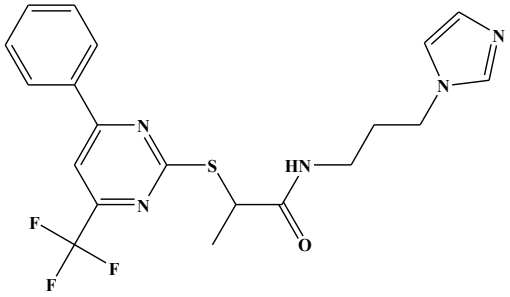

RR2

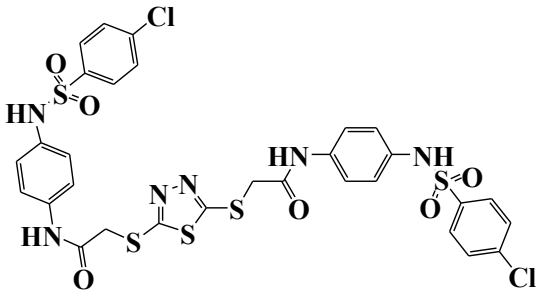

ND2

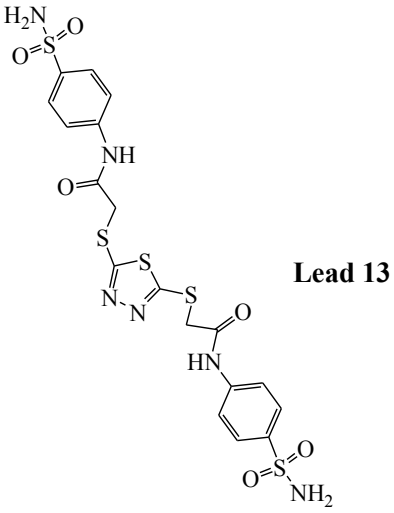

Lead 13

Two dimensional structures of the leads

7.2. Future perspective

Though, calculating GIC_{50} shed a light relating the synergic effect of both SIRT1 and NAMPT inhibitors, but many factors determining the molecular function of the target proteins should be known. Hence detail molecular mechanistic studies could improve the drug development strategies. Nevertheless, the current study has developed some novel leads; further optimization could increase the potency of the leads. To understand the effect of SIRT1 and NAMPT leads in treating cancer, benign prostate hyperplasia model was used. Though the testosterone induced prostate hyperplasia could not be the reason for all prostate cancer, instead cancer induced by the injection of prostate cancer cells could show the precise potency of NAMPT and SIRT1 inhibitors.

References

Avalos J. L., Celic I., Muhammad S., Cosgrove M. S., Boeke J. D., Wolberger C., Structure of a Sir2 enzyme bound to an acetylated p53 peptide. *Mol Cell.* **2002,** 10, 523-35.

Balkwill F. , Mantovani A., Inflammation and cancer: back to Virchow? *The Lancet*. 2001, **357**, 539-545.

Banks A. S., Kon N., Knight C., Matsumoto M., Gutiérrez-Juárez R., Rossetti L., Gu W., Accili D., SirT1 gain of function increases energy efficiency and prevents diabetes in mice. *Cell metabolism*. **2008**, 8, 333-341.

Berger S. L., Kouzarides T., Shiekhattar R., Shilatifard A., An operational definition of epigenetics. *Genes & development*. **2009**, 23, 781-783.

Bhaskara S., Chyla B. J., Amann J. M., Knutson S. K., Cortez D., Sun Z. W., Hiebert S. W., Deletion of histone deacetylase 3 reveals critical roles in S phase progression and DNA damage control. *Mol cell.* **2008**, 30, 61-72.

Bi J., Wang H., Xie J., Comparative genomics of NAD (P) biosynthesis and novel antibiotic drug targets. *J Cell Physiol.* **2011**, 226, 331-340.

Bird A., DNA methylation patterns and epigenetic memory. *Genes Dev.* **2002**, 16, 6-21.

Blum C. A., Ellis J. L., Loh C., Ng P.Y., Perni R. B., Stein R. L., SIRT1 modulation as a novel approach to the treatment of diseases of aging. *J Med Chem.* **2010**, 54, 417-432.

Bolden J. E., Peart M. J., Johnstone R. W., Anticancer activities of histone deacetylase inhibitors. *Nat Rev Drug discov*. **2006,** 5, 769-784.

Bolt H. M., Quantification of endogenous carcinogens: the ethylene oxide paradox. *Biochem Pharmacol.* **1996**, 52, 1-5.

Brunet A., Sweeney L. B., Sturgill J. F., Chua K. F., Greer P. L., Lin Y., Tran H., Ross S. E., Mostoslavsky R., Cohen H. Y., Hu L. S., Cheng H. L., Jedrychowski M. P., Gygi S. P., Sinclair D. A., Alt F. W., Greenberg M. E., Stress-dependent regulation of FOXO transcription factors by the SIRT1 deacetylase. *Science*. **2004,** 303, 2011-2015.

Burgos E. S., and Schramm V. L., Weak Coupling of ATP Hydrolysis to the Chemical Equilibrium of Human Nicotinamide Phosphoribosyltransferase. *Biochemistry*. **2008,** 47, 11086-11096.

Chandra N., Bhagavat R., Sharma E., Sreekanthreddy P., Somasundaram K., Virtual screening, identification and experimental testing of novel inhibitors of PBEF1/Visfatin/NMPRTase for glioma therapy. *J Clin Bioinforma*. **2011**, 1, 5.

Chen W. Y., Wang D. H., Yen R. C., Luo J., Gu W., Baylin S. B., Tumor suppressor HIC1 directly regulates SIRT1 to modulate p53-dependent DNA-damage responses. *Cell*. **2005,** 123, 437-448.

Colombano G., Travelli, C., Galli U., Caldarelli A., Chini M. G., Canonico P. L., Sorba G., Bifulco G., Tron G. C., Genazzani A. A., A novel potent nicotinamide phosphoribosyltransferase inhibitor synthesized via click chemistry. *Journal of medicinal chemistry***. 2009,** 53, 616-623.

Cosgrove M. S., Bever, K., Avalos J. L., Muhammad S., Zhang X., Wolberger C., The structural basis of sirtuin substrate affinity. *Biochemistry*. **2006**, 45, 7511-7521.

Coussens L. M. and Werb. Z., Inflammation and cancer. *Nature.* **2002**, 420, 860-867.

Dalamaga M., Nicotinamide phosphoribosyl-transferase/visfatin: a missing link between overweight/obesity and postmenopausal breast cancer? Potential preventive and therapeutic perspectives and challenges. *Med hypotheses,* **2012,** 79, 617-621.

Danaei G., Vander Hoorn S., Lopez A. D., Murray C. J., Ezzati M., Causes of cancer in the world: comparative risk assessment of nine behavioural and environmental risk factors. *Lancet***, 2005**, 366, 1784-1793.

Das P. M., Singal, R., DNA methylation and cancer. *J Clin Oncol.* **2004**, 22, 4632-4642.

Dietrich L., Muniz, O., Inhibition of nicotinamide phosphoribosyltransferase by pyridine nucleotides. *Biochemistry.* **1972,** 11, 1691-1695.

Disch J. S., Evindar G., Chiu C. H., Blum C. A., Dai H., Jin L., Schuman E., Lind K. E., Belyanskaya S. L., Deng J., Coppo F., Aquilani L., Graybill T. L., Cuozzo J. W., Lavu S., Mao C., Vlasuk G. P., Perni R. B., Discovery of thieno [3, 2-d] pyrimidine-6-carboxamides as potent inhibitors of SIRT1, SIRT2, and SIRT3. *J Med Chem.* **2013**, 56, 3666-3679.

Dvorak, H. F., Tumors: wounds that do not heal: similarities between tumor stroma generation and wound healing. *New Engl J Med.* **1986,** 315, 1650-1659.

Esteller M., Epigenetics in cancer. *New Engl J Med.* **2008**, 358, 1148-1159.

Fan Y., Meng S., Wang Y., Cao J., Wang C., Visfatin/PBEF/Nampt induces EMMPRIN and MMP-9 production in macrophages via the NAMPT-MAPK (p38, ERK1/2)-NF-κB signaling pathway. *Int J Mol Med.* **2011,** 27, 607-615.

Firestein R., Blander, G., Michan S., Oberdoerffer P., Ogino S., Campbell J., Bhimavarapu A., Luikenhuis S., de Cabo R., Fuchs C., Hahn W. C., Guarente L. P., Sinclair D. A., The

SIRT1 deacetylase suppresses intestinal tumorigenesis and colon cancer growth. *PloS one*, **2008, 3**-2020.

Ford J., Ahmed, S., Allison S., Jiang M., Milner J., JNK2-dependent regulation of SIRT1 protein stability. *Cell Cycle.* **2008,** 7, 3091-3097.

Ford J., Jiang, M., Milner J., Cancer-specific functions of SIRT1 enable human epithelial cancer cell growth and survival. *Cancer Res*. **2005,** 65, 10457-10463.

Formentini L., Moroni, F., Chiarugi A., Detection and pharmacological modulation of nicotinamide mononucleotide (NMN) in vitro and in vivo." *Biochem pharmacol.* **2009,** 77, 1612-1620.

Friesner R. A., Banks J. L., Murphy R. B., Halgren T. A., Klicic J. J., Mainz D. T., Repasky M. P., Knoll E. H., Shelley M., Perry J. K., Shaw D. E., Francis P., Shenkin P. S., Glide: a new approach for rapid, accurate docking and scoring. 1. Method and assessment of docking accuracy. *J Med Chem*. **2004,** 47, 1739-1749.

Galli, U., C. Travelli, Massarotti A., Fakhfouri G., Rahimian R., Tron G. C., Genazzani A. A., Medicinal chemistry of nicotinamide phosphoribosyltransferase (NAMPT) inhibitors. *J Med Chem*. **2013,** 56, 6279-6296.

Garten, A., S. Petzold, Barnikol-Oettler A., Körner A., Thasler W. E., Kratzsch J., Kiess W., Gebhardt R., Nicotinamide phosphoribosyltransferase (NAMPT/PBEF/visfatin) is constitutively released from human hepatocytes. *Biochem Biophys Res Comm.* **2010**, 391, 376-381.

Garten, A., Petzold, S., Körner A., Imai S., Kiess W., Nampt: linking NAD biology, metabolism and cancer. *Trends in endocrinology & metabolism.* **2009,** 20, 130-138.

Glozak M., and Seto, E., Histone deacetylases and cancer. *Oncogene.* **2007,** 26, 5420-5432.

Golbraikh A., and Tropsha A., Beware of q 2! *Journal of Molecular Graphics and Modelling*, **2002,** 20, 269-276.

Gossell-Williams, M., Davis, A., O'Connor N., Inhibition of testosterone-induced hyperplasia of the prostate of sprague-dawley rats by pumpkin seed oil. *J Med Food.* **2006,** 9, 284-286.

Gunzner-Toste J., Zhao G., Bauer P., Baumeister T., Buckmelter A. J., Caligiuri M., Clodfelter K. H., Fu B., Han B., Ho Y. C., Kley N., Liang X., Liederer B. M., Lin J., Mukadam S., O'Brien T., Oh A., Reynolds D. J., Sharma G., Skelton N., Smith C. C., Sodhi J., Wang W., Wang Z., Xiao Y., Yuen P. W., Zak M., Zhang L., Zheng X., Bair K. W., Dragovich P. S., Discovery of potent and efficacious urea-containing nicotinamide phosphoribosyltransferase (NAMPT) inhibitors with reduced CYP2C9 inhibition properties. *Bioorg Med Chem Lett.* **2013**, 23, 3531-3538.

Hanahan D., Weinberg, R. A., The hallmarks of cancer. *Cell.* **2000,** 100, 57-70.

Hanahan D., Weinberg R. A., Hallmarks of cancer: the next generation. *Cell*. **2011**, 144, 646-674.

Heltweg B., Gatbonton T., Schuler A. D., Posakony J., Li H., Goehle S., Kollipara R., Depinho R. A., Gu Y., Simon J. A., Bedalov A., Antitumor activity of a small-molecule inhibitor of human silent information regulator 2 enzymes. *Cancer Res.* **2006**, 66, 4368-4377.

Hjarnaa P. J., Jonsson, V. E., Latini S., Dhar S., Larsson R., Bramm E., Skov T., Binderup L.. CHS 828, a novel pyridyl cyanoguanidine with potent antitumor activity in vitro and in vivo. *Cancer Res.* **1999**, 59, 5751-5757.

Huffman D. M., Grizzle W. E., Bamman M. M., Kim J. S., Eltoum I. A., Elgavish A., Nagy T. R., SIRT1 is significantly elevated in mouse and human prostate cancer. *Cancer Res.* **2007**, 67, 6612-6618.

Huhtiniemi T., Suuronen Rinne. T., V. M., Wittekindt C., Lahtela-Kakkonen M., Jarho E., Wallén E. A., Salminen A., Poso A., Leppänen J., Oxadiazole-carbonylaminothioureas as SIRT1 and SIRT2 inhibitors. *J Med Chem.* **2008**, 51, 4377-4380.

Huhtiniemi T., Wittekindt C., Laitinen T., Leppänen J., Salminen A., Poso A., Lahtela-Kakkonen M., Comparative and pharmacophore model for deacetylase SIRT1. *J Comput Aided Mol Des* **2006**, 20, 589-599.

Hussain S. P., and Harris C. C., Molecular epidemiology and carcinogenesis: endogenous and exogenous carcinogens. *Mutat Res*. **2000,** 462, 311-322.

Imai S.I., Armstrong, C. M., Kaeberlein M., Guarente L., Transcriptional silencing and longevity protein Sir2 is an NAD-dependent histone deacetylase. *Nature*. **2000,** 403, 795-800.

Inoue S., Mai A., Dyer M. J., Cohen G. M., Inhibition of histone deacetylase class I but not class II is critical for the sensitization of leukemic cells to tumor necrosis factor–related apoptosis-inducing ligand–induced apoptosis. *Cancer Res.* 2006, 66, 6785-6792.

Jenuwein T., Allis C. D., Translating the histone code. *Science.* **2001,** 293, 1074-1080.

Jin L., Wei W., Jiang Y., Peng H., Cai J., Mao C., Dai H., Choy W., Bemis J. E,, Jirousek M. R., Milne J. C,, Westphal C. H,, Perni R. B., Crystal structures of human SIRT3 displaying substrate-induced conformational changes. *J Biol Chem*. **2009**, 284, 24394-24405.

Johnstone R. W., Histone-deacetylase inhibitors: novel drugs for the treatment of cancer. *Nat Rev Drug discov.* **2002***,* 1, 287-299.

Kaeberlein M., McVey M., Guarente L., The SIR2/3/4 complex and SIR2 alone promote longevity in Saccharomyces cerevisiae by two different mechanisms. *Genes Dev*. 1999, 13, 2570-2580.

Khan J. A., Tao X., Tong L., Molecular basis for the inhibition of human NMPRTase, a novel target for anticancer agents. *Nat Struct Mol Biol*. **2006**, 13, 582-588.

Kim J.E., Chen J., Lou Z., DBC1 is a negative regulator of SIRT1. *Nature*. **2008**, 451, 583-586.

Lain S., Hollick J. J., Campbell J., Staples O. D., Higgins M., Aoubala M., McCarthy A., Appleyard V., Murray K. E., Baker L., Thompson A., Mathers J., Holland S. J., Stark M. J.,Pass G., Woods J., Lane D. P., Westwood N. J., Discovery, in vivo activity, and mechanism of action of a small-molecule p53 activator. *Cancer cell*. **2008,** 13, 454-463.

Lara E., Mai A., Calvanese V., Altucci L., Lopez-Nieva P., Martinez-Chantar M. L., Varela-Rey M., Rotili D., Nebbioso A., Ropero S., Montoya G., Oyarzabal J., Velasco S.,Serrano M., Witt M., Villar-Garea A., Imhof A., Mato J. M., Esteller M., Fraga M. F., Salermide, a Sirtuin inhibitor with a strong cancer-specific proapoptotic effect. *Oncogene.* **2009,** 28, 781-791.

Liang X. J., Finkel T., Shen D. W., Yin J. J., Aszalos A., Gottesman M. M., SIRT1 contributes in part to cisplatin resistance in cancer cells by altering mitochondrial metabolism. *Molecular Cancer Research*. **2008,** 6 1499-1506.

Lim C. S., SIRT1: tumor promoter or tumor suppressor? *Med Hypotheses.* **2006**, 67, 341-344.

Liu, T., Liu, P. Y., Marshall G. M., The critical role of the class III histone deacetylase SIRT1 in cancer. *Cancer research.* **2009**, 69, 1702-1705.

Lövborg H., Burman R., Gullbo J., Structure-activity relationship analysis of cytotoxic cyanoguanidines: selection of CHS 828 as candidate drug. *BMC Res notes.* **2009,** 2, 114.

Loving K., Salam N. K., Sherman W., Energetic analysis of fragment docking and application to structure-based pharmacophore hypothesis generation. *J Comp Aided Mol Des*. **2009,** 23, 541-554.

Maeda H., Akaike T., Reviews-nitric oxide and oxygen radicals in infection, inflammation, and cancer. *Biochemistry*. **1998,** 63, 854-865.

Mai, A., Massa S., Lavu S., Pezzi R., Simeoni S., Ragno R., Mariotti F. R., Chiani F., Camilloni G., Sinclair D. A., Design, synthesis, and biological evaluation of sirtinol analogues as class III histone/protein deacetylase (Sirtuin) inhibitors. *J Med Chem.* **2005**, 48, 7789-7795.

Manjulatha K., Srinivas S., Mulakayala N., Rambabu D., Prabhakar M., Arunasree K. M., Alvala M., Basaveswara Rao M. V., Pal M., Ethylenediamine diacetate (EDDA) mediated synthesis of aurones under ultrasound: Their evaluation as inhibitors of SIRT1. *Bioorganic & medicinal chemistry letters*. **2012,** 22, 6160-6165.

McBurney M. W., Yang X., Jardine K., Bieman M., Th'ng J., Lemieux M., The Absence of SIR2α Protein Has No Effect on Global Gene Silencing in Mouse Embryonic Stem Cells1 1 National Cancer Institute of Canada and the Canadian Institutes of Health Research. *Mol Cancer Res.* **2003,** 1, 402-409.

Michan S., and Sinclair D., Sirtuins in mammals: insights into their biological function. *Biochem. J.* **2007** 404, 1-13.

Min J., Landry J., Sternglanz R., Xu R. M., Crystal structure of a SIR2 homolog–NAD complex. *Cell.* **2001***,* 105, 269-279.

Miremadi A., Oestergaard M. Z., Pharoah P. D., Caldas C., Cancer genetics of epigenetic genes. *Hum Mol Genet*. **2007**, 16, 28-49.

Morris C. J., Carrageenan-induced paw edema in the rat and mouse. *Methods Mol Biol.* **2003**, 225, 115-121.

Mottet D., Bellahcène A., Pirotte S., Waltregny D., Deroanne C., Lamour V., Lidereau R., Castronovo V., Histone deacetylase 7 silencing alters endothelial cell migration, a key step in angiogenesis. *Circ Res***. 2007,** 101, 1237-1246.

Müller A., Homey B., Soto H., Ge N., Catron D., Buchanan M. E., McClanahan T., Murphy E., Yuan W., Wagner S. N., Barrera J. L., Mohar A., Verástegui E., Zlotnik A., Involvement of chemokine receptors in breast cancer metastasis. *Nature.* **2001,** 410, 50-56.

Nakahata, Y., S. Sahar, et al. (2009). "Circadian control of the NAD+ salvage pathway by CLOCK-SIRT1." Science **324**(5927): 654-657.

Napper A. D., Hixon J., Astarita G., Kaluzova M., Sassone-Corsi P., Discovery of Indoles as Potent and Selective Inhibitors of the Deacetylase SIRT1. *J Med Chem.* **2007,** 50, 1086-1086.

Nayagam V. M., Wang X., Tan Y. C., Poulsen A., Goh K. C., Ng T., Wang H., Song H. Y., Ni B., Entzeroth M., Stünkel W., SIRT1 modulating compounds from high-throughput screening as anti-inflammatory and insulin-sensitizing agents. *J Biomol Screen.* **2006,** 11, 959-967.

Niesen F. H., Berglund H., Vedadi M., The use of differential scanning fluorimetry to detect ligand interactions that promote protein stability. *Nat protoc.* **2007,** 2, 2212-2221.

Pan P. W., Feldman J. L., Devries M. K., Dong A., Edwards A. M., Denu J. M., Structure and biochemical functions of SIRT6. *J Biol Chem.* **2011**, 286, 14575-14587.

Park, J. H., Kim, S. H., Choi M. C., Lee J., Oh DY., Im S. A., Bang Y. J., Kim T. Y., Class II histone deacetylases play pivotal roles in heat shock protein 90-mediated proteasomal degradation of vascular endothelial growth factor receptors. *Biochem Biophys Res Comm.* **2008**, 368, 318-322.

Pfluger P. T., Herranz D., Velasco-Miguel S., Serrano M., Tschöp M. H., Sirt1 protects against high-fat diet-induced metabolic damage. *Proc Natl Acad Sci.* **2008,** 105, 9793-9798.

Pittelli, M., Formentini L., Faraco G., Lapucci A., Rapizzi E., Cialdai F., Romano G., Moneti G., Moroni F., Chiarugi A., Inhibition of Nicotinamide Phosphoribosyltransferase cellular bioenergetics reveals a mitochondrial insensitive NAD pool. *J Biol Chem*. **2010**, 285, 34106-34114.

Pratim Roy P., Paul S., Mitra I., Roy K., On two novel parameters for validation of predictive QSAR models. *Molecules.* **2009,** 14, 1660-1701.

Preiss J., Handler P., Biosynthesis of diphosphopyridine nucleotide I. Identification of intermediates. *J Biol Chem.* 1958, 233, 488-492.

Pruitt K., Zinn, R. L., Ohm J. E., McGarvey K. M., Kang S. H., Watkins D. N., Herman J. G., Baylin S. B., Inhibition of SIRT1 reactivates silenced cancer genes without loss of promoter DNA hypermethylation. *PLoS Genet,* **2006,** 2, 40.

Reid G., Gallais R., Métivier R., Marking time: the dynamic role of chromatin and covalent modification in transcription. *Int J Biochem Cell Biol*. **2009,** 41, 155-163.

Revollo J. R., Körner A., Mills K. F., Satoh A., Wang T., Garten A., Dasgupta B., Sasaki Y., Wolberger C., Townsend R. R., Milbrandt J., Kiess W., Imai S., Nampt/PBEF/visfatin regulates insulin secretion in β cells as a systemic NAD biosynthetic enzyme. *Cell Metab*. **2007,** 6, 363-375.

Rous P., Kidd J. G., Conditional neoplasms and subthreshold neoplastic states A study of the tar tumors of rabbits. *J Exp Med.* **1941,** 73, 365-390.

Samal B., Sun Y., Stearns G., Xie C., Suggs S., McNiece I., Cloning and characterization of the cDNA encoding a novel human pre-B-cell colony-enhancing factor. *Mol Cell Biol.* **1994,** 14, 1431-1437.

Sanders B. D., Jackson B., Brent M., Taylor A. M., Dang W., Berger S. L., Schreiber S. L., Howitz K., Marmorstein R., Identification and characterization of novel sirtuin inhibitor scaffolds. *Bioorg MedChem*. **2009,** 17, 7031-7041.

Sasaki, T., B. Maier, Koclega K. D., Chruszcz M., Gluba W., Stukenberg P. T., Minor W., Scrable H.. Phosphorylation regulates SIRT1 function. *PloS one.* **2008,** 3, 4020.

Saunders L., Verdin E., Sirtuins: critical regulators at the crossroads between cancer and aging. *Oncogene*. **2007**, 26, 5489-5504.

Schrödinger, L. LigPrep, version 2.5. New York, NY. **2011.**

Schuetz, A., Min, J., Antoshenko T., Wang C. L., Allali-Hassani A., Dong A., Loppnau P., Vedadi M., Bochkarev A., Sternglanz R., Plotnikov A. N., Structural basis of inhibition of the human NAD+-dependent deacetylase SIRT5 by suramin. *Structure*. **2007**, 15, 377-389.

Schulz W. A., *Molecular biology of human cancers: an advanced student's textbook,* **2005**.

Seligson D. B., Horvath S., Shi T., Yu H., Tze S., Grunstein M., Kurdistani S. K., Global histone modification patterns predict risk of prostate cancer recurrence. *Nature*. **2005**, 435, 1262-1266.

Skokowa J., Lan D., Thakur B. K., Wang F., Gupta K., Cario G., Brechlin A. M., Schambach A., Hinrichsen L., Meyer G., Gaestel M., Stanulla M., Tong Q., Welte K., NAMPT is

essential for the G-CSF–induced myeloid differentiation via a NAD+–sirtuin-1–dependent pathway. *Nat Med*. **2009**, 15, 151-158.

Stünkel W., Peh B. K., Tan Y. C., Nayagam V. M., Wang X., Salto-Tellez M., Ni B., Entzeroth M., Wood J., Function of the SIRT1 protein deacetylase in cancer. *Biotechnol J.* **2007**, 2, 1360-1368.

Suzuki T., Asaba T., Imai E., Tsumoto H., Nakagawa H., Miyata N., Identification of a cell-active non-peptide sirtuin inhibitor containing N-thioacetyl lysine. *Bioorg Med Chem lett***. 2009,** 19, 5670-5672.

Suzuki T., Imai K., Imai E., Iida S., Ueda R., Tsumoto H., Nakagawa H., Miyata N., Design, synthesis, enzyme inhibition, and tumor cell growth inhibition of 2-anilinobenzamide derivatives as SIRT1 inhibitors. *Bioorganic & medicinal chemistry.* **2009,** 17, 5900-5905.

Suzuki T., Imai K., Nakagawa H., Miyata N., 2- Anilinobenzamides as SIRT Inhibitors. *ChemMedChem.* **2006**, 1, 1059-1062.

Tanaka M., Nozaki M., Fukuhara A., Segawa K., Aoki N., Matsuda M., Komuro R., Shimomura I., Visfatin is released from 3T3-L1 adipocytes via a non-classical pathway. *Biochem Biophys Res Comm.* **2007,** 359, 194-201.

Truchon J. F., Bayly C. I., Evaluating virtual screening methods: good and bad metrics for the "early recognition" problem. *J Chem Inf Model.* **2007**, 47, 488-508.

Vander Heiden M. G., Targeting cancer metabolism: a therapeutic window opens. *Nat Rev Drug discov.* **2011**, 10, 671-684.

Vaquero A., Scher M., Lee D., Erdjument-Bromage H., Tempst P., Reinberg D., Human SirT1 interacts with histone H1 and promotes formation of facultative heterochromatin. *Mol Cell*. **2004,** 16 93-105.

Waddington C. H., The epigenotype. 1942. *Int J Epidemiol.* **2012,** 41, 10-13.

Wang C., Chen L., Hou X., Li Z., Kabra N., Ma Y., Nemoto S., Finkel T., Gu W., Cress W. D., Chen J., Interactions between E2F1 and SirT1 regulate apoptotic response to DNA damage. *Nat Cell Biol.* **2006**, 8, 1025-1031.

Wang G. G., Allis C. D., Chi P., Chromatin remodeling and cancer, Part I: Covalent histone modifications. *Trends Mol Med.* **2007,** 13, 363-372.

Wang P., Xu T. Y., Guan Y. F., Su D. F., Fan G. R., Miao C. Y., Perivascular adipose tissue-derived visfatin is a vascular smooth muscle cell growth factor: role of nicotinamide mononucleotide. *Cardiovascular research.* **2008,** 81, 370-80

Wang R. H., Sengupta K., Li C., Kim H. S., Cao L., Xiao C., Kim S., Xu X., Zheng Y., Chilton B., Jia R., Zheng Z. .M, Appella E., Wang X. W., Ried T., Deng C. X., Impaired DNA damage response, genome instability, and tumorigenesis in SIRT1 mutant mice. *Cancer cell.* **2008**, 14, 312-323.

Wang R H., Zheng Y., Li C., Kim H. S., Cao L., Xiao C., Kim S., Xu X., Zheng Y., Chilton B., Jia R., Zheng Z. M., Appella E., Wang X. W., Ried T., Deng C. X., Interplay among BRCA1, SIRT1, and Survivin during BRCA1-associated tumorigenesis. *Mol cell.* **2008**, 32, 11-20.

Wang, T., Zhang X., Bheda P., Revollo J. R., Imai S., Wolberger C., Structure of Nampt/PBEF/visfatin, a mammalian NAD+ biosynthetic enzyme. *Nat Struct Mol Biol.* **2006,** 13, 661-662.

Wang Y., Leung, F. C., An evaluation of new criteria for CpG islands in the human genome as gene markers. *Bioinformatics.* **2004,** 20, 1170-1177.

Weichert W., Röske A. Niesporek S., Noske A., Buckendahl A. C., Dietel M., Gekeler V., Boehm M., Beckers T., Denkert C., Class I histone deacetylase expression has independent prognostic impact in human colorectal cancer: specific role of class I histone deacetylases in vitro and in vivo. *Clin Cancer Res.* **2008**, 14,1669-1677.

Wilson A. J., Byun D. S., Nasser S., Murray L. B., Ayyanar K., Arango D., Figueroa M., Melnick A., Kao G. D., Augenlicht L. H., Mariadason J. M., HDAC4 promotes growth of colon cancer cells via repression of p21. *Molecular biology of the cell.* **2008**, 19, 4062-4075.

Wilson A. J., Byun D. S., Popova N., Murray L. B., L'Italien K., Sowa Y., Arango D., Velcich A., Augenlicht L. H., Mariadason J. M., Histone deacetylase 3 (HDAC3) and other class I HDACs regulate colon cell maturation and p21 expression and are deregulated in human colon cancer. *J BiolChem.* **2006,** 281, 13548-13558.

Yager J. D., Endogenous estrogens as carcinogens through metabolic activation. *J Natl Cancer Inst Monogr.* **2000**, 67-73.

Yammani R. R., Loeser R. F., Extracellular nicotinamide phosphoribosyltransferase (NAMPT/visfatin) inhibits insulin-like growth factor-1 signaling and proteoglycan synthesis in human articular chondrocytes. *Arthritis Res Ther.* **2012**, 14, 23.

Yang, H., T. Yang, et al. (2007). "Nutrient-sensitive mitochondrial NAD+ levels dictate cell survival." Cell **130**(6): 1095-1107.

Yeung F., Hoberg J. E., Baur J. A., Perez E., Matsui T., Carmona J. J., Lamming D. W., Souza-Pinto N. C., Bohr V. A., Rosenzweig A., de Cabo R., Sauve A. A., Sinclair D. A., Modulation of NFκB dependent transcription and cell survival by the SIRT1 deacetylase. *EMBO J.* **2004,** 23, 2369-2380.

Yuan J., Pu M., Zhang Z., Lou Z., Histone H3-K56 acetylation is important for genomic stability in mammals. *Cell Cycle.* **2009**, 8, 1747-1753.

Zhang Q. J., Wang Z., Chen H. Z., Zhou S., Zheng W., Liu G., Wei Y. S., Cai H., Liu D. P., Liang C. C., Endothelium-specific overexpression of class III deacetylase SIRT1 decreases atherosclerosis in apolipoprotein E-deficient mice. *Cardiovasc Res.* **2008,** 80, 191-199.

Zhang R.Y., Qin Y., Lv X. Q., Wang P., Xu T. Y., Zhang L., Miao C. Y., A fluorometric assay for high-throughput screening targeting nicotinamide phosphoribosyltransferase. *Anal Biochem.* **2011,** 412, 18-25.

Zhang, Y., Cheng Y., Ren X., Hori T., Huber-Keener K. J., Zhang L., Yap K. L., Liu D., Shantz L., Qin Z. H., Zhang S., Wang J., Wang H. G., Shih IeM., Yang J. M., Dysfunction of nucleus accumbens-1 activates cellular senescence and inhibits tumor cell proliferation and oncogenesis. *Cancer Res.* **2012,** 72, 4262-4275.

Zhao X., Allison D., Condon B., Zhang F., Gheyi T., Zhang A., Ashok S., Russell M., MacEwan I., Qian Y., Jamison J. A., Luz J. G., The 2.5 Å crystal structure of the SIRT1 catalytic domain bound to nicotinamide adenine dinucleotide (NAD+) and an indole (EX527 analogue) reveals a novel mechanism of histone deacetylase inhibition. *J Med Chem.* **2013,** 56, 963-969.

Zheng X., Bauer P., Baumeister T., Buckmelter A. J., Caligiuri M., Clodfelter K. H., Han B., Ho Y. C., Kley N., Lin J., Reynolds D. J., Sharma G., Smith C. C., Wang Z., Dragovich P. S., Oh A., Wang W., Zak M., Gunzner-Toste J., Zhao G., Yuen PW., Bair K. W., Structure-based identification of ureas as novel nicotinamide phosphoribosyltransferase (Nampt) inhibitors. *J Med Chem.* **2013,** 56, 4921-4937.

Appendix

List of publications from thesis work

1. Pulla, V. K., M. B. Battu, et al. (2012). "Can targeting SIRT-1 to treat type 2 diabetes be a good strategy? A review." Expert opinion on therapeutic targets **16**(8): 819-832.

2. Venkat Koushik Pulla, Mallika Alvala, etal. (2014). "Structure-based drug design of small molecule SIRT1 modulators to treat cancer and metabolic disorders." Journal of Molecular Graphics and Modelling.

3. Venkat Koushik Pulla, Saketh sritam, etal. (2015). "Targeting NAMPT for therapeutic intervention in cancer and inflammation: Structure-based drug design and biological screening." Chemical Biology and Drug Design. (Accepted)

3. Venkat Koushik Pulla, Saketh sritam, etal. (2015). "Energy Based Pharmacophore and 3D QSAR Modeling Combined with Virtual Screening to Identify Novel Small Molecule Inhibitors of SIRT1." Journal of Chemical Information and Modeling. (Communicated)

Other publications

1. Jeankumar, V. U., M. Chandran, et al. (2012). "Development of 5-nitrothiazole derivatives: Identification of leads against both replicative and latent M. tuberculosis." Bioorganic & medicinal chemistry letters.

2. Suman, P., R. N. Rao, et al. "Anti-mycobacterial, cytotoxic activities of Knoevenagel and (E)-α, β-unsaturated esters and ketones from 2-chloronicotinaldehydes." Medicinal Chemistry Research: 1-8.

3. Panathur, N., U. Dalimba, et al. (2013). "Identification and characterization of novel indole based small molecules as anticancer agents through SIRT1 inhibition." European Journal of Medicinal Chemistry.

4. Jeankumar, V. U., R. Janupally, et al. (2013). "Development of novel N-linked aminopiperidine-based mycobacterial DNA gyrase B inhibitors: scaffold hopping from known antibacterial leads." International Journal of Antimicrobial Agents.

5. Janupally, R., V. U. Jeankumar, et al. (2014). "Structure-guided design and development of novel benzimidazole class of compounds targeting DNA GyraseB enzyme of Staphylococcus aureus." Bioorganic & Medicinal Chemistry

Conferences attended

P. Venkat Koushik, P. Yogeeswari, D. Sriram, Designing Small Molecule Inhibitors of NMPRTase as Anticancer leads using in silico approach, 3rd World Congress on Biotechnology,13-15 Septemeber 2012, Hyderabad, India.

Biography of Venkat Koushik Pulla

Venkat Koushik Pulla completed his Bachelor of Science from the Nizam college, Osmania University; Year 2008 and M.Sc (Pharmacology and Biotechnology) from Sheffield Hallam University, UK. He has been appointed as a Junior Research Fellow at Pharmacy department Birla Institute of Technology and Science at Birla Institute of Technology and Sciences (BITS-Pilani), Hyderabad campus, from 2011-2014 under the supervision of Prof. P. Yogeeswari. He was awarded CSIR-Senior Research Fellow from HRDG-CSIR, New Delhi in February 2014. He has published three scientific publications in well-renowned international journals and has presented papers at international conference.

Biography of Prof.P.Yogeeswari

Prof.P.Yogeeswari is presently working in the capacity of professor and Associate Dean (Sponsored Research and Consultancy Division), Department of Pharmacy, Birla Institute of Technology and Science, Pilani, Hyderabad Campus. She received Ph.D. degree in the year 2001 from Banaras Hindu University; Varanasi. She has been involved in research for the last 14 years and in teaching for 13 years. APTI honoured her with YOUNG PHARMACY TEACHER AWARD for the year 2007. In 2010, ICMR honoured her by awarding "Shakuntala Amir Chand Award" for her excellent biomedical research. She has also been granted IASP 2014 award for "Excellence in Pain Research and Management in Developing Countries" under the basic science research category received at the "15th World Congress on Pain" at Argentina in October 2014. She has collaborations with various national and international organizations that include National Institute of Mental Health and Neurosciences, Bangalore, Karolinska Institute, Stockholm, Sweden, National Institute of immunology, New Delhi, India, Pastuer Institute, University of Lille, France, Bogomoletz Institute of Physiology National Academy of Science, Ukraine and Faculty of Medicine of Porto, Portugal,. She has to her credit more than 200 research publications and one Indian Patent granted in November 2014. She is an expert reviewer of many international journals like Journal of Medicinal Chemistry (ACS), Journal of Chemical Information & Modelling (ACS, USA), Bioorganic Medicinal Chemistry (Elsevier), Recent Patents on CNS Drug Discovery (Bentham), etc. She has also co-authored a textbook on organic medicinal chemistry with Prof. D. Sriram titled "Medicinal Chemistry" published by Pearson Education and one book chapter in Jan 2013 by IGI Global. She is a lifetime member of Association of Pharmacy Teachers of India and Indian Pharmaceutical Society. She has

successively completed many sponsored projects and currently on projects sponsored by DST, DBT, INDO-BRAZIL, ICMR-INSERM, and CSIR. She has guided 12 Ph.D students and currently eight students are pursuing their Ph.D work.